ANALYSIS OF THE WTB VERTEX FROM THE MEASUREMENT OF TRIPLE DIFFERENTIAL ANGULAR DECAY RATES OF SINGLE TOP QUARKS PRODUCED IN THE T-CHANNEL AT $\sqrt{S}$ =8 TEV WITH ATLAS DETECTOR

by

Jun Su

B.S.,Sichuan University, 2010

Submitted to the Graduate Faculty of

the Kenneth P. Dietrich School of Arts and

Sciences in partial fulfillment

of the requirements for the degree of

Doctor of Philosophy

University of Pittsburgh

2017

UNIVERSITY OF PITTSBURGH

KENNETH P. DIETRICH SCHOOL OF ARTS AND SCIENCES

This dissertation was presented

by

Jun Su

It was defended on

March 16, 2017

and approved by

Dr.Joseph Boudreau, Professor, Department of Physics and Astromony

Dr.James A Mueller, Associate Professor, Department of Physics and Astronomy

Dr.Andrew R Zentner, Associate Professor, Department of Physics and Astronomy

Dr.Ayres Freitas, Associate Professor, Department of Physics and Astronomy

Dr.Manfred Paulini, Professor, Department of Physics, Carnegie Mellon University

Dissertation Director: Dr.Joseph Boudreau, Professor, Department of Physics and Astromony

ANALYSIS OF THE WTB VERTEX FROM THE MEASUREMENT OF TRIPLE DIFFERENTIAL ANGULAR DECAY RATES OF SINGLE TOP QUARKS PRODUCED IN THE T-CHANNEL AT $\sqrt{S}$ =8 TEV WITH ATLAS DETECTOR

Jun Su, PhD

University of Pittsburgh, 2017

The electroweak production and subsequent decay of single top quarks is determined by the properties of the *Wtb* vertex, which can be described by the complex parameters of an effective Lagrangian. An analysis of angular distributions of the decay products of single top quarks produced in the t-channel constrains these parameters simultaneously. The thesis presents an analysis using 20.2 fb^{-1} of proton–proton collision data at a centre-of-mass energy of 8 TeV collected with the ATLAS detector at the LHC. The fraction f_1 of decays containing transversely polarised W bosons is measured to be $f_1 = 0.296^{+0.048}_{-0.051}$ (stat. + syst.). The phase δ_- between amplitudes for transversely and longitudinally polarised W bosons recoiling against left-handed b quarks, is measured to be $\delta_- = 0.002\pi^{+0.016\pi}_{-0.017\pi}$ (stat. + syst.), giving no indication of CP violation. The fraction of longitudinal to transverse W bosons accompanied by right-handed b-quarks are also constrained at 95% C.L. to $f_1^+ < 0.118$ and $f_0^+ < 0.085$. Based on these measurements limits are placed at 95% C.L. on the ratio of the complex coupling parameters g_R and V_L such that $\mathrm{Re}\,[g_\mathrm{R}/V_\mathrm{L}] \in [-0.122, 0.168]$ and $\mathrm{Im}\,[g_\mathrm{R}/V_\mathrm{L}] \in [-0.066, 0.059]$. Constraints are also placed on the magnitudes of the ratios $|V_\mathrm{R}/V_\mathrm{L}|$, and $|g_\mathrm{L}/V_\mathrm{L}|$. Finally the polarisation of single top quarks in the t-channel is constrained to be $P > 0.718$ (95% C.L.). None of the above measurements make assumptions on the value of any of the other parameters or couplings and all of them are in agreement with the Standard Model.

TABLE OF CONTENTS

LIST OF TABLES

LIST OF FIGURES

1.0 INTRODUCTION

Particle physics is the study of the elementary building blocks of nature. It is often called High Energy Physics because of the tools- accelerators and particle detectors- used in the study of elementary particles.

The idea that matter consists of elementary "building blocks" can be traced back to ancient Greece when Democritus proposed the idea of the atom. However, the idea of atom lacked proof until the end of 19th century when experiment was able to study the constituents of matter. In 1898, Joseph Thompson discovered [13] cathode rays, or electrons-the first subatomic particle discovered, and Thompson's discovery encouraged many advances in the field of particle physics, such as the discovery of the nucleus by Ernest Rutherford [14]. In Rutherford's model, an atom consists of a heavy charged nucleus and a light negatively charged electron orbiting the nucleus. Later in 1932, James Chadwick discovered that all nuclei, except that of simple hydrogen, contains neutral constituents called "neutrons" [15, 16].

Meanwhile, early detector techniques were developed to study elementary particles. In the 1910's, Charles Wilson devised the cloud chamber[1]. In this device, water evaporates in an enclosed container to the point of saturation and under low pressure, producing a super-saturated volume of air. Charged particles pass through the chamber and condense the vapor into tiny droplets, producing a visible trail marking the particle's path. This device was widely used since then and proved to be highly effective in the study of elementary particles. The first "antiparticle", the *positron*, corresponding to the electron provides an

[1]There are other kinds of particle detectors-Geiger counter, bubble chambers, spark chambers, drift chambers, photographic emulsions, and so on. Most detector mechanisms rely on the fact that when high-energy charged particles pass through matter, they ionize atoms and leave tracks along their path

example. In 1928, the relativistic quantum theory of P.A.M Dirac hypothesized the existence of positively charged electron [17], which is the antiparticle of the electron. It was detected by Carl Anderson in 1932 [18] when he allowed cosmic rays to pass through a cloud chamber surrounded by a magnet.

The strong interaction is responsible for holding the nucleus together. The first theory of the strong force was proposed by Hideki Yukawa in 1934 [19, 20]. Yukawa suggested that a *meson* (a charged particle with a mass intermediate between those of the electron and the proton)[2] might be exchanged between nucleons. At that time, numerous studies of cosmic rays were in progress. The following year a particle of approximately the required mass (about 200 times that of the electron) was discovered in 1936 by the American physicists Carl D. Anderson and Seth Neddermeyer [21] separately, and named the mu meson, or muon($\mu^{\pm}$). In the same period, particle accelerators produced particle beams in the laboratory and these elementary particles were also produced.

With the detectors like cloud chambers, bubble chambers and even photographic plates, many new and exotic particles were discovered between 1940s and 1950s. In particular, in 1947, the *pion* ($\pi^{\pm}$) was discovered by Csar Lattes, Giuseppe Occhialini and Cecil Powell [22]. In the same year, G. D. Rochester and Clifford Charles Butler of the University of Manchester found heavy electronically neutral particles (called *kaons*) that decayed into pions [23]. As more and more new particles were discovered, theoretical and experimental evidence begin to indicate that the hadrons (proton, neutron, other baryons, and mesons that can make an two-page-long list) have composite structures and they are consisted with more fundamental particles. These fundamental particles (quarks and leptons) were discovered, together with the particles mediate in interactions between these constituents, made up the most complete theory framework till now, the Standard Model (SM), which was proposed by Steven Weinberg [24], Sheldon Glashow [25] and Abdus Salam [26] in 1967 and developed mainly in 1960s and 1970s.

The SM describes interactions between a set of matter fields (particles) and a set of force-carrying fields(interaction particles) which interact with each other. This model is a

[2]The electron is called a *lepton*('light-weight'), whereas the proton and neutron are *baryons*('heavy-weight')

relativistic quantum field theory. More specifically, it's a non-Abelian Yang-Mills relativistic quantum field theory of the topological group $SU(3)_C \otimes SU(2)_L \otimes U(1)_Y$. The $SU(3)_C$ group corresponds to quantum chromodynamics (the strong-nuclear force) and the the $SU(2)_L \otimes U(1)_Y$ corresponds to the electroweak model (the unified force of the weak-nuclear force and electromagnetic force). The SM is very successful in accounting for most of the observed phenomena at the microscopic frontier of physics, and has been repeatedly tested and verified in many experiments in the last decades[3]. The SM also includes the the last building block of matter called the Higgs boson, which has been searched for in many experiments. In the summer of 2012, both ATLAS (A Toroidal LHC Apparatus) and CMS (Compact Muon Solenoid) collaborations at the LHC (Large Hadron Collider) facility at CERN reported the discovery of a Higgs-like boson, which exhibits most of the predicted characteristics of the searched Higgs boson [27]. The elementary particles of the SM are tabulated in Figure 1.1.

1.0.1 Fermions

In the SM, elementary particles of spin $s = \frac{1}{2}$, called fermions, are the building blocks of matter. Their name comes from the description of the quantum mechanical statistics of such particles described by Fermi and Dirac. They obey the Pauli exclusion principle, which states that two identical fermions cannot occupy the same quantum state. Twelve of these fermions are included in the SM. Six of them are called as quarks and the other six are called leptons. We also say these fermions have different flavours, a terminology that indicates an intrinsic property of the fermions. Therefore, there are 6 flavours of leptons and 6 flavour of quarks. In addition, these twelve fermions are arranged into three generations. Each quark generation contains an up-type quark (up, charm, top) and a down-type quark (down, strange, bottom). As with quarks, leptons are also arranged into three generations. Each generation consists of one charged lepton and its corresponding neutrino. The mass of the

[3]The SM describes everything that has ever been observed in the laboratory except for neutrino masses and therefore also their oscillations, and cannot account for certain astronomical observations like dark matter or dark energy

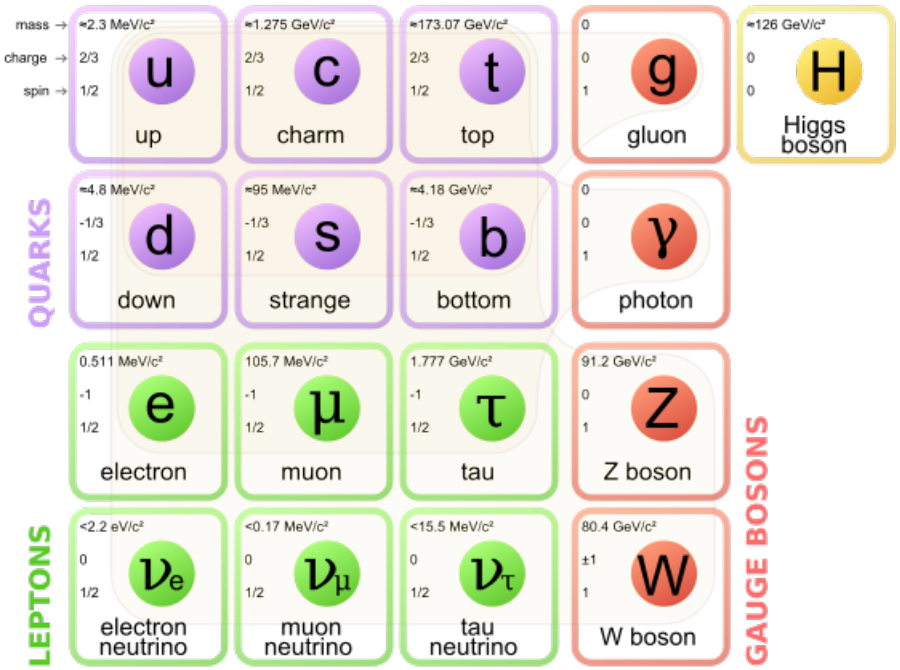

Figure 1.1: The particles of the Standard Model.

fermions increases with each generation, and the neutrinos are taken to be exactly massless in the SM, but evidence now exists for small neutrino masses, which represents a rare case of standard model violation. Leptons have integer charges only. Unlike the leptons, quarks carry fractional electric charge, which can be either $Q = +\frac{2}{3}$ or $Q = -\frac{1}{3}$.

Quarks carry an additional quantum number, the color charge. Three types of colors are used in the SM: red, green, or blue. A red quark carries one unit of redness only, a blue quark has only one unit of blueness and a green has one unit of greenness. A particle is colorless if the total amount of each color is zero or all three colors are present in equal amounts. Leptons have zero color. In fact, no free colored particles have been observed in nature; quarks are confined into color-less composite particles. These bound states of quarks are either baryons(consisting of three quarks) or mesons(consisting of quark and antiquark). Baryons and mesons are both called hadrons. The best known of hadrons are protons and neutrons, which are the building blocks of atomic nuclei.

Although the positron was the first antimatter particle discovered, every particle has

an anti-particle. Particles and their anti-particles have the same mass, identical spins and opposite electrical charges.

The fermions are responsible for making up "everyday matter". According to the Particle Data Group, around 300 different particles with different combinations of quarks have been discovered at present. Ordinary matter is constructed with only the first generation fermions. The higher generation fermions, once produced in high energy interactions, decay rapidly into ligher fermions of the first generations.

1.0.2 Gauge Bosons

The elementary particles having spin $s = 1$ in quantum field theory representing fields transmitting the forces are called gauge bosons. In the SM, there are three kinds of force mediating particles: photons (γ), massive bosons (the $W^{\pm}$ and Z) and gluons (g). The γ is a massless particles and interacts only with electrically charged particles. The weak force is experienced by all particles, and is mediated by three massive bosons: the $W^{\pm}$ and Z. At high energy scales, the electromagnetic force and the weak force are unified by a theory called *Electroweak* theory. The strong force between color charged particles is described by a non-abelian theory called *Quantum Chromo-Dynamics*(QCD). The electronically neutral gluon g is the mediator particle of QCD interaction. The only force in nature that is not included in the SM is gravity.

1.0.3 Higgs Boson

In the SM, to endow particles with mass, the Higgs mechanism was proposed by three independent groups in 1964: by Robert Brout and Franois Englert [28]; by Peter Higgs [29]; and by Gerald Guralnik, C. R. Hagen, and Tom Kibble [30, 31]. Through interaction with the Higgs field the particles can acquire their mass without breaking the gauge invariance of SM Lagrangian. The SM does not predict the magnitude of the mass of each particles. Higgs boson is also the only boson that has spin $s = 0$ in SM.

1.0.4 Top quark physics and the subject of this analysis

Understanding the constituents of particles and their interactions is the goal of the modern experimental high energy physics. The SM is a successful theory for describing both the elementary particles that constitues the matters in our universe and the interactions between them. On the other hand, high energy physicists are also interested to look at phenomenons beyond the SM–including searching for new particles and new interactions beyond the SM.

The top quark since its first observation in 1995 at the Tevatron (via the flavour- conserving strong interaction) and then subsequently through single top-quark production in 2009 (via charged-current electroweak, or EW process), has been known to be the heaviest fundamental particle and its large mass gives it many interesting properties, making the top quark a privileged window for searching new physics beyond the SM. At leading-order (LO) in EW perturbation theory, single top-quark production is described by three sub-processes: an exchange of a virtual W boson either in the t-channel or in the s-channel, or the associated production of a top quark and an on-shell W boson (Wt-channel). As for the its decays, because the top quark has a smaller lifetime than its hadronization scale, the top quark decays before hadronization, predominantly through the weak process $t \to Wb$ that governed by the Wtb vertex. This means that the spin of the top quark is transformed to its decay products.

The subject of this thesis is to analyze the Wtb vertex based on the measurement of angular distribution of the decay products of single top quarks produced in the t-channel from pp interactions at $\sqrt{8}$ TeV at Large Hadron Collider (LHC). The analysis applies to 20.2 fb^{-1} of collision data collected with the ATLAS detector at the LHC. Probes of new physics phenomena affecting the production or decay of the top quark is parameterized with a series of effective couplings. Six observables are determined simultaneously, five generalised helicity fractions and phases, as well as the polarisation of the top quarks. Fourier techniques, in particular a variant of the ordinary convolution theorem, are used for deconvolving the detector effects from the measured differential rates.

2.0 THEORETICAL BACKGROUND AND MOTIVATION

2.1 THE STANDARD MODEL OF PARTICLE PHYSICS

The Standard Model (SM) of particle physics is a $SU(3)_c \otimes SU(2)_L \otimes U(1)_Y$ relativistic Quantum Field Theory (QFT) developed to describe the electroweak and strong interactions of elementary particles in a single framework. The theory was initially designed to unify electrodynamics and the weak interaction by Sheldon Glashow in 1960 [25] and later in 1967 by Steven Weinberg [24] and Abdus Salam [26]. At almost the same time, the theory of the strong interaction, Quantum Chromodynamics (QCD), was developed in parallel through the 1960s-70s. Murray Gell-Mann and George Zweig [32] independently suggested the existence of quarks with different flavors as the components of hadrons and, in 1965, Moo-Young Han with Yoichiro Nambu [33] and Oscar W. Greenberg [34] proposed an additional $SU(3)_c$ gauge degree of freedom, the color charge. The modern SM form was reached in 1973 with the discovery of asymptotic freedom of strong interactions by David Politzer [35] and David Gross together with Frank Wilczek [36] allowing perturbation theory techniques to be applied.

In the SM, we use the Klein-Gordon Lagrangian to describe quantum scalar or pseudo-scalar field, a field whose quanta are spinless particles, and Dirac Lagrangian to describe free Fermions. In order to describe the interactions between particles, we introduce gauge principle. There are two possible types of gauge transformations, local and global. In the SM, we require that our general Lagrangian satisfies a local transformation. Gauge invariance on one hand can give us the interaction terms, but on the other hand, it requires the gauge fields have to be massless in order to preserve gauge invariance, which clearly does not describe nature. A typical weak interaction process (i.e beta decay) indicates W and Z gauge bosons have masses of the 80.4 GeV/c^2 and 91.2 GeV/c^2, respectively [37, 38]. In order to solve this

massness problem, we invoke Higgs mechanism with spontaneous symmetry breaking (SSB). An $SU(2)$ doublet of scalar field ϕ is introduced. With SSB, we postulate the existence of a boson field with an non-zero expectation value, then we re-express this Higgs field with respect to a true minimum of the field (vacuum). A transformation of the Lagrangian cannot change the physics, but a valid perturbation theory is expanded around its ground state. After this transformation, we break the manifest symmetry of the Lagrangian, but reap great benefits: the particles acquire mass.

In the SM, the electromagnetic force and weak force are unified within the so called electroweak interaction. The Lagrangian,

$$\begin{aligned}\mathcal{L} &= -\frac{1}{4}\vec{W}^{\mu\nu}\cdot\vec{W}_{\mu\nu} - \frac{1}{4}B^{\mu\nu}B_{\mu\nu} + \bar{\psi}_L\gamma^\mu iD_u\psi_L + \bar{\psi}_R\gamma^\mu(i\partial_\mu - g^{'}\frac{Y}{2}B_\mu)\psi_R \\ &+ |D_u\phi|^2 - V(\phi) - \left(G_1\bar{\psi}_L\phi\psi_R + G_2\bar{\psi}_L\phi_c\psi_R + h.c\right), \end{aligned} \tag{2.1}$$

contains four parts: the first part includes $W^{\pm}$,Z and photon (γ) kinetic terms and self-interactions; the second part includes lepton and quark kinetic terms and their interactions with $W^{\pm}$,Z and γ, the third part includes $W^{\pm}$,Z,γ, and Higgs masses and couplings; finally the last part includes lepton and quark masses and coupling to Higgs.

The kinetic term of the gauge fields contains three vector bosons $\vec{W}^\mu$ and a fourth vector B^μ. It can be seen below:

$$\begin{aligned}\vec{W}_{\mu\nu} &= \partial_\mu\vec{W}_\nu - \partial_\nu\vec{W}_\mu - g\vec{W}_\mu\times\vec{W}_\nu, \\ B_{\mu\nu} &= \partial_\mu B_\nu - \partial_\nu B_\mu. \end{aligned} \tag{2.2}$$

The D_u is a covariant derivative term defined as

$$D_u = \partial_u + ig\vec{W}_u\cdot\vec{\tau}/2 + ig^{'}\frac{1}{2}B_uY, \tag{2.3}$$

where g is a coupling constant and the covariant derivative term includes a vector of Pauli matrices $\vec{\tau}$, where $\{\tau_x,\tau_y,\tau_y\}$:

$$\tau_x = \begin{bmatrix}0 & 1\\ 1 & 0\end{bmatrix}, \tau_y = \begin{bmatrix}0 & -i\\ i & 0\end{bmatrix}, \tau_z = \begin{bmatrix}1 & 0\\ 0 & -1\end{bmatrix}, \tag{2.4}$$

Y is the *Weak-Hyper charge* Y. ψ_L denotes a left-handed fermion (quark or lepton) doublet, and ψ_R denotes a right-handed fermion singlet. In the last *Yukawa* term, G_1 and G_2 are arbitrary constants related to the mass of leptons and quarks, respectively. ϕ (and its charged-conjugation ϕ_c) is a 2-component matrix that represents complex Higgs field.

2.2 $SU(2)_L \otimes U(1)_Y$ SYMMETRY

Fermi's famous paper [39] in 1932 explains beta-decay with a postulated weak current inspired by the electromagnetic current from electron proton scattering. Fermi uses the EM interaction as model and assumes in the β-decay process, or

$$pe^- \rightarrow n\nu_e; \tag{2.5}$$

the current forms of lepton and proton are

$$\begin{aligned} J_{\text{lepton}} &= \bar{\psi}_e \gamma_\mu \psi_e, \\ J_{\text{proton}} &= \bar{\psi}_p \gamma_\mu \psi_p \end{aligned}$$

respectively. Fermi assumed weak interaction has a vector-vector form (as it is for the electromagnetic interaction). However, experimental results in the parity violation and CP invariance [40] indicate that Fermi's pure vector-vector form of the weak current needs to be modified to V-A (vector minus axial vector) form. The essential changes required in Fermi's original proposal are the replacement of γ^μ by $\gamma^\mu(C_V + \gamma_5 C_A)$, which C_V and C_A are free parameters to be determined by experiment[1]. A maximal violation V-A form $(1 - \gamma^5)$ is confirmed experimentally and used in the SM. We define left-handed and right-handed fermion fields as:

$$\psi_L = P_L \psi \quad \text{and} \quad \psi_R = P_R \psi, \tag{2.6}$$

where $P_L = \frac{1}{2}(1 - \gamma_5)$ and $P_R = \frac{1}{2}(1 + \gamma_5)$ are called projection operators.

[1] A mixture of γ^μ and $\gamma^5\gamma^\mu$ terms automatically violates parity conservation, i.e see [41].

Experimentally, the W couples to the left-handed ν_e and left-handed electron. The left-handed states form an isospin doublet[2], and the right-handed states form an isospin singlets.

$$\psi_1 = \begin{pmatrix} \nu \\ l^- \end{pmatrix}_L , \quad \psi_2 = \nu_R, \quad \psi_3 = l_R^- \tag{2.7}$$

$$\tag{2.8}$$

The left-handed u-quark and d-quark also form a weak isospin doublet.

$$\psi_1 = \begin{pmatrix} u \\ d \end{pmatrix}_L , \quad \psi_2 = u_R, \quad \psi_3 = d_R. \tag{2.9}$$

$$\tag{2.10}$$

Then a $SU(2)$ gauge symmetry applies to left-handed fermion doublet only, not to the right-handed singlet. However, since the mass term has the form $m\bar{\psi}\psi = m(\bar{\psi_L}\psi_R + \bar{\psi_R}\psi_L)$, it is not invariant under a $SU(2)_L$ symmetry, as we have discussed before, and is therefore disallowed. In next section, we'll see how the spontaneous symmetry broken solves this problem.

In addition, $U(1)_Y$ symmetry applies to both left-handed fermion and right-handed fermions. The weak hyper-charge Y is a good quantum number since each member of the weak doublet has the same *weak hyper-charge*. The SM defines a *weak hyper-charge* as $Y = 2(Q - T)$, in analogy with the *Gell-Mann-Nishijima* formula [42] for strong interaction quantum numbers. Table **??** lists all the weak numbers for the first generation of quark and lepton. In this expression, Q is the electromagnetic charge we usually use when we describe the electromagnetic force between two particles and T is the isospin we defined before.

In fact, a "covariant derivative" defined in 2.1 is used to replace ∂_μ.

$$D_u = \partial_u + ig\vec{W}_u \cdot \vec{T} + ig^{'}\frac{1}{2}B_u Y, \tag{2.11}$$

where

$$\vec{T} = \vec{\tau}/2. \tag{2.12}$$

[2]The left-handed states are grouped together but the right-handed states are not, as they don't interact with the W_μ fields. In addition, the SM doesn't include the right-handed neutrino, though evidences exist that neutrinos have masses and some extension of the SM is needed, i.e *seesaw mechanism*.

Lepton	T	T^3	Q	Y	Lepton	T	T^3	Q	Y
ν_e	$\frac{1}{2}$	$-\frac{1}{2}$	0	-1	u_L	$\frac{1}{2}$	$-\frac{1}{2}$	$+\frac{2}{3}$	$+\frac{1}{3}$
e_L^-	$\frac{1}{2}$	$-\frac{1}{2}$	-1	-1	d_L^-	$\frac{1}{2}$	$-\frac{1}{2}$	$-\frac{1}{3}$	$+\frac{1}{3}$
					u_R^-	0	0	$+\frac{2}{3}$	$+\frac{4}{3}$
e_R^-	0	0	-1	-2	d_R^-	0	0	$-\frac{1}{3}$	$-\frac{2}{3}$

Table 2.1: Weak Isospin and Hypercharge Quantum Numbers of Leptons and Quarks

The coupling constant g and g' are defined in terms of the Weinberg or weak mixing angle θ_W (see next section for detail 2.3)

$$g \sin\theta_W = g' \cos\theta_W = e, \tag{2.13}$$

The Lagrangian is invariant under the infinitesimal local gauge transformations for $SU(2)_L$ and $U(1)_Y$ independently, as described in Table 2.2.

$SU(2)_L$	$U(1)_Y$
$\psi_L \to [1 + ig\vec{T} \cdot \vec{\alpha}(x)]\psi_L$	$\psi_L \to [1 + ig'\frac{1}{2}Y\beta(x)]\psi_L$
$\psi_R \to \psi_R$	$\psi_R \to [1 + ig'\frac{1}{2}Y\beta(x)]\psi_R$
$\vec{W}_\mu \to \vec{W}_\mu - \partial_\mu\vec{\alpha}(x) - g\vec{\alpha}(x) \times \vec{W}_\mu$	$\vec{W}_\mu \to \vec{W}_\mu$
$B_\mu \to B_\mu$	$B_\mu \to B_\mu - \partial_\mu\beta(x)$

Table 2.2: The infinitesimal local gauge transformations for the terms in the Lagrangian.

The isotriplet $\vec{W}_\mu$ and the singlet B_μ are introduced in this derivative to preserve the local gauge invariance and $\vec{\alpha}(x)$ and $\beta(x)$ are the gauge parameters corresponding to the four gauge field $\vec{W}_\mu$ and B_μ respectively.

Following the discussion above and with the definition of the derivative D_μ, we have the covariant derivative of $\psi_j(x)(j=1,2,3)$ below:

$$\begin{aligned}
D_\mu \overbrace{\psi_1(x)}^{\text{left-handed fermion}} &= \left(\partial_\mu + i\frac{g}{2}\vec{\tau}\cdot\vec{W}_\mu + i\frac{g'}{2}Y_1 B_\mu\right)\psi_1(x), \\
D_\mu \overbrace{\psi_2(x)}^{\text{right-handed fermion}} &= \left(\partial_\mu + i\frac{g'}{2}Y_2 B_\mu\right)\psi_2(x), \\
D_\mu \overbrace{\psi_3(x)}^{\text{right-handed fermion}} &= \left(\partial_\mu + i\frac{g'}{2}Y_3 B_\mu\right)\psi_3(x).
\end{aligned} \tag{2.14}$$

It can be checked that the free Dirac Lagrangian for massless fermions

$$\mathcal{L}_{\text{free}} = \sum_{j=1}^{3} i\bar{\psi}_j(x)\gamma^\mu D_\mu \psi_j(x) \tag{2.15}$$

satisfies the invariance property under the local gauge transformation and the remaining gauge invariance kinetic terms are

$$L_{\text{kinetic}} = -\frac{1}{4}\mathbf{W}_{\mu\nu}\mathbf{W}^{\mu\nu} - \frac{1}{4}B_{\mu\nu}B^{\mu\nu}, \tag{2.16}$$

where

$$\begin{aligned}
\mathbf{W}_{\mu\nu} &= \partial_\mu \vec{W}_\nu - \partial_\nu \vec{W}_\mu - g\vec{W}_\mu \times \vec{W}_\nu, \\
B_{\mu\nu} &= \partial_\mu B_\nu - \partial_\nu B_\mu.
\end{aligned} \tag{2.17}$$

In this massless model, the full Lagrangian can be written out explicitly as :

$$\mathcal{L} = -\frac{1}{4}\mathbf{W}_{\mu\nu}\mathbf{W}^{\mu\nu} - \frac{1}{4}B_{\mu\nu}B^{\mu\nu} + \sum_{j=1}^{3}\bar{\psi}_j i\gamma^\mu D_\mu \psi_j, \tag{2.18}$$

or we can combine the left-handed terms and right-handed terms respectively to restore the form we showed at the beginning of this chapter.

$$\mathcal{L} = -\frac{1}{4}\mathbf{W}_{\mu\nu}\mathbf{W}^{\mu\nu} - \frac{1}{4}B_{\mu\nu}B^{\mu\nu} + \bar{\psi}_L\gamma^\mu(i\partial_\mu - \frac{g}{2}\vec{\tau}\cdot\vec{W}_\mu - g^{'}\frac{Y}{2}B_\mu)\psi_L + \bar{\psi}_R\gamma^\mu(i\partial_\mu - g^{'}\frac{Y}{2}B_\mu)\psi_R.$$

ψ_L denotes a left-handed fermion(quark or lepton) doublet, ψ_R denotes a right-handed fermion singlet. The last two terms are actually equivalent to $\sum_{j=1}^{3}\bar{\psi}_j i\gamma^\mu D_\mu \psi_j$.

2.3 ELECTROWEAK INTERACTION

The Lagrangian 2.18 contains interactions of the fermion fields with the gauge bosons, and using 2.14 we can write the interaction Lagrangian (ignore the kinetic terms) down as follows:

$$\begin{aligned}\mathcal{L} &\rightarrow \sum_{j=1}^{3}\left(\frac{g}{2}\bar{\psi}_j(x)\gamma^\mu(\vec{\tau}_j\cdot\vec{W}_\mu)\psi_j(x)+\frac{g'}{2}Y_jB_\mu\bar{\psi}_j(x)\gamma^\mu\psi_j(x)\right)\\ &= \frac{g}{2}\bar{\psi}_1(x)\gamma^\mu(\tau_1\cdot W^1_\mu+\tau_2\cdot W^2_\mu)\psi_1(x)+\frac{g}{2}\bar{\psi}_1(x)\gamma^\mu(\tau_3\cdot W^3_\mu)\psi_1(x)\\ &+ \sum_{j=1}^{3}\frac{g'}{2}Y_jB_\mu\bar{\psi}_j(x)\gamma^\mu\psi_j(x). \end{aligned} \tag{2.19}$$

The first term will give rise to charged-current interactions with the boson field $W^-_\mu = (W^1_\mu + iW^2_\mu)/\sqrt{2}$ and its conjugate $W^+_\mu = (W^1_\mu - iW^2_\mu)/\sqrt{2}$. If we define the isospin raising and lowering operator $T^\pm = (T^1 \pm iT^2)/\sqrt{2}$. Then the charged-current is [43]

$$\frac{g}{2}\bar{\psi}_1\gamma^\mu(\tau_1\cdot W^1_\mu+\tau_2\cdot W^2_\mu)\psi_1 = \frac{g}{\sqrt{2}}(J^{+\mu}_L W^+_\mu + J^{-\mu}_L W^-_\mu), \tag{2.20}$$

which $J^{\pm\mu}_L = \sqrt{2}\bar{\psi}\gamma^\mu T^\pm_L\psi$ and the operator T_L vanishes on ψ_R, since in our notation only ψ_1 is lefted-handed and ψ_2, ψ_3 are right-handed fermions.

For a single family of quarks and leptons, it is

$$L_{\text{cc}} = -\frac{g}{\sqrt{2}}\left(\bar{u}\gamma^\mu(1-\gamma_5)dW^+_\mu + \bar{\nu}_e\gamma^\mu(1-\gamma_5)eW^+_\mu\right) + h.c. \tag{2.21}$$

The remaining terms contain the neutral fields W^3_μ and B_μ. We will need a mixture of these two fields to find the photon current(A_μ) and the Z current(Z_μ). Indeed, when we break our symmetry (see next section), the two neutral field W^3_u and B_u must mix in such a way that A_μ and Z_μ are the physically distant mass eigenstates [41]:

$$\begin{pmatrix} W^3_\mu \\ B_\mu \end{pmatrix} = \begin{pmatrix} \cos\theta_W & \sin\theta_W \\ -\sin\theta_W & \cos\theta_W \end{pmatrix} = \begin{pmatrix} Z_\mu \\ A_\mu \end{pmatrix} \tag{2.22}$$

where θ_W is the electroweak mixing angle or Weinberg angle.

Thus the neutral-current Lagrangian is given in terms of Z_μ and A_μ as

$$L_{NC} = \sum_{j=1}^{3} \bar{\psi}_j \gamma^\mu \left\{ A_\mu \left[g T_L^3 \sin\theta_W + \frac{g'}{2} Y_j \cos\theta_W \right] + Z_\mu \left[g T_L^3 \cos\theta_W - \frac{g'}{2} Y_j \sin\theta_W \right] \right\} \psi_j, \tag{2.23}$$

here the subscript "L" in T_L indicates that the operator acts only upon left-handed fermion.

We have so far rewritten the electroweak neutral current as

$$\begin{aligned} g W_\mu^3 T_L^3 + \frac{g'}{2} B_\mu Y \quad &\rightarrow \quad A_\mu (g \sin\theta_W T_L^3 + g' \cos\theta_W \frac{1}{2} Y) \\ &+ \quad Z_\mu (g \cos\theta_W T_L^3 - g' \sin\theta_W \frac{1}{2} Y) \end{aligned} \tag{2.24}$$

The first term on the right hand side is the electromagnetic current $J^\mu_{\rm em} = \bar{\psi}\gamma^\mu Q \psi$, therefore the expression in the bracket must be $ieQ = ie(T_3 + \frac{1}{2}Y)$(right handed fermions have $T = 0$). We have to impose $g \sin\theta_W = g' \cos\theta_W = e$. Notice that, by introducing these new gauge fields, the old four orthogonal generator T^i, Y have been combined in a different way as $T^\pm$ and $e(T^3 + \frac{1}{2}Y)$ and $(g \cos\theta_W T^3 - g' \sin\theta_W \frac{1}{2} Y)$ (or $(T^3 \pm \frac{1}{2})$), which are corresponding to $W^\pm$, A_μ and Z.

Next, if we define $g_Z = e/(\sin\theta_W \cos\theta_W)$, we may also express neutral weak interaction Z term as

$$J_Z^\mu = \bar{\psi}\gamma^\mu (T_L^3 - \sin^2\theta_W Q)\psi$$

In summary, the interaction of gauge bosons with fermion arises from $\sum_{j=1}^{3} \bar{\psi}_j i\gamma^\mu D_\mu \psi_j$ can be written as

$$L' = e J^\mu_{\rm em} A_\mu + \frac{g}{\sqrt{2}} (J_L^{+\mu} W_\mu^+ + J_L^- W_\mu^-) + g_Z J_Z^\mu Z_\mu + \text{kinetic terms}, \tag{2.25}$$

where

$$\begin{aligned} J_L^{\pm\mu} &= \sqrt{2}\bar{\psi}\gamma^\mu T_L^\pm \psi \\ J_Z^\mu &= \bar{\psi}\gamma^\mu (T_L^3 - \sin^2\theta_W Q)\psi \\ J^\mu_{\rm em} &= \bar{\psi}\gamma^\mu Q \psi \end{aligned} \tag{2.26}$$

In the unbroken theory, the angle θ_W is a parameter of the model. For a θ_W, all gauge coupling can be fixed by the electrical charge e and the weak and electromagnetic interactions are therefore unified. But the Z and $W^{\pm}$ are all massless particles. Next section spontaneous symmetry broken (the broken theory) performs a miracle and save us.

For completeness, we also write down the cubic and quartic self-interaction terms among the gauge bosons from 2.16 [1]:

$$\begin{aligned} L_3 &= \\ &- ie\cot\theta_W\left\{(\partial^\mu W^\nu - \partial^\nu W^\mu)W^+_\mu Z_\nu - (\partial^\mu W^{\nu+} - \partial^\nu W^{\mu+})W_\mu Z_\nu + W_\mu W^+_\nu(\partial^\mu A^\nu - \partial^\nu Z^\mu)\right\} \\ &- ie\left\{(\partial^\mu W^\nu - \partial^\nu W^\mu)W^+_\mu A_\nu - (\partial^\mu W^{\nu+} - \partial^\nu W^{\mu+})W_\mu A_\nu + W_\mu W^+_\nu(\partial^\mu A^\nu - \partial^\nu A^\mu)\right\} \end{aligned} \tag{2.27}$$

$$\begin{aligned} L_4 &= \\ &- \frac{e^2}{2\sin^2\theta_W}\left\{(W^+_\mu W^\mu)^2 - W^+_\mu W^{\mu+} W_\nu W^\nu\right\} - e^2\cot^2\theta_W\left\{W^+_\mu W^\mu Z_\nu Z^\nu - W^+_\mu Z^\mu W_\nu Z^\nu\right\} \\ &- e^2\cot\theta_W\left\{2W^+_\mu W^\mu Z_\nu A^\nu - W^+_\mu Z^\mu W_\nu A^\nu - W^+_\mu A^\mu W_\nu Z^\nu\right\} \\ &- e^2\left\{W^+_\mu W^\mu A_\nu A^\nu - W^+_\mu A^\mu W_\nu A^\nu\right\} \end{aligned} \tag{2.28}$$

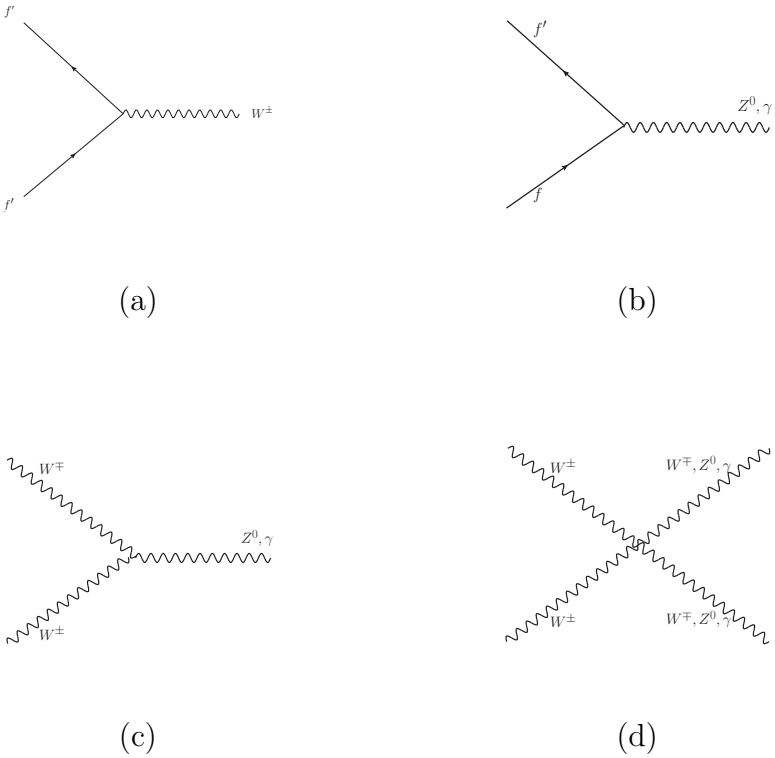

Figure 2.1: Allowed electroweak-interaction. (a) charged vertices, (b) neutral vertices, (c) three-boson couplings, and (e) four-boson couplings. These plots are from [1] and reformatted.

2.4 SPONTANEOUS SYMMETRY BREAKING

2.4.1 Introduction

The role of spontaneous symmetry breaking (SSB) is to introduce massive particles into the theory without breaking the $SU(2)_L$ and $U(1)_Y$ gauge symmetry of the electroweak

sector of the standard model, required for renormalizability. SSB gives masses to all the fermions and the gauge bosons. Only the photon remains massless. The problems of mass are circumvented by SSB, where the gauge symmetry is broken or rather "hidden" by the selection of a specific vacuum state. In addition to the acquisition of mass, SSB theory predicts a neutral scalar particle called "Higgs Boson", discovered at the LHC in 2012 by ATLAS and CMS.

2.4.2 A Toy model for SSB

In the SM, a complex isospin doublet field called the Higgs field is introduced to spontaneously break $SU(2)_L \otimes U(1)_Y$ symmetries. To understand how this works, we first discuss a simplified model-a scalar field before returning to a discussion of the Weinberg-Salam model. The interested reader can find its detail elsewhere. Consider a Lagrangian consisting of just one scalar field

$$\mathcal{L} \equiv T - V = \frac{1}{2}(\partial_\mu \phi)^2 - (\frac{1}{2}\mu^2\phi^2 + \beta\phi^4), \tag{2.29}$$

where we have used the he most general renormalizable potential form $V = \frac{1}{2}\mu^2\phi^2 + \beta\phi^4$.

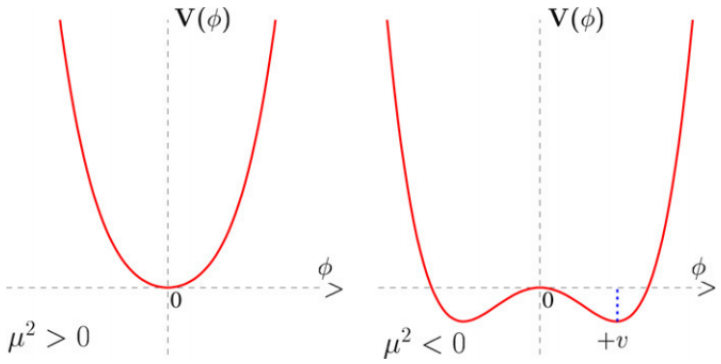

Figure 2.2: The potential $V(\phi) = \frac{1}{2}\mu^2\phi^2 + \beta\phi^4$ for $\mu^2 > 0$ and $\mu^2 < 0$.

Now we consider this model for two ranges of the vacuums μ^2, since they rise to two types of physics.

- If $u^2 > 0$, this Lagrangian simplifies describes a scalar field with a mass u. The ground state is easily to see from the potential curve, $\phi = 0$.

- If $u^2 < 0$, as shown in Figure 2.2, $\phi = 0$ is not the minimum state, but instead the two minimum point are $\phi = \pm\sqrt{-\mu^2/(4\beta)}$. Without any loss of generality, we can reparameterize our scalar field according to $\phi \to \phi(x) = \nu + \eta$, where ν is the vacuum expectation value of ϕ and $\eta(x)$ is a small term, and we expanded our field around its minimum.

We continue our discussion of the second case. The simple reparameterization of field ϕ indeed doesn't change any physics. The field η describes deviation from the ground state, or vacuum. There are now two ground states (vacuums) which both are far from $\phi = 0$. The new L' has $\phi(x) = \nu + \eta(x)$, and obviously the L' is not symmetric under the transformation $\eta \to -\eta$. We say the symmetry is broken, though more precisely the symmetry is hidden by the choice of a specific state as our ground state. Importantly, the theory remains renormalizable.

If we repeat the procedure using complex scalar field on a *local gauge* invariant theory, i.e $U(1)$ local gauge invariant theory (QED), with the same potential, we can generate a mass-term for the gauge boson (the photon). Without breaking the $U(1)$ symmetry of the Lagrangian, we then find that a scalar field (called Goldstone boson) is introduced. It may seem that an extra degree of freedom is introduced but in fact, this extra degree of freedom is actually unphysical, and a gauge transformation of the A_μ field (choice of a particular gauge called *unitary gauge*) will eliminate it. Therefore, the Goldstone boson actually does not appear in the theory and apparently this extra degree of freedom corresponds only to the freedom to make a gauge transformation. The unwanted massless Goldstone boson has been converted into the longitudinal polarization of the massive gauge photon. This is called the "Higgs Mechanism".

2.4.3 Choice of the Higgs Fields

2.4.4 Gauge Boson Mass

In the SM the $W^{\pm}$ and Z bosons acquire their mass through an $SU(2)$ doublet of complex fields ϕ (four scalar fields are used). In 1999, Weinberg and Salam added a $SU(2) \otimes U(1)$ invariant Lagrangians of 2.18 called L_ϕ where

$$L_\phi = (D_\mu \phi)\dagger(D^\mu \phi) - V(|\phi|^2), \tag{2.30}$$

which $D_u = (\partial_u + ig\mathbf{W}_u\mathbf{T} + ig^{'}\frac{1}{2}B_\mu Y)$ is the covariant derivative previously defined. Electroweak symmetry breaking happens when a new scalar partial ϕ is introduced in L_ϕ. In the kinetic term, this mechanism generates mass for charged and neutral interactions, represented by mixture of $\vec{W}_\mu$ and B_μ fields into the $W^{\pm}$ and Z bosons with mass M_W, M_Z and massless photon.

The renormalizable scalar potential V used in Weinberg's theory is

$$V = \mu^2 |\phi|^2 + \beta(\phi\dagger\phi)^2, \tag{2.31}$$

where $\mu^2 < 0$, $\beta > 0$ and ϕ is

$$\phi(x) = \frac{1}{\sqrt{2}} \begin{pmatrix} \phi^+ \\ \phi^0 \end{pmatrix} = \frac{1}{\sqrt{2}} \begin{pmatrix} \phi_1(x) + i\phi_2(x) \\ \phi_3(x) + i\phi_4(x) \end{pmatrix}. \tag{2.32}$$

To keep L_ϕ gauge invariant, the ϕ must belong to $S(2)_L \otimes U(1)_Y$ multiplet and we give these fields fixed quantum numbers given in table **??**. ϕ is a left-handed isospin doublet like the electron neutrino doublet. Both ϕ^+ and ϕ^0 are complex fields, with isospin $\frac{1}{2}$. In addition, the lower component has $Q = 0$ to ensure ϕ^0 does not couple to A^μ and the upper component has one more unit of charge Q than the lower component. These requirements are vital for reasons that will become more clear later.

Here we will introduce the Higgs mechanism so that the $W^{\pm}$ and Z become massive while the photon remains massless. Since the electric charge is a conserved quantity, only the neutral scalar field ϕ^0 can acquire a vacuum expectation value. Once we choose a particular ground state, the $SU(2)_L \otimes U(1)_Y$ symmetry will break to the electromagnetic

Lepton	T	T^3	Q	Y
ϕ^+	$\frac{1}{2}$	$\frac{1}{2}$	1	1
ϕ^0	$\frac{1}{2}$	$-\frac{1}{2}$	0	1

Table 2.3: Weak Isospin and Hypercharge Quantum Numbers of complex fields.

subgroup $U(1)_{em}$. According to Goldstone theorem three massless scalars should appear. We can redefine the scalar doublet as below generally and try to separate the neutral scalar from others:

$$\phi(x) \to \phi(x) = e^{i\vec{\tau}\cdot\vec{\theta}/2} \begin{pmatrix} 0 \\ (v + h(x))/\sqrt{2} \end{pmatrix} \tag{2.33}$$

where all the four scalar fields $\vec{\theta}$ and $h(x)$ all have zero vacuum expectation and we use $h(x)$ to indicate this will be a physical scalar Higgs field[3].

The local $SU(2)_L$ invariance of the Lagrangian allows us to rotate away any dependence on $\vec{\theta}$, so we can choose the *unitary gauge* and let $\vec{\theta} = 0$. We will see this particular gauge will eliminate the explicit appearance of θ_i in the Lagrangian. Moreover, the θ_i degree of freedom (in total 3) doesn't vanish, but essentially reappears as the longitudinal component of $W^\pm$ and Z when they acquire masses. Sometimes it is said that the Goldsone boson has been "eaten" by the gauge field.

The covariant derivative couples with this scalar multiplet giving

$$D_\mu\phi = \frac{i\nu}{\sqrt{8}} \begin{pmatrix} g(W_1 - iW_2) \\ -gW_3 + g'Y_{\phi^0}B_\mu \end{pmatrix},$$

[3]It's easy to check that the above ϕ after removing the phase chooses a ground state that is only invariant under a $U(1)_{em}$ transformation ($e^{i\alpha(\vec{x})Q}\phi_0 = 0$), but changes under $SU(2)_L$ or $U(1)_Y$ transformation. Alternatively, we can say T^i and Y generator symmetry are all broken, but one combination of T^3 and $Y(Q = T^3 + \frac{1}{2}Y)$ is not, hence a massless photon is predicted. The other three broken generators predicts three massive gauge bosons. This process of symmetry breaking can be summarized to the statement $SU(2)_L \otimes U(1)_Y \to U(1)_{em}$.

and

$$(D^\mu\phi)^\dagger(D_\mu\phi) = \frac{1}{8}\nu^2\left[g^2(W_1^2+W_2^2)+(-gW_3+g'Y_{\phi^0}B_\mu)^2)\right].$$

The first term will generate mass of M_W, and the second term affects the Z and γ. This demonstrates why the choice of quantum numbers are important. Specifically, expanding the second term, we have

$$(-gW_3+g'Y_{\phi^0}B_\mu)^2 = (W_3,B_\mu)\begin{pmatrix} g^2 & -gg'Y_{\phi^0} \\ -gg'Y_{\phi^0} & g'^2 \end{pmatrix}\begin{pmatrix} W_3 \\ B_\mu \end{pmatrix}. \tag{2.34}$$

Only when $Y_{\phi^0} = \pm 1$, the determinant of the mixing matrix vanishes and one of the combinations of W_3 and B_μ become massless (the requirement of forcing the coefficient of A_μ to be 0). In the usually notation, $Y_{\phi^0} = 1$ is used.

Following the calculations above and plugging in the potential term, the Lagrangian L_ϕ now is combined with two parts L_{HG^2} and L_H,

$$\begin{aligned} L_{HG^2} &= \frac{1}{8}g_Z^2 Z_\mu Z^\mu(\nu+h)^2 + \frac{1}{4}g^2W^+W^-(\nu+h)^2 - V[(\nu+h)] \\ &= \frac{1}{2}M_Z^2 Z_\mu Z^\mu(\frac{\nu+h}{\nu})^2 + M_W^2W^+W^-(\frac{\nu+h}{\nu})^2. \end{aligned}$$

Thus we find mass terms for gauge bosons are

$$M_W = \frac{1}{2}g\nu, \quad M_Z = \frac{1}{2}g_Z\nu, \quad M_\gamma = 0. \tag{2.35}$$

The kinetic and potential terms generate the Higgs mass and its self-couplings:

$$L_H = \frac{1}{2}(\partial h)^2 - \frac{1}{2}M_H^2h^2 - \frac{M_H^2}{2\nu}h^3 - \frac{M_H^3}{8\nu^2}h^4 + \frac{1}{4}h\nu^4,$$

which $M_H = \sqrt{-2\mu^2} = \sqrt{2\beta}\nu$. By using the relation $M_W = \frac{1}{2}g\nu$ and the measured values for M_W and g, the vacuum expectation value of the Higgs field is found to be $\nu \approx 246GeV$.

2.4.5 Generation of fermion mass

Spontaneous symmetry breaking will generate lepton and quark masses if we add a Yukawa interaction of fermion and ϕ fields. Proceeding as before, we can find the general $SU(2)_L \otimes U(1)$ gauge invariant Yukawa interaction for one fermion is

$$L_\phi^F = -\left(G_1 \bar{\psi}_L \phi \psi_R + G_2 \bar{\psi}_L \phi_c \psi_R + h.c\right). \tag{2.36}$$

which $\phi_c = -i\tau_2 \phi^*$ represents the charge conjugation of ϕ. Again, ψ_L denotes a left-handed fermion (quark or lepton) doublet, ψ_R denotes a right-handed fermion singlet. To show how this Yukawa interaction generates electron or a quark doublet masses, we choose the minimal choice of a single Higgs doublet. Two examples are shown below.

For the terms which generate the electron mass, the above expression is

$$\begin{aligned} L_\phi^F(\text{electron}) &= -G_e \left[(\bar{\nu}_e, \bar{e})_L \begin{pmatrix} 0 \\ \frac{\nu+h}{\sqrt{2}} \end{pmatrix} e_R + \bar{e}_R (0, \frac{\nu+h}{\sqrt{2}}) \begin{pmatrix} \nu_e \\ e \end{pmatrix}_L \right], \\ &= -m_e \bar{e} e - \frac{m_e}{\nu} \bar{e} e h, \end{aligned} \tag{2.37}$$

where $m_e = \frac{G_e \nu}{\sqrt{2}}$ generates the electron mass. The Yukawa coupling G_e and thus the quark mass is not predicted by the SM. The second term is the interaction term coupling the Higgs scalar to the electron.

The second term including the conjugated ϕ that transforms identically to ϕ and is used to generate the quak mass,

$$\phi_c = i\tau_2 \phi^* \xrightarrow{\text{SSB}} \begin{pmatrix} \frac{\nu+h}{\sqrt{2}} \\ 0 \end{pmatrix}, \tag{2.38}$$

$$\begin{aligned} L_\phi^F((\mu, d)_L) &= -G_d (\bar{\mu}, \bar{d})_L \begin{pmatrix} 0 \\ \frac{\nu+h}{\sqrt{2}} \end{pmatrix} d_R - G_u (\bar{\mu}, \bar{d})_L \begin{pmatrix} \frac{\nu+h}{\sqrt{2}} \\ 0 \end{pmatrix} \mu_R + h.c \\ &= -m_\mu \bar{\mu} \mu - m_d \bar{d} d - \frac{m_\mu}{\mu} \bar{\nu} \mu h - \frac{m_d}{\nu} \bar{d} d h, \end{aligned} \tag{2.39}$$

where the mass are defined similarly as electron mass

$$m_\mu = \frac{G_\mu \nu}{\sqrt{2}} \text{ and } m_d = \frac{G_d \nu}{\sqrt{2}}. \tag{2.40}$$

However, this example is incomplete. The weak interaction operates not only on the double $(\mu, d)_L$, but on a linear combination of the flavor eigenstates. A mixture of these flavor eigenstates (with a *CKM* matrix) has to be considered to generate masses of all doublets and the coupling of scalar higgs to mixed generations. (See the 'Cabibbo angle' and GIM theory [44, 45]).

With the three generation assumption, the most general $SU(2)_L \otimes U(1)$ invariant Yukawa interaction is (comparing with Equation 2.39)

$$L = \sum_{i,j=1}^{3} \left[-G_d^{ij} (\bar{u}_i, \bar{d}_i)_L \phi d_{jR} - G_u^{ij} (\bar{u}_i, \bar{d}_i)_L \phi_c u_{jR} \right] + h.c. \tag{2.41}$$

Rewrite it with two matrices M^u and M^d that each of them has 9 complex parameters,

$$M_{i,j}^u = \frac{\nu}{\sqrt{2}} G_{i,j}^u, M_{i,j}^d = \frac{\nu}{\sqrt{2}} G_{i,j}^d. \tag{2.42}$$

Then we get the mass terms

$$-\overline{(d_1, d_2, d_3)}_L M_d \begin{pmatrix} d_1 \\ d_2 \\ d_3 \end{pmatrix}_R + h.c, \tag{2.43}$$

$$-\overline{(u_1, u_2, u_3)}_L M_u \begin{pmatrix} u_1 \\ u_2 \\ u_3 \end{pmatrix}_R + h.c. \tag{2.44}$$

Note that these $\overline{(u_1, u_2, u_3)}$ or $\overline{(d_1, d_2, d_3)}$ are not the quark mass eigenstates, but instead are the linear combinations of the mass eigenstates. Now we have assumed the quarks have three generations (correspond to three independent eigenstates), so the complex matrices $M_{u(d)}$ are diagonalizable. We can find unitary matrices U_R, U_L, D_R, D_L, that satisfy

$$\begin{pmatrix} u_1 \\ u_2 \\ u_3 \end{pmatrix}_{L,R} = U_{L,R} \begin{pmatrix} u \\ c \\ t \end{pmatrix}_{L,R}, \begin{pmatrix} d_1 \\ d_2 \\ d_3 \end{pmatrix}_{L,R} = D_{L,R} \begin{pmatrix} d \\ s \\ b \end{pmatrix}_{L,R}. \tag{2.45}$$

The charged-current weak interaction are also modified, i.e

$$\overline{u_1, u_2, u_3}_L \gamma_\mu \begin{pmatrix} d_1 \\ d_2 \\ d_3 \end{pmatrix}_L == \overline{(u, c, t)}_L U_L^\dagger D_L \gamma_\mu \begin{pmatrix} d \\ s \\ b \end{pmatrix}_L , \tag{2.46}$$

and the matrix

$$V = U_L^\dagger D_L \tag{2.47}$$

is the Cabibbo-Kobayashi-Maskawa (CKM) matrix. One can write the explicit form of the CKM matrix as

$$V_{\mathrm{CKM}} = \begin{pmatrix} V_{ud} & V_{us} & V_{ub} \\ V_{cd} & V_{cs} & V_{cb} \\ V_{td} & V_{ts} & V_{tb} \end{pmatrix} . \tag{2.48}$$

With this basis, the charge-current weak interaction for the quarks expressed interms of *CKM* matrix is

$$J^+_{L\mu} = \overline{(u, c, t)}_L \gamma_\mu V_{\mathrm{CKM}} \begin{pmatrix} d \\ s \\ b \end{pmatrix}_L . \tag{2.49}$$

There are nine elements in this *CKM* matrix, however these elements are not all independent. When three generations are assumed, the 3×3 *CKM* in fact has four free parameters. It can be reduced to a 'canonical form' in which three parameters called 'generalised angle', $(\theta_{12}, \theta_{2,3}, \theta_{1,3})$ are introduced, plus one additional phase factor δ. Cosines and sines of the angles are denoted c_{ij} and s_{ij}, respectively.

$$V_{\mathrm{CKM}} = \begin{bmatrix} c_{12}c_{13} & s_{12}c_{13} & s_{13}e^{-i\delta_{13}} \\ -s_{12}c_{23} - c_{12}s_{23}s_{13}e^{i\delta_{13}} & c_{12}c_{23} - s_{12}s_{23}s_{13}e^{i\delta_{13}} & s_{23}c_{13} \\ s_{12}s_{23} - c_{12}c_{23}s_{13}e^{i\delta_{13}} & -c_{12}s_{23} - s_{12}c_{23}s_{13}e^{i\delta_{13}} & c_{23}c_{13} \end{bmatrix} . \tag{2.50}$$

The magnitude of the elements in the *CKM* are determined by experimental results. In this analysis, the Wtb vertex that governs the weak production and decay of single top quarks will be discussed, as will effect beyond the standard model which may enter through six dimensional operators from an *Effective Theory*.

3.0 TOP QUARK PHYSICS

3.1 TOP QUARK PRODUCTION

There are two mechanisms for the production of top quarks at hadron colliders. The strong interaction produces top and antitop pairs (called $t\bar{t}$ production); either from quark and antiquark annihilation ($q\bar{q}$) or from gluon fusion (gg), as depicted in Figure 3.1.

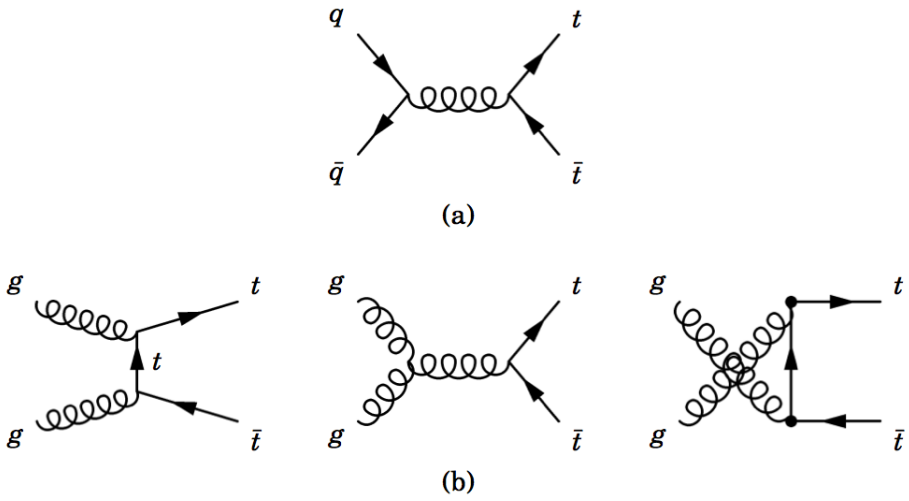

Figure 3.1: Leading order Feynman diagrams of top pair production at the LHC: (a) $q\bar{q}$ annihilation (b) *gluon fusion*.

Another mechanism is electroweak production of single top quark. There are three distinct channels which produce single top. Those three classes of production process, s-channel Drell-Yan, t-channel Wb fusion, and associated Wt diagrams are shown in Figure 3.2. In this thesis we are concerned with single top produced in t-channel Wb fusion. The

corresponding production rate can be calculated in two different schemes: in Figure 3.2, the top right diagram illustrates the so called four-flavor scheme (4FS, or 2 to 3 process) where the proton is considered to be composed of only four light quarks (u, d, c and s) and when b and $\bar{b}$ quarks arise from the splitting of a virtual gluon into $b\bar{b}$. The top left diagram in Figure in 3.2 illustrates the five-flavor (5FS, or 2 to 2 process). Some details about these two processes are presented in Appendix A.1 and their simulation with Monte is presented in Section 6.2.3.

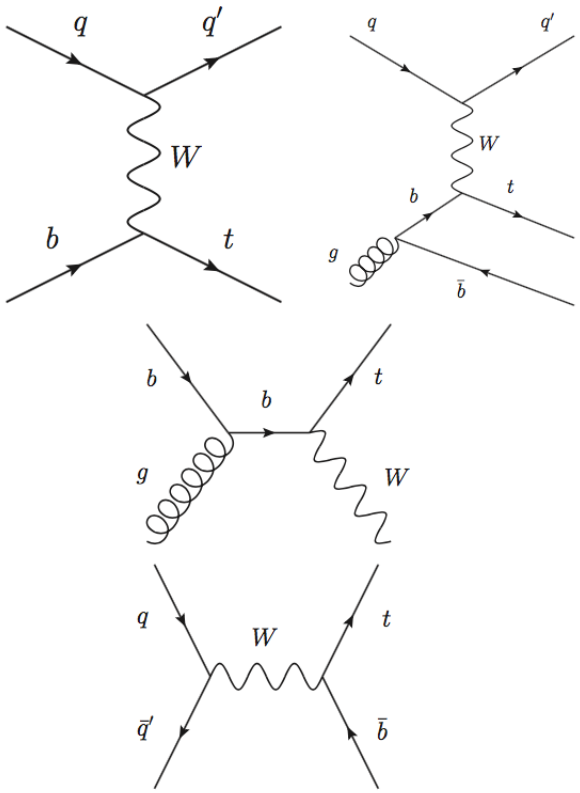

Figure 3.2: Leading order Feynman diagram of single top production at the LHC: (top) t-channel (middle) Wt associated production (bottom) s-channel.

The $t\bar{t}$ and single top quark production cross sections have been measured at the LHC. Figure 3.4 is shows the cross section measured by ATLAS compared to theoretical predictions. At $\sqrt{s} = 8$ TeV the production rates are approximately 242.9 pb for $t\bar{t}$ [46] and 89.6 pb for electroweak production of single top quark in the t-channel [47].

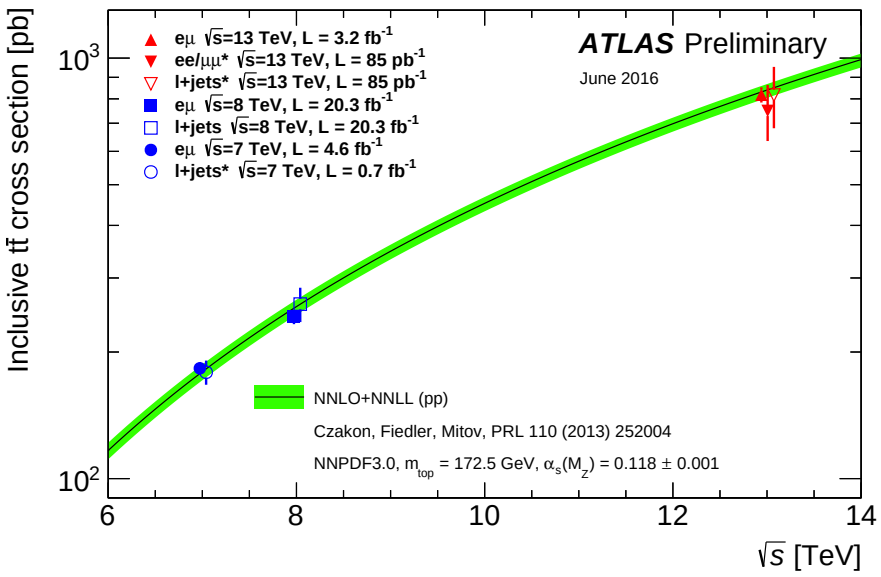

Figure 3.3: Summary of ATLAS measurements of the $t\bar{t}$ production cross-section as a function of the center-of-mass energy compared to the NNLO QCD calculation.

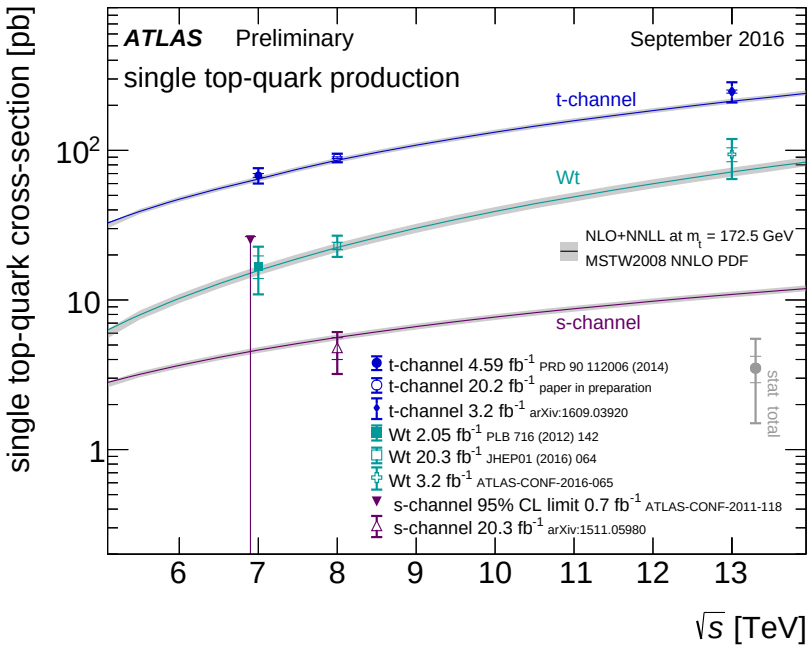

Figure 3.4: Summary of ATLAS measurements of the single top quark production cross-section as a function of the center-of-mass energy compared to the NNLO QCD calculation.

3.1.1 Single top decay and the structure of the Wtb vertex in the standard model

In the SM, the top quark decays weakly into a down-type quark d, s, b and a on-shell W boson. The size of the weak transition from top quarks to W and d, s, b is given by *Cabibbo-Kobayashi-Maskawa(CKM)* matrix element V_{td},V_{ts} and V_{tb} respectively. The dominant decay channels for a top quark is $t \to Wb$ with the decay width given by [48]:

$$\begin{aligned} \Gamma_t &= |V_{tb}|^2 \frac{G_F m_t^3}{8\pi\sqrt{2}} (1 - \frac{m_W^2}{m_t^2})^2 (1 + 2\frac{m_W^2}{m_t^2}) \left[1 - \frac{2\alpha_s}{3\pi}(\frac{2\pi^2}{3} - \frac{5}{2})\right] \\ &\approx 1.5 \text{ GeV} \approx \frac{1}{0.5 \times 10^{-24} \text{ s}}. \end{aligned} \tag{3.1}$$

The other SM decays of top quark including $t \to Wd$ and $t \to Ws$ are negligible contributions to the total decay width because the values of $|V_{td}|^2, |V_{ts}|^2$ are both significantly smaller than $|V_{tb}|^2$.

In addition, the numerical calculation of the decay width Equation 3.1 implies that the lifetime of the top quark is approximately 0.5×10^{-24} s, which is significantly shorter than the hadronization time $\tau_{\text{had}} \approx 3 \times 10^{-24}$ s [49]. Therefore, a top quark will decay via weak interaction before it can form a hadron.

The subsequent decay of W boson can be further divided into two categories: hadronic decays to two light quarks or weak decays to a lepton and an anti-neutrino. In this analysis, we consider only the leptonic decay of t-channel single top quark into electron or muon and their corresponding neutrinos.

3.1.2 Effective field theory and anomalous couplings.

In the SM the structure of the Wtb vertex appearing in the single top-quark t-channel production and decay is described by the Lagrangian

$$L^{\text{SM}} = -\frac{g}{\sqrt{2}} \bar{b} \gamma^\mu \frac{1}{2}(1 - \gamma^5) t W_\mu^- + \text{h.c.} \tag{3.2}$$

where g is the weak coupling constant and $(1 - \gamma^5)/2$ is the left-handed projection operator.

New physics at the Wtb transition can be described by an effective Lagrangian, which modifies the structure of the Wtb vertex, presented by dimension-six effective couplings

$$\mathcal{L}_{\text{eff}} = \sum \frac{C_x}{\Lambda^2} O_x + \cdots , \tag{3.3}$$

where O_x are effective operators invariant under the SM gauge symmetry, C_x are dimensionless constants, and Λ is a new physics scale chosen such that higher-dimension operators are sufficiently suppressed by higher powers of Λ, and $\Lambda \gg \frac{v}{\sqrt{2}}$, where v is the Higgs vacuum expectation value. Of the standardized set of dimension-six operators set forth in Ref. [50], four contribute independently to the Wtb vertex at tree level:

$$\begin{aligned} O_{\phi q}^{(3,3+3)} &= \frac{i}{2}\left[\phi^\dagger(\tau^I \overrightarrow{D}_\mu - \overleftarrow{D}_\mu \tau^I)\phi\right]\left(\bar{q}_{L3}\gamma^\mu \tau^I q_{L3}\right), \\ O_{\phi\phi}^{3,3} &= i\left(\tilde{\phi}^\dagger \overrightarrow{D}_\mu \phi\right)\left(\bar{t}_R \gamma^\mu b_R\right), \\ O_{dW}^{3,3} &= \left(\bar{q}_{L3}\sigma^{\mu\nu}\tau^I b_R\right)\phi W_{\mu\nu}^I, \\ O_{uW}^{3,3} &= \left(\bar{q}_{L3}\sigma^{\mu\nu}\tau^I t_R\right)\tilde{\phi} W_{\mu\nu}^I. \end{aligned} \tag{3.4}$$

Fields q_{L3} are the third-generation left-handed doublets, t_R and b_R are right-handed singlets, ϕ is the Higgs doublet, $\tilde{\phi} = i\sigma_2\phi^*$, and τ^I, $I = 1, 2, 3$ are the Pauli matrices. Electroweak symmetry breaking of the SM Wtb Lagrangian plus these operators results in a general Lorentz-covariant Lagrangian, expressed by Ref. [51, 52], where radiative corrections to the vertex are absorbed into four non-renormalizable effective complex couplings called anomalous couplings:

$$\mathcal{L}_{Wtb} = -\frac{g}{\sqrt{2}}\bar{b}\gamma^\mu \left(V_{\text{L}}P_{\text{L}} + V_{\text{R}}P_{\text{R}}\right) t W_\mu^- - \frac{g}{\sqrt{2}}\bar{b}\frac{i\sigma^{\mu\nu}q_\nu}{m_W}\left(g_{\text{L}}P_{\text{L}} + g_{\text{R}}P_{\text{R}}\right) t W_\mu^- + \text{h.c.}, \tag{3.5}$$

where the four complex effective couplings $V_{\text{L,R}}$, $g_{\text{L,R}}$ can be identified with the coefficients C_x,

$$V_{\text{L}} = V_{tb} + C_{\phi q}^{(3,3+3)}\frac{v^2}{\Lambda^2}, \quad V_{\text{R}} = \frac{1}{2}C_{\phi\phi}^{3,3*}\frac{v^2}{\Lambda^2}, \quad g_{\text{L}} = \sqrt{2}\, C_{dW}^{3,3*}\frac{v^2}{\Lambda^2}, \quad g_{\text{R}} = \sqrt{2}\, C_{uW}^{3,3}\frac{v^2}{\Lambda^2}. \tag{3.6}$$

Here, g is the weak coupling constant, and m_W the mass and q_ν the four-momentum of the W boson. $P_{\text{L,R}} \equiv (1 \mp \gamma^5)/2$ are the left and right-handed projection operators and $\sigma^{\mu\nu} = i[\gamma^\mu, \gamma^\nu]/2$. $V_{\text{L,R}}$ and $g_{\text{L,R}}$ are the left- and right-handed vector and tensor complex couplings, respectively. Within the SM, $V_L = V_{tb} \sim 1$ and V_R,g_L,g_R vanish at the tree level. If CP is conserved in the decay, the coupling constants can be taken to be real.

3.1.3 W-boson helicity fraction

Top quark decay in the framework of the standard model proceeds via the left-handed charged current weak interaction, exhibiting a vector minus axial vector $V-A$ structure. This is reflected in the observed helicity states of the W boson, which can be exploited to examine the couplings at the Wtb vertex.

Using the helicity basis to quantize spin, the $W^{\pm}$ bosons produced in the decay can have helicity 0, +1, and −1, with corresponding helicity fractions F_0, F_R, F_L, satisfying $F_L+F_R+F_0=1$. The $V-A$ structure forces the decay amplitude into $W(\lambda=+1)$ suppressed by a factor m_b^2/M_W^2. In fact, the $V-A$ structure in the SM couples only negative-helicity b quark, and if b were massless, then its helicity is equivalent to its chirality and in this case, F_R vanishes Figure 3.5.

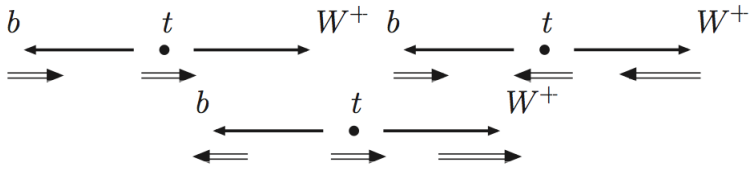

Figure 3.5: Illustration of top-quark decay into a b quark and a W^+ boson with $\lambda_{W^+}=0,\pm1$. The double arrows represent the spin of the particles, while the single arrows stand for their momenta. The conservation law of angular momentum determines the spin distribution between b quark and W^+ and here the orbital part is zero when top quark is at stationary. For W^+, the b quark must have positive helicity, which vanishes for $m_b \to 0$.

In a typical W-helicity analysis in experimental high energy physics, we consider the decay $t \to bW^+ \to bl^+\nu_l$ and define one single angle θ^* to be the angle between the direction of l^+ in the W^+ rest frame and the momentum direction of W^+ in the top rest frame. Then we can obtain the lepton distribution of this angle:

$$\frac{1}{\Gamma}\frac{d\Gamma}{d\cos\theta_l^*} = \frac{3}{8}(1+\cos\theta_l^*)^2F_R + \frac{3}{8}(1-\cos\theta_l^*)^2F_L + \frac{3}{4}\sin^2\theta_l^*F_0 \tag{3.7}$$

with $F_i \equiv \frac{\Gamma_i}{\Gamma}$ the helicity fractions. The interference between those three terms vanishes as we can see from the equation. In the SM, the NNLO QCD calculation gives $F_0 \approx 0.689$,

$F_L \approx 0.309$, $F_R \approx 0.0017$, for $m_t = 173.5$ GeV, M_W=80.385 GeV, m_b=0 [53]. In the presence of anomalous couplings, the helicity fraction $F_{i(i=L,R,0)}$ are modified with respect to SM values:

$$\begin{aligned} F_0 &= \frac{1}{\Gamma}\frac{g^2|\vec{q}|}{32\pi}\Big\{\frac{m_t^2}{M_W^2}[V_L^2+V_R^2](1-x_W^2-2x_b^2-x_W^2x_b^2+x_b^4) \\ &+ [g_L^2+g_R^2](1-x_W^2+x_b^2)-4x_b\,[V_LV_R+g_Lg_R] \\ &- 2\frac{m_t}{M_W}V_L\,[g_R-x_bg_L]\,(1-x_b^2)-2\frac{m_t}{M_W}V_R\,[g_L-x_bg_R]\,(1-x_b^2) \\ &+ 2x_WV_L[g_R+x_bg_L]+2x_WV_R[g_L+x_bg_R]\Big\} \end{aligned} \tag{3.8}$$

$$\begin{aligned} F_{R,L} &= \frac{1}{\Gamma}\frac{g^2|\vec{q}|}{32\pi}\Big\{[V_L^2+V_R^2](1-x_W^2+x_b^2)-4x_b[V_LV_R+g_Lg_R] \\ &+ \frac{m_t^2}{M_W^2}[g_L^2+g_R^2](1-x_W^2-2x_b^2-x_W^2x_b^2+x_b^4) \\ &- 2\frac{m_t}{M_W}V_L[g_R-x_bg_L](1-x_b^2)-2\frac{m_t}{M_W}V_R[g_L-x_bg_R](1-x_b^2) \\ &+ 2x_WV_L[g_R+x_bg_L]+2x_WV_R[g_L+x_bg_R]\Big\} \\ &\pm \frac{g^2}{64\pi}\frac{m_t^3}{M_W^2}\Big\{-x_W^2[V_L^2-V_R^2]+[g_L^2-g_R^2](1-x_b^2)+2x_WV_L[g_R+x_bg_L] \\ &- 2x_WV_R[g_L+x_bg_R]\Big\}(1-2x_W^2-2x_b^2-2x_b^2x_W^2+x_W^4+x_b^4) \end{aligned} \tag{3.9}$$

where $x_W = M_W/m_t$, $x_b = m_b/m_t$ and $\vec{q}$ represents the momentum of W boson in the top rest frame with expression:

$$|\vec{q}| = \frac{1}{2m_t}(m_t^4+M_W^4+m_b^4-2m_t^2M_W^2-2m_t^2m_b^2-2M_W^2m_b^2)^{1/2}. \tag{3.10}$$

Their variations are plotted in Fig.3.9 considering that only one coupling is different from zero at a time and restricting ourselves to the CP-conserving case of real V_R, g_R and g_L. Due to the interference term $V_Lg_R^*$, F_L and F_0 are much more sensitive to g_R than to g_L and V_R.

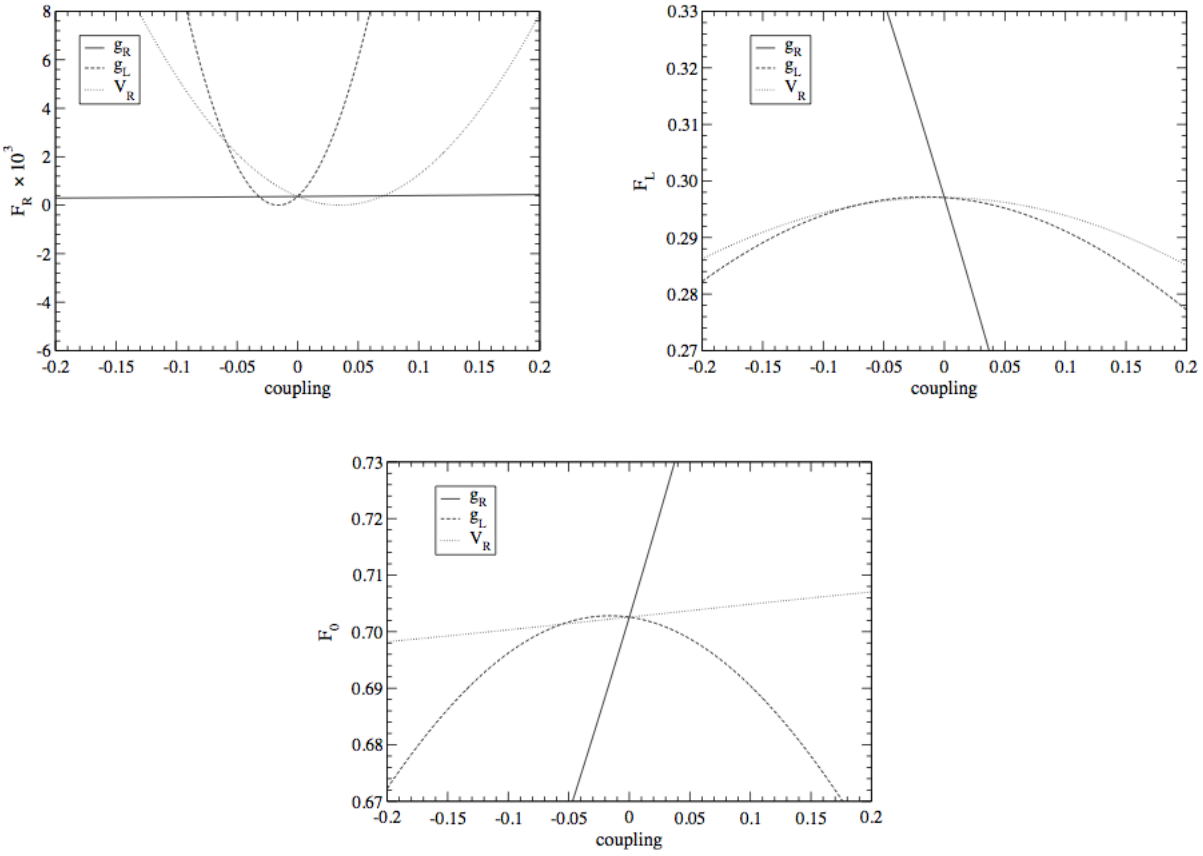

Figure 3.6: Dependence of the helicity fractions $F_i = \Gamma_i/\Gamma$ on the anomalous couplings in the CP-conserving case.

3.1.4 From decay amplitude to an angular distribution of top quark decay products

The analysis presented in this thesis is a powerful extension which uses the full decay kinematics described by three angles to simultaneously constrain all of the anomalous couplings.

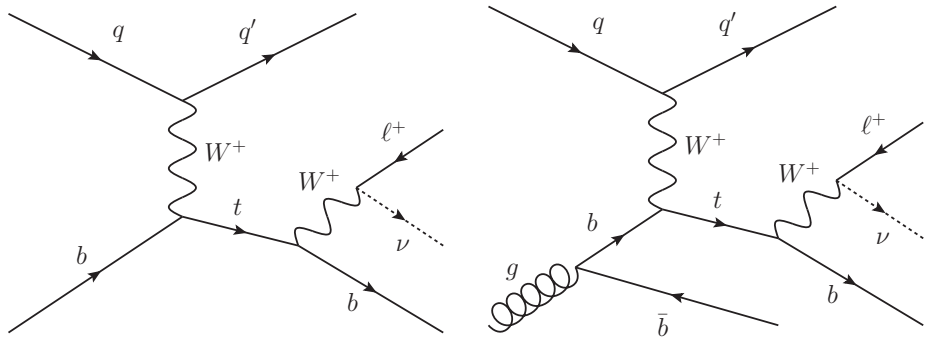

(a) 2→2 process (b) 2→3 process

Figure 3.7: Representative LO Feynman diagrams for t-channel single top-quark production and decay. Here q represents a u or $\bar{d}$ quark, and q' represents a d or $\bar{u}$ quark, respectively. The initial b-quark arises from (a) a sea b-quark in the $2 \to 2$ process, or (b) a gluon splitting into a $b\bar{b}$ pair in the $2 \to 3$ process.

Figure 3.7 shows the t-channel single top quark production and decay at the LHC. We use this figure to illustrate how we can construct a coordinate system and use it to describe the full kinematics of the top decay. Experimentally one can detect and fully reconstruct the decay $t \to W^+b; W^+ \to l^+\nu$ and measure the momentum of the spectator jet. The neutrino in the decay can be reconstructed from missing transverse energy in a "hermetic" detector covering a solid angle of approximately 4π. The coordinate system then can be constructed as follows. The momentum of the W boson in the top quark rest frame is called $\vec{q}$ and the spectator quark jet direction $\vec{s}_t$ in space orthogonal to $\vec{q}$ are meaningful as proposed in [54] and described in Fig 3.8:

$$\vec{N} = \vec{s}_t \times \vec{q},$$
$$\vec{T} = \vec{q} \times \vec{N}.$$

Using these directions we can construct a right-handed coordinate system such that the $\hat{x}$ direction points along $\vec{T}$; the $\hat{y}$ direction lies along $\vec{N}$, and the $\hat{z}$ direction points along $\vec{q}$. The momentum of the charged lepton as measured in the W rest frame is called $\vec{p}_l$. We define θ as the angle between $\vec{s}_t$ and $\vec{q}$ in the top quark rest frame, the θ^* between $\hat{q}$ and $\vec{p}_l$ and the complementary azimuthal angle ϕ^*. This θ^* is the same angle as used to measure the W boson helicity fraction.

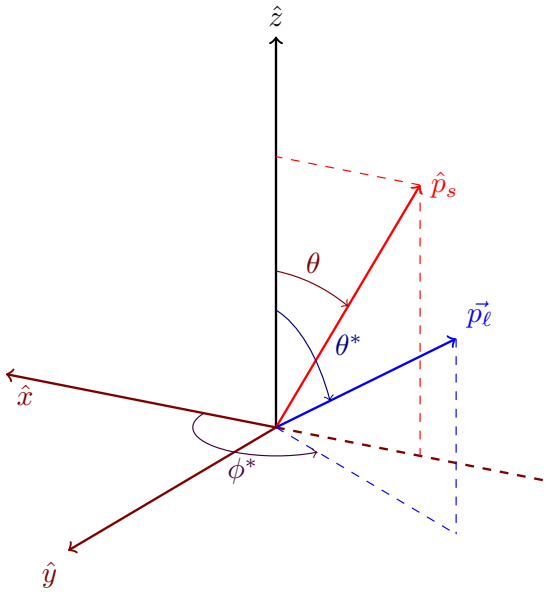

Figure 3.8: Definition of the right-handed coordinate system with $\hat{x}$, $\hat{y}$, and $\hat{z}$ defined as shown from the momentum directions of the W boson, $\hat{q} \equiv \hat{z}$, and the spectator quark, $\hat{p}_\mathrm{s}$, in the top-quark rest frame. The angles θ^* and ϕ^* indicate the lepton direction $\hat{p}_\ell$ while the angle θ indicates the spectator quark direction $\hat{p}_\mathrm{s}$ in this coordinate system.

With this coordinate system, we construct the angular dependence of the decay $t \to W^+b; W^+ \to l^+b$ using the helicity formalism [55]. The angular dependence of the amplitude for two-body decay is given by

$$A(a \to f_1 f_2) = \sqrt{\frac{2J+1}{4\pi}} D^{J*}_{M,\lambda}(\phi, \theta, -\phi) A_{\lambda_1,\lambda_2} \tag{3.11}$$

where λ_1 and λ_2 are the helicities of the outgoing particles and $\lambda = \lambda_1 - \lambda_2$. J and M are the spin and helicity of the decaying particle, $D^J_{M,L}$ is the Wigner D-function, and the angles

are defined in the rest frame of the decaying particle. A_{λ_1,λ_2} is the amplitude for the decay to the specified helicity states as depicted in Fig 3.9.

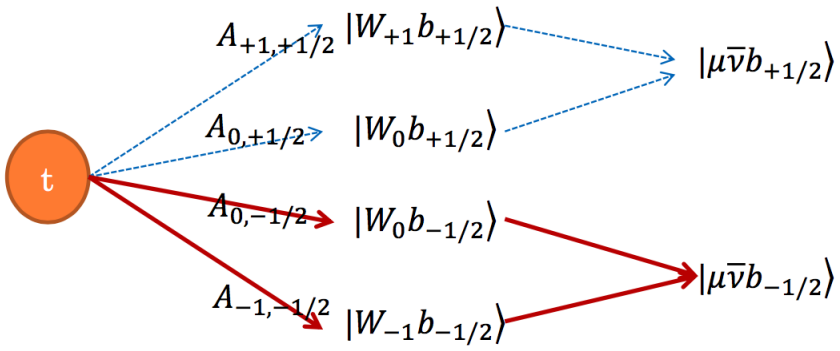

Figure 3.9: The subscripts λ_1,λ_2 in the decay amplitude A_{λ_1,λ_2} represent the helicity of the W boson and b quark respectively. Nature takes all of these four paths at the same time. There is interference in transitions to these two final states in top (and bottom) but no interference between the upper two paths and the lower two paths in this diagram.

One can construct the full triple differential decay rate for the angular distribution by including the amplitude for $t \to W^+b$ and $W^+ \to l^+\nu$. For $W^+ \to l^+\nu$, $J = 1, \lambda_1 = \frac{1}{2}, \lambda_2 = -\frac{1}{2}$, and $\lambda = 1$:

$$\begin{aligned} A(t \to W^+b) &= \sqrt{\frac{1}{2\pi}} D^{\frac{1}{2}*}_{\frac{1}{2},\lambda_W-\lambda_b}(\phi,\theta,-\phi) A_{\lambda_W,\lambda_b} \\ A(W^+ \to l^+\nu_l) &= \sqrt{\frac{3}{4\pi}} D^{1*}_{\lambda_W,1}(\phi,\theta,-\phi) A_{\frac{1}{2},\frac{1}{2}} \end{aligned} \tag{3.12}$$

We then obtain the total angular distribution from summing the amplitude over possible intermediate W helicities, squaring the magnitude and summing over the possible final state b-helicities:

$$\begin{aligned} |M(t \to W^+b \to l^+\nu_l b|^2 \equiv \frac{dN}{d\Omega d\Omega^*} &= \sum_{\lambda_b} |\sum_{\lambda_W} A(t \to W^+b) A(W^+ \to l^+\nu|^2 \\ &= \sum_{\lambda_b} \left| \sum_{\lambda_W} \frac{6}{4\pi} D^{\frac{1}{2}*}_{\frac{1}{2},\lambda_W-\lambda_b}(\phi,\theta,-\phi) D^{1*}_{\lambda_W,1}(\phi^*,\theta^*,-\phi^*) \right| \end{aligned}$$

For $\lambda_b = \frac{1}{2}$, only intermediate W helicities $\lambda_W = 1, 0$ are possible, while for $\lambda_b = -\frac{1}{2}$, $\lambda_W = -1, 0$ are possible. Thus the angular distribution contains 6 possible terms: 4 proportional to the square of each of the possible general amplitudes, as depicted in Figure 3.9, and 2 for the two possible interference terms. So although there are general amplitudes with 3 relative phases, only 2 relative phases are accessible in the decay information for polarised single top quark decay. The interference term between intermediate Ws with helicity ± 1 above has zero amplitude from the $t \to Wb$ decay. Note that the direction definition $\varphi = 0$ is arbitrary, but will be the same for φ (the plane defined by the top quark polarisation direction and the W direction in the top quark rest frame), and φ^* (the plane defined by the W direction in the top quark rest frame and lepton direction in the W rest frame). Thus all dependences appear in the combined formula as $\phi^* = \varphi^* - \varphi$.

The total angular distribution of top quark decay including the top polariation P be expressed in terms of the *spherical harmonics* Y_l^m and the associated Legendre functions P_l^m:

$$
\begin{aligned}
\rho(\theta,\theta^*,\phi^*) &= \frac{1}{N}\frac{dN}{d\Omega d\Omega^*} \\
&\quad \frac{1}{(4\pi)^{\frac{3}{2}}}\Bigg[\Bigg\{ \left(|A^2_{1,\frac{1}{2}|} + |A_{-1,-\frac{1}{2}}|^2 + |A_{0,\frac{1}{2}}|^2 + |A_{0,-\frac{1}{2}}|^2\right) P_0^0(\cos\theta) \\
&+ P\left(|A_{1,\frac{1}{2}}|^2 - |A_{0,\frac{1}{2}}|^2 + |A_{0,-\frac{1}{2}}|^2 + |A_{-1,-\frac{1}{2}}|^2\right) P_1^0(\cos\theta)\Bigg\} Y_0^0(\theta^*,\phi^*) \\
&+ \frac{\sqrt{3}}{2}\Bigg\{ |A_{1,\frac{1}{2}}|^2 - |A_{-1,-\frac{1}{2}}|^2 P_0^0(\cos\theta) \\
&+ P(|A_{1,\frac{1}{2}}|^2 + |A_{-1,-\frac{1}{2}}|^2) P_1^0(\cos\theta)\Bigg\} Y_1^0(\theta^*,\phi^*) \\
&+ \frac{1}{2\sqrt{5}}\Bigg\{ \left(|A_{1,\frac{1}{2}}|^2 - 2|A_{0,\frac{1}{2}}|^2 - 2|A_{0,-\frac{1}{2}}|^2 + |A_{-1,-\frac{1}{2}}|^2\right) P_0^0(\cos\theta) \\
&+ P\left(|A_{1,\frac{1}{2}}|^2 + 2|A_{0,\frac{1}{2}}|^2 - 2|A_{0,-\frac{1}{2}}|^2 - |A_{-1,-\frac{1}{2}}|^2\right) P_1^0(\cos\theta)\Bigg\} Y_2^0(\theta^*,\phi^*) \\
&- P\Bigg\{ \frac{\sqrt{3}}{2}\left(A_{1,\frac{1}{2}}A^*_{0,\frac{1}{2}} + A^*_{-1,-\frac{1}{2}}A_{0,-\frac{1}{2}}\right) P_1^1(\cos\theta) Y_1^1(\cos\theta^*,\phi^*) \\
&- \frac{\sqrt{3}}{2}\left(A^*_{1,\frac{1}{2}}A_{0,\frac{1}{2}} + A_{-1,-\frac{1}{2}}A^*_{0,-\frac{1}{2}}\right) P_1^1(\cos\theta) Y_1^{-1}(\cos\theta^*,\phi^*) \\
&+ \frac{\sqrt{3}}{2\sqrt{5}}\left(A_{1,\frac{1}{2}}A^*_{0,\frac{1}{2}} - A^*_{-1,-\frac{1}{2}}A_{0,-\frac{1}{2}}\right) P_1^1(\cos\theta) Y_2^1(\cos\theta^*,\phi^*) \\
&- \frac{\sqrt{3}}{2\sqrt{5}}\left(A^*_{1,\frac{1}{2}}A_{0,\frac{1}{2}} - A_{-1,-\frac{1}{2}}A^*_{0,-\frac{1}{2}}\right) P_1^1(\cos\theta) Y_2^{-1}(\cos\theta^*,\phi^*)\Bigg\}\Bigg]. \qquad (3.13)
\end{aligned}
$$

It is interesting to note that if we integrate out the angle θ and ϕ appears in the expression above, with proper notation (use F_i instead of A_{λ_a,λ_b}), we can restore the Equation 3.7.

In the analysis we will discuss in later chapter, we will use this triple differential decay rate for constructing our physics observables, analyzing the interested events, and estimating the anomalous couplings. This specifically chosen method provides us:

- a simultaneous measurements of all our physics parameters.
- the usage of full information from each event.
- without assumptions on other parameters including top polarisation and obtaining an estimation of the polarisation.
- getting all the correlations of physics observables.

3.2 PREVIOUS MEASUREMENTS

Previous measurements have constrained the anomalous couplings and theoretical scenarios that give rise to them.

Tight indirect constraints are on some of the anomalous couplings come from the measured branching ratio $\bar{B} \to X_s\gamma$ in Ref.[56]. A recent update of this calculation [2] yields $\mathrm{Re}\,[V_R] \in [-0.0008, 0.0021]$, $\mathrm{Re}\,[g_L] \in [-0.0011, 0.0004]$, $\mathrm{Re}\,[g_R] \in [-0.19, 0.48]$. These bounds obtained by assuming the anomalous couplings to be real and allowing only one of the couplings to be non-zero in one single measurement.

The best constraints on $\mathrm{Re}\,[g_R]$ come from W boson helicity fractions in top-quark decays, with $\mathrm{Re}\,[g_R]$ constrained to be in $[-0.08, 0.04]$ and $[-0.08, 0.07]$, both at 95% C.L., from ATLAS [57] and from CMS [58], respectively. These limits use the measured single top-quark production cross-section [59, 60] along with the assumption that $V_L = 1$ and $\mathrm{Im}\,[g_R] = 0$. Without these assumptions, no value within the range $0.0 \leq \mathrm{Re}\,[g_R/V_L] \leq 0.8$ can be excluded.

The limits presented in paper [12] remove these assumptions and extend the knowledge of g_R to the whole complex plane by simultaneously measuring information about $\mathrm{Re}\,[g_R/V_L]$ and $\mathrm{Im}\,[g_R/V_L]$. It gives a tight measurement on $\mathrm{Im}\,[g_R/V_L] \in [-0.17, 0.23]$ but a looser measurement on $\mathrm{Re}\,[g_R/V_L] \in [-0.36, 0.10]$. In addition, the correlation of these two variables are given as $\rho(\mathrm{Re}\,[g_R/V_L]\,, \mathrm{Im}\,[g_R/V_L]) = 0.11$. This measurement assumes $V_R/V_L = 0$.

On the theoretical side, there have been a number of studies on new physics contributions to top decay process, such as vectorlike quark model, two-Higgs double models, G(221) models (with a new gauge boson W' introduced and mixed with the SM gauge boson), top-color assisted technicolor models, the minimal supersymmetric extension of the standard model(MSSM) and etc. Two of these models are briefly described below and more details about new physics models modifying the Wtb vertex can be found in [2, 3, 52, 61–64].

- Vectorlike quark model

  The vector-like quark (VQL) model is a common extension of SM models to new physics. In VQL, the Wtb coupling is modified by the mixing between top-quark with their corresponding partner, called T. The spontaneous symmetry breaking gives the mass

terms of the top-quark and T in the singlet or triplet models:

$$L^t_{\text{mass}} = -\frac{y_t \nu}{\sqrt{2}} \bar{t}_L t_R - x_t \bar{t}_L T_R - M \bar{T}_L T_R + h.c. \tag{3.14}$$

where y_t is the Yukawa coupling of top quark in the SM, x_t is the mixing parameter between t and T, and M is the mass of the new vectorlike quark T.

For the doublet vectorlike quark mode, the mass terms are:

$$L^t_{\text{mass}} = -\frac{y_t \nu}{\sqrt{2}} \bar{t}_L t_R - x_t \bar{T}_L t_R - M \bar{T}_L T_R + h.c. \tag{3.15}$$

In addition, the mass eigenstates can be transformed to the weak eigenstates as:

$$\begin{pmatrix} t_{L,R} \\ T_{L,R} \end{pmatrix}_{\text{weak}} = \begin{pmatrix} c^t_{L,R} & s^t_{L,R} \\ -s^t_{L,R} & c^t_{L,R} \end{pmatrix} \cdot \begin{pmatrix} t'_{L,R} \\ T'_{L,R} \end{pmatrix} \tag{3.16}$$

where $t'_{L,R}$ and $T'_{L,R}$ represent the mass eigenstates. $c^t_{L,R}$ and $s^t_{L,R}$ denote the cosine and sine of the mixing angles between left-handed and right-handed top quark with its top partner and can be computed in the singlet and triplet model:

$$s^t_L = \frac{M x_t}{\sqrt{(M^2 - m_t^2)^2 + M^2 x_t^2}}, s^t_R \frac{m_t}{M} s^t_L. \tag{3.17}$$

For the doublet

$$s^t_R = \frac{M x_t}{\sqrt{(M^2 - m_t^2)^2 + M^2 x_t^2}}, s^t_L \frac{m_t}{M} s^t_R, \tag{3.18}$$

where m_t is the top quark mass.

In table 3.1, we show the seven possible vector-like models and their V_L and V_R. The Figure 3.10 shows allowed parameter space of $s^t_{L,R}$ and $s^b_{L,R}$ obtained by a fit with previous ATLAS and CMS data [2]. The $c^b_{L,R}$ and $s^b_{L,R}$ denote the cosine and the sine of the mixing angles between left-handed and right-handed bottom quark with the bottom partner $B_{L,R}$.

model	(T)	(B)	(X,T)	(T,B)	(B,Y)	(X,T,B)	(T,B,Y)
V_L	c_L^t	c_L^b	c_L^t	$c_L^t c_L^b + s_L^t s_L^b$	c_L^b	$c_L^t c_L^b + \sqrt{2} s_L^t s_L^b$	$c_L^t c_L^b + \sqrt{2} s_L^t s_L^b$
V_R	0	0	0	$s_R^t s_R^b$	0	$\sqrt{2} s_R^t s_R^b$	$\sqrt{2} s_R^t s_R^b$

Table 3.1: The Wtb vertex in seven models.

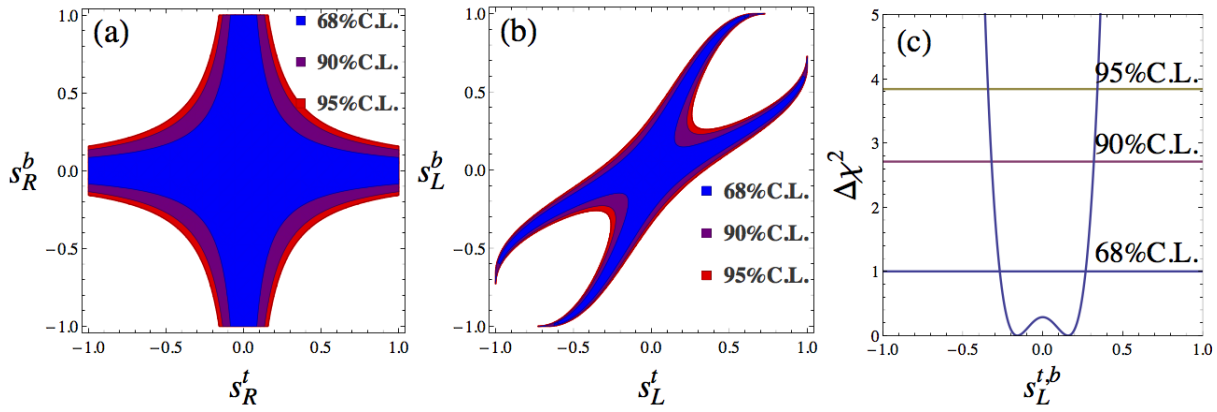

Figure 3.10: The possible values for $s_{L,R}^t$ using a global fit on CMS and ATLAS data. (a) Doublet (T, B) model; (b) Triplet models; (c) Singlet, Doublet (X, T), (B,Y) models. From reference [2].

- Two-Higgs doublet extensions

  The two-Higgs-doublet model (2HDM) is an extension of the Standard Model in which two Higgs doublets are employed. In a general type-II 2HDM, where the Higgs doublets ϕ_1 and ϕ_2 couple only to right-handed down-type fermions and up-type fermions, respectively.

  In the case when the tree-level Higgs potential is CP-invariant. In addition to the two neutral Higgs boson masses m_{h^0},m_{H^0}, one pseudoscalar Higgs boson mass m_{A^0}, and two charged Higgs bosons m_{H^+}, the model has two more free parameters, ν_1 and ν_2, which are the vacuum expectation values of the Higgs fields $\phi_{1,2}$ respectively. After considering

the contribution in Figure 3.11 for the decay amplitudes. Two generic features about the anomalous coupling form factors can be found [3]

$$|\delta V_L = V_L - V_{tb}| \gg |g_R| \gg |V_R|, |g_L|,$$
$$|\mathrm{Re}\,[\delta V_L]\,| \gg |\mathrm{Re}\,[g_R]\,| \gg |\mathrm{Im}\,[\delta V_L]\,|, |\mathrm{Im}\,[g_R]\,|. \tag{3.19}$$

based on the constrained experimental results

$$m_{h^0}, m_{H^0}, m_{A_0} \geq 120\ \mathrm{GeV}, m_{H^+} \geq 320\ \mathrm{GeV}, 0.5 \leq \tan\beta = \tan\frac{\nu_2}{\nu_1} \leq 50. \tag{3.20}$$

Besides, for low $\tan\beta$, the possible magnitudes of δV_L and g_R are 6×10^{-3} and 5×10^{-4}, while only 2×10^{-2} and 2×10^{-4} are expected for high $\tan\beta$, respectively.
As for the CP-violating neutral Higgs-boson exchange in the 2HDM, $|\mathrm{Im}\,[\delta V_L]\,| \leq 5 \times 10^{-4}$ and $|\mathrm{Im}\,[g_R]\,| \leq 3.5 \times 10^{-4}$ is expected when $m_{\phi_1} = 120\ \mathrm{GeV}, m_{\phi_2} = m_{\phi_3} = 700\ \mathrm{GeV}, m_{H^+} = 320\ \mathrm{GeV}, \tan\beta = 1$ (CP violation effects are largest).

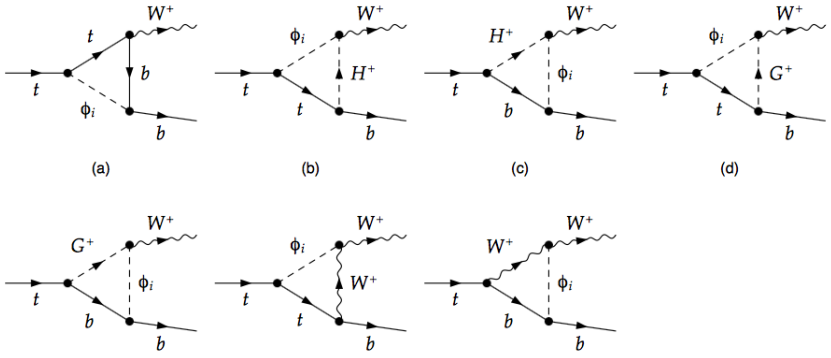

Figure 3.11: The possible Higgs contribution to the Wtb vertex in the type-II 2HDM. The self-energy correction Feynman diagrams are not included here. From reference [3].

4.0 THE LHC AND THE ATLAS EXPERIMENT

The status of top quark physics require collision data from high energy experiments. Since the top quark is very massive and its production requires a large amount of energy. In this chapter we discuss the Large Hadron Collider (LHC) used to produce proton-proton collisions, and the ATLAS particle detector operating in the LHC. Millions of top quarks are produced in these collisions at the LHC annually. Top quarks are then detected by the particle detectors, recorded as data and analyzed by us.

4.1 THE LARGE HADRON COLLIDER

4.1.1 Overview of LHC

Large Hadron Collider (LHC) [65] is the worlds longest and highest energy circular proton-proton collider. It is located at CERN[1], fitted in a tunnel that was previously built for the large electron positron collider [67] (LEP). At the collision points, four large experiments sits below ground in huge carven over the LHC rings.

The physics of strong interacting matter is studied at extreme energy densities using a Large Heavy Ion Collider Experiment (ALICE [68]). CMS [69] and ATLAS [70] are two general purpose detectors. Both the detectors serve the same purpose however they differ in their magnetic system designs. The Large Hadron Collider Beauty (LHCb [71]), experiment designed to study heavy quark flavor b and c, and to investigate *CP violation*. The analysis described in this thesis is performed using the data produced by the LHC and collected by

[1]The European Organisation for Nuclear Research(CERN) laboratory is the largest particle physics lab in operation [66].

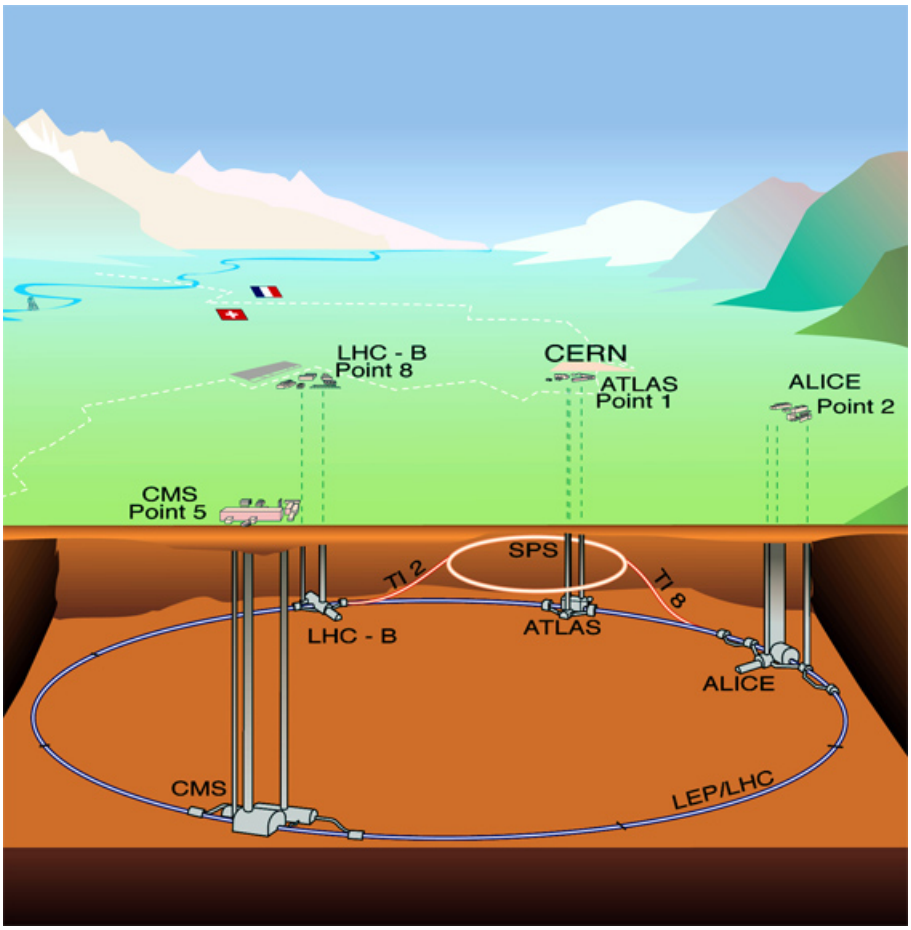

Figure 4.1: The LHC is a particle accelerator of 27 km length. Four main experiment (ATLAS, CMS, ALICE, and LHCb) built around the collision points at LHC are shown. The biggest operational particle physics lab CERN is situated in the border between Switzerland and France near Geneva. (Courtesy of CERN)

the ATLAS detector during 2012.

4.1.2 The collision and luminosity

The LHC can be used for producing both the heavy ion (HI) collision and proton-proton (pp) collisions [72]. The protons or heavy ion are accelerated in many pre-accelerators before they are injected into the LHC.

The beginning of the path of a proton, in pp collision is a bottle of hydrogen gas at the linear accelerator [73]. Hydrogen atoms are stripped of their electrons by a strong electric field for injection into the LINAC-2 accelerator. As the Fig 4.2 shows, the protons are then accelerated in the Proton Synchrotron Booster (PSB), the Proton Synchrotron (PS), the Super Proton Synchrotron (SPS) and finally the proton-bunches are divided into two halves, where they are injected into the LHC in opposite directions.

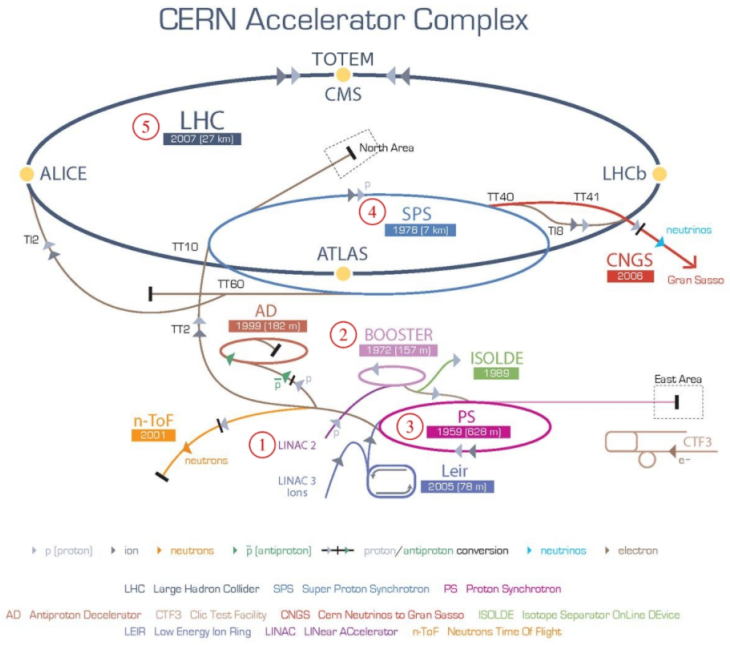

Figure 4.2: Accelerator facilities at CERN and associated experiments. This figure is taken from [4].

The performance of LHC can be summarized with two parameters, the instantaneous luminosity, L, and the center-of-mass energy, $\sqrt{s}$. The instantaneous luminosity is a measure the number of collisions produced per cm^2 per second in a detector. It relates the production rate of a given process to its cross section:

$$\frac{dN}{dt} = L \times \sigma. \tag{4.1}$$

The integrated luminosity is the integral of the instantaneous luminosity. In 2012, the beam energy of the LHC was 4 TeV, giving a center-of-mass energy of $\sqrt{s} = 8$ TeV. At

this energy, the corresponding peak instantaneous is around 7.7×10^{33} [74]. Fig 4.3 shows the luminosity delivered by the LHC (23.3 fb^{-1}) as well the luminosity recorded by ATLAS (21.7 fb^{-1}).

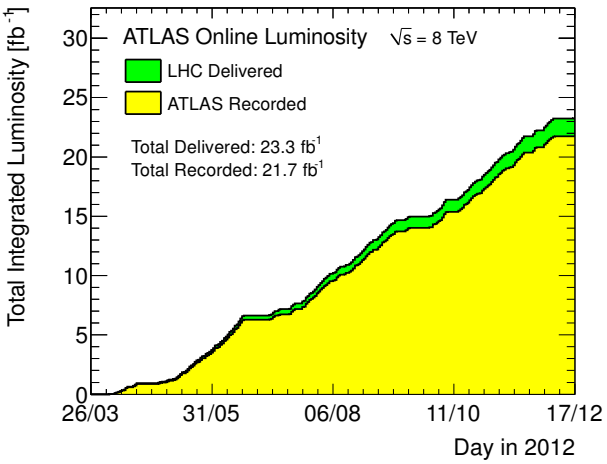

Figure 4.3: Cumulative luminosity versus day delivered to (green), and recorded by ATLAS (yellow) during stable beams and for *pp* collisions at 8 TeV centre-of-mass energy in 2012. (ATLAS Courtesy)

4.2 THE ATLAS DETECTOR

The ATLAS (A Toroidal LHC Apparatus) detector is a general purpose particle detector [70] used to identify particles that are produced in the collisions at the corresponding interaction region of the LHC. It is 46 meters in length and 25 meters in diameter, weighing 7 thousand tonnes. It consists of three main sub-detector systems. Figure 4.4 gives an overview of the components in each system. To identify, select and measure the final states of single top quark events produced in t-channel, all these subdetectors are used. The innermost layers of tracking detector are used to provide precision measurements of the impact parameter of charged particles. The electromagnetic and hadronic calorimeter that surround the tracking provide measurements of the energy of particles. For identifying and measuring the momentum of muons, an additional muon spectrometer is positioned outside the calorimeters. In addition, neutrinos, and other possible currently unknown weakly interacting particles must be inferred from an imbalance in the transverse momentum of all the particles measured in a collision. The magnet occupies most of the volume of the muon chambers and the calorimeter.

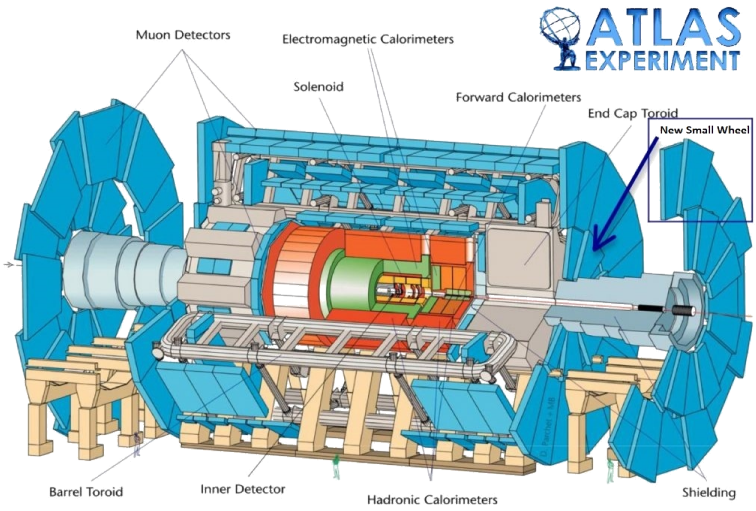

Figure 4.4: Sliced view of the ATLAS detector, with indication of the main sub-system. (Courtesy of ATLAS collaboration).

The detector hardware is integrated with a trigger and a data acquisition system. The

trigger is a multi-level system composed of electronics, computers and software. It selects useful events from millions more occurring per second. The data acquisition system processes the data from detector to storage device.

4.2.1 The ATLAS coordinate system

We describe the ATLAS detector using a right-handed coordinate system. The origin of the coordinate system is at the interaction point (IP) in the center of the detector. The $x - y$ plane is perpendicular to the beam axis. A positive Cartesian x-axis is defined as the horizontal direction towards the LHC center and the z-axis positions towards beam pipe axis. Polar coordinates (r, ρ) can be used in transverse plane. The pseudo-rapidity of particle measured is defined as:

$$\eta = -\ln\left[\tan\left(\frac{\theta}{2}\right)\right], \tag{4.2}$$

where θ is the angle between the particle three-momentum $\mathbf{p}$ and the positive direction of the beam axis.

In terms of momentum above equation can be written as:

$$\eta = \frac{1}{2}\ln\left(\frac{|\mathbf{P}| + p_L}{|\mathbf{P}| - p_L}\right), \tag{4.3}$$

where $p_L = p_z$ is the momentum along the beam direction.

If the particle travels with the speed of light pseudo-rapidity approaches the rapidity defined by particle experimental physics:

$$y = \frac{1}{2}\ln\left(\frac{E + p_L}{E - p_L}\right). \tag{4.4}$$

Here E is the total energy of the particle and $E \sim p$.

Tracks and other physics objects can be described by in terms of other useful parameters which will help in reconstruction of objects physics.

- p_T the transverse component of the momentum which is the projection of total momentum into $x - y$ plane.
- $\Delta R = \sqrt{(\eta_2 - \eta_1)^2 + (\phi_2 - \phi_1)^2}$ quantifies the $\eta - \phi$ distance corresponds to a rectangular coordinate system in η and ϕ.

4.2.2 Inner detector

The inner detector (ID) [75, 76] is the first sub-detector through which particles pass. The Figure 4.5 shows its layout. It is comprised of three sub-detectors: a silicon pixel detector (PIX), a silicon micro-strip (SCT) detector and a transition radiation detector (TRT). The superconducting solenoid provides a magnetic field of 2T around the inner detector. This magnetic field bends the paths of charged particles.

Primary and secondary vertices [2] are reconstructed from hits measured in the inner detector. The pixel detector is installed as close as possible to the beam line for precise impact parameter measurement. A large number of tracks converge near to the beam line, so the inner detector require segments for pattern recognition and high resolution for precise measurement.

The coverage of inner detector is shown in Figure 4.6. Details of the pixel detector, the SCT, and the TRT are given below.

a. The Pixel Detector

   The innermost sub-detector of the ID is the silicon pixel detector [77]. The barrel region of the pixel detector consists of three cylindrical layers of silicon pixels. These layers are positioned at a radius of 50.5 mm, 88.5 mm , and 122.5 mm. Three disks are positioned as two end caps. Barrel and end caps both carry the basic element of a pixel detector which is a silicon sensor module. A single silicon module is a dimension 6×2 cm rectangular chip with 50,000 cells of pixels. A pixel cell has a uniform size of $50 \times 400 \mu m^2$. This size is required to obtain the desired spatial resolution of 12 μm [78]. The pixel detector has 80 million readout channels out of which 13 million are in the endcaps and about 67 million are in the barrels. The pixel detector has the highest spatial resolution of any ATLAS detectors. The number of precision layers is limited only by the dead material and the costs. Inner pixel layers can sustain an ionization does of 500kGy, which is the normal amount of expected dose during LHC's 5 year operational period [79]. Figure 4.6 shows the η coverage of pixel detector, which extends to a pseudo-rapidity 2.5 while covering full ϕ [77].

[2] The primary vertex refers to the collision point and the second vertex is due to the short lived particles such as B-Hadrons.

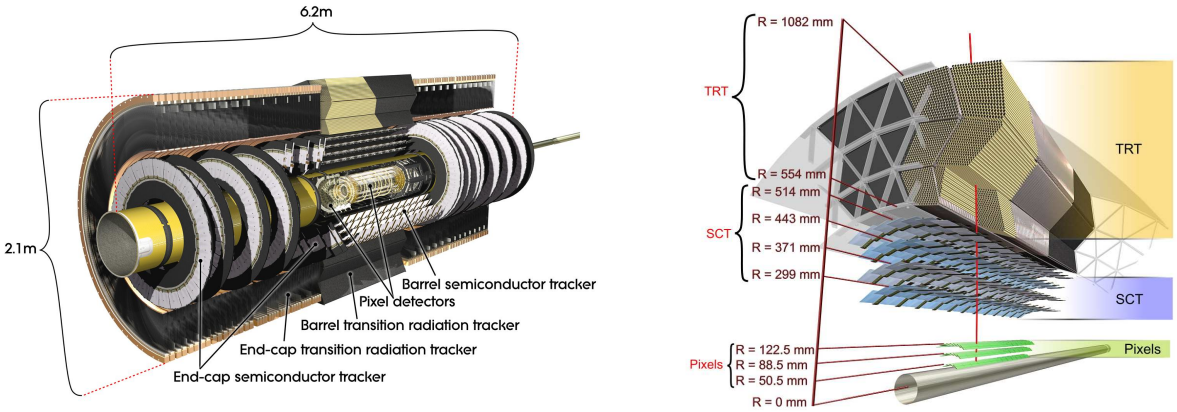

(a) (b)

Figure 4.5: The ATLAS inner detector overview(a) and the cross-section view at barrel(b). (Courtesy of CERN).

b. The SemiConductor Tracker

The semiconductor tracker(SCT) [80] is positioned concentrically around the silicon pixel detector. It provides four layers of micro-strip modules between 30 cm and 51 cm. The end-caps are positioned as indicated in the Figure 4.5. On each side of barrel there are 9 disks used which cover up to η of 2.5. The total number of readout channels for semiconductor tracker are 6.3 million divided into 4088 modules [5]. The functionality of both the silicon pixel detector and semiconductor tracker are similar. In semiconductor tracker strips are used rather than pixels.

The construction of a semiconductor module is based on two silicon strip layers through a stereo angle of 40 mrad with respect to the module axis [81]. Precision points in the $r\phi$ is provided by strips which are positioned parallel to the beam line. The resolution is 16 μm in $r\phi$ direction and z coordinate is also measured by using stereo angle up to 580 μm. Four different precision measurements hits are provided by semiconductor tracker including impact parameters, vertex positions and particle momentum [75].

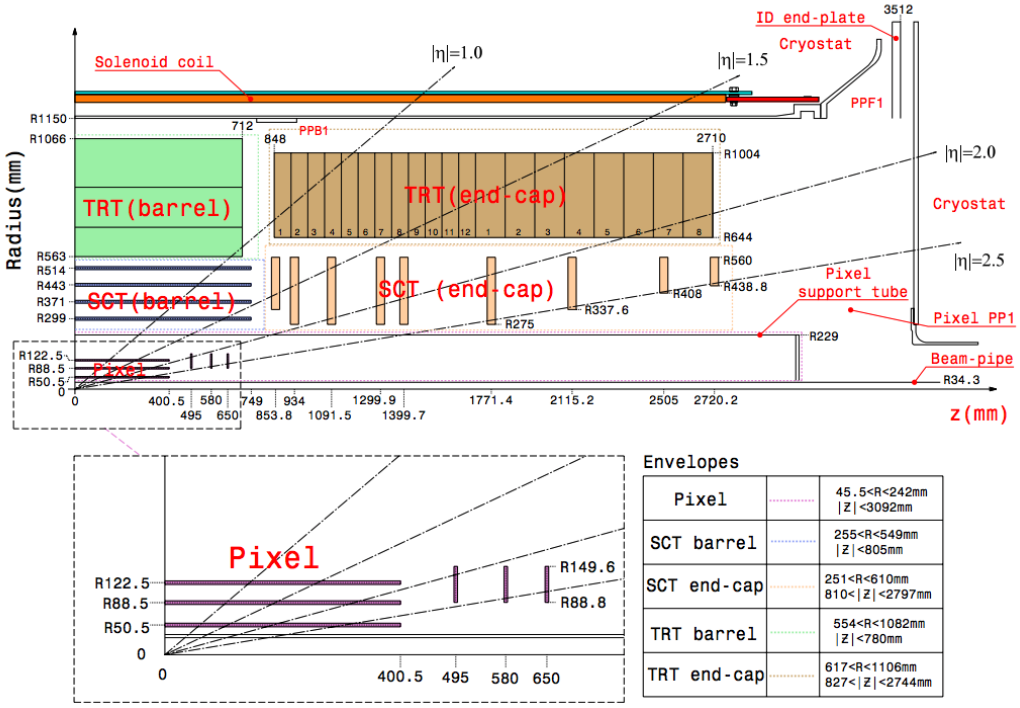

Figure 4.6: The overview of the η-coverage of the subdetectors in the inner detector. The overall η-coverage increases to the edge of the end-cap semiconductor tracker with $\eta = 2.5$ and it has a full ϕ coverage. Figure is from [5].

c. The Transition Radiation Tracker

The outermost inner detector – the transition radiation tracker (TRT) – lies between 55 and 108 cm in radius. The end-caps lie between 64 cm and 103 cm [75]. The pseudo-rapidity coverage over which the particles can be measured by TRT is from 0 to 2. Straw tubes are the basic detector elements of the transition radiation tracker. The diameter of a tube is 4 mm, which is chosen as a compromise between the response speed and operational stability [82]. The straws are filled with nonflammable mixture of Xenon, Carbon dioxide and oxygen gas [83]. A charged particle transversing the TRT ionizes the gas inside the straws and develops an electric signal on a sense wire within the straw. In addition to functioning as a straw tracker, the TRT plays a role in electron

identification by detecting transition-radiation of photons produced by electrons passing through the tubes. The end caps of the TRT contains about 320,000 radial straws and the barrel contains approximately 50,000 straws, making the total number of readout channels approximately to 420,000 [75]. This design ensures that charged particles with $p_T > 0.5$ GeV cross over 30 tubes (except for the transition region between barrel and endcap) [84]. The spatial resolution provided by a TRT straw tube is about 130 micro meter.

4.2.3 Calorimeters

A calorimeter system surrounds the inner detector as depicted in Figure 4.7. The calorimeter system measures the energy and position of both charged and neutral particles. On entering the calorimeters particles lose their energies and produce showers. Active and passive volumes alternate in the ATLAS calorimeter. In the active volume the energy of the shower is sampled. In the passive volume the showers are initiated and developed.

The calorimeters are further divided into two segments, electromagnetic and hadronic. Electromagnetic calorimeters [7] are designed to measure electrons, positrons, and photons. The hadronic calorimeters [85] measure heavy particles interacting through the strong interaction. The liquid argon (LAr) EM calorimeter covers the pseudo-rapidity region $|\eta| < 3.2$. Hadronic calorimeter in the barrel region is based on scintillator tiles. Liquid Argon is also used for hadronic endcap calorimeter. The barrel hadronic calorimeter covers $|\eta| < 1.7$, and LAr hadronic covers at end-caps between $1.5 < |\eta| < 3.2$. However, In the ATLAS detector at the LHC, the precision calorimetry for electrons and photons covers up to $|\eta| < 2.5$. A forward LAr calorimeters(FCal) is applied to cover the pseudo-rapidity $3.1 < |\eta| < 4.9$.

Both the hadronic and electromagnetic calorimeters are described in more detail below.

a. The Electromagnetic Calorimeter

The energy and position of photons and electrons is measured in the ATLAS electromagnetic calorimeter. The electromagnetic calorimeter adopts an accordion geometry (see Figure 4.8). Many layers of lead form the structure of accordion shape. Liquid argon is used in between these layers for sampling the energy of showering particles.

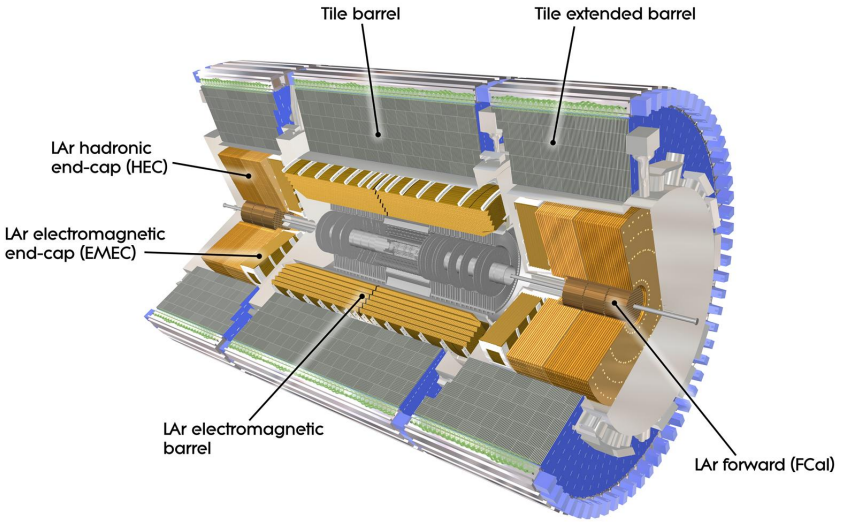

Figure 4.7: Schematic view of the ATLAS calorimeter system. In light yellow the electromagnetic and in grey the barrel hadronic calorimeter. The very forward calorimeter is shown in dark yellow, and the hadronic end-caps are also painted dark yellow. From reference [6].

The electromagnetic calorimeter is divided into two parts i.e. a central barrel located in a cylindrical cryostat and end-caps at both sides. These are perpendicular to the pipe beam. Two identical half barrels form a central barrel with coverage of $|\eta| < 1.475$. The two halves are separated by a small distance with $\eta = 0$. The two electromagnetic end-caps are further divided into coaxial wheels, denoted as outer and inner wheels. They covers pseudo-rapidity of $1.375 < |\eta| < 2.5$ and $2.5 < \eta < 3.2$ respectively.

b. The Hadronic Calorimeter

The Hadronic calorimeters include the Tile calorimeter, the liquid-argon Hadronic end-cap (HEC) and liquid-argon Forward hadronic calorimeters (FCals) as depicted in Figure 4.7.

The Tile calorimeter [85] is located behind the solenoid and the EM calorimeter and is a sampling calorimeter using steel as absorber and scintillating tiles as active material. It is further divided into four parts, two central barrels ($|\eta| < 1.0$) and two extended barrels

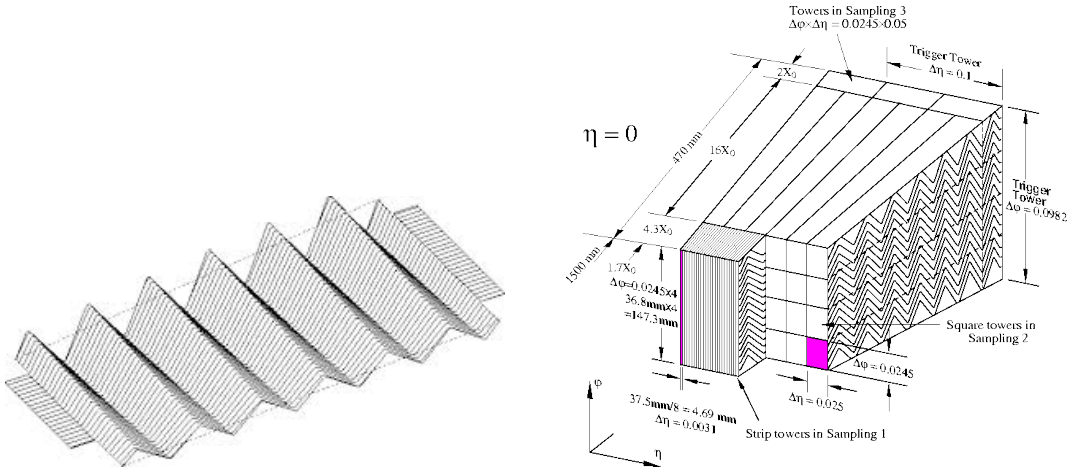

(a) (b)

Figure 4.8: This plots shows the accordion shape of the calorimeter. From reference [7].

($0.8 < |\eta| < 1.7$). These four partitions are segmented into 64 modules by the azimuth ϕ. Modules are divided longitudinally into three layers and into cells whose dimensions are optimized to obtain a structure of projective towers with a granularity in $\Delta\eta \times \Delta\phi = 0.1 \times 0.1$ in the inner two layers and $\Delta\eta \times \Delta\phi = 0.2 \times 0.1$ in the third layer.

The HEC is a liquid argon sampling calorimeter which provides hadronic coverage $1.5 < |\eta| < 3.2$. Liquid argon technology is used in Hadronic end-cap calorimeter because this region sustains more radiations than the barrel region. It consists of two independent wheels for each end-cap, each wheel containing two longitudinal sections, so there are four layers for each end-cap, 32 modules per wheel. The cells on these two HEC wheels are segmented into towers of $\Delta\eta \times \Delta\phi = 0.1 \times 0.1$ and $\Delta\eta \times \Delta\phi = 0.2 \times 0.2$ respectively .

The FCal is also separated into two components, the EM Forward calorimeter and the Hadronic Forward calorimeter. Three modules of two different types are installed in each end-cap of the FCal, 1 EM (Copper as absorber and closer to the collision point than the hadronic modules) and 2 Hadronic (Tungsten as absorber). The gap width between these

three modules is also different and as well as the total number of electrodes. These choices optimizes the measurement of electromagnetic fields in the first module and of hadronic energy in the other two modules. The coverage of the FCal is $3.1 < |\eta| < 4.9$. The position of the FCal is close to the beam line. It completes the nearly 4π coverage for the hadronic events with high p_T produced in the LHC, and calibrates in an important way to the determination of missing E_T^{miss}.

4.2.4 Muon Spectrometer

The largest system, sitting on the outside of the detector, is Muon spectrometer [8, 70, 86]. It is used for detecting masses and their momentum. The muon spectrometer assembly consists of three big superconducting air core toroids. It has precision tracking chambers for measurement of momentum resolution, including a cathode strip chambers (CSC), Monitored Drift Tube (MDT) and quick response chambers for triggering. These response chambers consists of resistive plate chamber (RPC) and thin gap chambers (TGC). The schematic diagram is shown in the figure Figure 4.9.

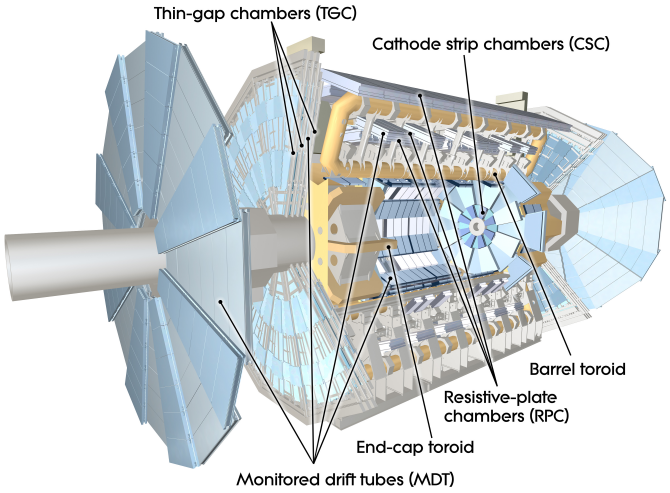

Figure 4.9: The muon spectrometer overview. (Courtesy of ATLAS Collaboration).

For high precision measurement, the MDTs are placed separately in three *stations* as depicted in the Figure 4.9. Each station has a multi-layer design that measures the η-coordinate of the particle passing by. The MDT covers most of the area except in the region

($|\eta| > 2.0$) where particle flux is high and the CSC is used instead to provide a better resolution. In addition, the CSC provides a rough measurement of the ϕ-coordinate.

The triggering function of the muon system is realized by the two other champers RPC and TGC. In practice, the trigger chambers for the Muon System have several purposes: in addition to the muon p_t trigger selection, it provides bunch-crossing identification and coordinate measurements in both η and ϕ (RPC at $|\eta| < 1.05$ and TGC at $1.05 < |\eta| < 2.4$).

4.2.5 Forward Detectors

In this analysis the luminosity is used to calculate backgrounds from their theoretical cross sections and to normalize the background estimation (section 7.1). Luminosity is measured in the so called *Forward Detectors*.Forward detectors [70, 87] are depicted in Figure 4.11. Different types of forward sub-detectors with functions are used in ATLAS to independently measure luminosity and monitor linearity. In Figure 4.11, the luminosity detectors are arranged in order of their distance from interaction point. At ±17 m from the interaction region is LUCID, which measures the integrated luminosity of ATLAS runs and performs monitoring of the instantaneous luminosity and beam conditions. The second system is the so-called zero degree calorimeter (ZDC) located at ±140m from the interaction point, just beyond the point where the beam pipes split into two inside the so-called TAN (Target Absorber Neutral) absorber. The most remote system is the ALFA (Absolute Luminosity For ATLAS) located at $\pm 240m$ from the interaction point. The main purpose of the ALFA is to the measure the elastic *pp*-scattering and small angles in the Coulomb-Nuclear Interference (CNI) region.

Various other sub-detectors including the Beam Condition Monitors (BCM), Minimum Bias Trigger Scintillators (MBTS) are also used for detection of luminosity.

4.2.6 Magnet System

Powerful magnetic fields [88] are produced by magnet system in the ATLAS. They are used to bend the path of particles in order to determine momentum of the particles. For the inner detector a solenoid magnetic system is used. In the two end caps and barrel, a toroidal mag-

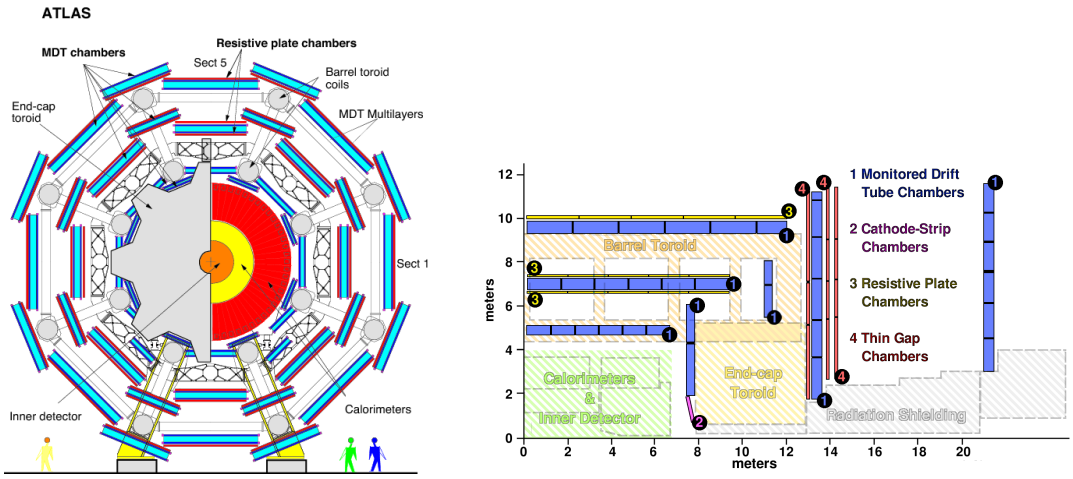

(a) (b)

Figure 4.10: A cross-section with details on the layout of muon detector. (a) cross-section in the x-y plane. (b) cross-section in the y-z plane. Image source: (a) ATLAS Experiment 2011 CERN. (b) From reference [8].

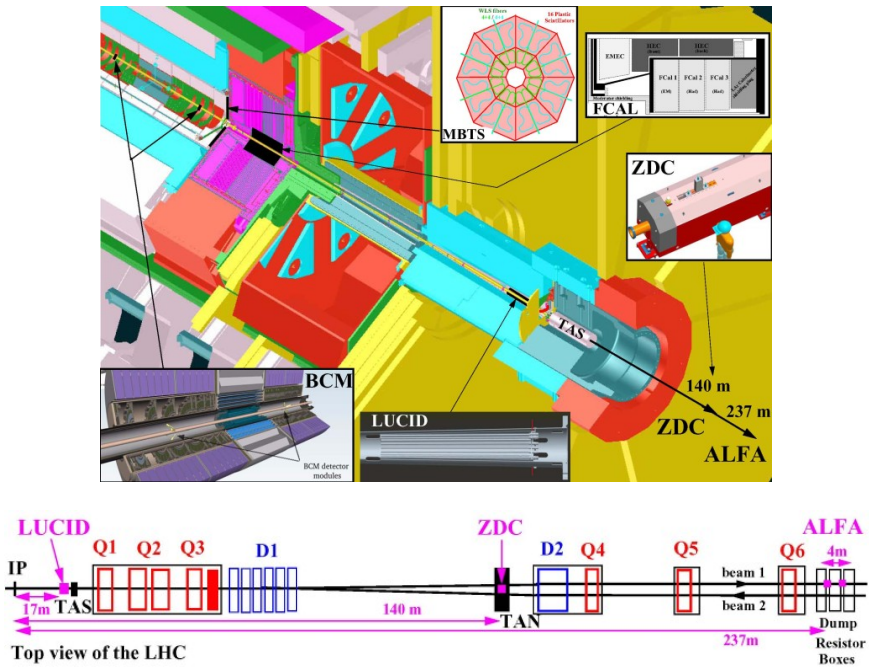

Figure 4.11: The top depicts the luminosity detectors and the bottom shows their distances from the ATLAS interaction point. From reference [9].

net is installed. An aluminum and Niobium-copper/Titanium alloy superconductor makes up the ATLAS solenoid (as a barrel around the beam as shown in Figure 4.12). The solenoid is located within the LAr cryostat and beyond the inner detector. The axial length is 5.3 m, the inner diameter is 2.44 m and the thickness is 0.1 m. The temperature of solenoid is cooled to 4.5 K by using liquid helium. A peak magnetic field of 2.6 T and central field of 2 T parallel to axis of beam are produced at the superconductor itself. The solenoid magnets are made of thin material to minimize the energy loss before the calorimeter.

The toroid magnet system consists an end cap toroid and a barrel toroid as depicted in the Figure 4.12. It is also one of the biggest systems in ATLAS. The outer diameter is 20 m and the length of the system is 26 m. Eight large superconducting coils provide toroidal magnetic field. A large amount of heat is produced, which is dissipated and the setup is cooled to 4.5 K and providing a peak value at 3.9 T for the muon spectrometer. The pseudo-rapidity range covered by this field is $\eta \in [0, 1.3]$ in the detector. The other two

endcap toroids are installed on opposite ends of the barrel, producing a magnetic field with the peak value at 4.1 T. The endcap toroid covers the region $\eta \in [1.6, 2.7]$. Three different magnets provide the magnetic field. Due to this construction relatively nonuniform field is produced. The field in transition regions between components is complex and a precise modelling is required to achieve an accurate measurement of track momentum.

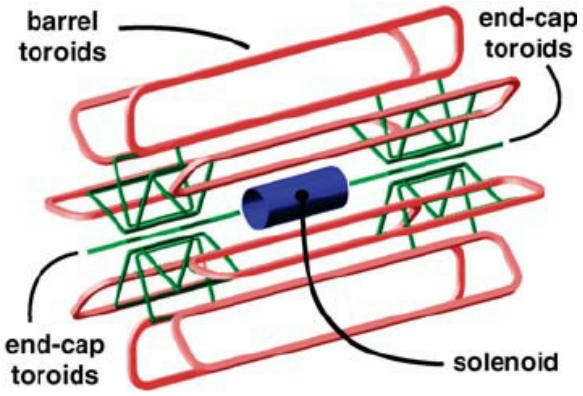

Figure 4.12: The overview of the ATLAS magnet system. (Courtesy of CERN).

4.2.7 The trigger system

Data is generated at the rate of 60 million megabytes per second when a bunch crossing (BC) rate of 40 MHz (one collision per 25 ns) is achieved in LHC. ATLAS is not able to save all of it due to limited storage and bandwidth; in addition, not all collisions are intersting for analysis. Only 1 out of 10 million events are stored in ATLAS. ATLAS incorporates a multi-layer triggering system [89–91] that determines in real time whether to store a particle event. It reduces the initial 40 MHz rate to 75 KHz.

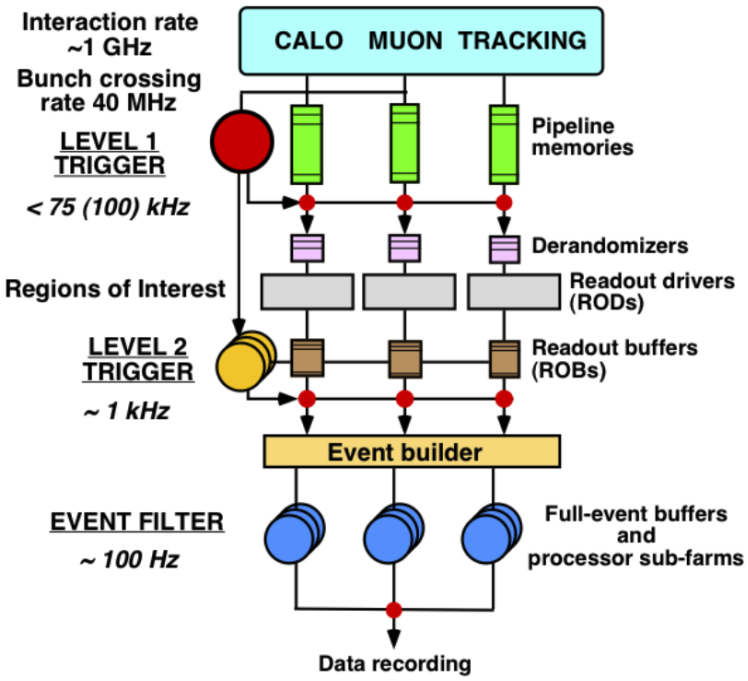

Figure 4.13: Block diagram of the ATLAS trigger system. From reference [10].

As depicted in the Figure 4.13, the system is divided in three levels. Its first level (LVL1) is implemented in electronics and firmware and consists of three parts: the Calorimeter Trigger (L1Calo), the Muon Trigger (L1Muon), and the LVL1 event-decision part (the red ball in Figure 4.14) implemented in a central trigger processor (CTP). A new decision is delivered every 25 ns, but the allowed latency 2.5 μs in the trigger mechanism is longer than the BC period. To solve this problem, detector data are held in the *pipeline memories* (the green pipes in the Figure 4.14) while L1 makes its decision. Thus the processing is

broken down into a series of steps each of which can be performed within a single BC period and many operations can be performed in parallel by having separate processing logic for each one. In addition, L1 inputs data from about 7200 analogue trigger towers of reduced granularity of $\Delta\eta \times \Delta\phi = 0.1 \times 0.1$, from all the ATLAS electromagnetic and hadronic calorimeters.

With information based on L1Calo, the trigger selects events with features of interesting physics. More specifically, it applies criteria to select high transverse-energy E_T events, such as high transeverse-energy electrons, photons, jets, and hadronically-decaying τ leptons. The L1Muon trigger is built to receive signals from the RPCs in the barrel and TGCs in the end-cap, as described in Sections 4.2.4. The information collected in these regions is combined with other information, to help identify objects such as high p_T muons. The tracking information from the inner detector is not used directly, since the readout and reconstruction time doesn't allow a fast trigger decision.

The LVL2 trigger recalculates full detector information from the data in Regions of Interest (RoIs) held in readout buffers and performs the predefined selection on the basis of this data by generating geometrical mapping of objects. Higher granularity calorimeter information can be used by LVL2 with information from internal detector. The objects are reconstructed and compared with selection cuts. The time limit of LVL2 is more relaxed, around 40 ms, which allow the processing in greater detail than in LVL1. Therefore, LVL2 uses algorithms such as tracking, cluster tracking match, and calorimeter clustering. Events from LVL2 pass to the dataflow manger (DFM) before entering the next stage called event filter (EF). All other events are rejected and cleared from readout sections. A rate of 3.5 KHz is achieved by the end of LVL2 trigger system.

The event building procedure is carried out by EF using the full offline software. It combines, integrates and processes information from all the sources in a sophisticated manner using reconstruction algorithms, including alignmentsand calibration. The final data is written at rate of 100Mb per second and further reduced to 200 Hz. The streams of data are categorized according to particles i.e. electron, muon, photon, tau, and b physics. Other topologies like Jet, Tau, E_T^{miss}, and Muons are also used in ATLAS. These streams accept events passing its corresponding trigger chain. Two physics streams used in the analysis of

single top events are the Muons and Egamma streams, which require that the event passes electron and photon trigger and the muon trigger chain. Events can pass through two trigger chains and are not mutually exclusive. They are stored separately.

Several steps are used by ATLAS to refine raw data as shown in the Figure 4.14. To reduce the final size, each step in the diagram makes several cuts. Reduced datasets called *TopD3PD* and *SingleTopD3PD* are standard and shared by the ATLAS top group and its single top subgroup. These dataset are the basis of the analysis described in this thesis.

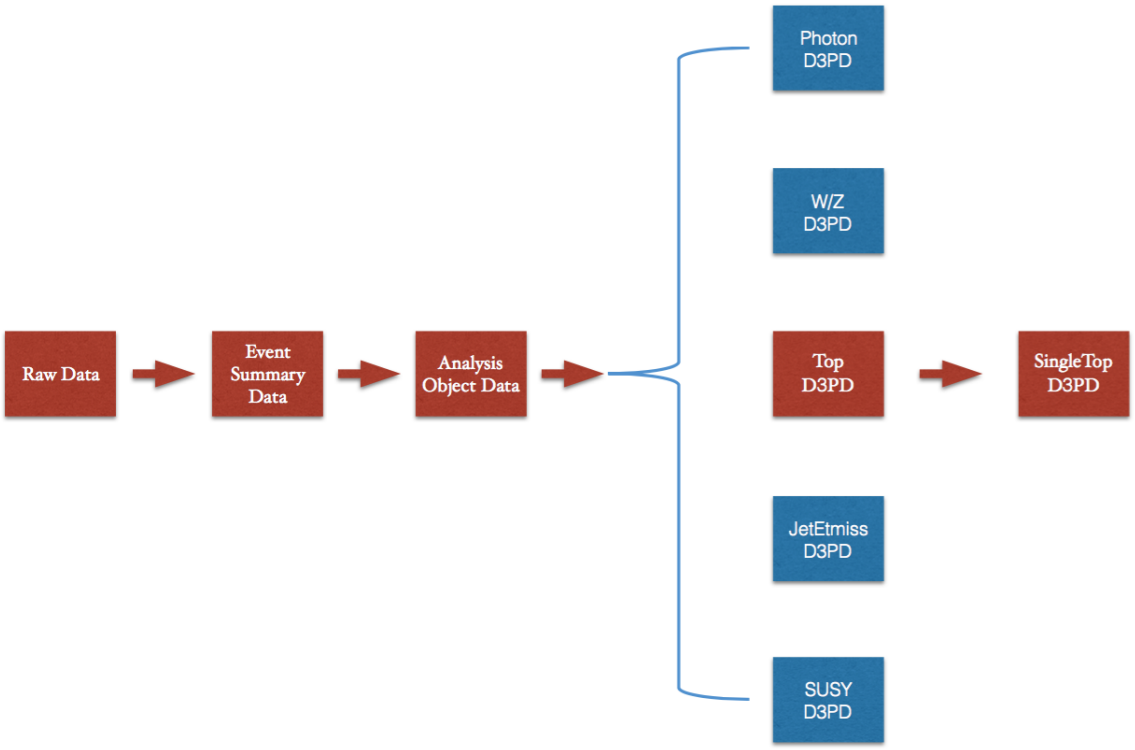

Figure 4.14: A dataflow diagram in ATLAS.

5.0 PHYSICS OBJECT IDENTIFICATION & RECONSTRUCTION

In the last chapter, the information from pp collisions recorded by ATLAS detector hardware has been explained in detail. The detector response includes the information about the position, magnitude and time of energy deposits in the inner detector, calorimeters, or muon spectrometers and can be further reconstructed into physics objects, such as tracks, electrons, muons, photons, light jets, b-jets, missing transverse energy. To interpret the detector signals of various sub-detector systems, reconstruction algorithms using dedicated software are employed. This chapter will give an brief introduction to the reconstructed physics objects needed for analysis of single top quark t-channel events. They include electrons, muons, jets and their corresponding b-flavor identification, and missing transverse momentum that indicates an undetected neutrino.

5.1 TRACKS AND PRIMARY VERTICES

Track reconstruction aims to provide a precise determination of the trajectories of charged particles. Due to solenoidal magnetic fields within the Inner Detector, charged particles are bent into helical trajectories. In this region, the path of such particles can be reconstructed by fitting ID hits with such a curve. Once the tracks are reconstructed, the proton-proton interaction points as well as the decay vertices of unstable particles in the corresponding process can be found by fitting the common interaction points between a set of particle trajectories.

In proton-proton collisions, a large number of charged particles are produced, resulting in numerous inner detector hits. It is the track reconstruction software's job to determine

which hits originate from a common particle and to fit a trajectory that best matches the measurements. Two methods to the reconstruction of tracks are used in ATLAS.

The first approach is an *inside-out* reconstruction strategy, where track seeds are chosen within three measurements in the Pixel and SCT and are propagated out towards the TRT using a combinational Kalman filter [92]. Specifically, three steps are used in the inside-out strategy. The inside-out strategy begins with the constructions of 3-dimensional *silicon space points* [93]. Each silicon space-point represents a 3D measurement that can be reconstructed from either a cluster of silicon pixels or the intersection of the front and backside silicon strips in the SCT module. A pattern recognition procedure is performed after these silicon space-point are formed. If any of these three space points are compatible with a minimum p_T cut of 500 MeV, a track seed is defined. Then the tracks are propagated out from the seed towards the TRT using a combinational Kalman filter and additional silicon hits are added to the seeds. Every track seed that contains a minimum of 7 silicon hits is defined as a track candidate. In fact, a large number of track seeds can be found depending on the underlying physics events, resulting in numerous fake track segments formed from them. To reduce the the number of track candidates, an ambiguity solving procedure is applied in the next step to remove track candidates with incorrectly assigned hits. The ambiguity solving process applies a quality criteria: a 'score' is assigned to each track candidate to indicate the likelihood that the track candidate originates from a real particle. The presence of 'holes', defined as the passage of the track through a detector element without producing a hit, reduces the track score. The χ^2 of the track fit is also used as one of the quality criteria. After the track reconstruction in the pixel and SCT detectors, the candidates are extrapolated into the TRT volume and combined with measurement there. Then the score from the fit with the included additional TRT measurements is compared with the one calculated by original fit, and only new track has a higher score is accepted as a successfully reconstructed track.

The second approach in track reconstruction is a *outside-in* algorithm, which is used in addition after the inside-out method is evaluated. It aims to reconstruct tracks that are missed by the inside-out method. It uses the same procedure but starts from unassigned TRT segments and looks for matching hits in the inner layers of the ID. Particles coming

from the late decays of neutral particles (secondary vertices, those outside the innermost beampipe), photon conversions, or electrons with catastrophic energy loss are reconstructed with the outside-in algorithm.

A typical pp collision contains multiple interactions distributed out along the beam spot. To find the interaction point of the hard scattering, the primary vertex[1]needs to be reconstructed. For some analysis, it's also vital to locate the secondary vertices, for instance in the case of b-jet identification. Vertex reconstruction in ATLAS uses reconstructed tracks to determine the locations of primary interactions and secondary decay. There are four main steps in a primary vertex reconstruction.

1. *Seeding*

   In this step, all the tracks that possibly originating form the interaction regions are considered. A vertex seed is pre-selected from the maximum of the distribution of tracks in z_0 direction, the longitudinal impact parameter with respect to the beam spot[2].

2. *Tracking assignment*

   Tracks that are compatible with the seed are grouped together for a χ^2 fit.

3. *Adaptive Fitting*

   The position of this vertex is fitted based on the seed location and the nearby tracks with an adaptive vertex fitter [94]. The fit is an iterative procedure and in each iteraction tracks that are incompatible with the vertex by more than 7σ are used to created a new vetex seed. Then the process is repeated with the new seed and the iteration stops only when all tracks are assigned to a vertex or a seed generated has no compatible tracks for fitting.

4. *Determination of the primary vertex*

   The reconstructed vertex with the highest $\sum p_T^2$ is assigned as the default primary interaction.

Various effects can affect the performance of the vertex reconstruction, such as the merging of two vertices, the splitting of a high p_T vertex into two separate vertices, or fake vertex.

[1]The IP, also called the Primary Vertex, is defined as the vertex with the highest sum of transverse p_T, $\sum_{\text{tracks}} p_T^2$.

[2]The definition of z_0 is based on the 'perigee', or the point of closest approach to the z-axis, and the z_0 is the z coordinate of the perigee.

For the topologies considered in this analysis, the primary vertex identification has a high efficiency.

5.2 OBJECT IDENTIFICATION & RECONSTRUCTION

5.2.1 Jet reconstruction

The aim of jet reconstruction is to reconstruct the particles from a single parton and estimate its momentum. In this analysis, jets are reconstructed using a so-called "anti-k_t algorithm" [95] with a width parameter 0.4, using topological clusters calibrated with the local calibration weighting method which partially corrects for detector response from the non-compensating nature of the calorimeters.

5.2.2 Identification of *b*-tagged jets

The identification of jets containing b hadrons is not only important to identify top-quark candidate events, but also plays an role to discriminate the large background with light-quark jets and c-quark jets from the signal. Jets originating from the fragmentation of b-quarks are identified by reconstructing secondary and tertiary vertices from the tracks associated to the jets and by combining their spatial parameters with lifetime-related information. This is because b-flavoured hadrons have a relatively long lifetime (about 10^{-13} s) resulting in a significant flight path length which leads to measurable secondary and/or tertiary vertices and impact parameters of the decay products.

5.2.3 Leptons

- Electrons

  Isolated electrons are an important component of the single top-quark event signature and their efficient identification as well as good background rejection are important. Offline electron candidates are reconstructed using information from the electromag-

netic calorimeter, where they deposit their energy, and from the inner detector. The reconstruction procedure begins of cells in the EM calorimeter from the sliding-window algorithm [96, 97], in which a window of 3×5 cells slides over a grid and sums the transverse energy in the window to form a cluster, keeping clusters with $E_T > 2.5$ 'GeV. Then the electron candidate formed in this way is matched with a track in the ID, and the cells are reclustered at size 3×7 (5×5) in the barrel (end-cap). The track-cluster matching is performed by extending the track to the electromagnetic calorimeter layer and comparing the impact point to the cluster. A match must satisfy $\Delta\eta < 0.05$, and, to account for the bremsstrahlung losses, $\Delta\phi < 0.1$ or $\Delta\phi < 0.05$. When an ambiguity arises when multiple tracks satisfy these conditions for one cluster, the track-cluster selects with the smallest $\Delta R = \sqrt{\Delta\eta^2 + \Delta\phi^2}$. More details about electron reconstruction, identification and their calibration can be found in [96, 97].

- Muons

  Offline muon candidates used in this analysis are reconstructed by combining track segments found in the inner detector and in the muon system, using the complete track information of both detectors and accounting for material effects of the ATLAS detector structure. Further details for the muon reconstruction can be found in [98].

5.2.4 Missing transverse momentum

In hadron colliders, the initial momentum of the colliding partons along the beam is not known due to the composite nature of the proton. However,with a good approximation the sum of the initial transverse momentum of the interacting partons can be considered equal to 0, allowing for the determination of the missing transverse energy E_T^{miss}, defined as:

$$E_T^{\text{miss}} = \sqrt{(E_x^{\text{miss}})^2 + (E_y^{\text{miss}})^2}. \tag{5.1}$$

If a momentum imbalance in the plane transverse to the beam axis is measured, it may signal the presence of undetectable particles, such as neutrinos or new weakly-interacting particles. Because the final state of semileptonically decaying top quarks include a neutrino, it is vital to have a good measurement of the missing transverse momentum.

The E_T^{miss} reconstruction mainly uses energy deposits in the calorimeters and muons reconstructed in the muon spectrometer [11]. Additionally, the deposits not associated to any reconstructed physics objects are taken into account. Thus the E_T^{miss} is calculated as follows:

$$E_{x(y)}^{\text{miss}} = E_{x(y)}^{\text{miss,e}} + E_{x(y)}^{\text{miss},\gamma} + E_{x(y)}^{\text{miss},\tau} + E_{x(y)}^{\text{miss,jets}} + E_{x(y)}^{\text{miss,softjets}} + E_{x(y)}^{\text{miss,CellOut}} + E_{x(y)}^{\text{miss},\mu}, \quad (5.2)$$

where the E_T^{miss} terms on the right hand side are calculated as the negative sum of the calibrated calorimeter cell energies of the corresponding objects. The calorimeter energy deposits are associated with a reconstructed and identified high-p_T parent object in a specific order: electron, photons, muon, hadronically decaying taus, jets and muons."Jets" denote reconstructed jets with $p_T > 20$ GeV and "soft jets" indicates reconstructed jets with transverse momentum of 7 GeV $< p_T \leq 20$ GeV. "CellOut" indicates the contribution that is from unassociated calorimeter clusters or tracks. $E_T^{\text{miss},\mu}$ is the negative sum of the momentum of the reconstructed muon. If a muon is isolated from all jets by at least $\Delta R > 0.3$, then the p_T of the isolated muon is calculated from the combined ID and MS information. In this case, the muon p_T measurement includes its energy deposit in the calorimeters and the muon contribution to the calorimeter term is omitted to avoid double counting. By contrast, non-isolated muon p_T is only measured from the muon spectrometer in a standalone way, after energy loss in the calorimeter, and the calorimeter muon term is added.

The E_T^{miss} is the measurement of the undetectable particles (as for example, escaping neutrinos) but also includes energy losses due to detector inefficiencies and its resolution, leading to the mis-measurement of the true E_T^{miss} of the final interacting objects.Additionally, a correction is applied for the energy lost in the cryostat, and several methods are used to suppress pile-up to restore the E_T^{miss} resolution to the ones observed in the absence of pile-up, without spoiling the E_T^{miss} response and creating fake E_T^{miss}. The performance of the E_T^{miss} reconstruction is studied using the process of $Z \to l^+l^-$ and $W^\pm \to l^\pm\nu$. More information on the E_T^{miss} reconstruction and performance of the measurement can be found in [11].

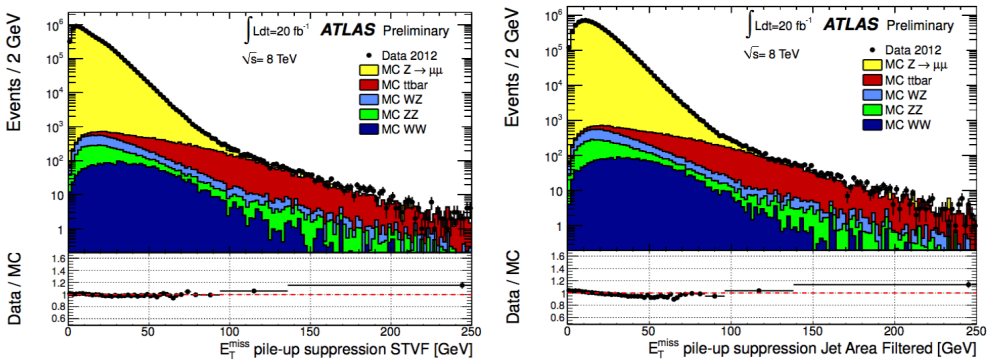

(a) (b)

Figure 5.1: The plots show distributions of E_T^{miss} reconstructed (a) as measured in a data sample of $Z \to \mu\mu$ events after pile-up suppression with the STVF (b), with the Jet Area Filtered methods. The expectation from Monte Carlo simulation is superimposed and normalized to data, after each MC sample is weighted with its corresponding cross-section. The lower parts of the figures show the ratio of data over MC. See Ref. [11]

5.3 OBJECT SELECTIONS

The object reconstruction and identification we have discussed so far is used generally in the analysis of ATLAS data. This section describes briefly the procedures used to reconstruct, calibrate and select the physics objects (electrons, muons, jets, b-tagged jets and missing transverse momentum) required to identify events with a t-channel signature. These procedures are standardized and recommendations of the ATLAS top-quark reconstruction working group [99]. More details on object selection and calibration can be found in Ref. [100, 101].

5.3.1 Jets

To suppress jets from in-time pile-up, at least 50% of the scalar p_T sum of the tracks associated with a jet, called jet-vertex fraction (JVF), is required to be from tracks compatible with the primary vertex. This cleaning cut is only applied to low p_T and central jets ($p_T < 50$ GeV and $|\eta| < 2.4$). Furthermore, a jet cleaning is applied and events which contain at least one jet with a $p_T > 10$ GeV and reconstructed from noisy calorimeter cells are removed. Jets overlapping with selected electron candidates within a cone of radius ΔR equal to 0.2 are removed from events, as the jet and the electron are very likely to correspond to the same physics object (only the jet closest to an accepted electron is rejected). If a remaining jets with $p_T > 25$ GeV is found close to an electron within a cone of radius $\Delta R = 0.4$, then the electron is discarded. Finally, jets considered in this analysis are required to have a p_T sufficiently high to be on the reconstruction efficiency plateau:

$$p_T > 30 \text{ GeV} \tag{5.3}$$

and the pseudo-rapidity acceptance is required to be in the range

$$|\eta| < 4.5, \tag{5.4}$$

which corresponds to the acceptance of the calorimeters.

To remove some mis-modelling in the transition region between the central and forward hadronic calorimeters, the p_T threshold is raised to 35 GeV for the jets failling in the transition region between $2.7 < |\eta| < 3.5$.

5.3.2 Leptons

5.3.2.1 Electron Several tight identification requirements [102] are also required in selecting an electron candidate. Electron candidates in this analysis are required to have a transverse energy $E_T^{\text{miss}} = E_{\text{cluster}}/\cosh(\eta_{\text{track}}) > 25$ GeV and a pseudo-rapidity for the calorimeter cluster position $|\eta_{\text{cluster}}| < 2.47$. Events with electrons falling in the calorimeter barrel–end-cap transition region, $1.37 < |\eta_{\text{cluster}}| < 1.52$, in which there is limited instrumentation, are rejected. High-quality electron candidates are selected using a set of cuts which include stringent requirements on the matching between the track and the calorimeter cluster (electrons of `tight++` quality in ATLAS terminology). Furthermore, the longitudinal impact parameter z_0 of the electron candidates has to be compatible with the primary vertex. This is ensured by requiring $|z_0| < 2$ mm.

In addition, isolation criteria are required in order to reject candidates coming from other sources than prompt W boson decays. Hadronic jets faking an electron, electrons from heavy-flavour decays, and photon conversions comprise the major backgrounds for isolated high-p_T electrons associated with W boson decay.

Signal electrons from W boson decay are typically isolated from jet activity; by comparison, leptons from a heavy flavor jet would be produced within a shower full of tracks and energy deposits, therefore making it non-isolated. The isolation cuts imposed on the electron candidates are tuned to achieve a uniform isolation efficiency across η_{cluster} and E_T^{miss}. This is achieved by applying cuts on the energy deposited in the calorimeter cells in a cone of radius $\Delta R = 0.2$ around the electron and on the transverse momentum sum of the tracks in a cone of size 0.3. The values of the cuts are chosen in order to have a simulated isolation efficiency of 90%.

Triggering and identification efficiencies for electron candidates are measured in Z/W boson data samples using a tag-and-probe method[3]. In addition, electron efficiency is measured in both data and MC. To take into account the differences between them, a scale factor

[3]To study the electron selection efficiency, this tag-and-probe method selects a sample of $Z \to e^+e^-$ candidates events by applying a very tight selection on one of the two decay electrons, the *tag leg*, and a relatively very loose selection on the other electron, *the probe leg*, i.e these selection cuts we concerned about their efficiencies in this analysis are all *probe*. Based on the *tag* electrons, the efficiency of a certain loose selection can be estimated. $W \to e\nu$ decays are used in certain circumstances, like identification or trigger efficiency measurements.

is introduced. The simulation-to-data correction factors determined from these studies are function of the electron transverse energy and pseudo-rapidity.

5.3.2.2 Muons Isolation criteria are applied in order to reduce contamination from events in which a muon is produced from a quark decay (for example heavy flavour quarks that decay leptonically and result in a muon inside a jet). For that purpose, muon candidates are required to pass a threshold on an isolation variable which is defined as the ratio between the transverse momentum sum of tracks belonging to a cone of variable size around the muon divided by the muon p_T. In addition, an overlap removal between jets and muons is applied: any candidate muon whose momentum direction is within a cone of size $\Delta R = 0.4$ around a jet with $p_T > 25$ GeV and a jet vertex fraction as defined in Section 5.2.1 are removed from events.

In addition, tight identification requirements must be passed [98]. They must have a transverse momentum $p_T > 25$ GeV and a pseudo-rapidity $|\eta| < 2.5$. Selected muons must additionally satisfy a series of cuts on the number of track hits present in the various tracking sub-detectors. The longitudinal impact parameter z_0 of the muon candidates with respect to the primary vertex is required to be smaller than ± 2 mm.

The muon triggering and identification efficiencies have been measured from Z boson data samples using the tag-and-probe method and corrections factors to match the simulation to the data have been extracted as a function of the pseudo-rapidity and azimuthal angle of the muon.

To estimate the fake and real selection efficiencies in the muon channel, candidate muons with no isolation cuts applied are considered.

Non-isolated low-$p_T$muon candidates with $p_T > 10$ GeV are also considered to veto dileptonic background events. As in the case of loose electrons, these low-p_T muon candidates are removed if they overlap within $\Delta R < 0.4$ with a tight muon candidate or jets. Hadronically decaying τ candidates are not considered, because of the low reconstruction efficiency for these objects below $p_T < 25$ GeV.

5.3.3 Identification of b-tagged jets

In this analysis, the MV1c b-tagging algorithm called MV1c is used, which in addition to identifying b-quark jets, is trained and optimized to reject charm quark induced jets. The MV1c is a neural network based algorithm and originates from the MV1 b-tagging algorithm. It combines the neural network response of three high performance taggers (IP3D, JetFitterCombNNc and SV1 algorithms).

The efficiency to identify a jet originating from a b-quark and the probability of mistakenly tagging a non b-quark jet (referred in this note as c-tagging, τ-tagging and mis-tagging rates) are measured in data and MC simulated event samples in order to calibrate the b-tagging algorithm. The b-tagging efficiency is measured in data by using different methods, referred to as $p_{\mathrm{T}}^{\mathrm{rel}}$ and `System8`, which are based on dijet event samples with muons in the final state [103]. The measurement of the b-tagging efficiency from simulated dileptonic $t\bar{t}$ events is described in detail in Ref [104].

The b-tagging scale factor, obtained by combining the `System8` calibration with calibration based on $t\bar{t}$ samples, defined as the ratio between the data and simulation b-tagging efficiencies, is derived as a function of the p_T and η of the jet. The b-tagging calibration also includes data-simulation correction factors corresponding to the c, τ and light-flavour mis-tagging rates.

The b-tagged jets must have a central pseudo-rapidity, $|\eta| < 2.5$; the forward jets ($2.5 < |\eta| < 4.5$) are therefore assumed as not containing b-quarks. In the following, the forward candidate jets and the central jets not passing the b-tagging requirement are referred to as non b-tagged jets or non b-jets.

6.0 DATA AND SIMULATION SAMPLES

In last chapter, we discussed object reconstruction and identification from detector signals to obtain the physics objects we are interested. In addition to looking at the generic selection criteria for physics objects, we discussed the selection cuts for selecting the single top quark events.

In this chapter, we present the data and simulation samples we will use in the analysis. This begins with a brief introduction of the data samples we use and the trigger selection. In Section 6.2.1, we discuss the single top quark signature and its background. A discussion of the Monte Carlo samples followed in Section 6.2.2. To model some backgrounds accurately, a data-driven method is required and a brief introduction the *a matrix method* is introduced. Next, in Section 6.3 we define the signal dominated regions called *signal region*, and three other background dominated *control/validation regions* that are used for evaluating the background modelling. Section 6.4 discusses the background normalisation. For most backgrounds, the initial normalisation step rescales the MC predicted cross section to the state-of-the-event theoretical cross section prediction. The multijet background estimation (see Section 6.2.1) uses no Monte Carlo and is entirely data-driven. The final signal and background normalisation are estimated through a simultaneous maximum-likelihood fit to the numbers of data events observed in the signal, control regions. Well modeled distribution shapes for the signal and backgrounds plus their normalisation scale factors in total give a good modelling of the data. Finally, event yields and distributions of some kinematic variables in t-channel signal regions are shown in Section 6.5.1. The distributions of three angles θ, θ^*, ϕ^* we defined in Section 3.1.4 are also included for completeness.

6.1 DATA

The data samples used in this analysis were from pp collisions delivered by the LHC in 2012 at a centre-of-mass energy of $\sqrt{s}$ =8 TeV and collected by the ATLAS detector. The amount of data used by this analysis corresponds to an integrated luminosity of 20.2 fb^{-1}. The uncertainty on the integrated luminosity is ±1.9% [105].

The ATLAS event trigger system is the hardware-based L1 trigger and software-based HLT discussed in Section 4.2.7. During the data taking period different triggers were used due to changing pile-up conditions. This analysis uses single-lepton triggers to select the *single top-quark t-channel signature* as discussed in Section 6.2.1.

Events selected in the electron channel are triggered by requiring at L1 a transverse energy deposit E_T^{miss} above 18 GeV, a reduced calorimetric granularity being considered at this stage. At the HLT, the full granularity of the calorimeter as well as tracking information are available and the reconstructed calorimeter cluster is matched to a track. The trigger electron object is then required to be isolated and to have $E_T^{\text{miss}} > 24$ GeV. The electron channel is also triggered on events with a E_T^{miss} threshold of 30 GeV at L1 and of 60 GeV at the HLT but without isolation requirement in that case.

Events selected with a muon in the final state are triggered by requiring at L1 a muon track with a transverse momentum p_T greater than 15 GeV, this first level track being matched to an EF muon track having $p_T > 24$ GeV and satisfying isolation criteria or having $p_T > 36$ GeV without passing any isolation cuts.

6.2 EVENT TOPOLOGY AND SIMULATIONS

6.2.1 Event topology

The final state of t-channel single top quark signal events has an isolated lepton with high p_T, one missing E_T from an undetected neutrino, a light jet in the forward region of the detector, a b-jet in the central region of η that is coming from the leptonic top decay, and

finally another b-jet in the forward region that originates from the gluon splitting. As we can see in Figure 3.7, the final states of the t-channel single top quark signal (which is described by a mix of the four-flavor-scheme (4FS) and five-flavor-scheme (5FS) process as we discussed in Appendix A.1.) have a three-jets *signature*, but since the b jet in the forward regions from the gluon splitting has a low acceptance, in this analysis, an exact two-jets signature "l+2jets" (l represent lepton) requirement is used when select the events, in which one of them is required to be b-tag jet, the other be the light jet called spectator jet. The other backgrounds to the t-channel signal come from single top-quark production in s-channel, Wt associated production, W boson production with jets, Z boson and disboson production, $t\bar{t}$ production, and multijet events.

For completeness, a summary of all the backgrounds in the single top quark t-channel is included below.

- Single top quark background

  The single top quark associated Wt and s-channel have very similar signature to the t-channel process (See Figure 3.2). The W boson comes from the top quark in the associated Wt with the other W can both decay hadronically or leptonically. If these two W boson decay differently, it can give a signature similar to t channel. The s channel production gives b-jet but can be mis-identified and thus mimic the signal.

- Single boson and diboson process

  Other important backgrounds for t-channel signal are the production of a vector boson (W or Z) in association with jets. If one of the jets comes from a heavy flavor quark, the vector boson plus jets events have the same signature as signal events. Furthermore, due to possible mis-identification of a light jet as b-quark jet, vector boson production in association with only light jets also contributes to background contamination. The diboson process (WW, WZ, and ZZ, where Z means Z/γ^*) can also contribute to the background, if one of the bosons decays leptonically while the other decays hadronically.

- $t\bar{t}$ background

  Top-quark pair production constitutes an important background to single top-quark events. Dileptonic $t\bar{t}$ events which have a "2l+2jets" signature may mimic the single

top-quark t-channel production final-state signature of two jets, if one of the leptons is not identified.

- multijet background

  Events originating from QCD processes are referred to as multijet backgrounds. Multijet events may show a similar event signature as the t-channel selected signal if, in addition to two reconstructed jets, and extra jet is mis-identified as an isolated lepton, or a non-prompt lepton appears to be isolated, or electron from photon conversions are mis-identified as prompt isolated leptons.

6.2.2 Monte Carlo simulations

The analysis of pp collisions at the LHC is challenging in two ways. On one hand, the possible final states of physics process are complex; on the other hand, the experiment setup is complicated by many sub-detectors of different geometric coverage and response. To predict observed distributions of measured quantities, Monte Carlos (MC) simulation is widely used in HEP. This analysis uses MC for the background estimates and the evaluation of systematics uncertainties.

Monte Carlos simulation of pp collisions at the LHC proceeds in several steps. The first step is the generation of the final state of the proton-proton collision. The second step is the simulation of the ATLAS detector response, including the the interactions between the particles and the detectors. Next, the electronic signals generated in sensitive components of the detectors are simulated in a step called digitization. Finally, simulated events are reconstructed in the same methods that applied to the actual data. The simulated events are then reformatted and subjected to the same trigger selection and reconstruction procedure as the real data.

Due to the complexity of the proton and of the final state hadron formation, the first step in the MC event generation can be further divided into the following processes in most event generators:

- Hard Process,
- Parton Shower (initial states and final states),

- Hadronization,
- Unstable particle decays,
- Underlying event,

The hard process is the collision of two partons within the proton, and the production of final state partons. The hard process simulation requires a full description of the momenta and spins of leptons, quarks and gluons, but does not include the fragmentation of hadrons.

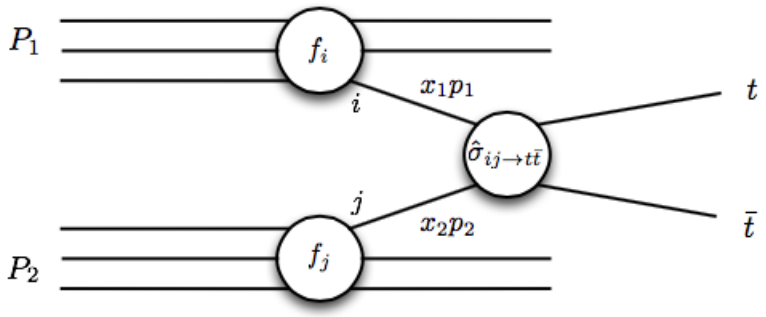

Figure 6.1: This figures shows the $t\bar{t}$ events production at the LHC.

To understand this process better, we look at one specific example – the $t\bar{t}$ events production at the LHC. In fact, in the hard scattering of two colliding protons in LHC, the top quarks are mostly produced in $t\bar{t}$ pairs through the QCD interaction process between protons. The subprocess of two interacting partons at high energy is illustrated in figure 6.1. The PDF $f_i(x_1, \mu_F)(f_j(x_2, \mu_F))$ which describes the probability of finding a parton with flavor $i(j)$ carrying momentum fraction $x_1(x_2)$ in proton $P_1(P_2)$. The μ_F is called factorization scale which is a reference scale at which the PDF's are calculated. For practical purposes, the PDFs are assumed to be universal objects, and any scattering process involving protons can be computed using the same PDFs with different perturbative calculations. The proton-proton cross section $\sigma_{1,2} \to X$ is obtained by the following equations, which reflects a factorization of the collisions into two components, one describing proton structure and the other describing the parton-parton interaction as illustrated in Figure 6.1:

$$\sigma_{P_1,P_2\to X} = \sum_{i,j} \int_0^1 dx_1 \int_0^1 dx_2 f_i(x_1, \mu_F) f_j(x_2, \mu_F) \cdot \hat{\sigma_{i,j}} \left(\hat{s}, \alpha_s(\mu_R), \frac{Q^2}{\mu_R^2}, \frac{Q^2}{\mu_F^2} \right),$$

or

$$\sigma_{P_1P_2\to t\bar{t}} = \sum_{i,j=q,\bar{q},g} \int_0^1 dx_1 \int_0^1 dx_2 f_i(x_1,\mu_F) f_j(x_2,\mu_F) \hat{\sigma}_{ij\to t\bar{t}}(x_1,x_2,m_t,\alpha_s(\mu_R),\mu_F) \quad (6.1)$$

if we consider the $t\bar{t}$ production.

In these equations, $\hat{\sigma}$ denotes the cross section of the hard scattering (calculated through perturbative QFT), $\hat{s} = x_1x_2s$ is the squared center of mass energy of the hard scattering, Q^2 is the energy scale of the virtual particle defined as the negative of momentum transfer of the hard collision $Q^2 \equiv -q^2$ and μ_R is the renormalization scale [106], another reference scale used in computing the cross section.

The common practice used in computing the QCD perturbative calculation in $t\bar{t}$ production is to set μ_F^2 and μ_R^2 to the order of the hard-scattering energy Q^2, which is the top mass m_t^2. The choice of scale is expected to have an effect on the observables, which can be estimated by varying its value in Monte Carlo.

When Q^2 is sufficiently large than the so-called *QCD scale* $\Lambda_{QCD} \sim 0.2$ GeV, the effective QCD coupling is small and the perturbative expansion converges quickly. The perturbative calculation gives an adequate approximation at high collision energies and the low-energy (non-perturbative) non-perturbative physics can be absorbed into renormalized PDFs. The PDFs cannot be predicted by theory but have been measured by experiments (i.e deep-inelastic scattering experiment [107] by the experiment ZEUS [ZEU92] and H1 [H197] at HERA) and can be evolved to the ATLAS energy scale using DGLAP equations [108]. The PDFs can be extracted in different ways and analyses using simulation based on these PDFs (such as the one in figure 6.2) are therefore dependent on the parametrization of the PDF fits.

With $\alpha_s(m_t) < 1$, the above cross section can be expanded in a fixed-order series in α_s as below:

$$\hat{\sigma}_{t\bar{t}} = \alpha_s^2[\hat{\sigma}^{(0)}_{ij\to t\bar{t}} + \alpha_s\hat{\sigma}^{(1)}_{ij\to t\bar{t}} + \alpha_s\hat{\sigma}^{(2)}_{ij\to t\bar{t}} + ...] \quad (6.2)$$

where the first term in the bracket is the leading-order (LO), the second the next-to-leading-order (NLO), the third term the next-to-next-to-leading-order (NNLO) and so on.

The simplest Monte Carlo generators use only LO in hard scattering process. NLO usually gives lengthy expressions and a longer running time for the Monte Carlo simulation.

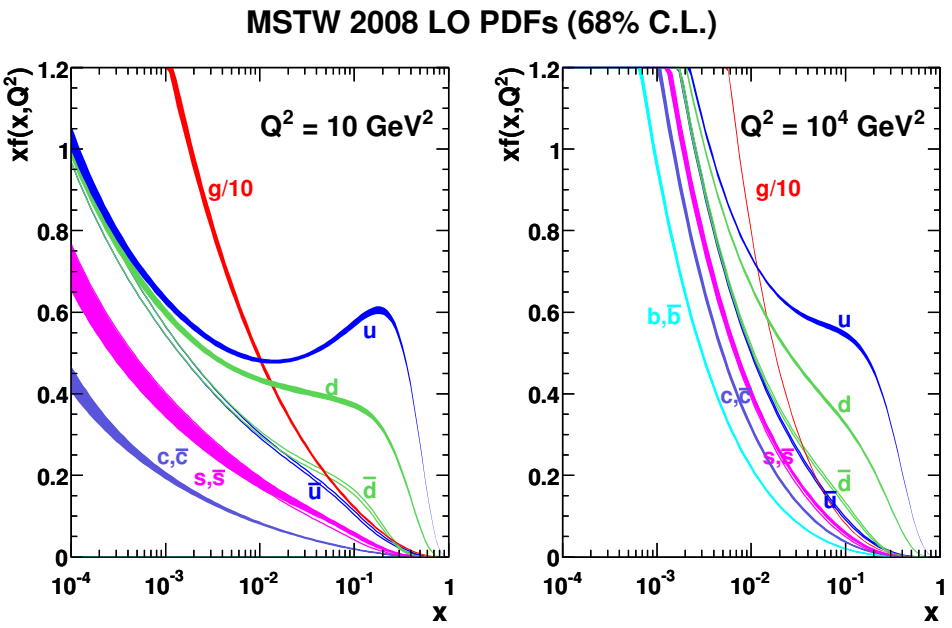

Figure 6.2: MSTW2008 LO parton distribution function at 68% C.L. of the gluon, the up, the down and the charm, the strange quark for low and high Q^2.

In the parton shower phase of event generators, the partons from the hard process are colored particles, quarks and gluons. Like the bremsstrahlung in quantum electrodynamic, in which scattered electric charges radiate photons, scattered colour charges radiate gluons. This lead to final state radiation (FSR) and initial state radiation (ISR) partons from the hard process. From quantum field theory, when a quark emits gluon in hard collision processes, perturbation theory cannot calculate the process very well in the collinear limit or when the gluon energy vanishes, because high order terms occur in the process when a soft gluon is emitted or when a gluon or light quark into two partons in collinear regions. Additionally, due to the non-Abelian structure of $SU(3)$, gluons themselves are coloured particles and so an emitted gluon can itself again cause further gluon radiation and parton multiplication. The evolution of the parton shower can be simulated as step-by-step process by Monte Carlo, starting from the hard process and working downwards to lower and lower energy scales to a point Λ_{QCD} where perturbation theory breaks down [109].

Here it is necessary to switch to hadronization phase, where the formation of colour-neutral hadrons takes place. After the hadronization, unstable hadrons decay into stable daughter particles that can interact with the detector materials in the subsequent detector simulation.

For Monte Carlo models that accurately simulate QCD hard-scattering events, one requires a good model that of beam-beam remnants (BBRs) and the multi parton interactions (MPI). Underlying events consist of the BBR and MPI and is an unavoidable background to most collider observables. At the LHC, multiple inelastic collisions also take place in each bunch-crossing between two neighboring protons, termed "pile-up" [1]. The resulting event contains particles that originate from the two outgoing partons and particles that come from the breakup of two outgoing partons. BBRs are the left over part after a proton is knocked out of each of the initial two beam hadrons, and these remnants are colour connected to the rest of the event [110], compensating the colour taken away by the colliding partons. Additionally, since the hadron is a composite object, the incoming partons in the collision may interact more than once, through different partons in one single event (MPI). However, on an event-by-event basis these two contributions to underlying events cannot be uniquely separated from particles that come from the initial and final state radiation.

A description of MC simulation used in the analysis is discussed in next section.

6.2.3 Simulated event samples

Samples of events generated using MC simulations were produced using different event generators interfaced to various shower/hadronisation generators within the MC12a/b production campaign [111, 112]. After the event generation step, trigger and detector simulation was performed with the dedicated ATLAS software infrastructure [113] either making fully use of GEANT4 [114] framework for a detailed physics description simulation or `Atlfast2` [115] framework for fast simulation. In this analysis, full simulated event samples were used as baseline samples while to estimate the impact of anomalous couplings in Section 7.6 and to evaluate most of the systematic effects, fast simulated event samples were used. Samples of

[1] This is actually called 'in-time pile-up', and there is also a notion of 'out-of-time' pile-up, referring to the effects of proceeding and subsequent bunch-crossing.

events generated using MC simulations were produced for t-channel signal and background processes, and were used to evaluate models of efficiency and resolution in Section 7.2.1, and to estimate systematic uncertainties in Section 7.8.

Parameters (such as one PDF input, the factorisation scale μ_F^2 discussed in Section 3.1) are tuned to the data from the proton-proton collision at the LHC. In some cases, input parameters have a non-negligible effect on the final results of the analysis and contribute to systematic uncertainty. Final measurements in this analysis depend on the top mass. In the baseline MC samples, the top mass is set to be 172.5 GeV.

In order to estimate the efficiency and resolution (i.e migration matrix, see Section 7.3.1), two LO simulated event samples were generated with *Protos*(version 2.2b using the CTEQ6L1 PDF sets [116]) and *AcerMC* (version 3.8) respectively. Events generated using PROTOS were produced within the four-flavour scheme, i.e. incorporating only the $2 \to 3$ process as depicted in the Figure 3.7. The factorisation scale is set to $\mu_{\mathrm{F}}^2 = -p_W^2$ for the spectator quark and $\mu_{\mathrm{F}}^2 = p_{\bar{b}}^2 + m_b^2$ for the gluon, where p_W and $p_{\bar{b}}$ are the three-momenta of the exchanged W boson and of the b-antiquark originating from the gluon splitting, respectively. This generator was also used to produce additional simulated event samples where different configuration of anomalous couplings were enabled in both the production and the decay vertices, varying just two couplings simultaneously in order to keep the top-quark width Γ_t invariant and therefore the cross-section. The ACERMC multi-leg LO generator [117] using the LO CTEQ6L1 PDF sets. This ME generator, ACERMC, incorporates both the $2 \to 2$ and $2 \to 3$ processes (see Figure 3.7(b)) featuring an automated procedure to remove the overlap in phase space between them [118]. The factorisation and renormalisation scales are set to $\mu_{\mathrm{F}} = \mu_{\mathrm{R}} = m_t = 172.5\mathrm{GeV}$.

The simulated samples for the t-channel single top signal and its background (except the QCD background) are listed in Tables 6.1-6.3. For more details about the studies and choices of these generators as well as the tunes of the generators, readers are suggested to read the upcoming paper [119].

t-channel description	Generator	PDF sets	σ [pb]	k-factor	MC events	Type
ℓ+jets (t)	POWHEG-BOX+PYTHIA+P2011C	CT10f4/CTEQ6L1	17.519	1.050	4994481	FS
ℓ+jets ($\bar{t}$)	POWHEG-BOX+PYTHIA+P2011C	CT10f4/CTEQ6L1	9.396	1.061	4999879	FS
ℓ+jets	PROTOS+PYTHIA+P2011C	CTEQ6L1	28.434	1.000	4999996	AFII
ℓ+jets	ACERMC+PYTHIA+P2011C	CTEQ6L1	25.750	1.104	8997672	FS
ℓ+jets (t)	POWHEG-BOX+PYTHIA+P2012	CT10f4/CTEQ6L1	17.520	1.0500	4989989	AFII
ℓ+jets ($\bar{t}$)	POWHEG-BOX+PYTHIA+P2012	CT10f4/CTEQ6L1	9.3935	1.0616	4999999	AFII

Table 6.1: Samples of simulated single top-quark t-channel events used as baseline samples.

Sample description	Generator	PDF sets	σ [pb]	k-factor	MC events	Type
s-channel (ℓ+jets)	POWHEG-BOX+PYTHIA+P2011C	CT10/CTEQ6L1	1.642	1.107	1200000	FS
Wt-channel (incl.)	POWHEG-BOX+PYTHIA+P2011C	CT10/CTEQ6L1	20.461	1.093	999692	FS
$t\bar{t}$	POWHEG-BOX+PYTHIA+P2011C	CT10/CTEQ6L1	114.48	1.1995	49918212	FS

Table 6.2: Top-quark background simulated event samples used as baseline samples for this analysis.

Sample description	Generator	PDF sets	σ [pb]	k-factor	MC events	Type
$ZW \to eeqq$	Sherpa	CT10	1.4622	1.0500	176000	FS
$ZZ \to eeqq$	Sherpa	CT10	0.24854	1.0000	30000	FS
$ZW \to \mu\mu qq$	Sherpa	CT10	1.4624	1.0500	176000	FS
$ZZ \to \mu\mu qq$	Sherpa	CT10	0.24747	1.0000	30000	FS
$ZW \to \tau\tau qq$	Sherpa	CT10	1.4523	1.0500	175999	FS
$ZZ \to \tau\tau qq$	Sherpa	CT10	0.24167	1.0000	30000	FS
$WW \to e\nu qq$	Sherpa	CT10	7.2790	1.0600	789998	FS
$WZ \to e\nu qq$	Sherpa	CT10	1.9022	1.0500	209999	FS
$WW \to \mu\nu qq$	Sherpa	CT10	7.2776	1.0600	779898	FS
$WZ \to \mu\nu qq$	Sherpa	CT10	1.9076	1.0500	209900	FS
$WW \to \tau\nu qq$	Sherpa	CT10	7.2756	1.0600	789995	FS
$WZ \to \tau\nu qq$	Sherpa	CT10	1.9086	1.0500	210000	FS
$W \to e\nu$ + B filter	Sherpa	CT10	140.340	1.100	14997980	FS
$W \to e\nu$ + C filter, B veto	Sherpa	CT10	537.840	1.100	9998989	FS
$W \to e\nu$ + C veto, B veto	Sherpa	CT10	10295.000	1.100	49855968	FS
$W \to \mu\nu$ + B filter	Sherpa	CT10	140.390	1.100	14989485	FS
$W \to \mu\nu$ + C filter, B veto	Sherpa	CT10	466.470	1.100	9992484	FS
$W \to \mu\nu$ + C veto, B veto	Sherpa	CT10	10368.000	1.100	49716964	FS
$W \to \tau\nu$ + B filter	Sherpa	CT10	140.340	1.100	14925982	FS
$W \to \tau\nu$ + C filter, B veto	Sherpa	CT10	506.450	1.100	9993984	FS
$W \to \tau\nu$ + C veto, B veto	Sherpa	CT10	10327.000	1.100	49830968	FS
$Z \to ee$ + B filter	Sherpa	CT10	31.046	1.120	3999000	FS
$Z \to ee$ + C filter, B veto	Sherpa	CT10	314.260	1.120	2999995	FS
$Z \to ee$ + C veto, B veto	Sherpa	CT10	764.410	1.120	1000000	FS
$Z \to \mu\mu$ + B filter	Sherpa	CT10	31.036	1.120	3997997	FS
$Z \to \mu\mu$ + C filter, B veto	Sherpa	CT10	314.800	1.120	2997995	FS
$Z \to \mu\mu$ + C veto, B veto	Sherpa	CT10	764.480	1.120	998999	FS
$Z \to \tau\tau$ + B filter	Sherpa	CT10	31.008	1.120	3997994	FS
$Z \to \tau\tau$ + C filter, B veto	Sherpa	CT10	314.490	1.120	2998998	FS
$Z \to \tau\tau$ + C veto, B veto	Sherpa	CT10	764.570	1.120	1000000	FS

Table 6.3: Diboson, W+jets and Z+jets background MC samples used as baseline samples for this analysis. All V+jets samples consider massive charm and bottom quarks.

6.2.3.1 Data-driven event samples The multijet background has a large cross-section, several orders of magnitude above top-quark and vector-boson productions, and a sizable misidentification probability. However, the multijet process cannot be modelled by Monte Carlo simulation accurately. In fact, the QCD background is usually estimated from the data due to its large theoretical uncertainty and the computation challenge. In this analysis, the multijet contribution, in the electron and muon channels, is estimated with a data-driven matrix method [120]. In multijet events, isolated energy deposits can be falsely reconstructed as a prompt lepton. The matrix method estimate the multijet background in data by determining the number of fake leptons passing the signal cuts. This method is presented in more detail in [120]. To summarize this method, we discuss briefly the estimation of the multijet contributions, which is then used to generate the multijet background samples.The method starts by defining two types of lepton selections which we call them *loose lepton* and *tight lepton*. Accordingly, we have the below four quantities:

- $N^{\text{loose(tight)}}$, the number of events with a lepton that pass the loose(tight) lepton selection.
- $\epsilon^{\text{real(fake)}} = \frac{N^{\text{tight}}_{\text{real(fake)}}}{N^{\text{loose}}_{\text{real(fake)}}}$, the fraction of the numbers of real(fake) lepton events passing the tight cuts in terms of the total number of real(fake) lepton events passing the loose cuts.

Additionally, we have two more equations to constrain our $N^{\text{loose(tight)}}$:

$$N^{\text{tight}} = N^{\text{tight}}_{\text{real}} + N^{\text{tight}}_{\text{fake}},$$
$$N^{\text{loose}} = N^{\text{loose}}_{\text{real}} + N^{\text{loose}}_{\text{fake}}.$$

The ϵ_{real} and ϵ_{fake} are estimated in regions dominated with real lepton ($Z \to e^+e^-$ and $Z \to \mu^+\mu^-$) or with fake leptons (like events with low E_T^{miss}). N^{loose} and N^{tight} can be obtained directly from data. And with these four quantities, $N^{\text{tight}}_{\text{fake}}$ is derived with:

$$N^{\text{tight}}_{\text{fake}} = \frac{\epsilon_{\text{fake}}}{\epsilon_{\text{real}} - \epsilon_{\text{fake}}} \left(\epsilon_{\text{real}} N^{\text{loose}} - N^{\text{tight}}\right), \tag{6.3}$$

With this data-drive multijet contribution expression, the QCD sample thus can be generated from data events passing the loose lepton selection, by applying the derived QCD weight factor. The matrix method is used to provide the shape modeling of the observables as well as the overall normalisation.

In additional, the multijet contributions in the electron and muon channels are alternatively estimated using the mixed data-simulation jet–electron and purely data-driven anti–muon models[2], respectively.

In summary, the single top backgrounds come from the Wt channel, s channel, as well as the $t\bar{t}$ channels productions are normalised to their theoretical predictions, while the normalisations of the multijet and W+jets contributions are estimated or rescaled, respectively, from data-driven techniques, due to their large uncertainties on their theoretical cross sections. On the other hand, the shapes of the distributions are given by the MC simulation for all background processes except for the multijet events for which data-derived templates are used.

6.3 EVENT SELECTION

With the selected objects in Section 5.3, we can proceed with events selections with more stringent requirements. This analysis uses four selections cuts to define four regions: a *signal region* with a high fraction of t-channel events, a *control region* with a high fraction of $t\bar{t}$ events, another *control region* with a high fraction of W-jets events and a validation region with a high fraction of W-jets. The cuts that define the *signal regions* further discriminate t-channel events from background contamination while these background dominant *control/validation regions* are defined to evaluate the good modelling of the data by the MC simulated predictions and thus determine their scale factors.

The events in these four regions are selected with a two step procedure. The first step is to define a *preselection signal region*; then, the four regions are further defined.

[2]In the electron channel, the jet-electron model is built from a simulated di-jet sample requiring one of the jets to be electron-like. The jet-lepton selection is applied to simulated di-jet events to obtain the templates. In the muon channel, the anti-muon model is used. This model is derived from data selecting a sample highly enriched in non-prompt muons. Details about these two methods are described in Ref. [120].

6.3.1 Event preselection in the signal region

In t-channel single top events, the lepton produced from the decay of the W boson usually emerges with high transverse momentum. Therefore, as discussed in Section 5.3.2, this analysis requires exactly one isolated charged light lepton (electron or muon) selected with transverse momentum $p_T > 25$ GeV and pseudo-rapidity $|\eta| < 2.5$.

The scattered forward light jet typically has a transverse momentum of around 30 ~ 40 GeV, while the central b-tagged jet has a hard p_T distribution that peaks at around 60 GeV. A p_T threshold helps to reject backgrounds with soft jets. Therefore, exactly one b-tagged jet with $|\eta| < 2.5$ and exactly one untagged jet with $|\eta| < 4.5$ are required in this analysis, both with $p_T > 30$ GeV ($p_T > 35$ GeV when $2.7 < |\eta| < 3.5$).

The b-tagged jet is selected with a MV1c value > 0.9195, which corresponds to a b-tagging efficiency of 50%. The second b-quark coming from gluon splitting can result in an additional b-tagged jet. This second b-tagged jet generally has a softer p_T spectrum and a broader η distribution compared to the b-tagged jet produced in the top-quark decay. To reject jets from pile-up collisions, $|\text{JVF}| > 0.50$ is considered for low p_T and central jets. The magnitude of the missing transverse momentum carries the rest of the mass from W boson and must be $E_T^{\text{miss}} > 30$ GeV.

Additional loose low-p_T leptons are vetoed therefore reducing the contribution of dilepton background events (mainly $t\bar{t}$ dilepton events since $t\bar{t}$ is the dominant dilepton backgrounds).

Two additional multijet background rejection criteria are applied. The transverse mass of the lepton–E_T^{miss} system, which is the transverse mass W mass,

$$m_T^W = \sqrt{p_T E_T^{\text{miss}} - \vec{p_T} \cdot \vec{E_T^{\text{miss}}}}$$

or

$$m_{\text{T}}(\ell E_T^{\text{miss}}) = \sqrt{2 p_T(\ell) E_T^{\text{miss}} \left(1 - \cos\Delta\phi(p_T(\ell), E_T^{\text{miss}})\right)},$$

is required to be larger than 50 GeV. In the second expression, $\Delta\phi\left(p_T(\ell), E_T^{\text{miss}}\right)$ is the difference in azimuthal angle between the p_T of the lepton and the E_T^{miss}. Events that do not contain a leptonically decaying W-boson is constructed with a lower $m_{\text{T}}(\ell E_T^{\text{miss}})$. A cut on this region removes these events.

Also, a more stringent isolation cut on the lepton p_T is applied to events in which the lepton and leading jet, j_1, are back-to-back,

$$p_T(\ell) > \frac{40}{\pi - 1} \left(|\Delta\phi(j_1, \ell)| - 1\right) \text{ GeV}$$

where $\Delta\phi(j_1, \ell)$ is the difference in azimuthal angle between the lepton p_T and the leading jet in p_T. As we can see from the Figure 6.3, multijet events are reduced by a cut on the of lower region of the lepton, where the value of the cut depends on the azimuthal angle between the leading jet and the lepton.

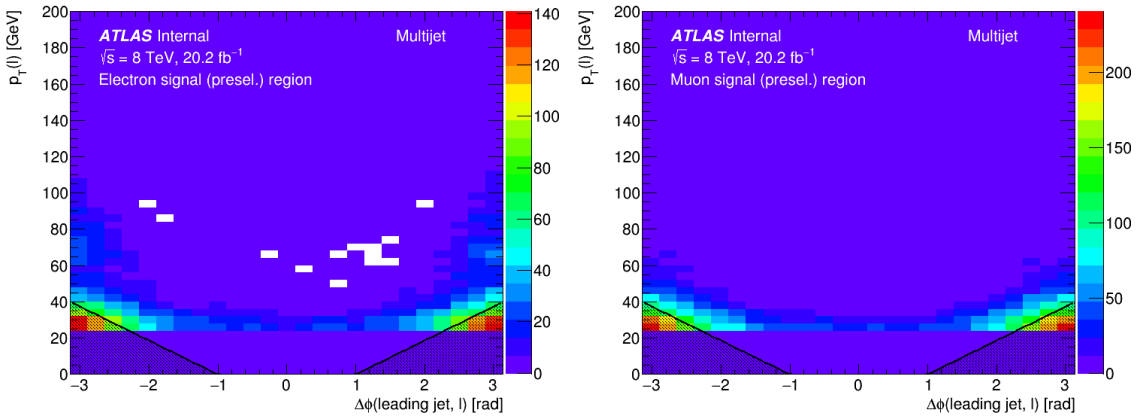

Figure 6.3: Distributions of the lepton p_T as a function of the difference in azimuthal angle between the leading jet j_1 in p_T and the lepton p_T, in the signal preselected region for electrons (left) and muons (right). The plots show the distribution of multijet data-driven prediction.

Finally two fiducial cuts are applied in order to remove a mis-modelling seen in the $|\eta|$ distribution of the non b-jet and in the $|\Delta\eta|$ distribution between the two required jets. These fiducial cuts are the following:

$$|\eta(\text{non } b\text{-jet})| < 3.6$$
$$|\Delta\eta(b\text{-jet, non } b\text{-jet})| < 4.5$$

This set of preselection requirements defines the so-called preselected signal region.

6.3.2 Event selection in the signal region

In addition to the signal event preselection, further discrimination between single top-quark t-channel events and background events is achieved by applying additional criteria following the methods previous ATLAS measurements of the single top production cross section [121] and the two angle analysis [12]:

- The pseudo-rapidity of the non b-tagged jet must satisfy $|\eta(\text{non } b\text{-jet})| > 2.0$, since the spectator jet tends to be forward in the t-channel signature.
- The sum of the p_T of all final-state objects, H_T, must be larger than 195 GeV, since the H_T distributions of the backgrounds peak at lower values than the t-channel signature.
- The mass of the reconstructed top quark, $m(\ell\nu b)$, from its decay products is required to be within 130–200 GeV, to reject background events from processes not involving top quarks.
- The distance in η between the non b-tagged jet and the b-jet must be $|\Delta\eta(b\text{-jet, non } b\text{-jet})| > 1.5$, to further reduce $t\bar{t}$ contributions.

These selection requirements optimise the expected signal significance at 8 TeV, taking into account the main systematic uncertainties. These criteria and the basic event selection together define the t-channel signal region of the analysis.

6.3.3 Event selection in the control and validation regions

Two specific background–enriched control regions are defined in order to estimate the contributions of the most important background processes in the t-channel signal region by computing scale factors for the overall normalisations. In addition to these two control regions a validation region is used to further control the modelling of the W+jets processes. These three specific background–enriched regions are:

- A control region enriched in $t\bar{t}$ events is defined by considering preselected events containing two additional non b-tagged jets (i.e. four jets are required being just one of them required to be b-tagged). The expected contribution of the signal process in this $t\bar{t}$ control region is about 3%.

- An enriched control region in W+jets events is defined in order to control the modelling of the W+jets background. Events in this control region are selected by considering the preselection criteria and vetoing the requirements of the signal selection. The signal fraction in this W+jets control region is expected to be of the order of 11%. This control region is enriched in W+jets events at a level of 36%.
- A third region is defined as a validation region enriched in W+jets events to further control the modelling of the W+jets background. Events in this validation region are selected by considering the preselection criteria imposing a relaxed b-tagging requirement as mentioned in Section 5.2.2. The loose b-tagged jets are selected by considering the MV1c working point corresponding to a b-tagging efficiency of 80%. In addition, all events passing the signal preselection, i.e. satisfying the tighter signal b-tagging requirement (i.e. MV1c value > 0.9195, corresponding to a b-tagging efficiency of 50%), are excluded. This region has much larger enrichment in W+jets events though the flavour composition is totally different to the signal region. The signal fraction in this W+jets control region is expected to be of the order of 3%. This control region is enriched in W+jets events at a level of 78%.

6.4 BACKGROUND ESTIMATION AND NORMALISATION

For all background processes, except multijet and W+jets production, the normalisations are initially estimated by using the MC simulation scaled to the theoretical cross-section predictions, and the event distribution modelling is taken from simulation.

The $t\bar{t}$ events are normalised to the NNLO in QCD including resummation of NNLL soft gluon terms with Top++2.0 [122–127], since its predicted cross-section is $252.89^{+13.30}_{-14.52}$ pb [127], in pp collisions at $\sqrt{s}$ =8 TeV. The inclusive cross-sections of vector-boson production are calculated to NNLO with the FEWZ program [128] and the MSTW2008 NNLO PDF sets, with an uncertainty of 4% [129] and 5% for W+jets and Z+jets, respectively. Finally, the cross-sections of diboson processes are calculated at NLO using the MCFM program [130], within an uncertainty of 5%.

The normalisation as well as the event modelling of the multijet background is estimated from data using the matrix method [120, 131] we discussed in Section 6.2.3. The alternative normalisation and modelling based on the mixed data-simulation jet–electron method [120, 121, 132] and the purely data-driven anti–muon selection [120] are also considered. From the comparison of these two models an overall normalisation uncertainty of 70% is assigned to the multijet contribution.

The final signal and background normalisation are estimated through a simultaneous maximum-likelihood fit to the numbers of data events observed in the signal, $t\bar{t}$ and W+jets control regions described in Section 6.3.3. The likelihood function [132] is given by the product of Poisson probability terms associated with the fitted regions, combined with the product of Gaussian priors to constrain the background rates to their predictions within the associated uncertainties. In the fit the t-channel contribution is treated as unconstrained. The top-quark background contributions ($t\bar{t}$, associated Wt and s-channel) are merged with their relative fractions taken from simulation, and the applied constraint is derived from the combination in quadrature of their cross-section uncertainties, that is 6%. The W+jets contribution is constrained to the normalisation uncertainty of 34% and its flavour composition is taken from simulation. In these three fitted regions the production of a W boson in association with heavy-flavour jets is the dominant contribution to the W+jets background, predicted to be around 95% in the each region. The Z+jets and diboson contributions, which are very low in the signal region (2% of the total expectation), are merged and fixed to the predictions. The multijet contribution is kept fixed to its data-driven estimate. The results of the maximum-likelihood fit together with the statistical post-fit uncertainties are found to be 1.010 ± 0.005 and 1.128 ± 0.013 for the top-quark and W+jets background contributions and 0.909 ± 0.022 for the t-channel signal. In the case of the W+jets validation region, just overall scale factors for the W+jets background are estimated. These are simply extracted by matching the total predicted event yields to the number of events observed in this validation region. All these scale factors are presented as overall scale factors to be applied to the simulated event yields. The results are found to be stable when the constraints set to the top-quark and W+jets backgrounds are significantly relaxed.

The overall normalisation scale factors are used to control the modelling of the kine-

matic and angular variable distributions in the signal, control and validation regions. In the subsequent steps of the analysis, the overall scaling of the t-channel prediction is not relevant while the W+jets and top-quark backgrounds are normalised using these overall scale factors.

6.5 EVENT YIELDS AND DISTRIBUTIONS

6.5.1 Event yields

Table 6.4 shows the number of observed and expected events for the the electron and muon combined channels (labeled as "Combined") in the signal, $t\bar{t}$ and W+jets control and validation regions after applying the overal normalisation scale factors to compute the event yields.

The uncertainties correspond to the statistical uncertainty from the size of the simulated event samples (data-driven samples for multijet background). The table also shows the signal to background ratio, S/B, for each region, being greater than one in the signal region and small in the control and validation regions. Good agreement (within statistical uncertainties) is observed between data and prediction when these overall normalisation scale factors are used.

In addition to the event yields tables, Figure 6.4 shows the pie charts with the expected contribution of the t-channel signal and different background processes in the signal, control and validation regions.

6.5.2 Kinematic distributions in the signal region

The procedure used to simulate background together with those procedures used to estimate multijet contamination, and to rescale the simulated samples using information from the control regions, and to rescale the simulated samples using information from the control regions, and validated by a series of control plots to check the background estimate with different selection criteria, give confidence that the physics modelling, the detector modeling,

Process	Signal region	$t\bar{t}$ control region	W+jets control region	W+jets validation region
t-channel	4395±17	1688±12	11601±29	9306±27
$t\bar{t}$, Wt, s-channel	2017±15	62864±77	48120±82	23937±61
W+heavy-jets	1910±49	6898±65	45410±200	157260±480
W+light-jets	87±31	218±38	3110±200	130900±1000
Z+jets, Diboson	157±7	1118±37	4734±77	17750±300
Multijet	375±13	862±27	8910±61	20140±120
Total expected	8941±64	73650±120	121890±310	359300±1200
Data	8939	73662	121913	359320
S/B	0.97	0.02	0.11	0.03

Table 6.4: Event yields for the combined electron and muon channels (labeled as "Combined") in the signal, $t\bar{t}$ and W+jets control and validation regions. The predictions are derived from simulation samples together with their theoretical cross-section except multijet which is estimated using a data-driven matrix method. The uncertainties shown are statistical only.

and the background estimate are accurate. We can now proceed to investigate the properties of the t-channel events in the signal region, and in particular the distributions of the decay angles discussed in next chapter.

Figures 6.5-6.6 show the some important kinematic distributions in the signal region for reconstructed and selected objects. In all these figures distributions for electrons and muons are shown separately and additionally distributions for separate central and forward lepton η regions are also provided.

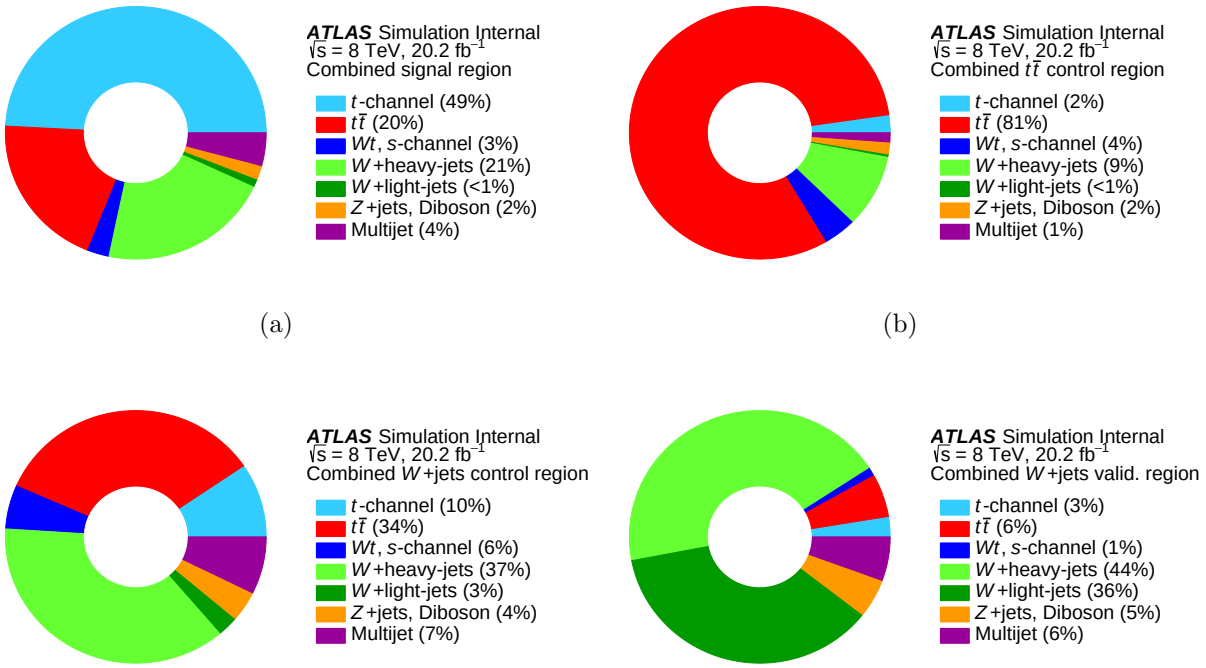

Figure 6.4: Relative contribution of the predicted signal and background processes in the signal, $t\bar{t}$ and W+jets control, and validation regions. The multijet background is estimated using data-driven techniques, while contributions from simulated W+jets, top-quark backgrounds and t-channel event samples are normalised to the results of a maximum-likelihood fit to event yields.

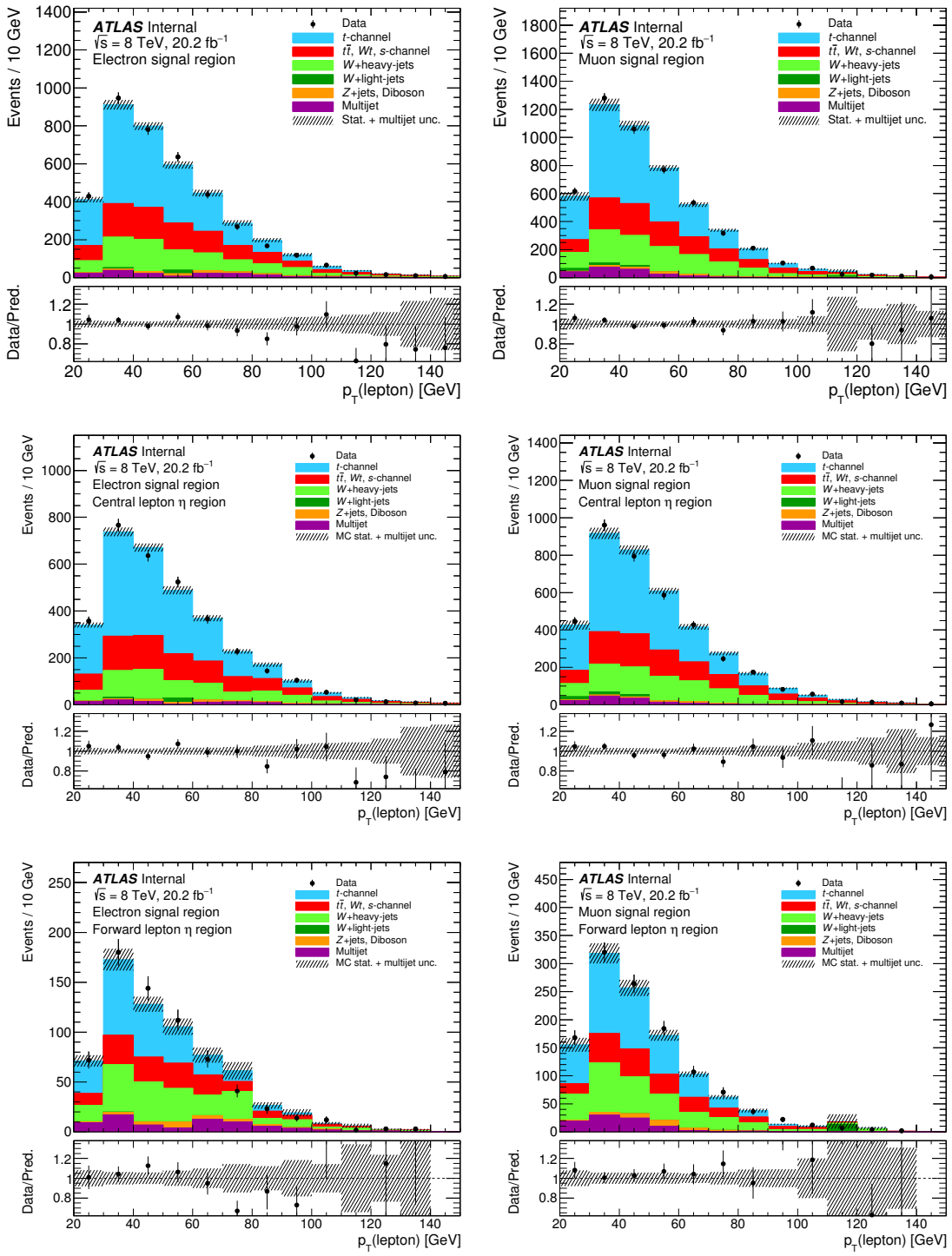

Figure 6.5: Kinematic distributions of the p_T of the lepton (including separate central and forward lepton η regions) in the signal region for the electron (left) and for the muon (right) channels, comparing observed data, shown as the black points with statistical uncertainties, to SM signal and background predictions. The lower plots show the ratio of data to prediction in each bin.

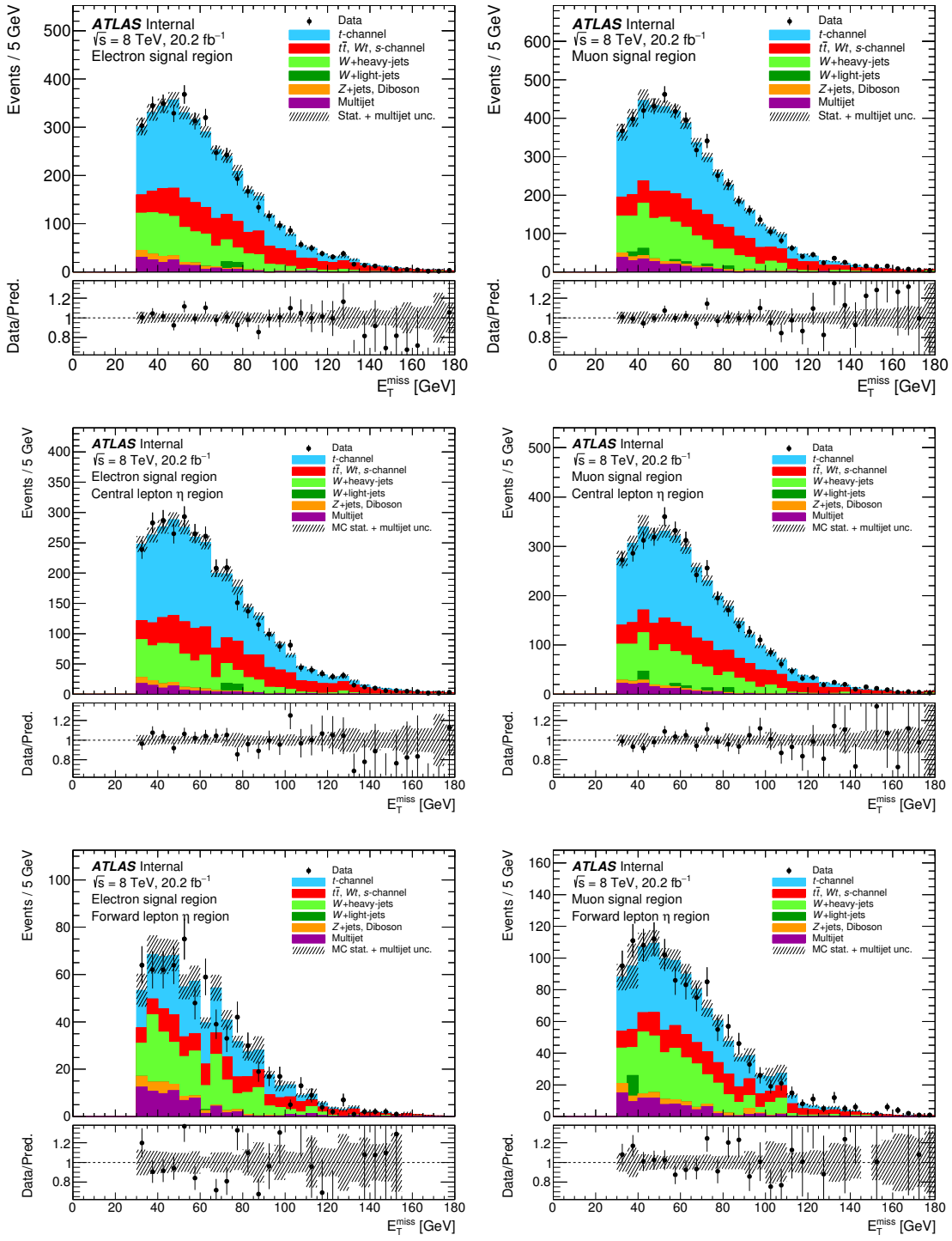

Figure 6.6: Kinematic distributions of the E_T^{miss} (including separate central and forward lepton η regions) in the signal region for the electron (left) and for the muon (right) channels, comparing observed data, shown as the black points with statistical uncertainties, to SM signal and background predictions. The lower plots show the ratio of data to prediction in each bin.

The distributions of the angular observables, θ, θ^* and ϕ^* that were introduced in Section 3.1.4, are shown in Figure 6.7.

Isolation requirements placed on the leptons play an important role in the shape of these angular distributions. From Figure 3.8 one can see that for $\cos\theta = -1$, the spectator jet overlaps with the b-tagged jet. Similarly, for $\cos\theta^* = -1$, the lepton overlaps with the b-tagged jet. Therefore, in both cases, the acceptance is significantly reduced. For $\cos\theta = +1$ the acceptance is maximal since the spectator jet is back-to-back to the b-tagged jet. For $\cos\theta^* = +1$ though the lepton is back-to-back to the b-tagged jet, the acceptance is not maximal since the lepton is in the same plane as the spectator jet and therefore it may overlap with this jet. For $\phi^* = 0$, π or 2π, the lepton is in the same plane as the spectator jet and therefore it may overlap with this jet. This is disfavored by the isolation criteria, so acceptance drops in these three regions. On the contrary, acceptance is maximal for $\phi^* = \pm\pi/2$, since the lepton is in a perpendicular plane to the spectator.

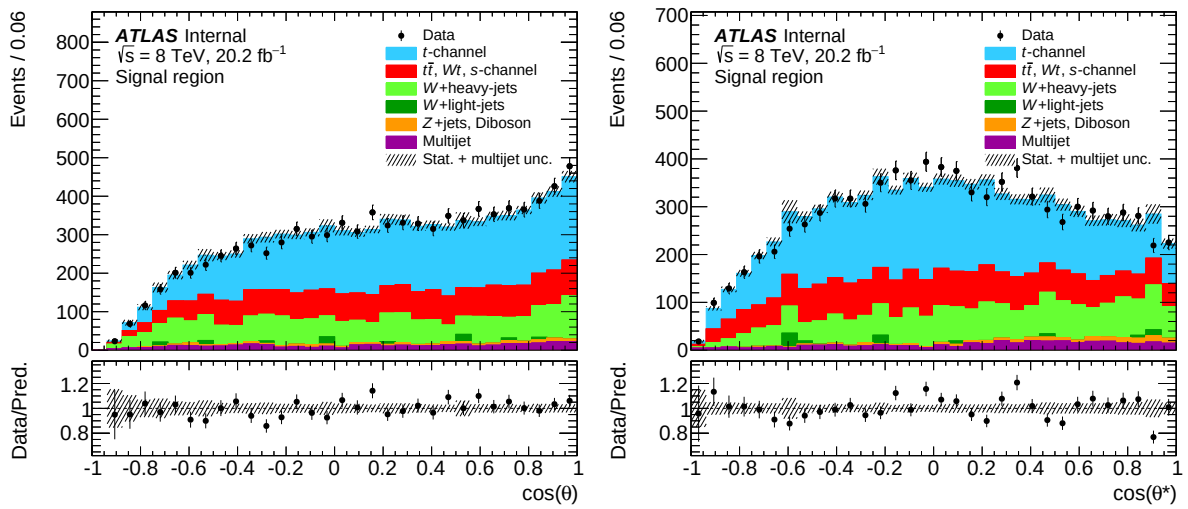

(a) (b)

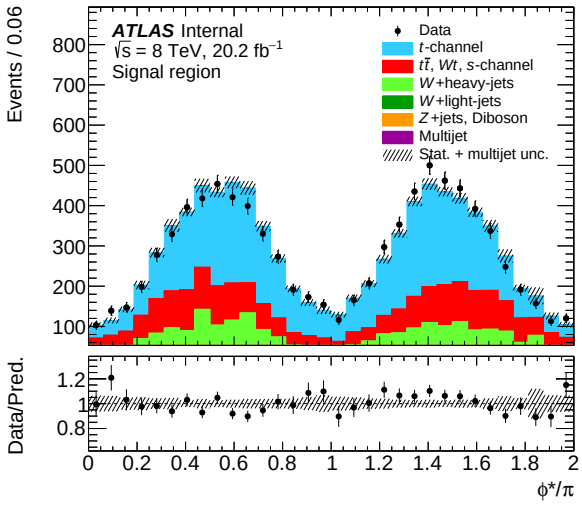

(c)

Figure 6.7: Angular distributions of $\cos\theta$ (a), $\cos\theta^*$ (b) and ϕ^* (c) in the signal region for the electron and muon channels merged, comparing observed data, shown as the black points with statistical uncertainties, to SM signal and background predictions.

7.0 MEASUREMENT OF ANOMALOUS COUPLINGS IN THE TOP-QUARK DECAY VERTEX WITH SINGLE TOP-QUARK EVENTS

7.1 INTRODUCTION

The effective contributions to the Wtb interaction vertex is called an effective couplings, and when those couplings do not exist at leading order in the SM, they are called anomalous couplings; i.e, measurable values of V_R, g_L or g_R are called "anomalous".

This Chapter presents a simultaneous measurement on the full space of parameters governing the Wtb vertex using the angular dependences of single top-quark t-channel events from the normalised triple differential decay rate of top-quark decays (see section 3.1.4), performed using single top events selected from data in 2012 at $\sqrt{s} = 8$ TeV. Conceptually this is a measurement of each of the anomalous coupling parameters V_{L}, V_{R}, g_{L}, and g_{R}; plus the polarisation P of the top quark, with a full covariance matrix.

The analysis is carried out in a Fourier-dual space of coefficients in an angular expansion. A "M-function", which is a product of a normalisation factor, an associated Legendre function $P_k^m(\cos\theta)$, and a spherical harmonic, $Y_l^m(\theta^*, \phi^*)$, is defined and used as the basis function for this procedure and for modelling background processes. To deconvolve detector effects, an angular analogue of the ordinary convolution theorem is used.

7.1.1 The triple differential decay rate of polarised single top quarks

In section 3.1.4 and Refs. [133, 134] it is shown that the helicity formalism [55] applied to the decay of polarised single top quarks, leads to the expression 3.13 for the triple differential decay rate for a top quark.

It proves useful to express the decay rate as a finite series in orthogonal functions. These functions are constructed as a direct product of spherical harmonics and an additional associated Legendre polynomial. Since there appears to be no shorthand notation for these functions in the literature, we have named them M-functions. These are defined and described in the next section.

7.1.2 Definition and properties of the M-functions

The function $M_{k,l}^{m}(\theta,\theta^*,\phi^*)$ is defined as the product of a normalisation factor, an associated Legendre function, $P_k^m(\cos\theta)$, and a spherical harmonic, $Y_l^m(\theta^*,\phi^*)$. The degrees k and l of the associated Legendre function and the spherical harmonic are arbitrary, but both functions must have the same order m:

$$M_{k,l}^{m}(\theta,\theta^*,\phi^*) \equiv \sqrt{\frac{2k+1}{2}\frac{(k-m)!}{(k+m)!}}P_k^m(\cos\theta)\,Y_l^m(\theta^*,\phi^*)\,. \tag{7.1}$$

It may also be expressed purely in terms of spherical harmonics:

$$\begin{aligned} M_{k,l}^{m}(\theta,\theta^*,\phi^*) &= \sqrt{\frac{2k+1}{2}\frac{(k-m)!}{(k+m)!}}P_k^m(\cos\theta)\,Y_l^m(\theta^*,\phi^*) \\ &= \sqrt{2\pi}Y_k^m(\theta,0)Y_l^m(\theta^*,\phi^*) \\ &= \sqrt{2\pi}Y_k^m(\theta,\phi^*)Y_l^m(\theta^*,0). \end{aligned} \tag{7.2}$$

Properties of the M-functions follow immediately from the well-known properties of the spherical harmonics. They form an orthonormal set with respect to the measure $d\Omega^M \equiv d\Omega d\Omega^* = d(\cos\theta)d\Omega^*$:

$$\begin{aligned} \int M_{k,l,m}(\theta,\theta^*,\phi^*)M_{k',l'}^{m'*}(\theta,\theta^*,\phi^*)d\Omega^M &= \\ \int_{4\pi}\int_0^{\pi} M_{k,l,m}(\theta,\theta^*,\phi^*)M_{k',l'}^{m'*}(\theta,\theta^*,\phi^*)\sin\theta d\theta d\Omega^* &= \delta_{k,k'}\delta_{l,l'}\delta_{m,m'}. \end{aligned} \tag{7.3}$$

The complex conjugate of an M-function is

$$M_{k,l}^{m*}(\theta,\theta^*,\phi^*) = M_{k,l}^{-m}(\theta,\theta^*,\phi^*). \tag{7.4}$$

In addition to these two properties, a third one, which may be called Gaunt's theorem in analogy to corresponding theorems for spherical harmonics and Legendre polynomials, is easily proven with their aid:

$$M_{k,l,m}(\theta,\theta^*,\phi^*)M^{m'}_{k',l'}(\theta,\theta^*,\phi^*) = W^{m,m'M}_{k,l,k',l',L,K} M^M_{K,L}(\theta,\theta^*,\phi^*), \tag{7.5}$$

where $W^{m,m'M}_{k,l,k',l',L,K} = \sqrt{2\pi} G^{m,m',M}_{k,k',K} G^{m,m',M}_{l,l',L}$, and $G^{m,m',M}_{k,k',K}$ and $G^{m,m',M}_{l,l',L}$ are the Gaunt coefficients, which are in turn related to the more familiar Clebsch–Gordan coefficients $C^{m,m',M}_{l,l',L}$ through the relation

$$G^{m,m',M}_{l,l',L} = \sqrt{\frac{(2l+1)(2l'+1)}{4\pi(2L+1)}} C^{m,m',M}_{l,l',L} C^{0,0,0}_{l,l',L}\,. \tag{7.6}$$

7.1.3 Triple differential decay rates in M-functions

The triple differential decay rate, Equation 3.13, written in terms of M-functions is:

$$\begin{aligned}
\varrho(\theta,\theta^*,\phi^*;P) &= \frac{1}{N}\frac{dN}{d\Omega d\Omega^*} \\
&= \frac{1}{2\sqrt{2\pi}}\Bigg[\left(|A_{1,\frac{1}{2}}|^2 + |A_{-1,-\frac{1}{2}}|^2 + |A_{0,\frac{1}{2}}|^2 + |A_{0,-\frac{1}{2}}|^2\right) M_{0,0,0}(\theta,\theta^*,\phi^*) \\
&+ \frac{\sqrt{3}}{2}\left(|A_{1,\frac{1}{2}}|^2 - |A_{-1,-\frac{1}{2}}|^2\right) M_{0,1,0}(\theta,\theta^*,\phi^*) \\
&+ \frac{1}{2\sqrt{5}}\left(|A_{1,\frac{1}{2}}|^2 - 2|A_{0,\frac{1}{2}}|^2 - 2|A_{0,-\frac{1}{2}}|^2 + |A_{-1,-\frac{1}{2}}|^2\right) M_{0,2,0}(\theta,\theta^*,\phi^*) \\
&+ P\Bigg\{\frac{1}{\sqrt{3}}\left(|A_{1,\frac{1}{2}}|^2 - |A_{0,\frac{1}{2}}|^2 + |A_{0,-\frac{1}{2}}|^2 - |A_{-1,-\frac{1}{2}}|^2\right) M_{1,0,0}(\theta,\theta^*,\phi^*) \\
&+ \frac{1}{2}\left(|A_{1,\frac{1}{2}}|^2 + |A_{-1,-\frac{1}{2}}|^2\right) M_{1,1,0}(\theta,\theta^*,\phi^*) \\
&+ \frac{1}{2\sqrt{15}}\left(|A_{1,\frac{1}{2}}|^2 + 2|A_{0,\frac{1}{2}}|^2 - 2|A_{0,-\frac{1}{2}}|^2 - |A_{-1,-\frac{1}{2}}|^2\right) M_{1,2,0}(\theta,\theta^*,\phi^*) \\
&- \frac{1}{\sqrt{2}}\left(A_{1,\frac{1}{2}}A^*_{0,\frac{1}{2}} + A^*_{-1,-\frac{1}{2}}A_{0,-\frac{1}{2}}\right) M_{1,1,1}(\theta,\theta^*,\phi^*) \\
&- \frac{1}{\sqrt{2}}\left(A^*_{1,\frac{1}{2}}A_{0,\frac{1}{2}} + A_{-1,-\frac{1}{2}}A^*_{0,-\frac{1}{2}}\right) M_{1,1,-1}(\theta,\theta^*,\phi^*) \\
&- \frac{1}{\sqrt{10}}\left(A_{1,\frac{1}{2}}A^*_{0,\frac{1}{2}} - A^*_{-1,-\frac{1}{2}}A_{0,-\frac{1}{2}}\right) M_{1,2,1}(\theta,\theta^*,\phi^*) \\
&- \frac{1}{\sqrt{10}}\left(A^*_{1,\frac{1}{2}}A_{0,\frac{1}{2}} - A_{-1,-\frac{1}{2}}A^*_{0,-\frac{1}{2}}\right) M_{1,2,-1}(\theta,\theta^*,\phi^*)\Bigg\}\Bigg].
\end{aligned} \tag{7.7}$$

More compactly, it can be written as

$$\begin{aligned}\varrho(\theta,\theta^*,\phi^*;P)=\frac{1}{N}\frac{dN}{d\Omega d\Omega^*} &= \sum_{k=0}^{2}\sum_{l=0}^{2}\sum_{m=-l}^{l} a_{k,l,m}\sqrt{2}Y_k^m(\theta,\phi^*)Y_l^m(\theta^*,0) \\ &= \sum_{k=0}^{2}\sum_{l=0}^{2}\sum_{m=-l}^{l} a_{k,l,m}M_{k,l,m}(\theta,\theta^*,\phi^*). \end{aligned} \tag{7.8}$$

The restriction to $k \leq 2$ and $l \leq 2$ in Equation 7.8 is caused by the limited spin states of the initial and final state fermions and the vector boson at the weak vertex.

Only nine of the coefficients $a_{k,l,m}$ are nonzero and can be parameterised with six physics parameters representing three amplitude fractions and two phases which are called the *generalised helicity fractions and phases*:

- f_1, the fraction of decays containing transversely polarised W bosons,

$$f_1 = \frac{\left|A_{1,\frac{1}{2}}\right|^2 + \left|A_{-1,-\frac{1}{2}}\right|^2}{\left|A_{1,\frac{1}{2}}\right|^2 + \left|A_{-1,-\frac{1}{2}}\right|^2 + \left|A_{0,\frac{1}{2}}\right|^2 + \left|A_{0,-\frac{1}{2}}\right|^2}, \tag{7.9}$$

- f_1^+, the fraction of transversely polarised W boson decays that are right-handed,

$$f_1^+ = \frac{\left|A_{1,\frac{1}{2}}\right|^2}{\left|A_{1,\frac{1}{2}}\right|^2 + \left|A_{-1,-\frac{1}{2}}\right|^2}, \tag{7.10}$$

- f_0^+, in events with longitudinally polarised W bosons, the fraction of b-quarks that are right-handed,

$$f_0^+ = \frac{\left|A_{0,\frac{1}{2}}\right|^2}{\left|A_{0,\frac{1}{2}}\right|^2 + \left|A_{0,-\frac{1}{2}}\right|^2}, \tag{7.11}$$

- δ_+, the phase between amplitudes for longitudinally polarised and transversely polarised W bosons recoiling against right-handed b-quarks,

$$\delta_+ = \arg\left(A_{1,\frac{1}{2}}A^*_{0,\frac{1}{2}}\right), \tag{7.12}$$

- δ_-, the phase between amplitudes for longitudinally polarised and transversely polarised W bosons recoiling against left-handed b-quarks,

$$\delta_- = \arg\left(A_{-1,-\frac{1}{2}}A^*_{0,-\frac{1}{2}}\right), \tag{7.13}$$

In what follows, we define $\vec{\alpha}$ as $\vec{\alpha} \equiv \left\{f_1, f_1^+, f_0^+, \delta_+, \delta_-\right\}$. In addition, P, the top-quark polarisation, is considered separately from $\vec{\alpha}$ because it depends on the production of the top quark, rather than the decay. There is no analytical expression for P in terms of the transition amplitudes, so P is treated as a nuisance parameter.

Using b-quark mass $m_b = 4.95$ GeV, $m_t = 172.5$ GeV, and $m_W = 80.399$ GeV, and using the LO expressions for $\vec{\alpha}$ [12, 135], their expected values are

$$f_1 = 0.304, \qquad f_1^+ = 0.001, \qquad f_0^+ = 6 \cdot 10^{-5}, \qquad \delta_+ = \delta_- = 0.0.$$

In addition, the parameterisation of Equations 7.9-7.13 can also be computed in terms of couplings $V_{\mathrm{L,R}}$ and $g_{\mathrm{L,R}}$. Approximate expressions (valid for $m_b = 0$) are given in Appendix A.2. Unless there are significant right-handed transitions, which is not expected in the SM, δ_+, is not observable in top-quark decays. The nine nonzero coefficients $a_{k,l,m}(\vec{\alpha}; P)$ are:

$$\begin{aligned}
a_{0,0,0} &= \frac{1}{\sqrt{8\pi}}\,, \\
a_{0,1,0} &= \frac{\sqrt{3}}{\sqrt{8\pi}} f_1 (f_1^+ - \frac{1}{2})\,, \\
a_{0,2,0} &= \frac{1}{\sqrt{40\pi}} (\frac{3}{2} f_1 - 1)\,, \\
a_{1,0,0} &= +P \frac{1}{\sqrt{24\pi}} \left(f_1 \left(2f_1^+ - 1\right)\right) + (1 - f_1)\left(1 - 2f_0^+\right)\right)\,, \\
a_{1,1,0} &= +P \frac{1}{\sqrt{32\pi}} f_1\,, \\
a_{1,2,0} &= +P \frac{1}{\sqrt{480\pi}} \left(f_1 \left(2f_1^+ - 1\right)\right) - 2\,(1 - f_1)\left(1 - 2f_0^+\right)\right)\,, \\
a_{1,1,1} &= -P \frac{1}{\sqrt{16\pi}} \sqrt{f_1(1-f_1)} \left\{ \sqrt{f_1^+ f_0^+}\, e^{i\delta_+} + \sqrt{(1-f_1^+)(1-f_0^+)}\, e^{-i\delta_-} \right\}\,, \\
a_{1,1,-1} &= -P \frac{1}{\sqrt{16\pi}} \sqrt{f_1(1-f_1)} \left\{ \sqrt{f_1^+ f_0^+}\, e^{-i\delta_+} + \sqrt{(1-f_1^+)(1-f_0^+)}\, e^{i\delta_-} \right\}\,, \\
a_{1,2,1} &= -P \frac{1}{\sqrt{80\pi}} \sqrt{f_1(1-f_1)} \left\{ \sqrt{f_1^+ f_0^+}\, e^{i\delta_+} - \sqrt{(1-f_1^+)(1-f_0^+)}\, e^{-i\delta_-} \right\}\,, \\
a_{1,2,-1} &= -P \frac{1}{\sqrt{80\pi}} \sqrt{f_1(1-f_1)} \left\{ \sqrt{f_1^+ f_0^+}\, e^{-i\delta_+} - \sqrt{(1-f_1^+)(1-f_0^+)}\, e^{i\delta_-} \right\}\,.
\end{aligned} \tag{7.14}$$

All the other coefficients are zero in single top-quark decays.

The goal of this analysis is to extract simultaneous bounds on all of the physics parameters. Two parameterisation schemes are used. W boson helicity fractions via $f_1 = F_R + F_L$, where $F_R = f_1 f_1^+$ and $F_L = f_1(1 - f_1^+)$. One parameterisation scheme consists of the six generalised helicity fractions and phases $\vec{\alpha}$ of Equations 7.9-7.13. Another consists of the anomalous couplings V_L, V_R, g_L, and g_R. Bounds on these parameters are obtained by first determining the angular coefficients $a_{k,l,m}$. The techniques are described after first describing the event selection and background estimation.

7.2 ANALYSIS METHOD

7.2.1 Overview

An outline of the analysis follows; the steps described here will be explained in detail later in this section. A technique called orthogonal series density estimation (OSDE) [136] is used, which is essentially a Fourier technique, to determine moments of the angular distribution in data (or in a validation sample). Using a MC training sample and employing a generalised convolution theorem, the migration matrix, introduced in Section 7.3.1, is determined, differing from that of a more standard analysis in that it operates in the domain of angular coefficients rather than the domain[1] of the original kinematic variables θ, θ^*, and ϕ^*. The migration matrix is then used to deconvolve the detector response from the physics, and recover the angular moments $a_{k,l,m}(\vec{\alpha})$. The extracted values of the angular moments can be propagated to values of the parameters $\vec{\alpha} \equiv \left\{f_1, f_1^+, f_0^+, \delta_+, \delta_-, P\right\}$, using Equation 7.14 or further propagated to the parameters $V_{L,R}$ and $g_{L,R}$.

The procedure outlined here is complicated by the presence of nonlinearities. The description offered in following section neglects these complications, which are described later, in Section 7.6.

[1]The language here is inspired by Fourier analysis, where one refers to the "time domain" and the "frequency" domain.

7.2.2 Orthogonal series density estimation

Imagine a dataset $\mathcal{D}$

$$\mathcal{D} = \left\{(\theta_1, \theta_1^*, \phi_1^*), (\theta_2, \theta_2^*, \phi_2^*), ...\right\} \tag{7.15}$$

distributed according to the probability distribution $\varrho(\theta, \theta^*, \phi^*)$ of Equation 7.8. From this dataset one wishes to determine, the coefficients $a_{k,l,m}$. These coefficients can formally be expressed, using the orthonormality of the M-functions, as

$$a_{k,l,m} = \int \varrho(\theta, \theta^*, \phi^*) M_{k'l'}^{m'*}(\theta, \theta^*, \phi^*) d\Omega^M \,. \tag{7.16}$$

Suppose one wanted to employ MC techniques to calculate the value of the integral on the right, which, one can notice, expresses the expectation value of the quantity $M_{k'l'}^{m'*}(\theta, \theta^*, \phi^*)$ for a dataset distributed according to $\varrho(\theta, \theta^*, \phi^*)$. Since the dataset is already on hand, one can simply compute the mean value of $M_{k'l'}^{m'*}(\theta, \theta^*, \phi^*)$:

$$a_{k,l,m} = \langle M_{k,l}^{m*}(\theta, \theta^*, \phi^*) \rangle \tag{7.17}$$

where the average is taken over the dataset $\mathcal{D}$. This average is the MC estimate of the coefficient $a_{k,l,m}$.

The technique, called Orthogonal Series Density Estimation (OSDE), is extremely useful for fitting any type of data for which the PDF has a natural decomposition in a basis of orthogonal functions. Such a basis can, for multivariate PDFs, be constructed by taking the product of lower-dimensional basis functions. The M-functions furnish, in fact, an example of that.

The dataset can consist of real or simulated data. In either case the coefficients $a_{k,l,m}$ have statistical uncertainties and correlations. A full covariance matrix for the complete vector of parameters, i.e. both the real and imaginary parts of each coefficient, can be computed from the usual MC techniques.

To interpret the measurement of the coefficients $a_{k,l,m}$ as a measurement of the parameters $\vec{\alpha}$, the real and imaginary parts of the coefficients $a_{k,l,m}$ are packed into a vector $\vec{v}_0$ and the corresponding covariance matrix, obtained from OSDE, into a real-valued matrix C. The coefficient $a_{0,0,0}$ is omitted in this procedure because it is constrained by normalisation, and

not determined by physics. Since the number of parameters used to describe the complex coefficients $\dim(\vec{v}) = 9$ exceeds $\dim(\vec{\alpha}) = 6$, an over-constrained system is found, i.e. more equations than unknowns. A fit which profiles the quantity

$$\chi^2(\vec{\alpha}) = (\vec{v}(\vec{\alpha}) - \vec{v}_0)^T \, C^{-1} \, (\vec{v}(\vec{\alpha}) - \vec{v}_0) \tag{7.18}$$

over the parameters $\vec{\alpha}$ is therefore performed, using Markov chain MC (MCMC) [137].

7.2.3 Measuring the *Wtb* vertex with orthogonal series density estimation

In this section the OSDE technique is applied to the problem of estimating parameters $\vec{\alpha}$ defined in Equation 7.14 in the absence of detector effects. This is not part of the normal analysis flow, but is done here in order to familiarise the reader with the techniques in their simplest form. The exercise is first carried out with simplified (`Toy`) MC, then with PROTOS MC. It does not only illustrates OSDE technique, but also provides some information on how the dataset constrains the parameters $\vec{\alpha}$. Good constraints are in principle possible on all of the parameters with the exception of the parameter δ_+. A substantial amount of right-handed coupling at the Wtb vertex is required before angular distribution become sensitive to δ_+.

7.2.3.1 Simplified MC simulation A simplified MC is developed to test the extraction of physics parameters from these simulation data distributed according to Equation 7.8. This MC generates uniformly in $\cos\theta$, $\cos\theta^*$, and ϕ^*, and performs J. von Neumann rejection [138] against the PDF in Equation 7.8. A total of 5M events are generated. Then, OSDE is applied to the simulation data to determine the angular coefficients. Figure 7.1 shows the table of OSDE fitted parameter values and the nine angular coefficients compared with their input values. The so-determined function is then overlaid with the simulation data. The figure also includes two-dimensional elliptical Mollweide-like projections of the extracted probability density, θ vs. ϕ^* and θ^* vs. ϕ^*. Finally one-dimensional projections of the probability density for θ, θ^*, and ϕ^* are also shown and compared with the input simulation data.

Parameter	measured value	deviation	pull
f_1	0.30320 ± 0.00052	−0.00038	−0.74
δ_- [rad]	-0.00012 ± 0.00045	−0.00012	−0.31
P	0.89903 ± 0.00098	0.00002	0.03
Re $[g_{\mathrm{R}}]$	-0.00029 ± 0.00050	−0.00029	−0.58
Im $[g_{\mathrm{R}}]$	-0.00024 ± 0.00076	−0.00024	−0.31

(a) Fit results

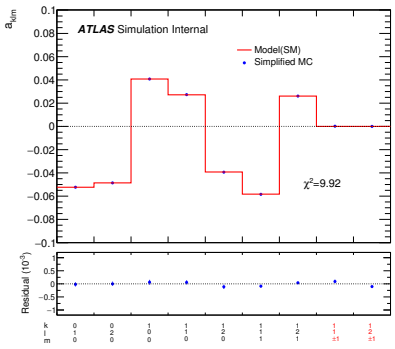

(b) Fitted angular coefficients

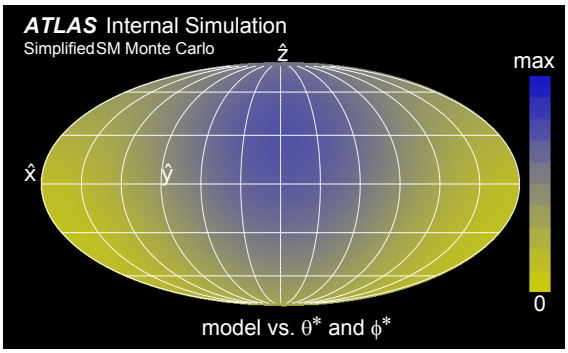

(c) $\cos\theta$ vs. ϕ^*

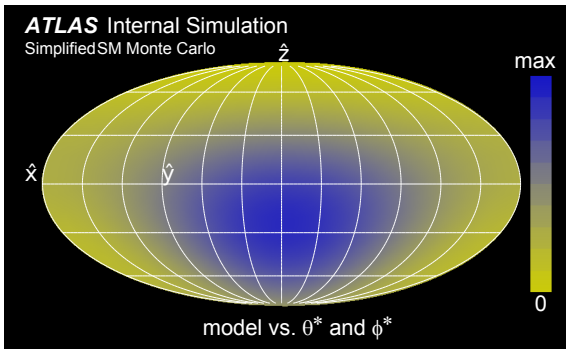

(d) $\cos\theta^*$ vs. ϕ^*

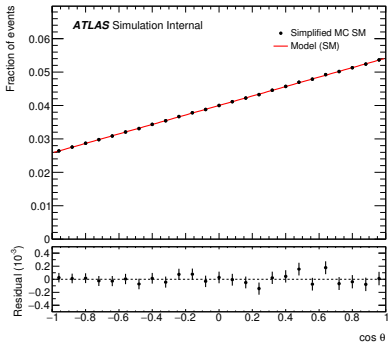

(e) $\cos\theta$

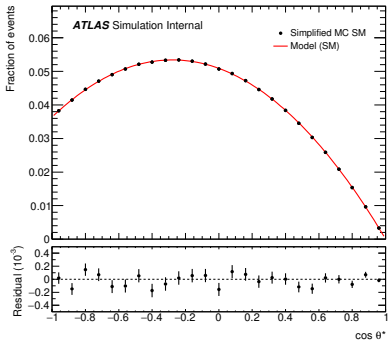

(f) $\cos\theta^*$

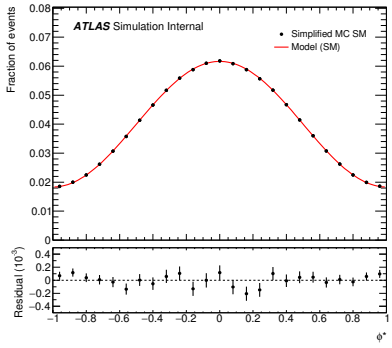

(g) ϕ^*

Figure 7.1: Results of an OSDE fit to generator-level simplified MC as input simulation data. The nine extracted angular coefficient values with the tree-level model are also shown in (b). Two-dimensional elliptical Mollweide-like projections of the extracted probability density are shown in (c) and (d). One-dimensional projections of the probability density for three angles ompared with the input data are shown in (e), (f), (g) respectively.

7.2.3.2 Protos MC simulation The fits in this section are performed to simulated event samples of single top-quark t-channel events generated with SM values of all parameters, using the PROTOS generator at $\sqrt{s}$ =8 TeV. In Figure 7.2 (a) the angular coefficients are compared with their input values, and the so-determined function is then overlaid with the simulation data. This figure includes a table of the fitted parameter values. Figure 7.2 (b) shows the coefficients compared with the model. Its lower plot shows the residuals from this comparison. These residuals are significant; they come from finite width effects in the PROTOS MC. They are taken into account when computing the systematic uncertainty as it is discussed in Section 7.8, but they are negligible in comparison to other contributions. Figure 7.2 (c–d) show two-dimensional elliptical Mollweide-like projections of the extracted probability density for θ vs. ϕ^* and θ^* vs. ϕ^*, respectively. Finally, Figure 7.2 (e–g) show one-dimensional projections of the probability density for $\cos\theta$, $\cos\theta^*$ and ϕ^*, compared with the input simulation data. In their lower plots the residuals from this comparison are shown.

In simulated event samples produced with the PROTOS generator the top-quark mass is drawn from a Breit–Wigner distribution. The average mass of the top quark in the simulation sample differs from the top-quark mass set in the generator input parameters. The shift however depends upon an acceptance window as well as phase space. The residuals can be eliminated by using the average top-quark mass within the simulation PROTOS sample in the calculation of the model, but this depends upon the acceptance window and does not represent a more accurate description of the physics.

Parameter	measured value	deviation	pull
f_1	0.30006 ± 0.00065	−0.0035	−5.41
δ_- [rad]	0.00089 ± 0.000615	0.00089	1.45
P	0.8998 ± 0.0019	−0.0092	−4.79
$\mathrm{Re}\,[g_\mathrm{R}]$	0.00357 ± 0.00079	0.0036	4.53
$\mathrm{Im}\,[g_\mathrm{R}]$	-0.0017 ± 0.0012	−0.0017	−1.44

(a) Fit results

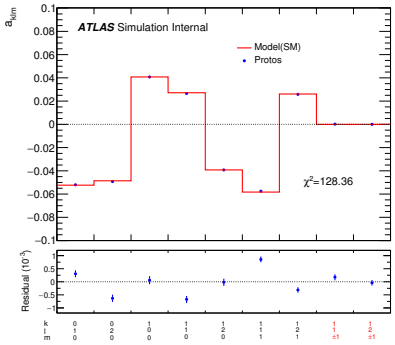

(b) Fitted angular coefficients

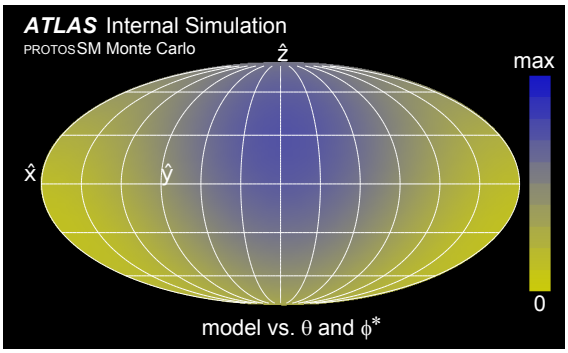

(c) $\cos\theta$ vs. ϕ^*

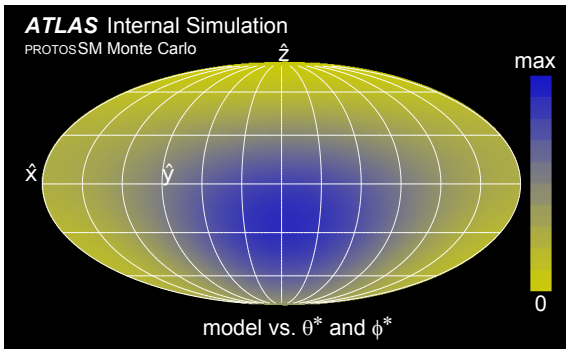

(d) $\cos\theta^*$ vs. ϕ^*

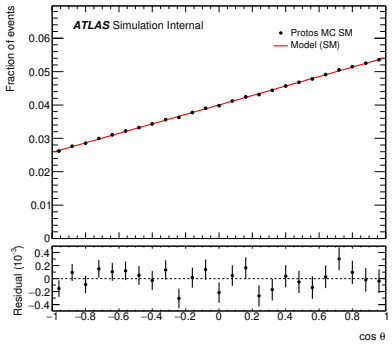

(e) $\cos\theta$

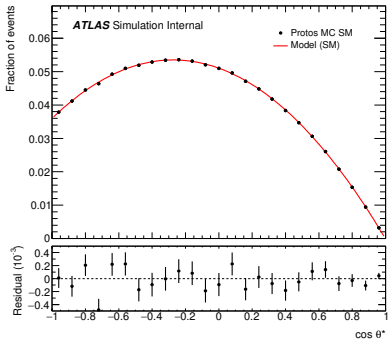

(f) $\cos\theta^*$

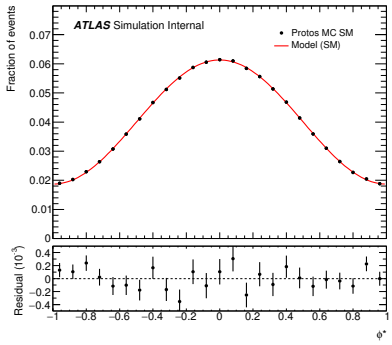

(g) ϕ^*

Figure 7.2: Results of an OSDE fit to generator-level PROTOS MC as input simulation data.

7.3 DECONVOLUTION OF DETECTOR EFFECTS

Angular distributions of decay products of the top quark are heavily sculpted and smeared by detector effects, namely efficiency and resolution[2]. Dramatic effects appear even at the level of the trigger. Nonetheless, OSDE can be applied to reconstructed quantities even though their distribution has no known analytic form, even approximate. The results of an OSDE analysis are shown separately for electrons and muons in Figures 7.3-7.4 for PROTOS simulation. Figures 7.3-7.4 (a) show the angular coefficients obtained from reconstructed quantities. Many more coefficients are present this time, owing to the more complicated angular structure of the measured distributions. The challenge is to recover the underlying physics coefficients from these reconstruction-level coefficients. In addition, residuals are not shown here since there is no model for the reconstructed coefficients. Figures 7.3-7.4 (b–c) show two-dimensional elliptical Mollweide-like projections of the extracted probability density for θ vs. ϕ^* and θ^* vs. ϕ^*, respectively. Finally, Figures 7.3-7.4 (d–f) show one-dimensional projections of the probability density for $\cos\theta$, $\cos\theta^*$ and ϕ^*, compared with the input simulation data. In their lower plots the residuals from this comparison are shown.

Detector effects, both efficiency and resolution, are treated simultaneously in this analysis. Their description is in terms of an expansion in direct products of M-functions, because in this form their incorporation into the analysis is mathematically simple and computationally efficient, thanks to a type of convolution theorem for M-functions that it is developed in this section. Starting with a few definitions, one can designate the true values of the angular variables as $\theta_{\rm T}$, $\theta^*_{\rm T}$, and $\phi^*_{\rm T}$, and the reconstructed values as $\theta_{\rm R}$, $\theta^*_{\rm R}$, and $\phi^*_{\rm R}$. In addition, one can introduce a discrete variable s which takes the value 0 or 1, according to whether (s=1) or not (s=0) the event has been reconstructed and passed the final selection criteria. The probability for the variable s can be expressed in terms of the Kronecker delta,

$$P(s) = \varepsilon\delta_1(s) + (1-\varepsilon)\delta_0(s) \tag{7.19}$$

where $\delta_i(s) \equiv \delta_{is}$ and ε is the efficiency. The two functions δ_i for i=0,1 form a complete set

[2]Background is also an important effect, but is discussed later.

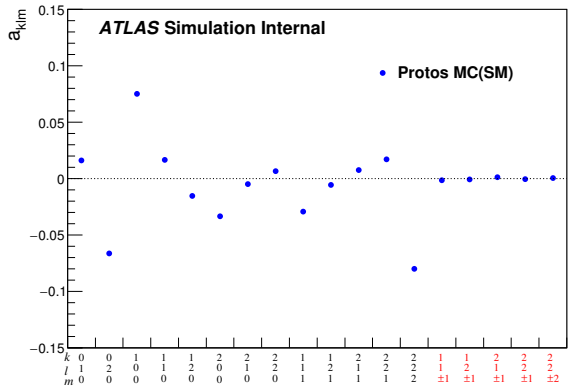

(a) Fitted angular coefficients

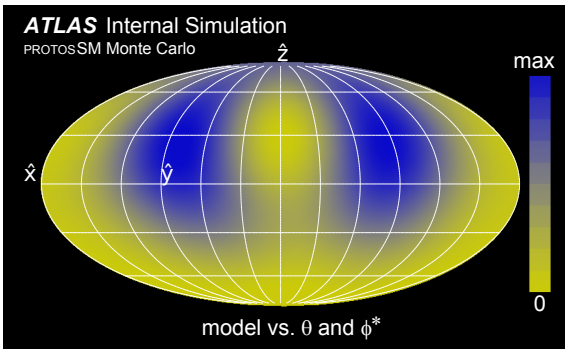

(b) $\cos\theta$ vs. ϕ^*

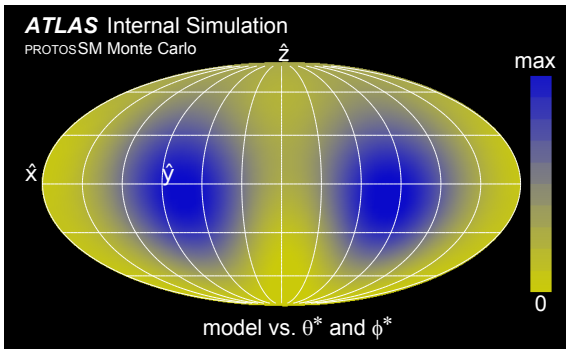

(c) $\cos\theta^*$ vs. ϕ^*

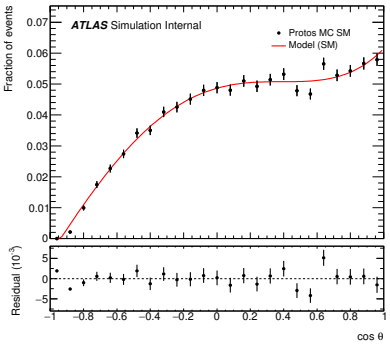

(d) $\cos\theta$

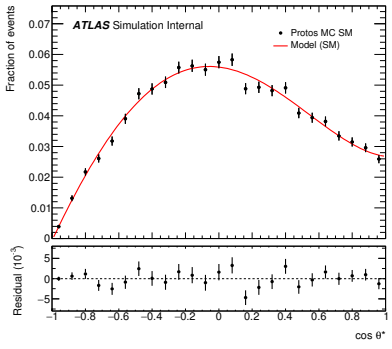

(e) $\cos\theta^*$

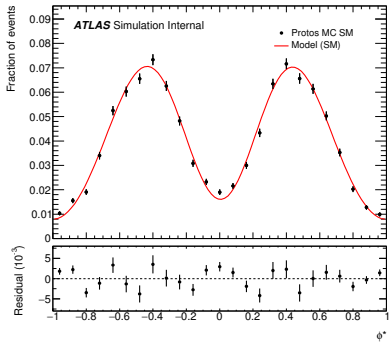

(f) ϕ^*

Figure 7.3: Results of an OSDE fit to reconstructed events with deconvoluted detector effects in the electron channel for PROTOS MC as input simulation data.

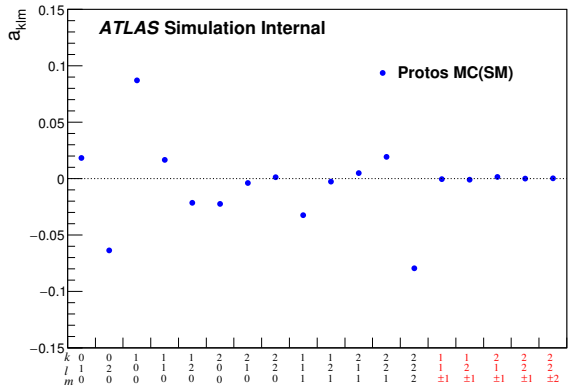

(a) Fitted angular coefficients

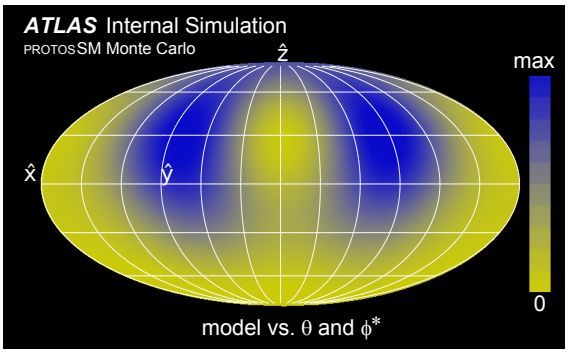

(b) $\cos\theta$ vs. ϕ^*

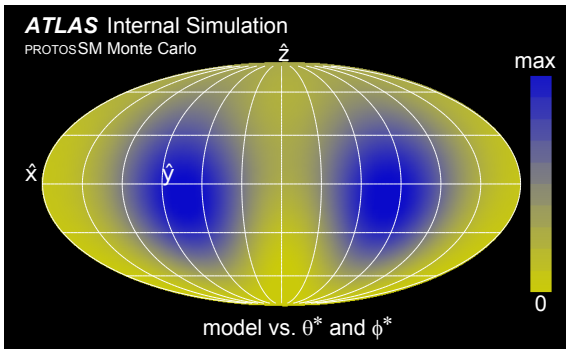

(c) $\cos\theta^*$ vs. ϕ^*

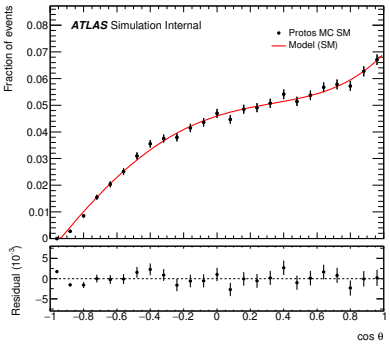

(d) $\cos\theta$

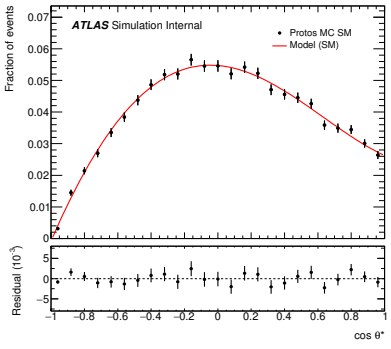

(e) $\cos\theta^*$

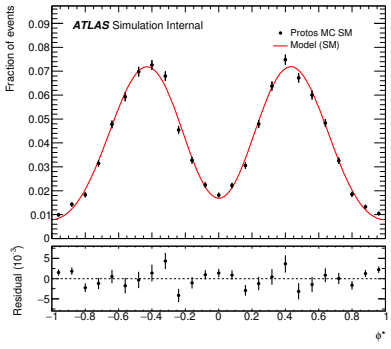

(f) ϕ^*

Figure 7.4: Results of an OSDE fit to reconstructed events with deconvoluted detector effects in the muon channel for PROTOS MC as input simulation data.

of orthonormal functions for the discrete variable s, in the sense that

$$\sum_{s=0,1} \delta_i(s)\delta_j(s) = \delta_{ij} \tag{7.20}$$

The joint PDF for an event to have some particular value of s to have been produced with $\theta_{\rm T}$, $\theta^*_{\rm T}$, and $\phi^*_{\rm T}$ and to have been reconstructed at $\theta_{\rm R}$, $\theta^*_{\rm R}$, and $\phi^*_{\rm R}$ will be denoted as

$$\mathcal{R}(s, \theta_{\rm T}, \theta^*_{\rm T}, \phi^*_{\rm T}, \theta_{\rm R}, \theta^*_{\rm R}, \phi^*_{\rm R}) \tag{7.21}$$

It will be seen that this "resolution function" can be incorporated into the decay rate distributions if it is expressed in a basis of functions based upon M-functions, and the δ's. Such a basis is the set of functions defined as products of

- a δ function in s
- an M-function in $\theta_{\rm T}$, $\theta^*_{\rm T}$, and $\phi^*_{\rm T}$, and
- an M-function in $\theta_{\rm R}$, $\theta^*_{\rm R}$, and $\phi^*_{\rm R}$.

Then,

$$\mathcal{R}(s, \theta_{\rm T}, \theta^*_{\rm T}, \phi^*_{\rm T}, \theta_{\rm R}, \theta^*_{\rm R}, \phi^*_{\rm R}) = r_{i,k,l,m,k',l',m'} \delta_i(s) M^m_{k,l}(\theta_{\rm T}, \theta^*_{\rm T}, \phi^*_{\rm T}) M^{m'}_{k',l'}(\theta_{\rm R}, \theta^*_{\rm R}, \phi^*_{\rm R}). \tag{7.22}$$

An infinite series will describe any well-behaved function.

From MC simulation, a dataset is obtained

$$\mathcal{D}_{\rm T} = \left\{(\theta_{T,1}, \theta^*_{T,1}, \phi^*_{T,1}, \theta_{R,1}, \theta^*_{R,1}, \phi^*_{R,1}), (\theta_{T,2}, \theta^*_{T,2}, \phi^*_{T,2}, \theta_{R,2}, \theta^*_{R,2}, \phi^*_{R,2} ...)\right\} \tag{7.23}$$

called the training dataset. To describe this dataset does not require an infinite number of terms, and therefore the series can be truncated, Equation 7.22, at a maximum value of k, l, k', and l'. The joint probability density $\mathcal{R}(s, \theta_{\rm T}, \theta^*_{\rm T}, \phi^*_{\rm T}, \theta_{\rm R}, \theta^*_{\rm R}, \phi^*_{\rm R})$ is therefore completely described by a finite number of coefficients $r_{i,k,l,m,k',l',m'}$, and these can be determined by applying OSDE to the training dataset.

We will be interested in the probability that a *detected* event migrates from a set of true angles to a set of detected angles, i.e., with s=1, so

$$\begin{aligned} \mathcal{R}(1, \theta_{\rm T}, \theta^*_{\rm T}, \theta_{\rm R}, \theta^*_{\rm R}, \phi^*_{\rm R}) &= r_{i,k,l,m,k',l',m'} \delta_i(1) M^m_{k,l}(\theta_{\rm T}\theta^*_{\rm T}, \phi^*_{\rm T}) M^{m'}_{k',l'}(\theta_{\rm R}, \theta^*_{\rm R}, \phi^*_{\rm R}). \\ &= r_{1,k,l,m,k',l',m'} M^m_{k,l}(\theta_{\rm T}\theta^*_{\rm T}, \phi^*_{\rm T}) M^{m'}_{k',l'}(\theta_{\rm R}, \theta^*_{\rm R}, \phi^*_{\rm R}). \end{aligned} \tag{7.24}$$

so that we will only need the coefficients $r_{1,k,l,m,k',l',m'}$. We can get those by applying OSDE to $\mathcal{R}$.

$$\begin{aligned} r_{1,k,l,m,k',l',m'} &= \langle \delta_1(s) M^{m*}_{k,l}(\theta_{\rm T}\theta^*_{\rm T}, \phi^*_{\rm T}) M^{m'*}_{k',l'}(\theta_{\rm R}, \theta^*_{\rm R}, \phi^*_{\rm R}) \rangle \\ &= \left[\sum_{n\in\mathcal{S}} w_n M^{m*}_{k,l}(\theta_{Tn}\theta^*_{Tn}, \phi^*_{Tn}) M^{m'*}_{k',l'}(\theta_{Rn}, \theta^*_{Rn}, \phi^*_{Rn}) \right] / \sum_n w_n \end{aligned} \tag{7.25}$$

In this expression, which allows for weighted events, the sums run over events in the training sample $\mathcal{D}_{\rm T}$, restricted, in the numerator, to those events in the subsample $\mathcal{S}$ of events passing all selection cuts, and unrestricted in the denominator. One might have objected that an event which is, say lost to the trigger, may not have a of $\theta_{\rm R}$, $\theta^*_{\rm R}$, and $\phi^*_{\rm R}$, since it is not reconstructed, but one can see from Ref. 7.25 and from the above discussion that such events are never used, anyway.

7.3.1 Migration coefficients

The expression for the joint probability density, Equation 7.21, and its coefficients, Equation 7.25, needs to be recast as a conditional probability in order to be useful. We will require the probability

$$\mathcal{P}(s=1, \theta_{\rm R}, \theta^*_{\rm R}, \phi^*_{\rm R} | \theta_{\rm T}, \theta^*_{\rm T}\phi^*_{\rm T}) \tag{7.26}$$

for an event which is produced with a given value of, $\theta_{\rm T}$, and $\theta^*_{\rm T}$ to be detected (implying s=1), *and* to be reconstructed with angles $\theta_{\rm R}$, $\theta^*_{\rm R}$, and $\phi^*_{\rm R}$. The relation between the two PDFs is:

$$\mathcal{P}(s=1, \theta_{\rm R}, \theta^*_{\rm R}, \phi^*_{\rm R} | \theta_{\rm T}, \theta^*_{\rm T}, \phi^*_{\rm T}) = \frac{\mathcal{R}(s=1, \theta_{\rm T}, \theta^*_{\rm T}, \phi^*_{\rm T}, \theta_{\rm R}, \theta^*_{\rm R}, \phi^*_{\rm R})}{\mathcal{P}(\theta_{\rm T}, \theta^*_{\rm T}, \phi^*_{\rm T})} \tag{7.27}$$

where $\mathcal{P}(\theta_{\rm T}, \theta^*_{\rm T}, \phi^*_{\rm T})$ is the probability density value of $\theta_{\rm T}$, $\theta^*_{\rm T}$, and $\phi^*_{\rm T}$. The conditional probability can also be expanded:

$$\mathcal{P}(s=1, \theta_{\rm R}, \theta^*_{\rm R}, \phi^*_{\rm R} | \theta_{\rm T}, \theta^*_{\rm T}, \phi^*_{\rm T}) = g_{k,l,m,k',l',m'} M^m_{k,l}(\theta_{\rm T}, \theta^*_{\rm T}, \phi^*_{\rm T}) M^{m'}_{k',l'}(\theta_{\rm R}, \theta^*_{\rm R}, \phi^*_{\rm R}) \,, \tag{7.28}$$

The denominator of Equation 7.27 is

$$\mathcal{P}(\theta_{\rm T}, \theta^*_{\rm T}, \phi^*_{\rm T}) = a_{k,l,m} M^m_{k,l}(\theta, \theta^*, \phi^*) \tag{7.29}$$

Substituting Equation 7.29 into Equation 7.27, using the expansions in Equation 7.24 and 7.28, integrating, applying Gaunt's theorem (Equation 7.5) and rearranging gives us the relation:

$$a_{\kappa,\lambda,\mu} W^{\mu',\mu,M}_{\kappa',\lambda',\kappa,\lambda,K,L} \cdot g_{\kappa',\lambda',\mu',K',L',M'} = r_{1,K,L,M,K',L',M'} \tag{7.30}$$

Each value of K, L, M, K', L', M', gives a separate complex matrix equation which can be inverted to determine the coefficients $g_{\kappa',\lambda',\mu',K',L',M'}$. The coefficients $a_{\kappa,\lambda,\mu}$ and $r_{1,K,L,M,K',L',M'}$ are taken from the training sample. The `Eigen` package is used for the matrix inversion. The resulting set of coefficients $g_{\kappa',\lambda',\mu',K',L',M'}$ will be referred to as the migration coefficients, for reasons to be seen.

It is also worth to mention that the coefficients $a_{\kappa,\lambda,\mu}$ are indeed needed to compute the coefficients $g_{\kappa',\lambda',\mu',K',L',M'}$. In other words the migration matrix depends on the physics parameters. This will be discussed in Section 7.6 though it can anticipate that this dependance is taken into account, as shown by Equation 7.42, by the reweighting procedure used in the analysis described in this note to remove the nonlinearities.

In summary, OSDE is applied to the training sample in order to obtain coefficients of the joint probability distribution, and Equation 7.30 is inverted to obtain the coefficients of a conditional probability distribution, which will next be applied as described in the next section.

7.3.2 Convolution

The observable distribution of reconstructed events is the underlying physics PDF, Equation 7.8 convolved with the conditional probability density, Equation 7.26:

$$\varrho(\theta_{\mathrm{R}}, \theta^*_{\mathrm{R}}, \phi^*_{\mathrm{R}}) = \int \varrho(\theta_{\mathrm{T}}, \theta^*_{\mathrm{T}}, \phi^*_{\mathrm{T}}) \mathcal{P}(\theta_{\mathrm{R}}, \theta^*_{\mathrm{R}}, \phi^*_{\mathrm{R}} | s = 1, \theta_{\mathrm{T}}, \theta^*_{\mathrm{T}}, \phi^*_{\mathrm{T}}) d\Omega^M_{\mathrm{T}} \tag{7.31}$$

This equation can be expressed as a matrix relation between coefficients:

$$
\begin{aligned}
& \mathcal{A}_{k,l,m} M^{m}_{kl}(\theta_{\rm R}, \theta^{*}_{\rm R}, \phi^{*}_{\rm R}) \\
= & \int a_{K,L,M} M^{M}_{KL}(\theta_{\rm T}, \theta^{*}_{\rm T}, \phi^{*}_{\rm T}) g_{K',L',M',k,l,m} M^{M'}_{K',L'}(\theta_{\rm T}, \theta^{*}_{\rm T}, \phi^{*}_{\rm T}) M^{m}_{k,l}(\theta_{\rm R}, \theta^{*}_{\rm R}, \phi^{*}_{\rm R}) d\Omega^{M}_{\rm T} \\
= & \int a_{K,L,M} M^{-M*}_{KL}(\theta_{\rm T}, \theta^{*}_{\rm T}, \phi^{*}_{\rm T}) g_{K',L',M',k,l,m} M^{M'}_{K',L'}(\theta_{\rm T}, \theta^{*}_{\rm T}, \phi^{*}_{\rm T}) M^{m}_{k,l}(\theta_{\rm R}, \theta^{*}_{\rm R}, \phi^{*}_{\rm R}) d\Omega^{M}_{\rm T} \\
= & \; a_{K,L,M} \delta_{K,K'} \delta_{L,L'} \delta_{-M,M'} g_{K',L',M',k,l,m} M^{m}_{k,l}(\theta_{\rm R}, \theta^{*}_{\rm R}, \phi^{*}_{\rm R}) \\
= & \; a_{K,L,M} g_{K,L,-M,k,l,m} M^{m}_{k,l}(\theta_{\rm R}, \theta^{*}_{\rm R}, \phi^{*}_{\rm R})
\end{aligned}
\tag{7.32}
$$

Or

$$
\mathcal{A}_{k,l,m} = g_{K,L,-M,k,l,m} a_{K,L,M}. \tag{7.33}
$$

This important equation is analogous to the *convolution theorem* in ordinary Fourier analysis.

The real and imaginary parts of the reconstructed coefficients $\mathcal{A}_{k,l,m}$, together with their variance and correlations, can be determined from real or simulated data, by applying OSDE as described in Section 7.2.2 to reconstructed quantities. The next step is to recover the true coefficients, $a_{K,L,M}$ from the reconstructed coefficients $\mathcal{A}_{k,l,m}$. This is an exercise in deconvolution. We have set ourselves up to carry out the deconvolution of detector effects in the Fourier-dual space of angular coefficients, and we are now ready to take the next step. Before doing so, we want to re-express the key elements of the procedure in a more convenient form.

7.3.2.1 Matrix notation The coefficients $\mathcal{A}_{k,l,m}$ and $a_{K,L,M}$ appearing in Equation 7.33 can be represented as vectors denoted as $\vec{\mathcal{A}}$ and $\vec{a}$, respectively, while $g_{K,L,-M,k,l,m}$ can be represented as a matrix denoted as $\mathbf{G}$. Let us say that the vector $\vec{a}$ belongs to the "true-space" while the vector $\vec{\mathcal{A}}$ belongs to the "reconstruction-space" or just the "reco-space". Generally, reco-space will be larger than true-space. The vector $\vec{a}$ is defined in the following way. First, "pack" the real and imaginary parts of the coefficients $a_{K,L,M}$ in true-space into

a flat array of real numbers in the following order.

$$\vec{a} = \begin{pmatrix} \mathrm{Re}\,[a_{0,0,0}] \\ \mathrm{Re}\,[a_{1,0,0}] \\ \mathrm{Re}\,[a_{0,2,0}] \\ \mathrm{Re}\,[a_{1,0,0}] \\ \mathrm{Re}\,[a_{1,1,0}] \\ \mathrm{Re}\,[a_{1,1,1}] \\ \mathrm{Im}\,[a_{1,1,1}] \\ \mathrm{Re}\,[a_{1,2,0}] \\ \mathrm{Re}\,[a_{1,2,1}] \\ \mathrm{Im}\,[a_{1,2,1}] \end{pmatrix} \tag{7.34}$$

This vector is arranged so that the value of the index M increases most rapidly, followed by L, followed by K (though any unique ordering of the elements is equally valid if used consistently). For other coefficients with M=0, the imaginary parts are omitted because they are determined by the condition that the PDF be real; and both real and imaginary parts of coefficients with $M < 0$ are omitted because they are merely the complex conjugates of the coefficients with $M > 0$. When included, the imaginary part of a coefficient always follows immediately the corresponding real part, in the vector.

The same scheme is then used to pack a real valued vector $\vec{\mathcal{A}}$ of coefficients in reco-space, determined using OSDE. However, the length of the vector (i.e. the dimensionality of reco-space) depends upon the number of coefficients needed to model the full, detector-sculpted PDF for accepted, reconstructed events. The covariance matrix associated with the vector, also obtained from OSDE, is called $\mathbf{C}$; its inverse. the "weight matrix" is $\mathbf{W} = \mathbf{C}^{-1}$.

Finally, the migration coefficients can also be expressed in matrix form. The mapping is as follows. For each row i and each column j, first determine the indices k, l, m of the coefficients in reco-space corresponding to i and the indices k', l', m' of the coefficients in true-space corresponding to j. Locate the complex migration coefficient $g_{k',k',-m',k,l,m}$ using those indices. Then, define a real-valued migration matrix $\mathbf{G}$ whose elements $(\mathbf{G})_{ij}$ are

- $+\mathrm{Re}\left[g_{k',k',-m',k,l,m}\right]$ if $i(k,l,m)$ is the index of a *real* element of $\vec{a}$, and $j(k',l',m')$ is the index of a *real* element of $\vec{\mathcal{A}}$.
- $+\mathrm{Re}\left[g_{k',k',-m',k,l,m}\right]$ if $i(k,l,m)$ is the index of an *imaginary* element of $\vec{a}$, and $j(k',l',m')$ is the index of an *imaginary* element of $\vec{\mathcal{A}}$.
- $-\mathrm{Im}\left[g_{k',k',-m',k,l,m}\right]$ if $i(k,l,m)$ is the index of an *real* element of $\vec{a}$, and $j(k',l',m')$ is the index of an *imaginary* element of $\vec{\mathcal{A}}$.
- $+\mathrm{Im}\left[g_{k',k',-m',k,l,m}\right]$ if $i(k,l,m)$ is the index of an *imaginary* element of $\vec{a}$, and $j(k',l',m')$ is the index of an *real* element of $\vec{\mathcal{A}}$.

With these definitions, Equation 7.33 can be written as:

$$\vec{\mathcal{A}} = \mathbf{G} \cdot \vec{a} \tag{7.35}$$

7.3.3 Deconvolution

Equation 7.35 cannot be inverted in practice because the matrix $\mathbf{G}$ has more rows than columns, indicating a situation in which too many equations constrain two few variables. Owing to statistical fluctuations in the measured quantities, they cannot all be simultaneously satisfied. The number of rows can be reduced by considering fewer equations. The higher order terms in reco-space, of which there are an infinite number, will be truncated since they represent high-frequency components bringing little information on the true coefficients. In what follows a truncation is done at $L^{\mathrm{reco}}_{\mathrm{max}} = K^{\mathrm{reco}}_{\mathrm{max}} = 2$ (subscript "reco" represents indices in the reco-space while superscript "max" is the maximum index value of a given series) a choice that will be justified later. When so truncated, the matrix $\mathbf{G}$ is still not invertible, but since a full covariance matrix for $\mathbf{C} = \mathbf{W}^{-1} = Cov(\vec{\mathcal{A}})$ is available, one can invert in the sense of minimizing the function

$$\chi^2(\vec{a}) = (\vec{\mathcal{A}} - \mathbf{G} \cdot \vec{a})^T \cdot \mathbf{W} \cdot (\vec{\mathcal{A}} - \mathbf{G} \cdot \vec{a}) \tag{7.36}$$

over the vector $\vec{a}$. This can be done analytically, and yields the solution

$$\vec{a} = \mathbf{V}\mathbf{G}^T\mathbf{W}\vec{\mathcal{A}} \tag{7.37}$$

where

$$\mathbf{V} = Cov(\vec{a}) = (\mathbf{G}^T\mathbf{W}\mathbf{G})^{-1}\,. \tag{7.38}$$

(These equations will be familiar to anyone who has implemented a track fit, or a vertex fit. A derivation is given in Appendix A.3.). In this way one has deconvolved the detector effects, obtaining again a measurement (central values and covariance matrix) for the real and imaginary parts of the coefficients $a_{k,l,m}$.

7.3.4 Closure tests

The procedure described in the preceding section has been applied and tested with simulated LO t-channel events generated with PROTOSİn addition, this closure tests are performed independently to electrons and muons. In all cases, the efficiency and resolution models (i.e. the migration matrix) are build from an independent subsample of the given simulated event sample, in particular, taking 4/5 of the total sample while the rest of simulated events, i.e. 1/5 of the total sample, are used as the validation sample. This choice is found to be the best option in order to have the statistical uncertainty low enough. Figure 7.5 show the results of these closure tests using simulated events samples produced with PROTOS generators. Figure 7.5 (a–b) show the nine deconvolved angular coefficients for electrons and muons separately. The model is compared with input data in all these distributions.

From the deconvolved angular coefficients one can obtain the generalised helicity fractions (f_1, f_1^+ and f_0^+), the phase δ_-, and the polarisation P. This is done by first performing a statistical combination of measured coefficients for electrons and for muons, and then propagating the measurement of angular coefficients to the generalised helicity fractions and phases by minimizing the χ^2 in Equation 7.18. Fit results are shown in Figure 7.5(c).

7.3.5 Optimisation of $K_{\max}^{\text{reco}}$ and $L_{\max}^{\text{reco}}$

From Equation 7.38 one can identify two sources of statistical uncertainty in the final estimator for $\vec{a}$, one is the statistical uncertainty on the reconstructed coefficients $\vec{\mathcal{A}}$ and its covariance $\mathbf{C}$, and the other is statistical uncertainty on the migration matrix $\mathbf{G}$. The former comes from data fluctuations, while the latter comes from training sample fluctuations. As

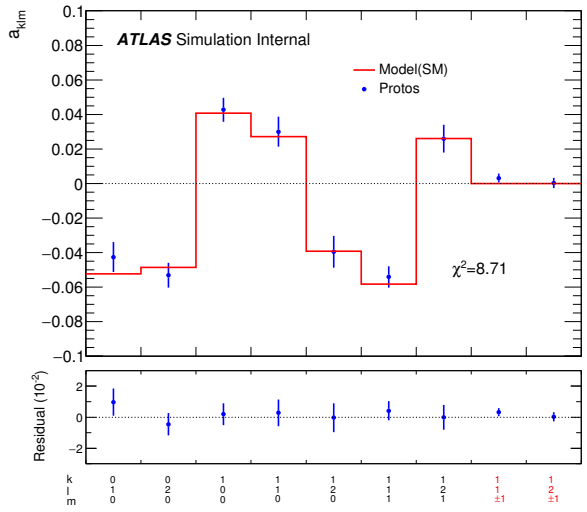

(a) Fitted angular coefficients (electrons)

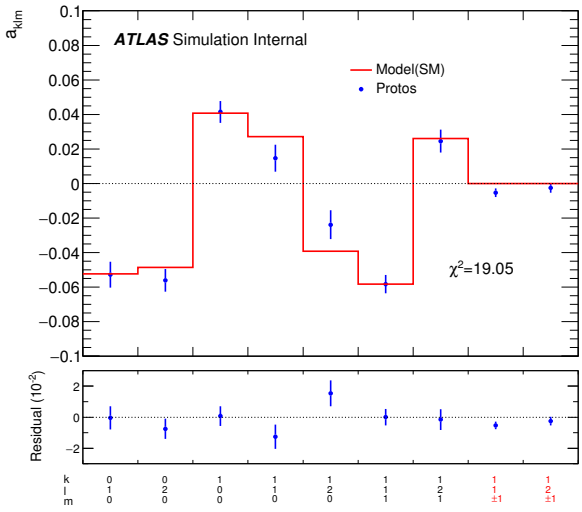

(b) Fitted angular coefficients (muons)

Parameter	measured value	deviation	pull
f_1	0.291733 ± 0.0211668	−0.0118565	−0.560145
δ_- [rad]	-0.0167406 ± 0.0345881	−0.0167406	−0.484
P	0.889926 ± 0.045926	−0.00907426	−0.197585
Re $[g_R]$	0.0136336 ± 0.0281602	0.0136336	0.484145
Im $[g_R]$	0.00961913 ± 0.0198118	0.00961913	0.485525

(c) Fit results

Figure 7.5: Results of the closure tests using a simulation sample produced with the Protos generator are shown. Table (c) displays the fit results using the deconvolved angular coefficients.

the number of reconstructed coefficients used in the deconvolution equation increases, the precision on true quantities increases, but so does the noise from training sample fluctuations. In principle, one could carry out an optimisation exercise in which both quantities are quantified for various values of $K_{\text{max}}^{\text{reco}}$ and $L_{\text{max}}^{\text{reco}}$, which are algorithmic parameters affecting, potentially, the precision of the measurement. Table 7.1 show the results of varying $K_{\text{max}}^{\text{reco}}$ and $L_{\text{max}}^{\text{reco}}$ on the Protos SM samples, to determine the sensitivity of the final measurement

on these algorithmic parameters. From these studies one sees that beyond $K_{\max}^{\text{reco}} = L_{\max}^{\text{reco}} = 2$, there is no increase in precision on measured quantities. Therefore no benefit in increasing these values is observed, and $K_{\max}^{\text{reco}} = L_{\max}^{\text{reco}} = 2$ are taken to be the default values for the deconvolution algorithm.

Parameter	measured value	deviation	pull
$K^{\text{reco}}_{\text{max}} = L^{\text{reco}}_{\text{max}} = 2$			
f_1	0.30375 ± 0.01425	0.00016	0.0112281
δ_- [rad]	-0.0003 ± 0.0069	−0.0003	−0.0434783
P	0.904688 ± 0.0303125	0.0056875	0.187629
$K^{\text{reco}}_{\text{max}} = L^{\text{reco}}_{\text{max}} = 3$			
f_1	0.30125 ± 0.01425	−0.00234	−0.164211
δ_- [rad]	-0.0009 ± 0.0069	−0.0009	−0.130435
P	0.899062 ± 0.030625	6.25e−05	0.00204082
$K^{\text{reco}}_{\text{max}} = L^{\text{reco}}_{\text{max}} = 4$			
f_1	0.30275 ± 0.013	−0.00084	−0.0646154
δ_- [rad]	-0.0009 ± 0.0066	−0.0009	−0.136364
P	0.898438 ± 0.0303125	−0.0005625	−0.0185567
$K^{\text{reco}}_{\text{max}} = L^{\text{reco}}_{\text{max}} = 5$			
f_1	0.30325 ± 0.01325	−0.00034	−0.0256604
δ_- [rad]	-0.0003 ± 0.0066	−0.0003	−0.0454545
P	0.900313 ± 0.0284375	0.0013125	0.0461538
$K^{\text{reco}}_{\text{max}} = L^{\text{reco}}_{\text{max}} = 6$			
f_1	0.30325 ± 0.0125	−0.00034	−0.0272
δ_- [rad]	0.0003 ± 0.0063	0.0003	0.047619
P	0.904688 ± 0.026875	0.0056875	0.211628

Table 7.1: $K^{\text{reco}}_{\text{max}}$ and $L^{\text{reco}}_{\text{max}}$ are varied on the PROTOS SM sample to determine the sensitivity of the final measurement on these algorithmic parameters. No appreciable change is seen beyond $K^{\text{reco}}_{\text{max}} = L^{\text{reco}}_{\text{max}} = 2$, which are taken to be the default values for the deconvolution algorithm.

7.4 BACKGROUND SUBTRACTION

In the following two subsections it is described the determination of the background coefficients and the validation of background-enabled fits to a combined validation sample consisting of simulated signal and background.

7.4.1 Determination of background shape

The shape of the background is determined through an OSDE analysis of a hybrid sample consisting of background events from simulation samples, and selected data events from samples enriched in multijet events used to estimate multijet backgrounds as described in Section 6.4. Coefficients are determined through $K_{\max}^{\text{reco}} = L_{\max}^{\text{reco}} = 4$, although the standard working point as determined by the studies of Section 7.3.5 is $K_{\max}^{\text{reco}} = L_{\max}^{\text{reco}} = 2$. Note that the inclusion of higher order terms has no effect on the extracted value of lower order terms. This is similar to the results discussed in Section 7.3.5 for signal-only studies. The results of the OSDE fits with the reconstructed background are shown in Figures 7.6-7.7 for electrons and for muons respectively.

7.4.2 Background-enabled fits to a MC validation sample

The coefficients determined from the background fit, and their covariance, are saved and applied to the final fit to data or, alternately, to a validation sample consisting of signal plus background. This background-enabled fit requires only a simple modification to the deconvolution procedure introduced in Section 7.3.3: in Equation 7.35, the vector $\vec{\mathcal{A}}$, containing the real and imaginary parts of reconstructed coefficients, is modified by subtracting the background coefficients $\vec{\mathcal{B}}$ and rescaling:

$$\vec{\mathcal{A}} \to \frac{1}{f_{\text{s}}}\vec{\mathcal{A}} + \left(1 - \frac{1}{f_{\text{s}}}\right)\vec{\mathcal{B}}, \tag{7.39}$$

where f_{s} is the signal fraction. On the other hand, the covariance matrix $\mathbf{C}$ is modified to include the contribution from the background,

$$\mathbf{C} \to \left(\frac{1}{f_{\text{s}}}\right)^2 \mathbf{C} + \left(1 - \frac{1}{f_{\text{s}}}\right)^2 \vec{\mathbf{C}}_{\text{b}}, \tag{7.40}$$

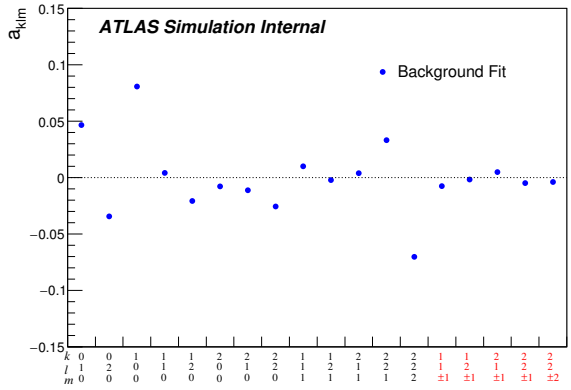

(a) Fitted angular coefficients

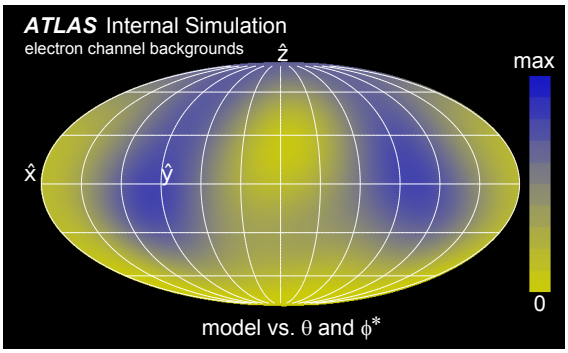

(b) $\cos\theta$ vs. ϕ^*

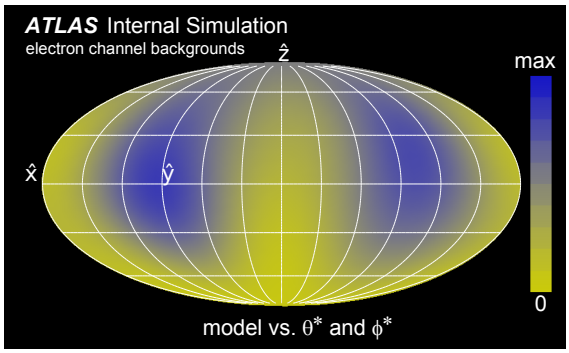

(c) $\cos\theta^*$ vs. ϕ^*

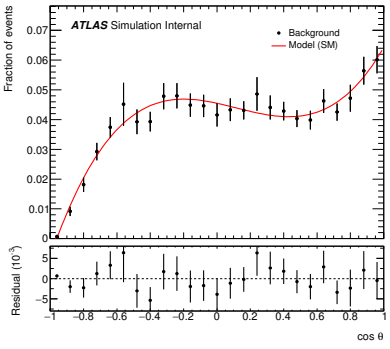

(d) $\cos\theta$

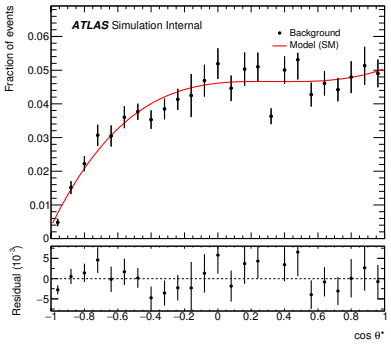

(e) $\cos\theta^*$

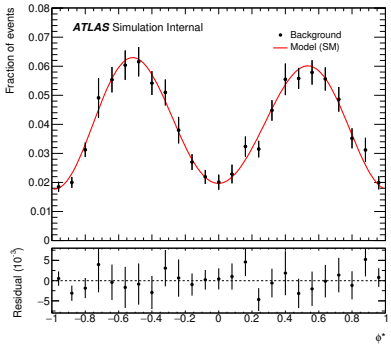

(f) ϕ^*

Figure 7.6: Results of an OSDE fit to reconstructed background in the electron channel as input simulation data. The extracted angular coefficient values from reconstructed background events are also shown as blue points with statistical uncertainties in (a).

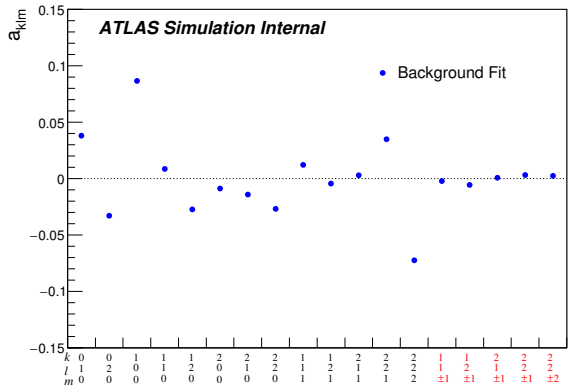

(a) Fitted angular coefficients

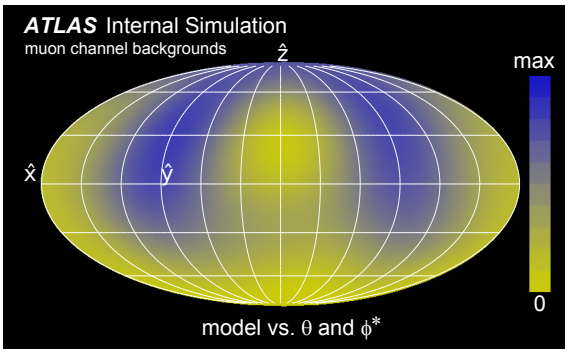

(b) $\cos\theta$ vs. ϕ^*

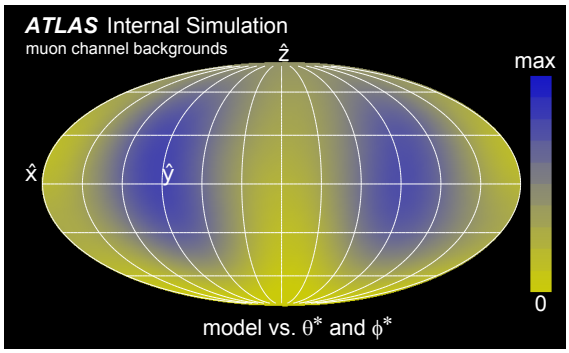

(c) $\cos\theta^*$ vs. ϕ^*

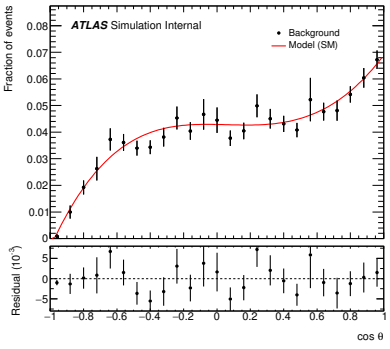

(d) $\cos\theta$

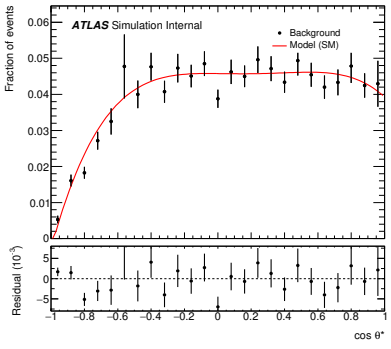

(e) $\cos\theta^*$

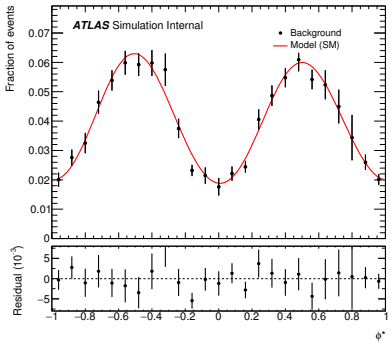

(f) ϕ^*

Figure 7.7: Results of an OSDE fit to reconstructed background in the muon channel as input simulation data. The extracted angular coefficient values from reconstructed background events are also shown as blue points with statistical uncertainties in (a).

where $\mathbf{C}_\mathrm{b}$ is the covariance matrix for the background coefficients alone. The second term in this expression represents a systematic uncertainty due to statistical uncertainties in the background estimate, and may be included or omitted according to whether one wishes to consider total uncertainty or just the statistical uncertainty.

Closure tests have been performed using a validation sample consisting of signal-contaminated (simulated or data-driven) event samples of background. The results are shown in Figures 7.8-7.9 using the simulated signal event sample produced with the PROTOS generator. Finally, fitted parameter values, deviations, and pulls are shown in Table 7.2. These tables demonstrate that the main generalised helicity fractions (i.e. f_1 and δ_-) and the polarisation P can be successfully extracted in the presence of background and detector effects. In addition, also the anomalous couplings $\mathrm{Re}\,[g_\mathrm{R}]$ and $\mathrm{Im}\,[g_\mathrm{R}]$ can be successfully extracted.

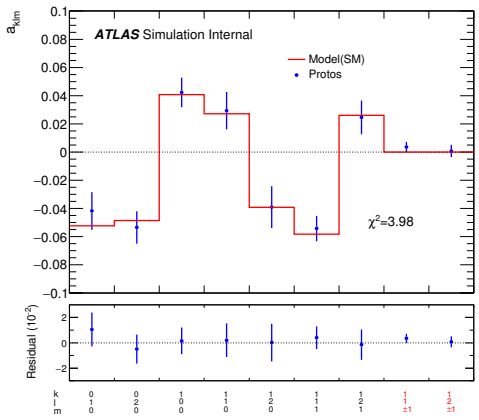

(a) Fitted angular coefficients

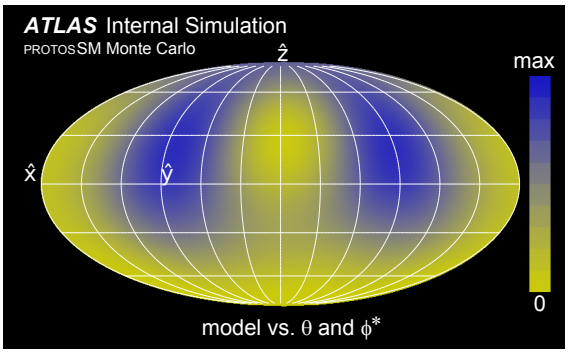

(b) $\cos\theta$ vs. ϕ^*

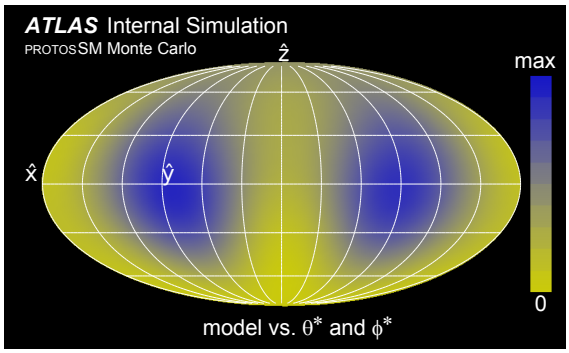

(c) $\cos\theta^*$ vs. ϕ^*

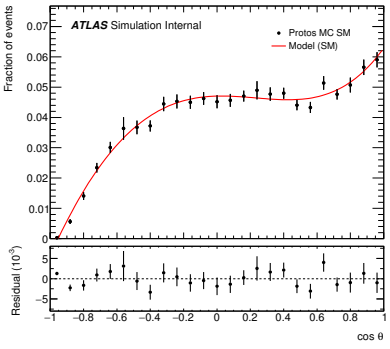

(d) $\cos\theta$

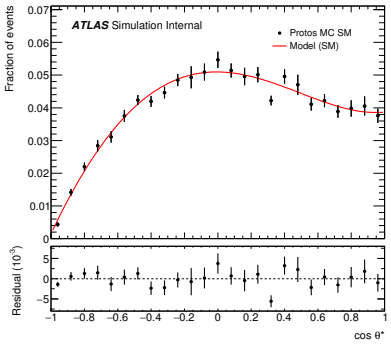

(e) $\cos\theta^*$

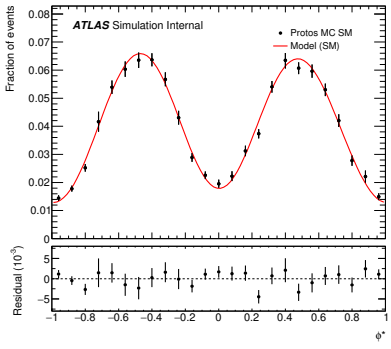

(f) ϕ^*

Figure 7.8: Results of an OSDE fit to reconstructed signal plus background events in the electron channel as input simulation data. For the signal, simulated events produced with the PROTOS generator are used.

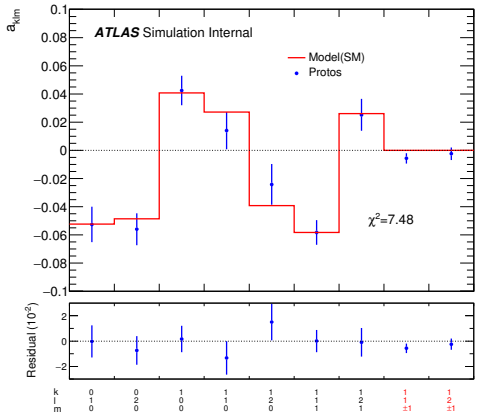

(a) Fitted angular coefficients

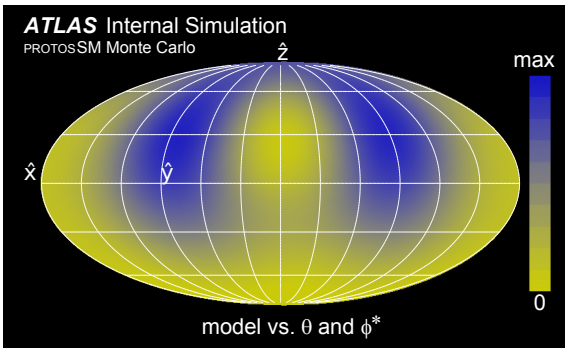

(b) $\cos\theta$ vs. ϕ^*

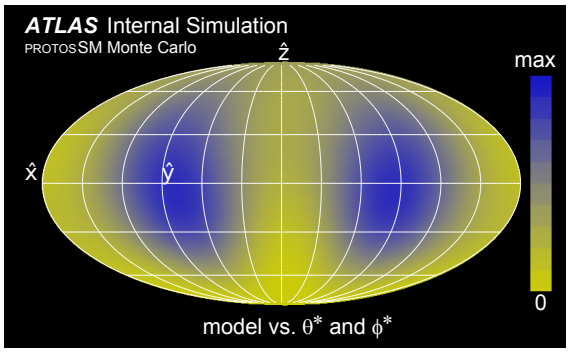

(c) $\cos\theta^*$ vs. ϕ^*

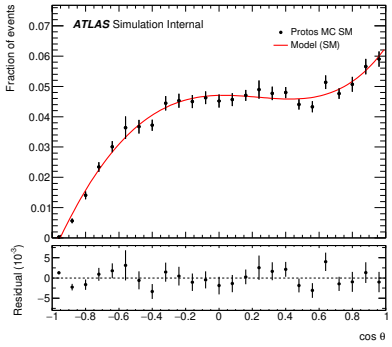

(d) $\cos\theta$

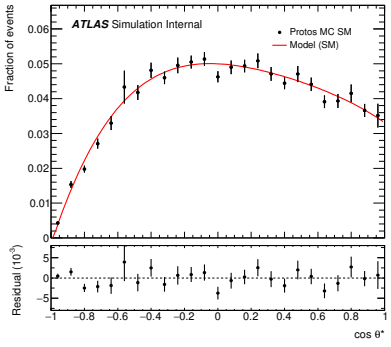

(e) $\cos\theta^*$

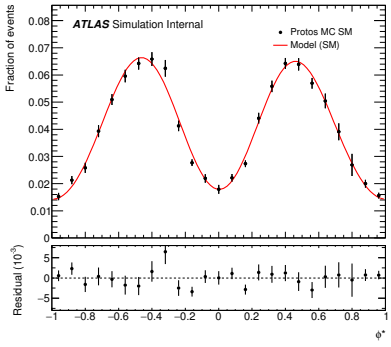

(f) ϕ^*

Figure 7.9: Results of an OSDE fit to reconstructed signal plus background events in the muon channel as input simulation data. For the signal, simulated events produced with the PROTOS generator are used. The extracted angular coefficient values from reconstructed events are also shown as blue points with statistical uncertainties in (a). Two-dimensional elliptical Mollweide-like projections of the extracted probability density are shown for three angles in (b) and (c). The lower plots show the residual of input data and the model in each bin.

Parameter	measured value	deviation	pull
f_1	0.284432 ± 0.0345329	−0.0191581	−0.554777
δ_-[rad]	-0.0114499 ± 0.0526142	−0.0114499	-0.217619
P	0.885102 ± 0.0627653	−0.0138977	−0.221423
Re $[g_{\mathrm{R}}]$	0.0259808 ± 0.04513	0.0259808	0.575687
Im $[g_{\mathrm{R}}]$	0.00638962 ± 0.0291451	0.00638962	0.219235

(a) Fit Results (PROTOS)

Table 7.2: Parameters extracted from a fit to PROTOS signal MC in the presence of background. The fit includes both electron and muon samples.

7.5 HIGH-STATISTICS TESTS OF THE BACKGROUND SUBTRACTION AND DECONVOLUTION PROCEDURES

In this section we describe the statistical properties of fits used to obtain the angular coefficients a_{kl}^m. We have developed a pseudoexperiment generator providing data in the same format as that provided to the fitter. We do not consider nonlinearities in the section; they are considered later, in Section 7.6.

Pseudoexperiment generation is based upon a simplified MC. SM values for all of the physics parameters $\vec{\alpha}$ are input to the MC, along with a migration matrix determined from ACERMC and background coefficients determined from an analysis of the combination of all background sources, both those that are estimated using MC and those that are data-driven. This is performed separately for electrons and for muons. This procedure allows us to generate multiple statistically independent pseudoexperiments which include detector effects. Fits to the pseudo-data are then performed using the migration matrix determined from ACERMC. The migration matrix is not varied in the analysis.

We performed 100k signal-only experiments with the expected sample size in 8 TeV data.

As with the data, a statistical combination of coefficients from muon and electron channels is performed, and then the result is fit to determine the parameters from the combined electron/muon sample.

Pull distributions are computed and shown in Figures 7.10-7.11 for the real and imaginary part of all of the deconvolved angular coefficients that have been extracted using OSDE.

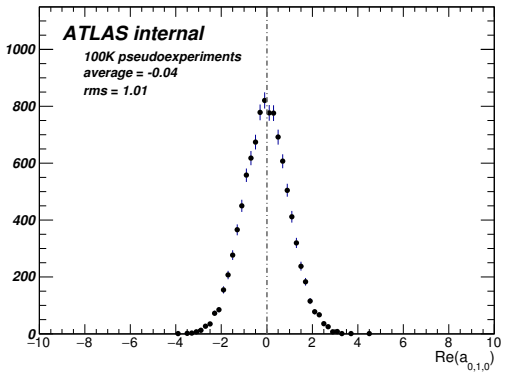

(a) Re $[a_{0,1,0}]$

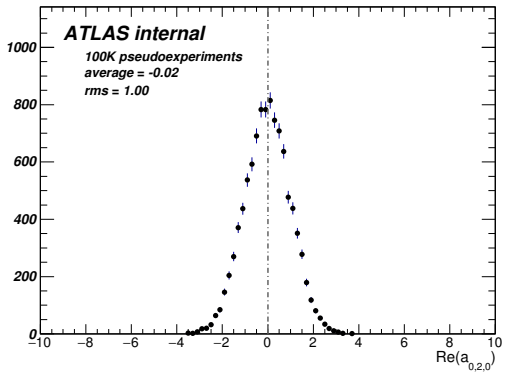

(b) Re $[a_{0,2,0}]$

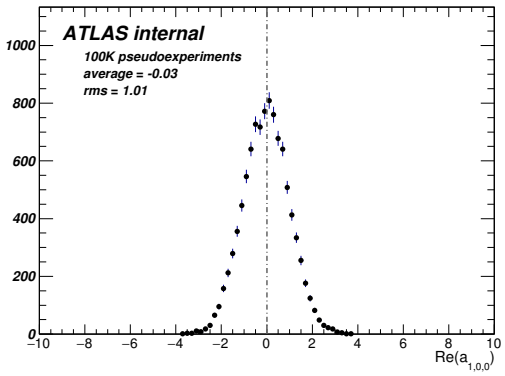

(c) Re $[a_{1,0,0}]$

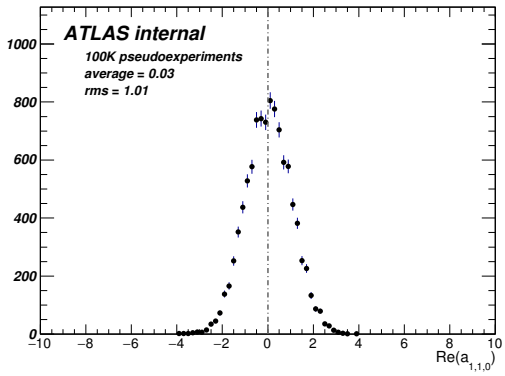

(d) Re $[a_{1,1,0}]$

Figure 7.10: Results of a fit to 100k pseudoexperiments. The plot shows the pull distributions of the first four of nine angular coefficient parameters.

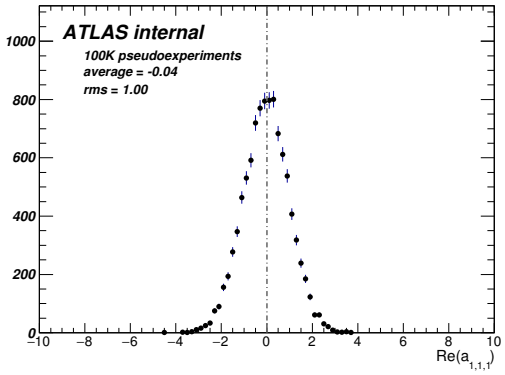

(a) $\mathrm{Re}\,[a_{1,1,1}]$

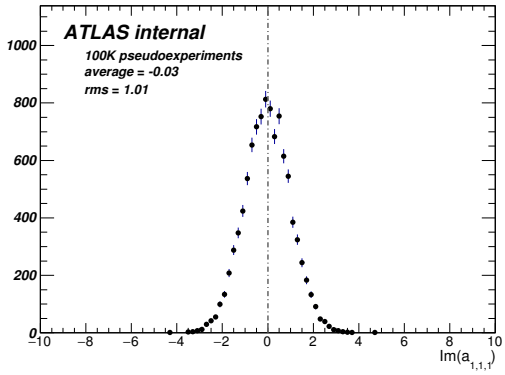

(b) $\mathrm{Im}\,[a_{1,1,1}]$

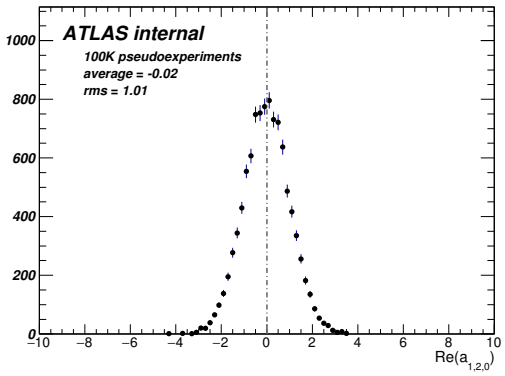

(c) $\mathrm{Re}\,[a_{1,2,0}]$

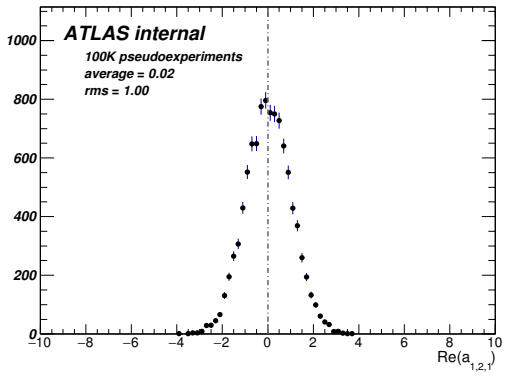

(d) $\mathrm{Re}\,[a_{1,2,1}]$

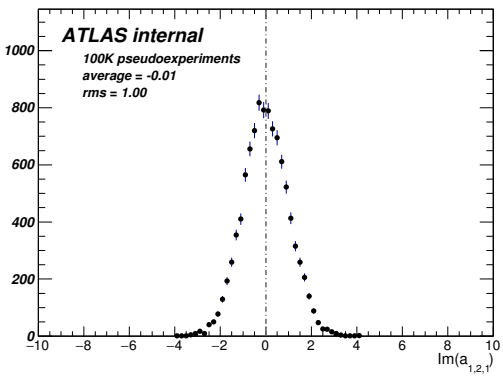

(e) $\mathrm{Im}\,[a_{1,2,1}]$

Figure 7.11: Results of a fit to 100k pseudoexperiments. The plot shows the pull distributions of the nine angular coefficient parameters.

7.6 NONLINEARITIES AND THEIR ELIMINATION

The triple differential decay rate is a projection of a higher dimensional PDF governing the production and decay of single top quarks in the t-channel. Because of the integration over production kinematics, the migration matrix depends on the physics parameters.

7.6.1 Variation of the migration matrix

For fits to validation samples at the reconstruction level, the following terminology is used. The "external" migration matrix is always the migration matrix coming from the t-channel SM event sample. The "internal" migration matrix is taken from the validation event sample itself. For the SM point, "internal" and "external" migration matrices are the same. Distributions of the linearity under each set of conditions is shown in Figure 7.12, together with distributions at the generator level where detector effects are absent. Because no analytic form for the true polarisation exists Figure 7.13 shows the extracted polarisation values vs. generator level polarisation, using the internal migration matrix and the other using the external migration matrix. For samples in which $V_{\mathrm{R}} = g_{\mathrm{L}} = 0$, the constraint $f_0^+ = f_1^+ = 0$ in the fit to polarisation.

At the generator level there are no sizeable nonlinearities; detector effects introduce nonlinearities on the order of up to $\sim 15\%$ when the external migration matrix is applied, but they disappear when the internal migration matrix is used instead. We conclude that the effect arises, as expected, because the migration matrix varies with the physics parameters. By following the variation in a final fit we can hope to eliminate it.

We proceed as follows. The final fit is obtained by minimizing the value of χ^2 (Equation 7.18). The value of the physics parameters change at each evaluation point; so does the migration matrix and so, therefore do the deconvolved coefficients. Conceptually, Equation 7.35 can be thought of as

$$\vec{a} = \mathbf{G}^{-1} \cdot \vec{\mathcal{A}} \tag{7.41}$$

and we now consider the possibility that $\mathbf{G}$ depends upon the physics parameters, i.e:

$$\mathbf{G}^{-1} = \mathbf{G}^{-1}(\vec{\alpha}) \tag{7.42}$$

and in that case Equation 7.35 (conceptually, Equation 7.41) is no longer the correct solution; indeed no closed-form solution at all can be found to the minimisation problem.

The practical scheme we have adopted to implement the required variation is reweighting an existing sample of SM PROTOS MC. The event-per-event reweighting factor z_i for event i in the training sample is defined as a ratio of event-per-event matrix elements $\mathcal{M}$:

$$z_i \equiv \frac{|\mathcal{M}(p_{Ai}, p_{Bi} p_{Ci}, p_{Di} | V_L', V_R', g_L', g_R')|^2}{|\mathcal{M}(p_{Ai}, p_{Bi}, p_{Ci}, p_{Di} | V_L, V_R, g_L, g_R)|^2}$$

where p_{Ai} and p_{Bi} (p_{Ci} and p_{Di}) are the four-momentum of the incoming (outgoing) partons in the hard scattering process of the i^{th} event; the primed coupling constants denote the varied parameters, and the unprimed coupling constants represent unvaried parameters, corresponding to those used during the original run of simulation. The procedure uses the matrix element calculation implemented within PROTOS. These on-the-fly computations allow a training sample produced with any value of the couplings (e.g. SM) to be transformed to another sample with different couplings; the transformation can be executed in about one second on a single node of the Pittsburgh Tier 3 system. This is fast enough to be completed at each time that χ^2 is evaluated. Because now the deconvolution χ^2 (Equation 7.36) depends upon the physics parameters, it is included in the likelihood together with the χ^2 for the parameterized physics model to match the deconvolved coefficients, which is described by Equation 7.18, such that the total χ^2 to be minimized is the sum of the two terms.

In Figure 7.14 shows the non-SM samples compared to the SM sample produced with the PROTOS generator, both before and after the reweighting procedure. The anomalous coupling configuration of the latter samples are such that the so-called normal forward-backward asymmetry [139, 140] is $A_{\mathrm{FB}}^{\mathrm{N}} = \pm 0.1$(additionally, Appendix A.4 shows the derivation of this asymmetry in terms of this analysis). One can see significant differences in all plots before reweighting, and excellent agreement after.

Thousands of pseudoexperiments are required to understand the statistical properties of the estimates, to produce pull distributions, etc. The reweighting procedure, even though it is highly parallel, cannot generate such a large number of experiments in reasonable time.

Instead, the migration matrix is computed on a four-dimensional grid in f_1, f_1^+, f_0^+, and δ_- and use Lagrange interpolation between the grid points. Two points are used in

f_1^+, f_0^+, while four are used in f_1 and δ_-. The range of interpolation is $f_1 \in [0.24, 0.36]$, $f_1^+ \in [0.0, 0.25]$, $f_0^+ \in [0.0, 0.25]$, $\delta_- \in [-0.5, 0.5]$.

In Figure 7.15 one can see that the linearity has been restored by the adopted reweighting procedure, for almost all of the points on the graph. The exception is a point generated with a large values of $f_1 = 0.5$, which is well outside of the interpolation window. The point is show in red in Figure 7.15 and is omitted from other plots. This shows that the linearity corrections *and* interpolation methods work well within the chosen interpolation window and even outside of the window. Nonlinearities are again apparent at values of $f_1 \sim 0.5$. A small scatter in points reflects the statistical errors in the samples, as well as statistical fluctuation in the reweightable sample used to obtain the migration matrix. We conclude that no significant nonlinearity is present in the algorithm in a broad window around the SM point in parameters space. The nonlinearity correction is then applied in our final fits, in addition to reweighting of the $t\bar{t}$ background, which is the subject of the next section.

7.6.1.1 About the polarisation Figure 7.15 shows the best fit to a linear relationship between generated and extracted polarisation. It is investigated whether deviation from the relationship $y = x + 0$ is significant. To decorrelate the slope and intercept parameters, the relationship is re-parameterised as:

$$(y - 0.9) = m(x - 0.9) + b \tag{7.43}$$

and fit for the slope m and the intercept b. The fitted values are $m = 0.933 \pm 0.079$ and $b = 0.012 \pm 0.009$. While a collective offset appears possibly significant, one notes that all of the input points are subject to a common systematic uncertainty, due to the statistical uncertainty from the migration matrix. This results in a common offset whose magnitude is estimated to be 0.015, equal to the statistical uncertainty on the polarisation of the SM point. Adding this uncertainty (on the slope) in quadrature with the full covariance matrix of from the linear fit, it is obtained the 68% C.L. uncertainty ellipse as shown in Figure 7.16, compared there with the parameters expected for perfect linearity. It can be concluded that the nonlinearity in Figure 7.15 is not statistically significant.

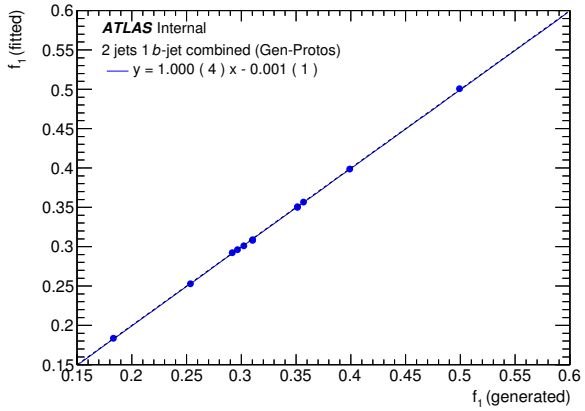

(a) Fitted f_1 vs. input f_1 (gen. level)

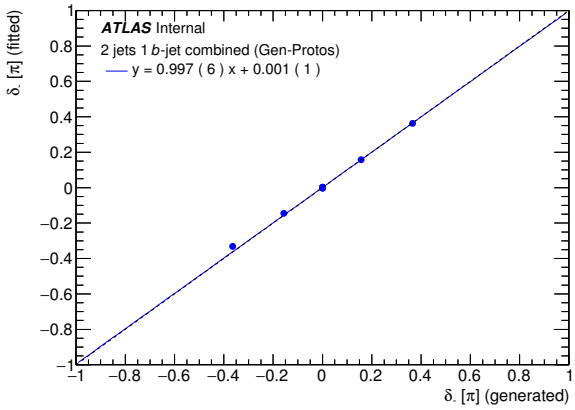

(b) Fitted δ_- vs. input δ_- (gen. level)

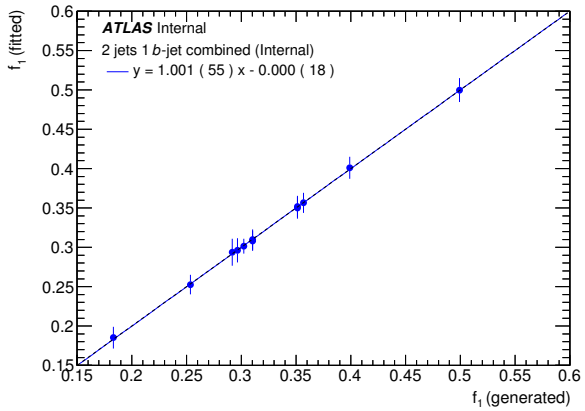

(c) Fitted f_1 vs. input f_1 (internal)

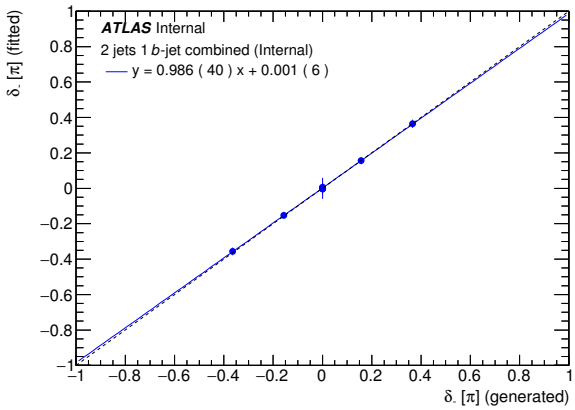

(d) Fitted δ_- vs. input δ_- (internal)

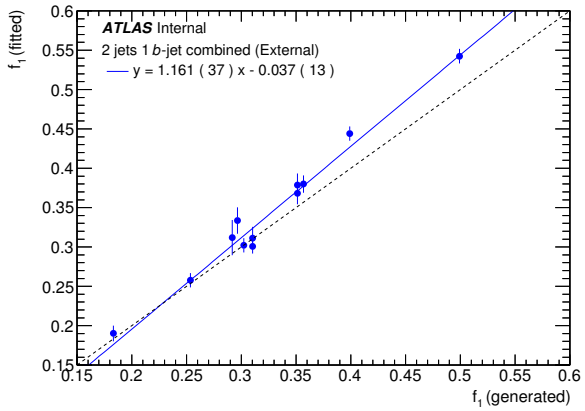

(e) Fitted f_1 vs. input f_1 (external)

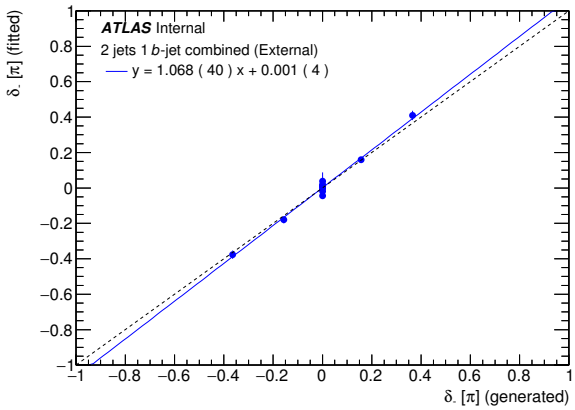

(f) Fitted δ_- vs. input δ_- (external)

Figure 7.12: Fitted values of selected parameters vs. input values to the PROTOS generator. Figures (a) and (b) show distributions made at the generator level. Figures (c) and (d) show distribution made after deconvolution with the SM internal migration matrix. Figures (e) and (f) show distributions made with external migration matrix.

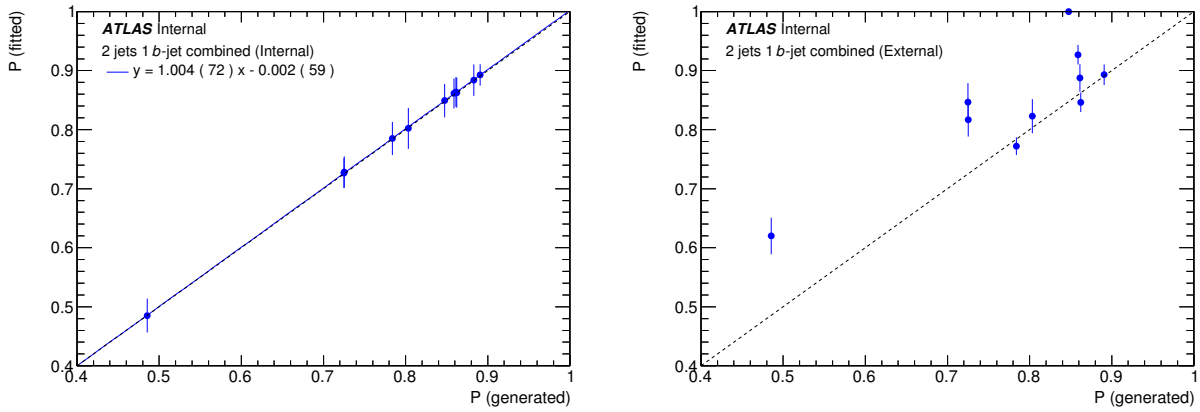

(a) Fitted P vs. input P (internal)

(b) Fitted P vs. input P (external)

Figure 7.13: Fitted values of the polarisation P vs. P determined from PROTOS at generator level. Figure (a) shows distribution made after deconvolution with the SM internal migration matrix. Figure (b) shows distribution made with external migration matrix.

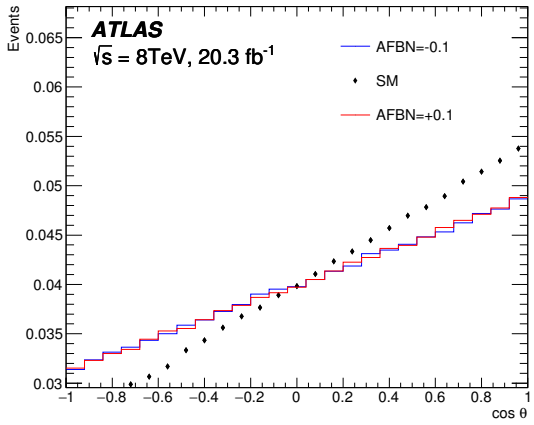

(a) $\cos\theta$

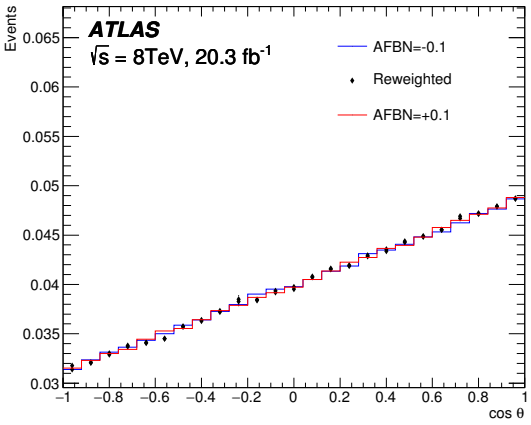

(b) $\cos\theta$ reweighted

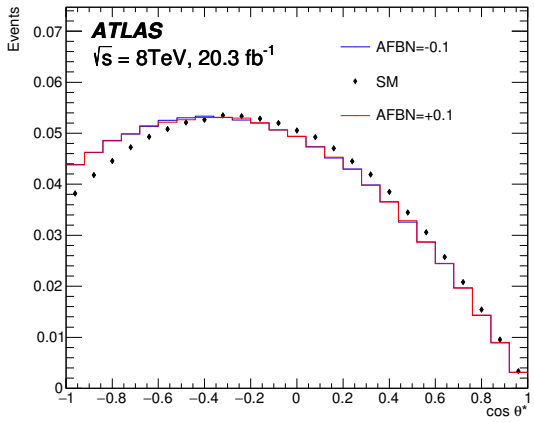

(c) $\cos\theta^*$

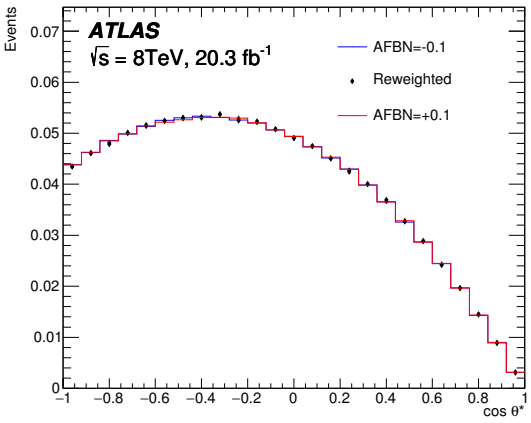

(d) $\cos\theta^*$ reweighted

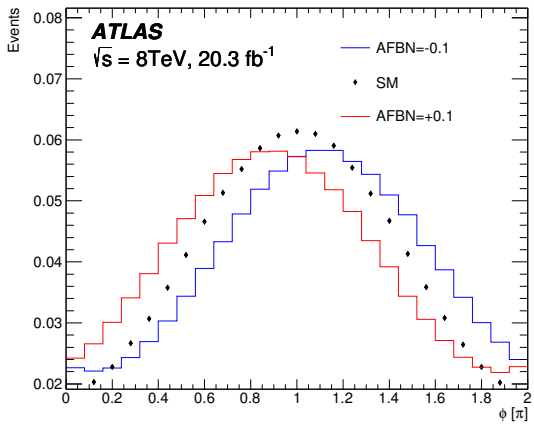

(e) ϕ^*

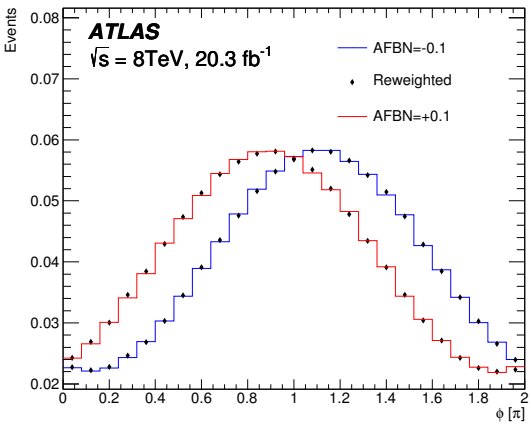

(f) ϕ^* reweighted

Figure 7.14: Demonstration of the reweighting procedure applied to adjust the migration matrix to varied physics parameters in the $\cos\theta$, $\cos\theta^*$ and ϕ^* distributions. Figures show angular distributions of MC event samples generated with $A_{\mathrm{FB}}^{\mathrm{N}} = \pm 0.1$, shown as blue or red lines, compared with SM (left) or *reweighted* SM (right) MC event samples, shown as the black points.

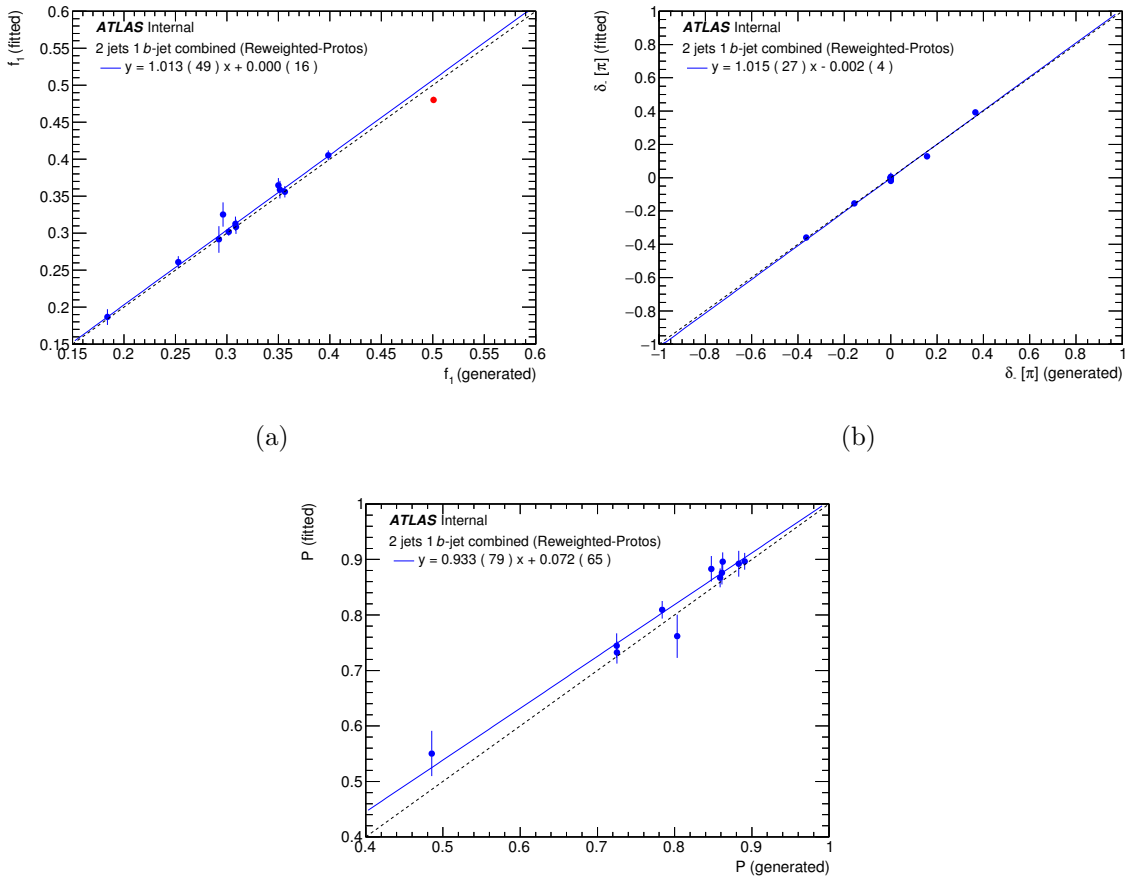

(a) (b)

(c)

Figure 7.15: Fitted values of selected parameters vs. values input to the PROTOS generator, after the application of the reweighting procedure.

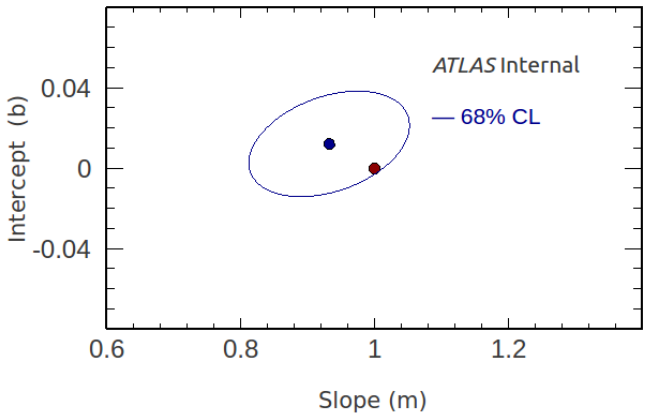

Figure 7.16: Details of a fit to reconstructed polarisation P as a function of the input P value. The measured values are consistent with a zero nonlinearity.

7.6.2 Variation of the $t\bar{t}$ background shape

The $t\bar{t}$ production is a significant source of background contamination in this analysis as shown in Section 6. Angular distributions of this background depends upon the value of the anomalous couplings. Therefore, not only the signal but also the background model needs to be adjusted during a fit to the data.

The way in which this is accomplished is similar to the procedures, discussed in the previous subsection, for eliminating nonlinearities. An event-per-event weight is calculated for simulated $t\bar{t}$ events based upon a ratio of matrix elements. The denominator of this ratio is the matrix element computed using the same SM parameter values used during the original generation of $t\bar{t}$ events. The numerator is the matrix element re-computed with the parameter values at which the χ^2 is evaluated. During the fit, the ratio is then used to reweight the $t\bar{t}$ baseline sample at each evaluation of χ^2.

However, only the LO Protos event generator is capable for the moment of generating matrix elements with different configuration of anomalous couplings, though the NLO Powheg-Box generator (used as baseline) gives the best description of the $t\bar{t}$ background. Thus, the two generators are combined in the following way in order obtain the advantages of each. The background coefficients ($\vec{\mathcal{A}}$ in Equation 7.39) are obtained from events generated with Powheg-Box while their variation only is obtained from events produced with Protos. The reweighting factor is computed using the Protos matrix element calculation.

In order to have a feeling about how important is the dependance of the anomalous couplings in the $t\bar{t}$ background, Figure 7.17 shows the effect of varying different anomalous couplings[3] on the shape of the $t\bar{t}$ process prediction. In most cases the size of the effect is small; only a variation in f_0^+ and f_1^+ (a rather large one is shown in the figure) has a significant effect on the distributions. Additionally, Figure 7.18 shows how the angular coefficients vary with different anomalous couplings for the electron channel. As in the previous case, significant effects are just seen for f_0^+ and f_1^+.

[3]Different values of f_1, f_1^+, f_0^+ or δ_- is achieved by considering different values of anomalous couplings.

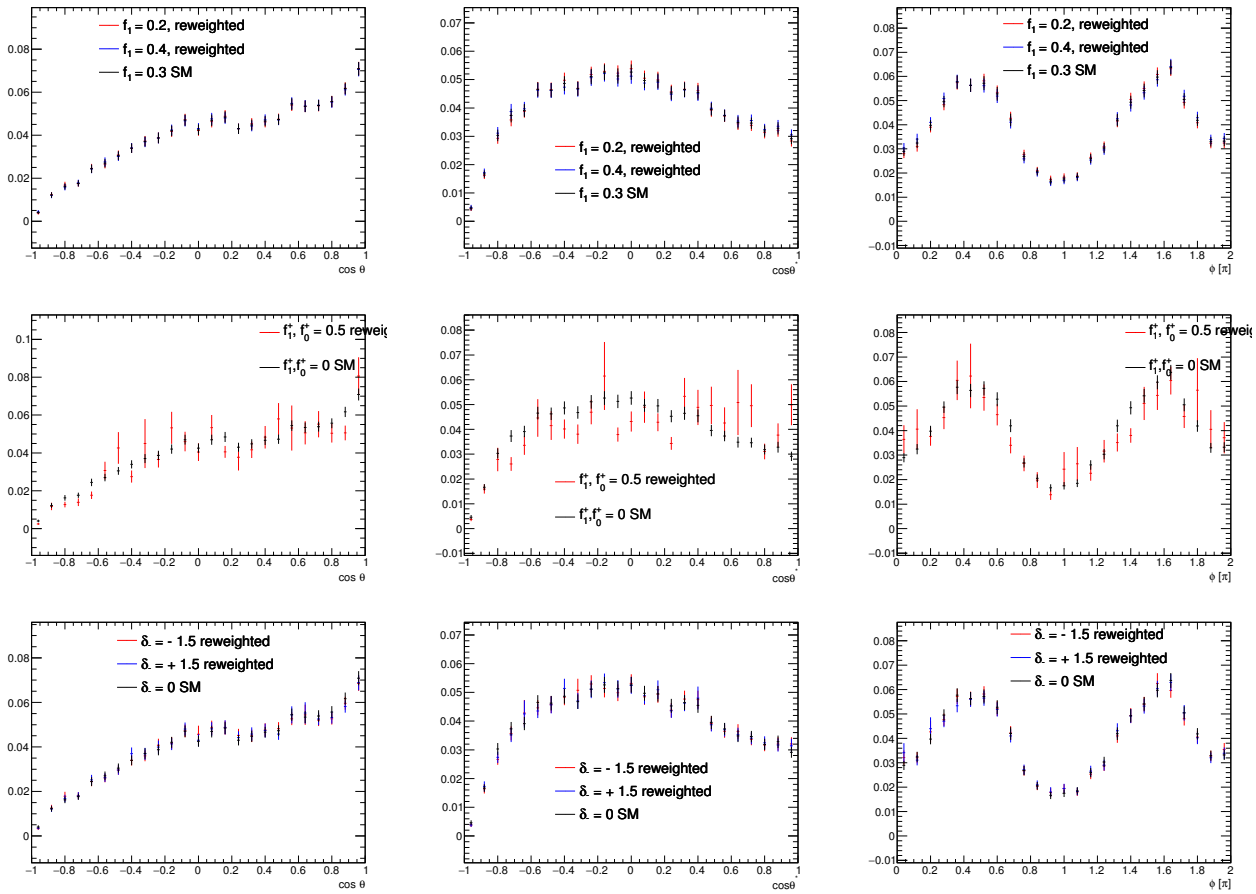

Figure 7.17: These distributions show the effect of anomalous couplings on the shape of the $t\bar{t}$ background. The PROTOS generator is used to obtain all of the plots. In each row, distributions with SM parameters are compared, with the same distributions reweighted to varied couplings. Histograms are normalised to the same area. The top row shows the effect of a change in the parameter f_1, the middle row shows the effect of a simultaneous change in parameters f_0^+ and f_1^+, and the bottom row shows the effect of a change in δ_-.

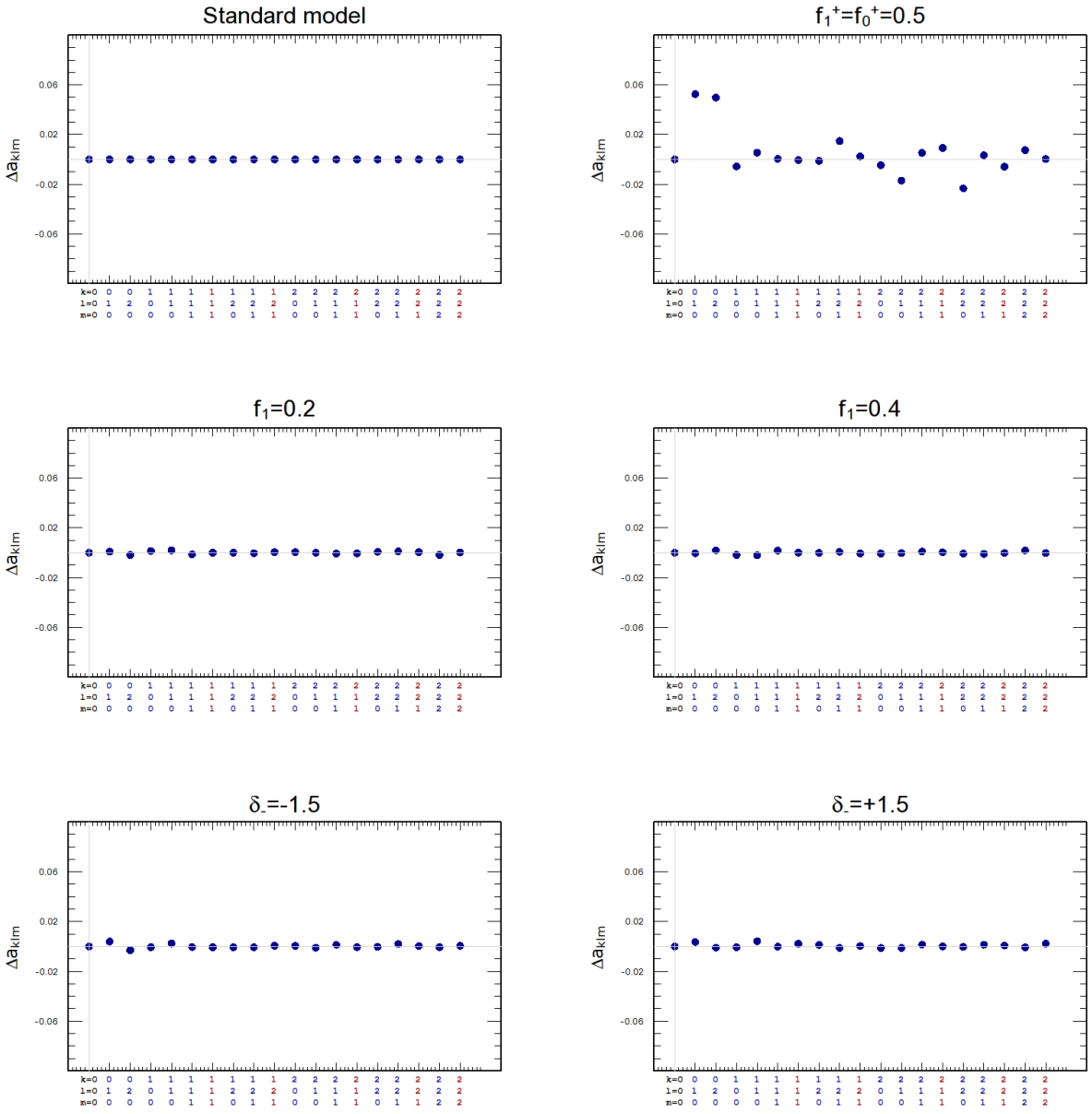

Figure 7.18: These distributions show the effect of anomalous couplings on the shape of the $t\bar{t}$ background coefficients. Shown in the slewing of the angular coefficients with variation in the different parameters. These plots were obtained using the electron channel.

7.7 STATISTICAL PROPERTIES OF THE FINAL ESTIMATOR

7.7.1 Pull distributions

Pull distributions are a standard way of checking the accuracy of a fit procedure and validating the errors on fitted quantities. In our analysis, as one can see in the figures of the next section, likelihood profiles are highly non-Gaussian; in the best cases they exhibit obvious asymmetries; and in the worst cases they reach their maxima at the boundary of the physical parameter space. Among the helicity fraction parameters, only f_1 and δ_- are eligible for point estimation, and even these require asymmetric error bars. We require a practical scheme to evaluate the pull of a single pseudoexperiment when the likelihood is non-Gaussian.

The following definition is based upon likelihood ratios (as are our final confidence intervals). For each parameter under study, we minimise the likelihood function $\mathcal{L}$ twice; first, over all parameters; second, over all parameters *except* the parameter μ under study, which is constrained to the "true" (input) value μ_{input} of the pseudoexperiment. The difference $-2\Delta\log(\mathcal{L}) \equiv -2\log(\mathcal{L}(\mu_{\text{input}})) + 2\log(\mathcal{L}(\mu_{\text{best}}))$ is a quantity of interest, where μ_{best} is the optimal value of μ, i.e., the one which minimises $-2\ln(\mathcal{L}(\mu))$. In the case of Gaussian likelihood functions with ideal coverage, this quantity takes a value less than 1.0 in 68.3 % of the pseudoexperiments, and less than 4.0 in 94% of the pseudoexperiments, and in general is distributed as a χ^2 distribution with one degree of freedom. Thus, for a single pseudoexperiment, the standard distance between μ_{best} and μ_{input} is $[-2\Delta\log(\mathcal{L})]^{1/2}$. This is almost what we want, except that it is an unsigned quantity. We therefore give it a positive sign if the optimal value is greater than the input value, and negative otherwise. This definition is useful only in cases where input values are sufficiently far from the boundaries of the physical parameter space, i.e. for f_1 and δ_-, but not for f_1^+, f_0^+, or P. In these cases we can still check coverage properties of likelihood profiles from the distribution of $-2\Delta\log(\mathcal{L})$.

The procedure illustrated in the previous section, including nonlinearity corrections, is repeated on an ensemble of independent pseudoexperiments. The pseudoexperiments are generated for different points in the space of physics parameters, consisting of 25 equally

spaced points on the interval [-0.5,0.5], for δ_- and also 25 equally spaced points the interval [0.1,0.5] for f_1. The likelihood function includes both systematic and statistical errors. Distributions of $[-2\Delta \log(\mathcal{L})]^{1/2}$ are shown in Figure 7.19. A clear bias can be seen in the distributions for f_1, and small distortions are visible in the δ_- distribution. This indicates a need for somewhat heavier statistical techniques.

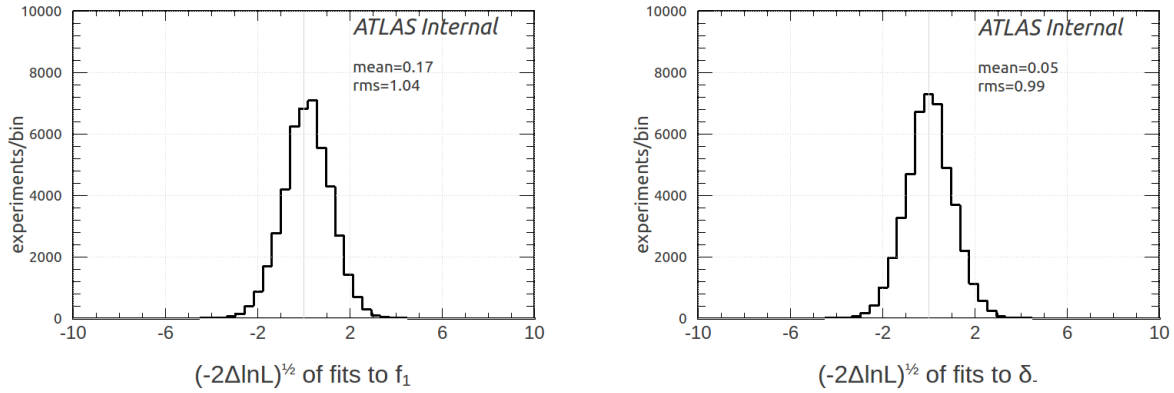

Figure 7.19: Pull distributions for f_1 and δ_- from pseudoexperiments. The plot includes pseudoexperiments generated over a wide range of input values, from -0.5 to 0.5 for δ_-, and from 0.1 to 0.5 for f_1. A clear bias can be seen in a point estimate of f_1, while δ_- has an apparently reasonable shape.

Now, we look at data from the pseudoexperiments in another way, plotting $-2\Delta \log(\mathcal{L})$ rather than its signed square root. This is shown in Figure 7.20, together with the χ^2 distribution for one degree of freedom (red curve), which is the ideal case. In these plots we can see that there is a near perfect agreement between the pseudoexperiments and the ideal curve, not only for δ_- and f_1, but for the other physics parameters as well. Our next step will be to divide the experiments up by the input value of the parameter under study.

To set a Feldman–Cousins confidence interval [141] on a parameter we use the likelihood ratio $-2\Delta \log(\mathcal{L})$ as a test statistic, and determine cutoff values for 68.3% and 95.4% confidence levels. These cutoff values, which in the Gaussian limit are 1.0 and 4.0, are shown in Figure 7.21 and Figure 7.22, for different input value of each parameter. Shown in black on these plots are the likelihood profiles from the data. The points at which these black curves

intersect the red (blue) dotted lines define the 68.3% (95.4%) confidence intervals. These intersection points show small only differences from the ideal case. These plots are used to determine final confidence intervals on parameters of interest. The data from the f_1 scan is also used for coverage adjustment on $\mathrm{Re}\,[g_\mathrm{R}/V_\mathrm{L}]$, while data from the δ_- scan is also used for coverage adjustment on $\mathrm{Im}\,[g_\mathrm{R}/V_\mathrm{L}]$.

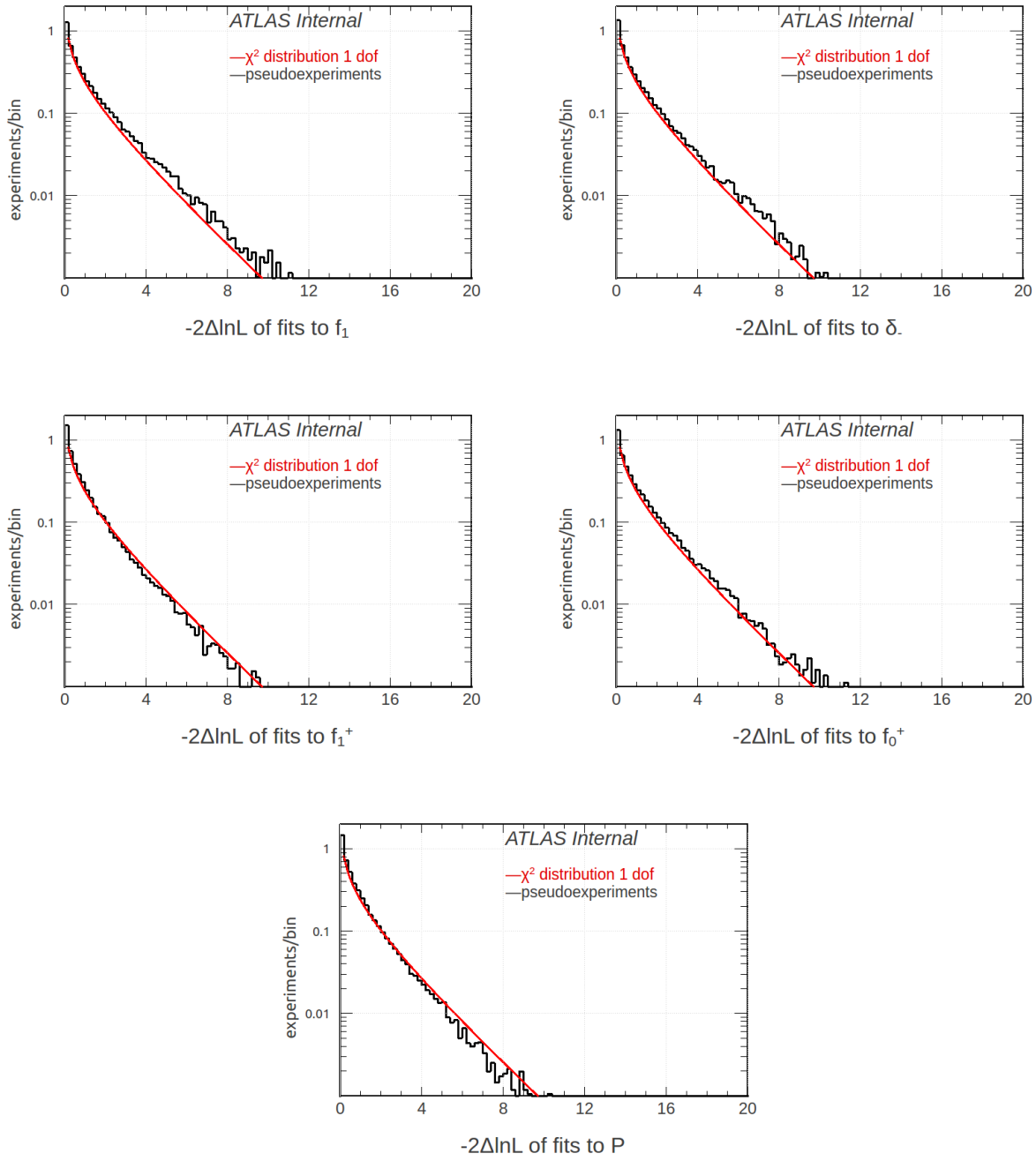

Figure 7.20: $-2\Delta \log(\mathcal{L})$ distributions for helicity fractions and phases from pseudoexperiments. The plot includes pseudoexperiments generated over a wide range of input values, from -0.5 to 0.5 for δ_-, and from 0.1 to 0.5 for f_1.

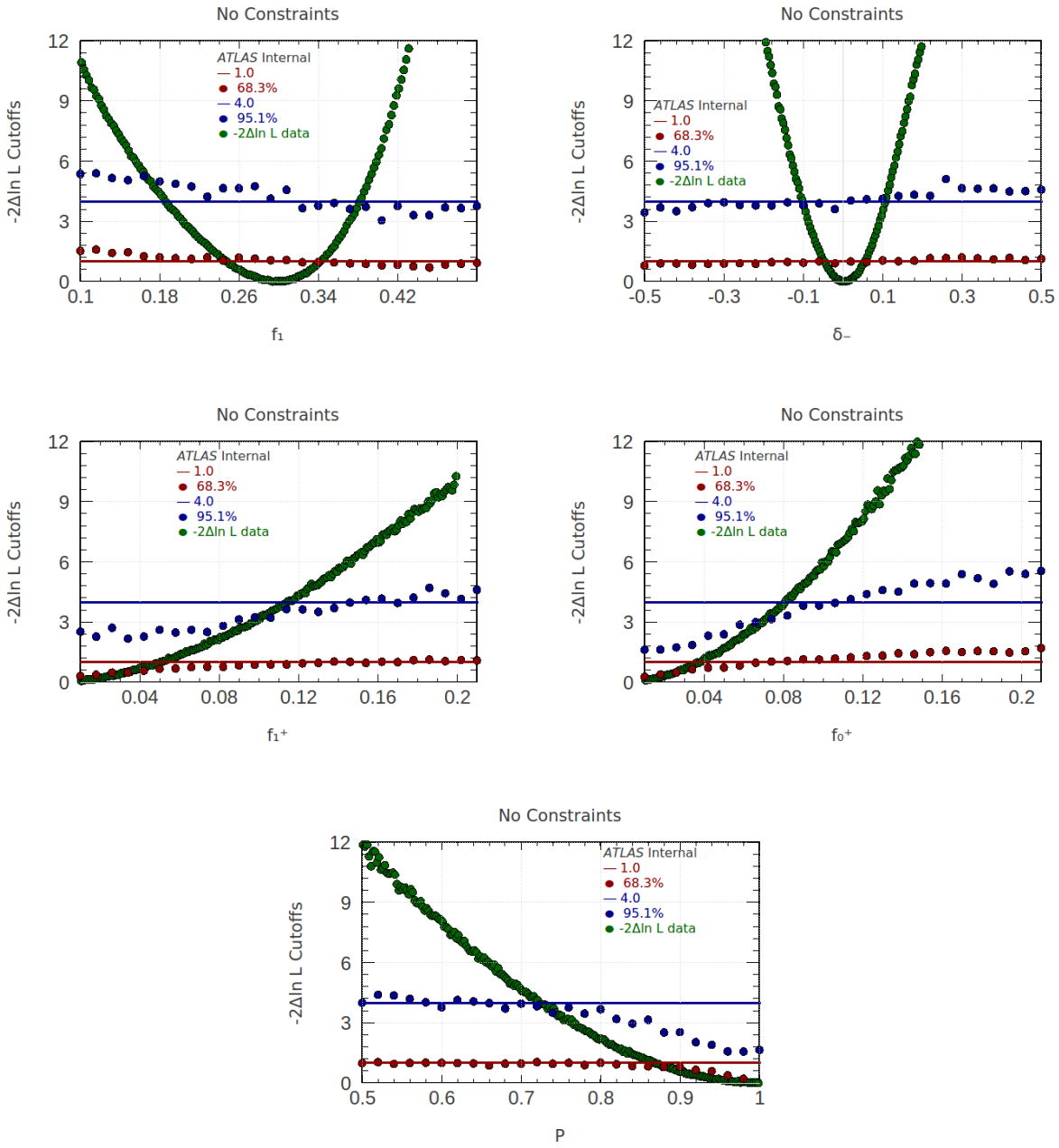

Figure 7.21: Cutoff values in $-2\Delta \log(\mathcal{L})$ for helicity fractions and phases obtained from pseudoexperiments in a scan over input values.

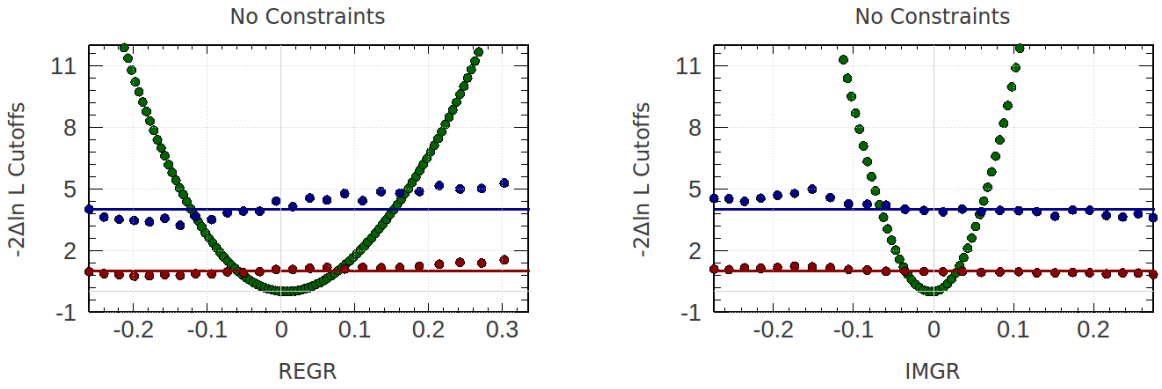

Figure 7.22: Cutoff values in $-2\Delta \log(\mathcal{L})$ for anomalous couplings obtained from pseudoexperiments in a scan over input values.

7.8 SOURCES OF SYSTEMATIC UNCERTAINTY

Systematic uncertainties are evaluated in the angular coefficients $a_{k,l,m}$ and then propagated to the physics parameter or anomalous coupling spaces.

Unless addressed specifically, the efficiency and resolution models (i.e. migration matrix) in t-channel events used to estimate the impact on the deconvolved measurements of the various sources of uncertainties are those extracted from the nominal SM-like simulation sample produced with the PROTOS generator. The background models are determined from MC simulation samples with either alternative generators or parameters varied by their uncertainties. A likelihood is constructed from the resulting model, using events generated with nominal values of the varied parameters. The difference between the central values estimated at the nominal value of a parameter and at the value varied by its uncertainty, or half the difference between central values estimated with the parameter varied up and down by its uncertainty, is used to construct a covariance matrix for each source of systematic uncertainty. The total covariance matrix for the systematic uncertainties and its correlation matrix are found from the sum of the covariance matrices determined for individual uncertainties.

When estimating the impact of the various sources of uncertainties, the variations are propagated in a correlated way to the rates and to the shapes. The variations due to the systematic uncertainties are also propagated in a correlated way to the signal region and to the two control regions used to constrain the top-quark and W+jets background contributions. For the statistical uncertainties, the variations in the signal and control regions are considered as independent. A set of overall scale factors associated with the top-quark and W+jets backgrounds and with the signal events are extracted for each source of systematic or statistical variation, through the procedure explained in Section 6.4. The backgrounds are then re-normalised with the extracted overall scale factors before being subtracted to the observed data. Then the systematic and statistical uncertainties on the fitted normalisation factors are propagated to the measurement.

The sources of systematic uncertainties are split into the following categories:

Detector modelling: the systematic uncertainties on the reconstruction and energy

calibration of electrons, muons and jets are propagated in the analysis through variations in the modelling of the detector response. Uncertainties related to leptons come from trigger, identification and isolation efficiencies, as well as from the energy scale and resolution [97, 98]. For the jets, the main source of uncertainty is the energy scale, evaluated using a combination of in situ techniques [142]. Other jet-related uncertainty sources are the modelling of the energy resolution [143] and reconstruction efficiency [142], and the modelling of the tagging efficiencies of b-quark jets, c-quark jets and light-quark jets [104, 144]. The uncertainties from the energy scale and resolution corrections applied to leptons and jets are propagated to the computation of the E_T^{miss}. The scale and resolution uncertainties due to soft jets and to contributions of calorimeter energy deposits not associated with any reconstructed objects are also considered independently. For all detector modelling uncertainties, positive and negative uncertainties are estimated separately from the corresponding shifts.

Background normalisation: the uncertainties on the normalisation of the top-quark and W+jets background processes are determined from the maximum-likelihood fit. For the Z+jets and diboson processes a normalisation uncertainty of 34%, which is the result of adding in quadrature the theory uncertainty of 5% as mentioned in Section 6.4 and 24% per additional jet, accordingly to the Berends–Giele scaling [145], is applied to the predictions. For the data-driven normalisation of the multijet background the uncertainty of 70% estimated from the comparison of the matrix method estimates with those given by the jet–electron and anti–muon methods is used. The uncertainty on the integrated luminosity is 1.9% [105] and it is propagated through the normalisation of the simulated backgrounds.

Signal and background modelling: Systematic uncertainties associated with the signal and background modelling are estimated by comparing different generators and by varying parameters in the event generation. The uncertainty on the predicted efficiency and resolution models for the t-channel single top-quark process, used to deconvolve reconstructed quantities (from POWHEG-BOX interfaced to PYTHIA), is estimated by comparing the nominal PROTOS with ACERMC, both interfaced to PYTHIA. The uncertainty on the ME calculation in the simulation of the t-channel process is estimated in two ways; by comparing PROTOS with POWHEG-BOX, both interfaced to PYTHIA, to account for the mis-modelling of a LO generator to the NLO process and by by comparing POWHEG-BOX

with MG5_aMC@NLO, both interfaced to Herwig, to account for different NLO generators. For the $t\bar{t}$ process, Powheg-Box is compared with MC@NLO, both also interfaced to Herwig. The uncertainty on the PS and hadronisation is evaluated by comparing Powheg-Box interfaced with Pythia and Herwig for both, the t-channel and $t\bar{t}$ processes. The uncertainty on the amount of radiation is evaluated for the t-channel and $t\bar{t}$ processes by comparing the Powheg-Box samples generated with varied hard-process interfaced to Pythia with different hadronisation scales or sets of tuned parameters. In this case, the uncertainty is defined by the maximal shift with respect the nominal measurement.

The impact of the flavour composition on the modelling of the W+jets distributions is determined by propagating an uncertainty of 50% on the ratio between $W+bb$ and $W+cc$ contributions. As reported in Section 6, W+light jets events give a small contribution in the signal region and no associated modelling uncertainty is taken into account. An additional shape modelling uncertainty is considered for the W+jets contribution by applying an event-by-event shape reweighting procedure. This reweighting is derived from the matching to the data (after subtraction of all processes other than W+jets) in the distribution of the p_T of the W boson in the W+jets validation region.

Systematic uncertainties related to the PDFs are evaluated for all processes, except for the multijet contribution. The uncertainty is estimated, following a procedure based on the PDF4LHC prescription [146], by calculating a multidimensional envelope of the uncertainties at 68% C.L. of the CT10, MSTW2008NLO and NNPDF2.3 [147] sets.

Finally, two additional uncertainties are also considered in this analysis. The uncertainty due to possible polarisation nonlinearities and their elimination through event reweighting is estimated by considering the deviation from the ideal polarisation linearity to a true polarisation of 100% or as low as 80%. Furthermore, an uncertainty is derived to account for top-quark finite-width effects, arising from the combination of a Breit–Wigner line-shape of the generated top-quark mass and acceptance cut.

Limited size of simulation samples: The uncertainty due to the limited size of the MC samples arise from the statistics of background MC on one hand, and from the statistics of signal MC on the other. Statistical uncertainty due to simulated background statistics enters through the background coefficients and it is estimated during the OSDE analysis

of simulated background. It is evaluated by subtracting, in quadrature, the covariance of the deconvolved coefficients with and without the inclusion of the statistical uncertainties from the background. Statistical uncertainty to simulated signal statistics enters through the migration matrix and it is evaluated by subdividing the simulated signal into equally-sized sub-samples. Migration matrices are computed for each sub-sample, each one being used to deconvolve the full nominal signal sample. From these results a covariance matrix is computed due to simulated signal statistics.

The expected uncertainties due to data statistics are evaluated from pseudoexperiments. The covariance matrix is evaluated for each experiment and then averaged. The result is taken as the expected covariance for the signal. The square root of diagonal elements are the predicted uncertainties on the coefficients.

Tables 7.3-7.5 show a detailed breakdown of the contributions to the systematic and statistical uncertainties on the measured angular coefficients. The tables are sorted following the classification discussed in the previous subsections: detector modelling, background normalisation and signal and background modelling. The individual contributions are given with its sign for the up and down variations in order to explicitly show their behaviour. Note that the "Up" and "Down" columns show the comparison of the nominal measured angular coefficients with the $+1\sigma$ and -1σ measured angular coefficients respectively. In addition, the column "Symmetrised" shows the final symmetrised uncertainty[4]. When just one number is shown, just one variation of a given source of systematic uncertainty is available and therefore compared with the nominal. In this case, this uncertainty is symmetrised (i.e. its $\pm$ value is considered) when computing the total systematic uncertainty. The "Up", "Down" and "Symmetrised" columns represent the same as in the previous tables. The total systematic uncertainty is computed by adding in quadrature all the individual systematic uncertainties and the MC statistics uncertainties after the symmetrisation. Finally the total statistics and systematic uncertainty is computed by adding in quadrature the total systematics and the expected data statistics.

[4]The symmetrisation of the "Up" and "Down" uncertainties is simply done as Symmetrised $= \sqrt{\frac{\mathrm{Up}^2+\mathrm{Down}^2}{2}}$

Units (10^{-4})	$\mathrm{Re}\,[a_{0,1,0}]$			$\mathrm{Re}\,[a_{0,2,0}]$			$\mathrm{Re}\,[a_{1,0,0}]$		
Systematic source	Up	Down	Symmetrised	Up	Down	Symmetrised	Up	Down	Symmetrised
Electron energy resolution	−24	−28	±26	+24	+19	±21	−7	−4	±6
Electron energy scale	+15	−42	±31	+18	+3	±13	+7	−24	±18
Electron scale factor (id.)	−1	+1	±1	+2	−2	±2	−1	+1	±1
Electron scale factor (recon.)	<0.5	<0.5	<0.5	+1	−1	±1	<0.5	<0.5	<0.5
Electron scale factor (trigger)	−4	+4	±4	+2	−2	±2	+1	−1	±1
Muon momentum resolution (id.)		−1			−2			−1	
Muon momentum smearing resolution		+2			+4			−5	
Muon scale factor (id.)	<0.5	<0.5	<0.5	<0.5	<0.5	<0.5	<0.5	<0.5	<0.5
Muon scale factor (reco.)	<0.5	<0.5	<0.5	<0.5	<0.5	<0.5	<0.5	<0.5	<0.5
Muon momentum scale	+5	−5	±5	−2	+3	±2	+2	−5	±4
Muon scale factor (trigger)	<0.5	<0.5	<0.5	<0.5	<0.5	<0.5	<0.5	<0.5	<0.5
Jet energy scale	±44	±49	±47	±58	±54	±56	±65	±52	±59
Jet energy resolution		−43			+82			+9	
Jet reconstruction efficiency		+1			<0.5			+1	
Jet vertex fraction	+4	+11	±8	−4	−8	±6	+3	+10	±7
Jet b-tagging scale factor	−3	+3	±3	−1	+1	±1	+5	−5	±5
Jet c-tagging scale factor	+8	−9	±8	+4	−4	±4	−7	+8	±8
Jet mis-tagging scale factor	<0.5	+1	±1	+3	−4	±3	<0.5	<0.5	<0.5
$E_{\mathrm{T}}^{\mathrm{miss}}$ (cell-out + soft jet resolution)	−5	−15	±11	−1	+9	±7	−5	−10	±8
$E_{\mathrm{T}}^{\mathrm{miss}}$ (cell-out + soft jet scale)	−3	−8	±6	+17	−5	±13	−6	−2	±4
Top-quark background normalisation (overall scale factors)	−1	+1	±1	<0.5	<0.5	<0.5	<0.5	<0.5	<0.5
W+jets normalisation (overall scale factors)	+1	−1	±1	<0.5	<0.5	<0.5	−1	+1	±1
Z-jets normalisation	+6	−6	±6	+8	−8	±8	+1	−1	±1
Diboson normalisation	−1	+1	±1	<0.5	<0.5	<0.5	<0.5	<0.5	<0.5
Multijet normalisation	<0.5	<0.5	<0.5	<0.5	<0.5	<0.5	<0.5	<0.5	<0.5
Luminosity	<0.5	<0.5	<0.5	<0.5	<0.5	<0.5	<0.5	<0.5	<0.5
t-channel LO modelling		+13			−42			+5	
t-channel LO/NLO modelling		−49			+53			−35	
t-channel NLO modelling		−26			+45			−55	
t-channel hadronisation		−62			−2			−25	
t-channel scale variation	+23	−51	±39	+3	−2	±3	+50	−66	±58
t-channel colour reconnection		−18			+3			−20	
t-channel underlying event		+10			−14			+18	
t-channel top-quark finite width effect		+3			−6			+1	
$t\bar{t}$ NLO modelling		+18			−20			+36	
$t\bar{t}$ hadronisation		−3			−29			+23	
$t\bar{t}$ scale variation	+10	−19	±15	−19	+23	±21	−2	−8	±5
W+jets shape modelling		+16			−10			+42	
W+heavy-jets flavour composition	−17	+30	±24	−12	+23	±18	+19	−36	±29
Possible polarisation nonlinearity	<0.5	<0.5	<0.5	<0.5	<0.5	<0.5	+8	+3	±6
PDF		+27			+23			+23	
MC statistics (signal)		±24			±19			±16	
MC statistics (background)		±51			±72			±62	
Expected data statistics		±130			±101			±102	
Total systematics		±150			±156			±159	
Total statistics ⊕ systematics		±198			±186			±189	

Table 7.3: Breakdown of the contribution of each source of uncertainty to total uncertainties on the measurement of $\mathrm{Re}\,[a_{0,1,0}]$, $\mathrm{Re}\,[a_{0,2,0}]$ and $\mathrm{Re}\,[a_{1,0,0}]$.

Units (10^{-4})	$\mathrm{Re}\,[a_{1,1,0}]$			$\mathrm{Re}\,[a_{1,2,0}]$			$\mathrm{Re}\,[a_{1,1,1}]$		
Systematic source	Up	Down	Symmetrised	Up	Down	Symmetrised	Up	Down	Symmetrised
Electron energy resolution	+14	+14	±14	−29	−29	±29	−5	−14	±11
Electron energy scale	−1	+19	±14	−21	−14	±18	+27	−36	±32
Electron scale factor (id.)	+1	−1	±1	−1	+1	±1	−1	+1	±1
Electron scale factor (recon.)	<0.5	<0.5	<0.5	<0.5	<0.5	<0.5	<0.5	<0.5	<0.5
Electron scale factor (trigger)	+1	−1	±1	−1	+1	±1	−3	+3	±3
Muon momentum resolution (id.)		−1			−2			+2	
Muon momentum smearing resolution		−4			−7			+1	
Muon scale factor (id.)	<0.5	<0.5	<0.5	<0.5	<0.5	<0.5	<0.5	<0.5	<0.5
Muon scale factor (reco.)	<0.5	<0.5	<0.5	<0.5	<0.5	<0.5	<0.5	<0.5	<0.5
Muon momentum scale	−3	+5	±4	+2	−2	±2	+4	−5	±4
Muon scale factor (trigger)	<0.5	<0.5	<0.5	<0.5	<0.5	<0.5	+1	−1	±1
Jet energy scale	±99	±111	±105	±46	±43	±44	±94	±97	±96
Jet energy resolution		+28			+10			+3	
Jet reconstruction efficiency		−2			<0.5			+1	
Jet vertex fraction	−6	−14	±10	+2	+5	±4	+6	−2	±4
Jet b-tagging scale factor	−2	+2	±2	−1	+1	±1	+1	−1	±1
Jet c-tagging scale factor	−4	+5	±4	+12	−14	±13	+5	−6	±6
Jet mis-tagging scale factor	<0.5	<0.5	<0.5	−2	+2	±2	+6	−7	±7
$E_{\mathrm{T}}^{\mathrm{miss}}$ (cell-out + soft jet resolution)	+9	+13	±11	−1	−7	±5	+7	+1	±5
$E_{\mathrm{T}}^{\mathrm{miss}}$ (cell-out + soft jet scale)	+8	−3	±6	−18	−7	±14	<0.5	−2	±1
Top-quark background normalisation (overall scale factors)	<0.5	<0.5	<0.5	<0.5	<0.5	<0.5	<0.5	<0.5	<0.5
W+jets normalisation (overall scale factors)	+1	−1	±1	−1	+1	±1	−1	+1	±1
Z-jets normalisation	+6	−6	±6	−2	+2	±2	−1	+1	±1
Diboson normalisation	+1	−1	±1	<0.5	<0.5	<0.5	+1	−1	±1
Multijet normalisation	<0.5	<0.5	<0.5	<0.5	<0.5	<0.5	<0.5	<0.5	<0.5
Luminosity	<0.5	<0.5	<0.5	<0.5	<0.5	<0.5	<0.5	<0.5	<0.5
t-channel LO modelling		−47			+29			+63	
t-channel LO/NLO modelling		+4			−30			−27	
t-channel NLO modelling		<0.5			−12			−27	
t-channel hadronisation		−9			−44			−18	
t-channel scale variation	−52	+55	±53	+54	+3	±38	+17	−76	±55
t-channel colour reconnection		+22			−14			−13	
t-channel underlying event		−22			+33			−12	
t-channel top-quark finite width effect		−7			<0.5			+9	
$t\bar{t}$ NLO modelling		−37			+14			+22	
$t\bar{t}$ hadronisation		−29			+15			+5	
$t\bar{t}$ scale variation	−17	+22	±19	+47	−21	±36	+3	−6	±5
W+jets shape modelling		−14			+6			+12	
W+heavy-jets flavour composition	+10	−19	±15	−25	+47	±37	−14	+25	±20
Possible polarisation nonlinearity	+5	+2	±4	−8	−3	±6	−12	−5	±9
PDF		+25			+29			+28	
MC statistics (signal)		±19			±24			±16	
MC statistics (background)		±61			±69			±33	
Expected data statistics		±130			±133			±84	
Total systematics		±167			±129			±151	
Total statistics ⊕ systematics		±212			±185			±173	

Table 7.4: Breakdown of the contribution of each source of uncertainty to total uncertainties on the measurement of $\mathrm{Re}\,[a_{1,1,0}]$, $\mathrm{Re}\,[a_{1,2,0}]$ and $\mathrm{Re}\,[a_{1,1,1}]$.

Units (10^{-4})	$\mathrm{Im}\,[a_{1,1,1}]$			$\mathrm{Re}\,[a_{1,2,1}]$			$\mathrm{Im}\,[a_{1,2,1}]$		
Systematic source	Up	Down	Symmetrised	Up	Down	Symmetrised	Up	Down	Symmetrised
Electron energy resolution	+1	<0.5	±1	+16	+17	±16	−4	<0.5	±3
Electron energy scale	+3	−2	±2	+8	+2	±6	−1	−3	±2
Electron scale factor (id.)	<0.5	<0.5	<0.5	+3	−3	±3	<0.5	<0.5	<0.5
Electron scale factor (recon.)	<0.5	<0.5	<0.5	+1	−1	±1	<0.5	<0.5	<0.5
Electron scale factor (trigger)	<0.5	<0.5	<0.5	+3	−3	±3	<0.5	<0.5	<0.5
Muon momentum resolution (id.)		−1			−1			<0.5	
Muon momentum smearing resolution		−2			−3			<0.5	
Muon scale factor (id.)	<0.5	<0.5	<0.5	<0.5	<0.5	<0.5	<0.5	<0.5	<0.5
Muon scale factor (reco.)	<0.5	<0.5	<0.5	<0.5	<0.5	<0.5	<0.5	<0.5	<0.5
Muon momentum scale	<0.5	−1	±1	−4	+4	±4	+1	<0.5	±1
Muon scale factor (trigger)	<0.5	<0.5	<0.5	−1	+1	±1	<0.5	<0.5	<0.5
Jet energy scale	±25	±15	±21	±36	±36	±36	±13	±9	±11
Jet energy resolution		−6			−27			+23	
Jet reconstruction efficiency		<0.5			−1			<0.5	
Jet vertex fraction	+1	−3	±2	−5	+1	±3	<0.5	+3	±2
Jet b-tagging scale factor	<0.5	<0.5	<0.5	+3	−3	±3	+1	−1	±1
Jet c-tagging scale factor	−1	+1	±1	−10	+11	±11	−2	+3	±2
Jet mis-tagging scale factor	<0.5	<0.5	<0.5	−6	+6	±6	+2	−1	±2
$E_{\mathrm{T}}^{\mathrm{miss}}$ (cell-out + soft jet resolution)	+1	+7	±5	+16	+10	±13	−3	+6	±5
$E_{\mathrm{T}}^{\mathrm{miss}}$ (cell-out + soft jet scale)	−2	+2	±2	+8	−8	±8	−1	−6	±4
Top-quark background normalisation (overall scale factors)	<0.5	<0.5	<0.5	+1	−1	±1	<0.5	<0.5	<0.5
W+jets normalisation (overall scale factors)	<0.5	<0.5	<0.5	−1	+1	±1	<0.5	<0.5	<0.5
Z-jets normalisation	+1	−1	±1	+2	−2	±2	<0.5	<0.5	<0.5
Diboson normalisation	<0.5	<0.5	<0.5	+1	−1	±1	<0.5	<0.5	<0.5
Multijet normalisation	<0.5	<0.5	<0.5	<0.5	<0.5	<0.5	<0.5	<0.5	<0.5
Luminosity	<0.5	<0.5	<0.5	<0.5	<0.5	<0.5	<0.5	<0.5	<0.5
t-channel LO modelling		−15			+17			−9	
t-channel LO/NLO modelling		+1			−27			−8	
t-channel NLO modelling		+7			−61			−24	
t-channel hadronisation		−14			−2			−2	
t-channel scale variation	−1	+11	±8	−20	+80	±59	+14	−16	±15
t-channel colour reconnection		+10			+9			−12	
t-channel underlying event		−2			+34			<0.5	
t-channel top-quark finite width effect		−3			+2			<0.5	
$t\bar{t}$ NLO modelling		+6			−4			−10	
$t\bar{t}$ hadronisation		+7			+7			−3	
$t\bar{t}$ scale variation	−1	+2	±2	−15	+15	±15	<0.5	+2	±1
W+jets shape modelling		<0.5			−18			−2	
W+heavy-jets flavour composition	<0.5	<0.5	<0.5	+29	−54	±43	+7	−13	±11
Possible polarisation nonlinearity	<0.5	<0.5	<0.5	+5	+2	±4	<0.5	<0.5	<0.5
PDF		+6			+34			+12	
MC statistics (signal)		±9			±24			±8	
MC statistics (background)		±16			±53			±21	
Expected data statistics		±26			±109			±32	
Total systematics		±39			±139			±52	
Total statistics ⊕ systematics		±47			±177			±61	

Table 7.5: Breakdown of the contribution of each source of uncertainty to total uncertainties on the measurement of $\mathrm{Im}\,[a_{1,1,1}]$, $\mathrm{Re}\,[a_{1,2,1}]$ and $\mathrm{Im}\,[a_{1,2,1}]$.

7.9 RESULTS

Distributions and tables in this section are based upon a numerical calculation of the likelihood function which is computed from observed data and MC inputs, and includes the interpolated reweighting procedure as described in this note. This is a function of the generalised helicity fractions and phases f_1, f_1^+, f_0^+, δ_-, δ_+ and P, or alternately of the anomalous couplings V_{L}, V_{R}, g_{L}, g_{R}, and P.

Limits on parameters of interest can be obtained from likelihood profiles, or joint likelihood profiles; allowing many conclusions to be drawn from the collected pp collision data at a centre-of-mass energy of 8 TeV. This section discusses the more pertinent ones.

7.9.1 Bounds on generalised helicity fractions and phases

No external constraints or assumptions on couplings are imposed in this section. The physics parameters, $\vec{\alpha} \equiv \left\{f_1, f_1^+, f_0^+, \delta_+, \delta_-, P\right\}$, are uniquely measured in the analysis described in this note and they are constrained as follows.

In the first place, likelihood profiles for the quantities f_0^+ and f_1^+ are shown in Figure 7.23. The 68% contours represent the statistical or the total uncertainty on the measurement.

The measured limit for f_0^+, i.e. for the fraction of b-quarks that are right-handed in events with longitudinally polarised W bosons, is

$$\begin{aligned} f_0^+ &< 0.041 \qquad (68\%\ \text{C.L.}) \\ f_0^+ &< 0.085 \qquad (95\%\ \text{C.L.}) \end{aligned} \tag{7.44}$$

consistent with the SM expectation of $f_0^+ = 6 \cdot 10^{-5}$. The measured limit for f_1^+, i.e. for the fraction of transversely polarised W boson decays that are right-handed, is

$$\begin{aligned} f_1^+ &< 0.053 \qquad (68\%\ \text{C.L.}) \\ f_1^+ &< 0.118 \qquad (95\%\ \text{C.L.}) \end{aligned} \tag{7.45}$$

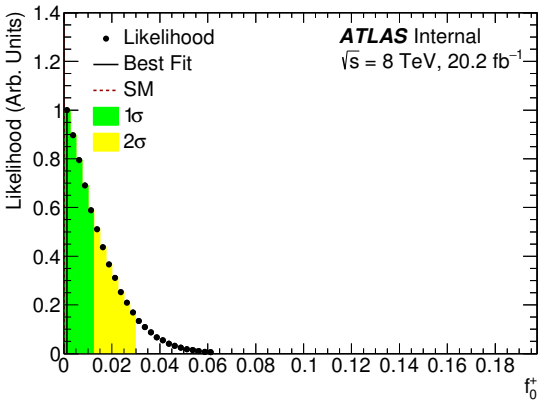

(a) f_0^+(stat. only)

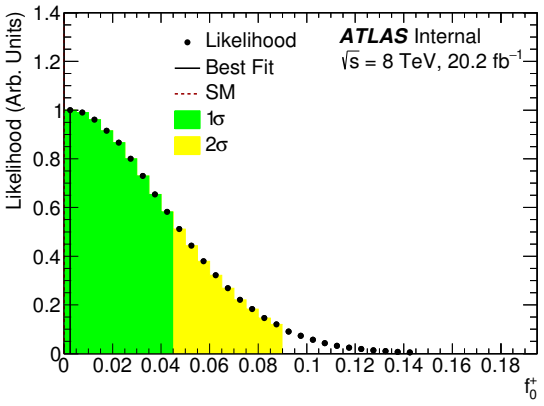

(b) f_0^+(stat. + syst.)

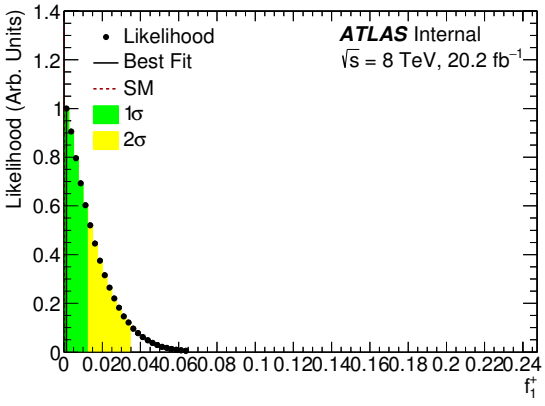

(c) f_1^+(stat. only)

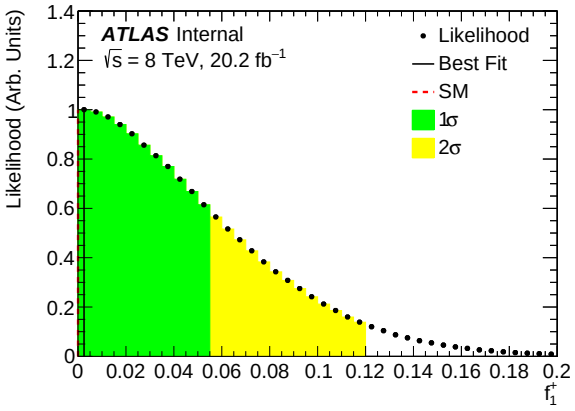

(d) f_1^+(stat. + syst.)

Figure 7.23: Likelihood profiles for the parameters f_0^+ (a–b) and f_1^+ (c–d) with statistical only (left) and statistical and systematic (right) uncertainties incorporated. The black points indicate the largest evaluated likelihood in each bin of the profiled variable. The red dashed line represents SM expectation. Regions shown in green and yellow represent the 68% and 95% C.L., respectively. A black line indicates the observed value.

consistent with the SM expectation $f_1^+ = 0.001$. All the intervals for f_0^+ and f_1^+ include all statistic and systematic uncertainties. Conservatively, no correction is made for over-coverage of these intervals.

Next, likelihood profiles are shown in Figure 7.24 (a–b) for the parameter f_1, i.e. the

fraction of decays containing transversely polarised W bosons.

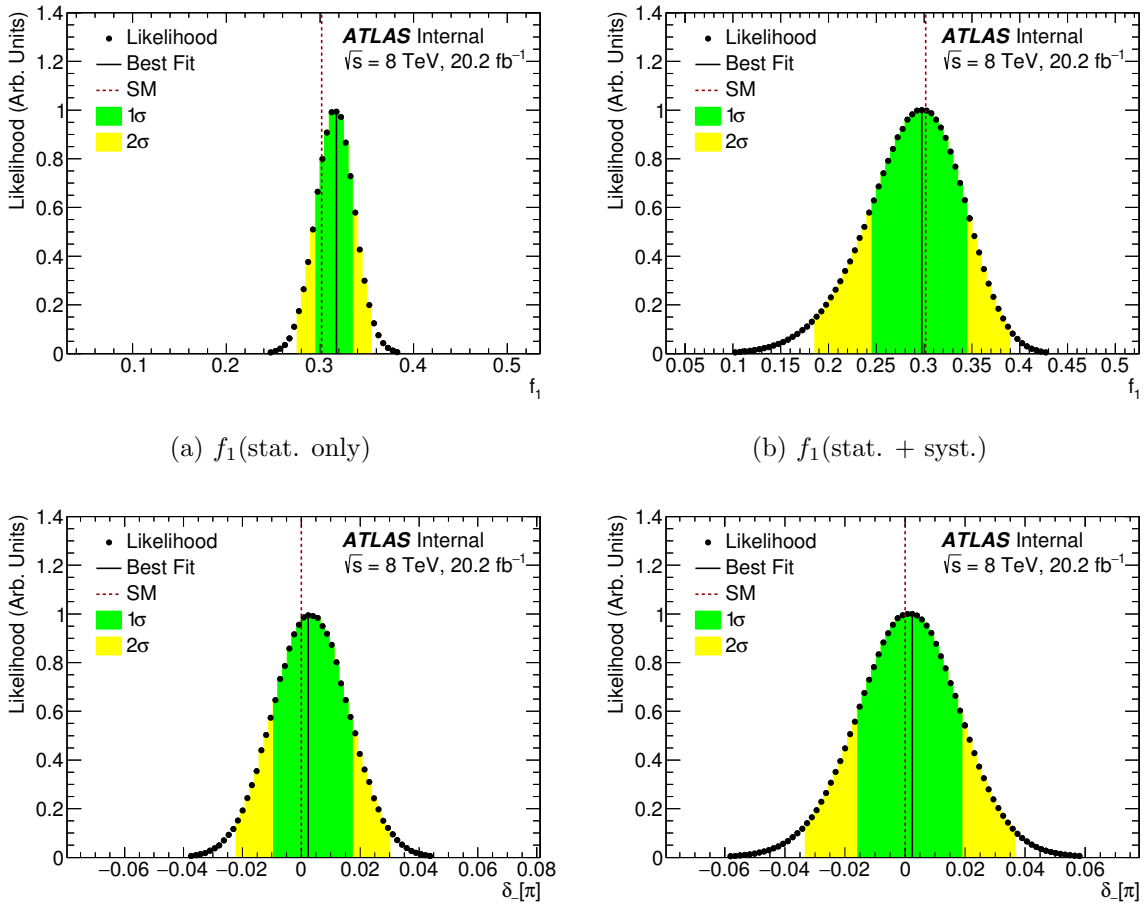

(a) f_1(stat. only)

(b) f_1(stat. + syst.)

(c) δ_- (stat. only)

(d) δ_- (stat. + syst.)

Figure 7.24: Likelihood profiles for the parameters f_1 (a–b) and δ_- (c–d) with statistical only (left) and statistical and systematic (right) uncertainties incorporated. The black points indicate the largest evaluated likelihood in each bin of the profiled variable. The red dashed line represents SM expectation. Regions shown in green and yellow represent the 68% and 95% C.L., respectively. A black line indicates the observed value.

The profiles can be summarised as:

$$f_1 = 0.296^{+0.020}_{-0.023}\ \text{(stat.)}\ ^{+0.044}_{-0.046}\ \text{(syst.)} = 0.296^{+0.048}_{-0.051}\ \text{(stat. + syst.)} \tag{7.46}$$

which agrees with the SM expectation of $f_1 = 0.304$. Furthermore this result improves the previous ATLAS measurement [12] of $f_1 = 0.37 \pm 0.05$ (stat.) ± 0.05 (syst.) without imposing here any SM constraints on f_1^+ and f_0^+. No coverage correction is required for these estimates.

The phase between amplitudes for longitudinally polarised and transversely polarised W bosons recoiling against right-handed b-quarks, δ_-, has been obtained from likelihood profiles, which are shown in Figure 7.24 (c–d). The resulting measurement is

$$\delta_- = 0.002\pi^{+0.013\pi}_{-0.014\pi}\ \text{(stat.)}\ ^{+0.009\pi}_{-0.010\pi}\ \text{(syst.)} = 0.002\pi^{+0.016\pi}_{-0.017\pi}\ \text{(stat. + syst.)} \tag{7.47}$$

which shows no discrepancy with the SM value of zero, and therefore shows no sign of BSM $\mathcal{CP}$ violation at the Wtb vertex. In addition, this result also improves the previous ATLAS measurement [12] of $\delta_- = -0.014\pi \pm 0.023\pi$ (stat.) $\pm 0.028\pi$ (syst.) again without imposing any SM constraints on f_1^+ and f_0^+. Again, no coverage correction is required.

Finally, likelihood profiles for the top-quark polarisation P have also been obtained and are shown in Figure 7.25.

They lead to the following constraint on the top-quark polarisation

$$\begin{aligned} P &> 0.864 \qquad (68\%\ \text{C.L.}) \\ P &> 0.718 \qquad (95\%\ \text{C.L.}) \end{aligned} \tag{7.48}$$

No coverage correction is required. This is consistent with the SM prediction of $P \approx 0.9$ at $\sqrt{s}$ =8 TeV as shown in Refs. [148–150].

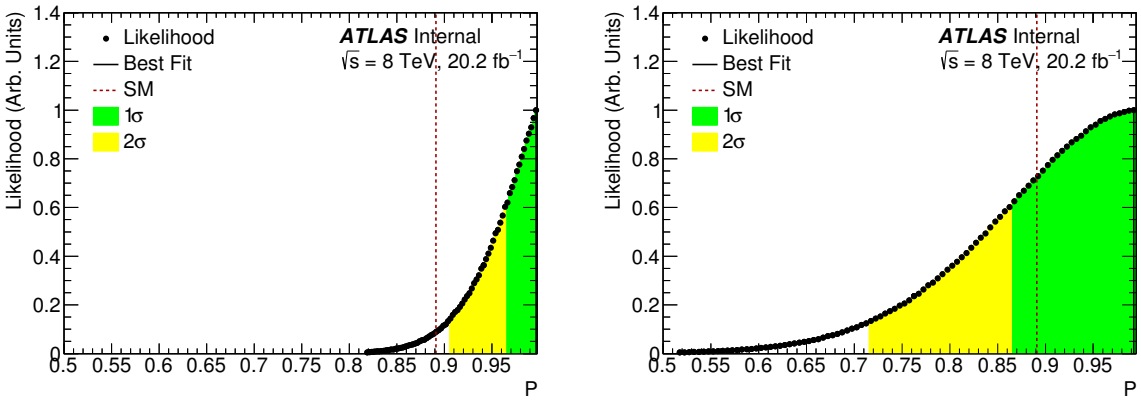

(a) P (stat. only)

(b) P (stat. + syst.)

Figure 7.25: Likelihood profiles for the top-quark polarisation parameter P with statistical only (a) and statistical and systematic (b) uncertainties incorporated. The black points indicate the largest evaluated likelihood in each bin of the profiled variable. The red dashed line represents SM expectation. Regions shown in green and yellow represent the 68% and 95% C.L., respectively. A black line indicates the observed value.

7.9.2 Joint likelihood profiles for the generalised helicity fractions and phases

Correlations between the extracted parameters can be identified by producing joint likelihood profiles. Thus Figures 7.26-7.27 show the joint likelihood profiles for the parameters f_1^+, f_0^+ and δ_- as a function of f_1. In general these distributions show only weak correlation between the parameters. This is shown already for f_1 and δ_- parameters in Ref. [12] (where the correlation is $\rho(f_1, \delta_-) = 0.15$).

Additionally, Figure 7.28 shows joint likelihood profiles for P as a function of f_1 (a–b) and δ_- (c–d). A weak correlation is found between P and f_1 while no correlation is found between P and δ_-. More joint likelihood profiles can be found in Appendix A.5.

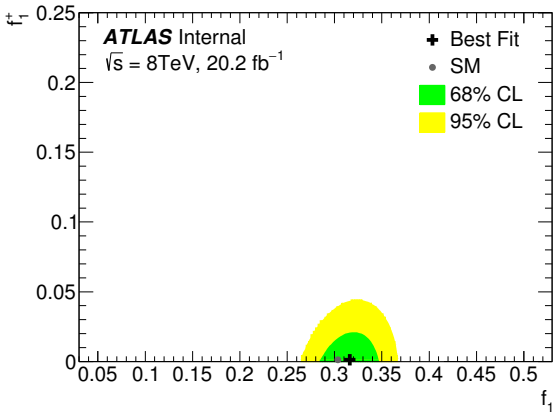

(a) f_1^+ vs. f_1 (stat. only)

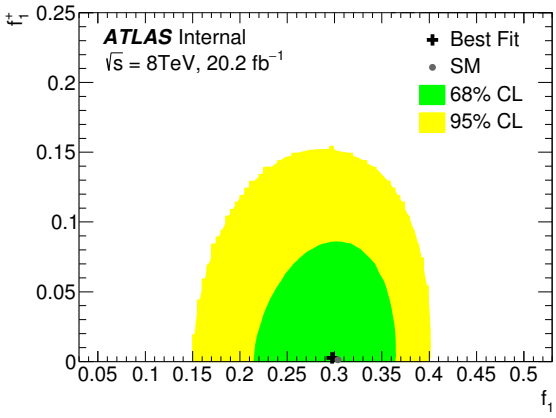

(b) f_1^+ vs. f_1 (stat.+ syst.)

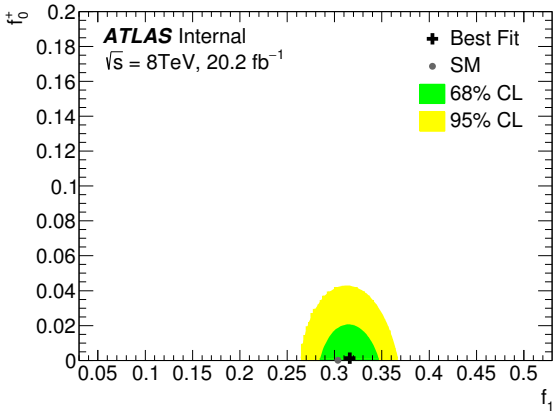

(c) f_0^+ vs. f_1 (stat. only)

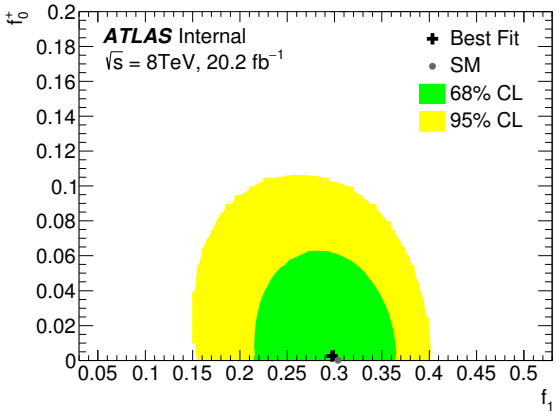

(d) f_0^+ vs. f_1 (stat. + syst.)

Figure 7.26: Joint likelihood profiles for the parameters f_1^+ (top) and f_0^+ (bottom) as a function of f_1 with statistical only (left) and statistical and systematic (right) uncertainties incorporated.

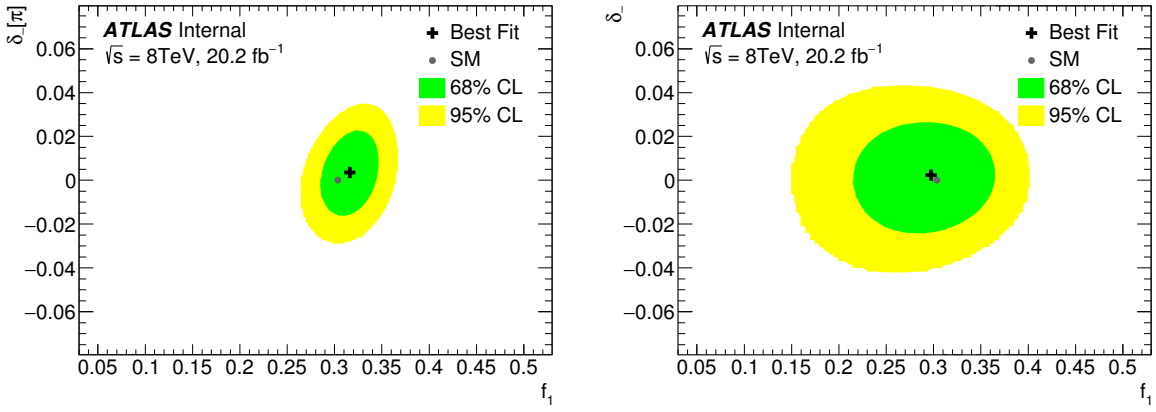

(a) δ_- vs. f_1 (stat. only)

(b) δ_- vs. f_1 (stat. + syst.)

Figure 7.27: Joint likelihood profiles for the parameter δ_- as a function of f_1 with statistical only (left) and statistical and systematic (right) uncertainties incorporated.

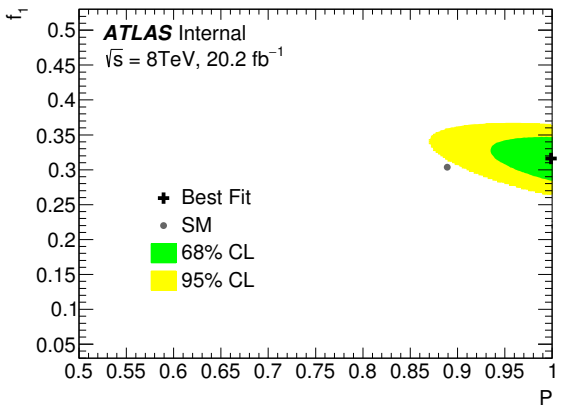

(a) f_1 vs. P

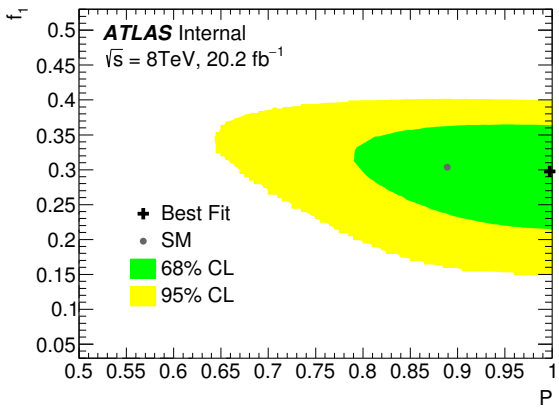

(b) f_1 vs. P

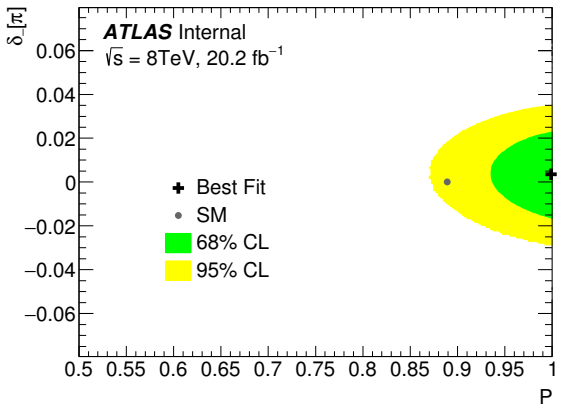

(c) δ_- vs. P

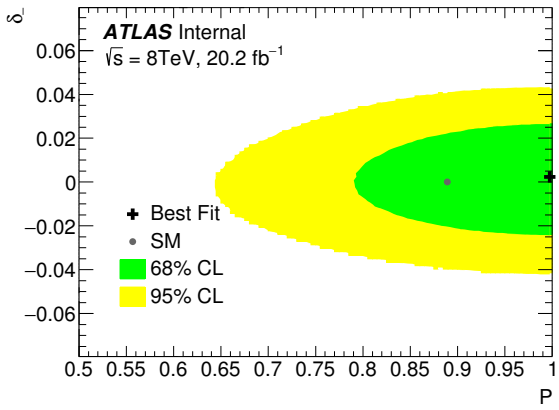

(d) δ_- vs. P

Figure 7.28: Joint likelihood profiles for the parameters f_1 (a–b) and δ_- (c–d) as a function of the top-quark polarisation P with statistical only (left) and statistical and systematic (right) uncertainties incorporated.

In summary, Table 7.6 shows the contribution of each source of systematic uncertainty to the two most sensitive physics parameters f_1 and δ^-, respectively. The total systematic uncertainty is obtained by adding in quadrature all the individual systematic uncertainties and the MC statistics uncertainties. Finally the total statistics and systematic uncertainty is computed by adding in quadrature the total systematics and the expected data statistics. The leading systematic uncertainties for f_1 come from the jet measurements and the generator modelling. For this parameter, data statistics is also an important uncertainty. In the case of δ_-, the leading systematic uncertainties are jet measurements, the generator modelling and MC statistics. Anyhow, the measurement of δ_- is dominated by the data statistics uncertainty.

Source	$\sigma(f_1)$	$\sigma(\delta_-)/\pi$
Data statistics	0.022	0.013
Jets	0.029	0.007
Leptons	0.014	0.002
E_T^{miss}	<0.001	<0.001
Generator	0.027	0.006
Parton shower and hadronisation	0.004	0.003
PDF variations	0.008	0.004
Background normalisation	<0.001	<0.001
Multijet normalization	<0.001	<0.001
W+jets shape	0.015	0.005
Luminosity	<0.001	<0.001
MC statistics	0.009	0.006
Other	<0.001	<0.001
Total systematics	0.044	0.011
Total statistics + systematics	0.049	0.017

Table 7.6: Sources of systematic uncertainty on the measurement of physics parameters f_1 and δ_-. Individual sources are evaluated separately for shifts up and down, and symmetrised uncertainties $\sigma(f_1)$ and $\sigma(\delta_-)$ are given. The total systematic uncertainty is computed by adding in quadrature all the individual systematic uncertainties and the MC statistics uncertainties. Finally the total statistics and systematic uncertainty is computed by adding in quadrature the total systematics and the expected data statistics.

7.9.3 Likelihood profiles for the anomalous coupling constants

The results of the previous subsections can also be interpreted in terms of anomalous couplings, V_{R}, g_{L}, and g_{R}. Likelihood profiles and joint likelihood contours for these couplings are shown in Figures 7.29-7.30 and Figure 7.31 respectively. In each case the measured values are consistent with the SM prediction, i.e. $V_{\mathrm{R}} = g_{\mathrm{L,R}} = 0$.

The bounds obtained on V_{R} and g_{L}, and shown in Figure 7.29, and are far weaker than those which may be obtained from radiative b-quark decays [151], but show consistency with b-quark physics.

For the coupling constant $\mathrm{Re}\,[g_{\mathrm{R}}]$, it has been obtained

$$\mathrm{Re}\left[\frac{g_{\mathrm{R}}}{V_{\mathrm{L}}}\right] = 0.006^{+0.033}_{-0.028}\ (\mathrm{stat.})\ ^{+0.063}_{-0.059}\ (\mathrm{syst.}) = 0.006^{+0.071}_{-0.065}\ (\mathrm{stat.}\ +\ \mathrm{syst.}) \tag{7.49}$$

or

$$\mathrm{Re}\left[\frac{g_{\mathrm{R}}}{V_{\mathrm{L}}}\right] \in [-0.122, 0.168] \qquad (95\%\ \mathrm{C.L.}) \tag{7.50}$$

which is consistent with the SM prediction. This result improves the previous ATLAS measurement at 7 TeV [12] of $\mathrm{Re}\,[g_{\mathrm{R}}/V_{\mathrm{L}}] = -0.13 \pm 0.07\ (\mathrm{stat.}) \pm 0.10\ (\mathrm{syst.})$ or $\mathrm{Re}\,[g_{\mathrm{R}}/V_{\mathrm{L}}] \in [-0.36, 0.10]$ at 95% C.L., where $V_{\mathrm{R}} = g_{\mathrm{L}} = 0$ is explicitly assumed. A small correction for under-coverage is applied to the upper edge of the 95% confidence interval, only (without which we would have quoted 0.153 as the upper limit).

Meanwhile for $\mathrm{Im}\,[g_{\mathrm{R}}/V_{\mathrm{L}}]$ it is obtained

$$\mathrm{Im}\left[\frac{g_{\mathrm{R}}}{V_{\mathrm{L}}}\right] = -0.005 \pm 0.027\ (\mathrm{stat.})\ ^{+0.020}_{-0.012}\ (\mathrm{syst.}) = -0.005^{+0.034}_{-0.030}\ (\mathrm{stat.}\ +\ \mathrm{syst.}) \tag{7.51}$$

or

$$\mathrm{Im}\left[\frac{g_{\mathrm{R}}}{V_{\mathrm{L}}}\right] \in [-0.066, 0.059] \qquad (95\%\ \mathrm{C.L.}) \tag{7.52}$$

showing consistency with the SM prediction. No coverage correction is required. This measurement also improves all previous ATLAS results. These are the results presented in Ref. [12] based on 7 TeV data and the most recent results based on 8 TeV data presented in Ref. [140]. In the former, $\mathrm{Im}\,[g_{\mathrm{R}}/V_{\mathrm{L}}]$ is measured to be $0.03 \pm 0.06\ (\mathrm{stat.}) \pm 0.07\ (\mathrm{syst.})$ or $\mathrm{Im}\,[g_{\mathrm{R}}/V_{\mathrm{L}}] \in [-0.17, 0.23]$ at 95% C.L., assuming $V_{\mathrm{R}} = g_{\mathrm{L}} = 0$. In the latter, $\mathrm{Im}\,[g_{\mathrm{R}}]$ is measured to be within $[-0.17, 0.06]$ at 95% C.L., assuming $V_{\mathrm{L}} = 1$ and all anomalous

couplings other than $\mathrm{Im}\,[g_\mathrm{R}]$ vanishing ($V_\mathrm{R} = g_\mathrm{L} = 0$ and $\mathrm{Re}\,[g_\mathrm{R}] = 0$). None of these assumptions are considered in the analysis presented in this note.

The joint likelihood profile in the space of the parameters $\mathrm{Re}\,[g_\mathrm{R}/V_\mathrm{L}]$ and $\mathrm{Im}\,[g_\mathrm{R}/V_\mathrm{L}]$ is also shown in Figure 7.31. A small correlation is observed from these contours.

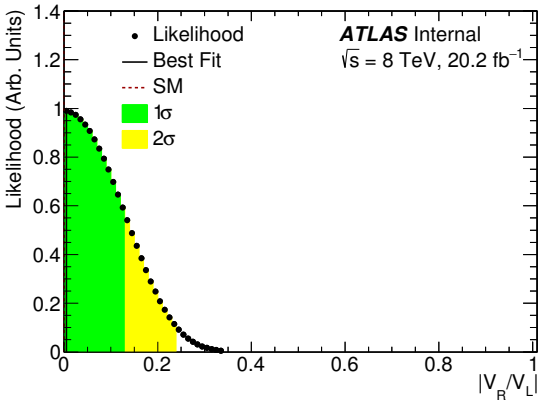

(a) $|V_\mathrm{R}/V_\mathrm{L}|$ (stat. only)

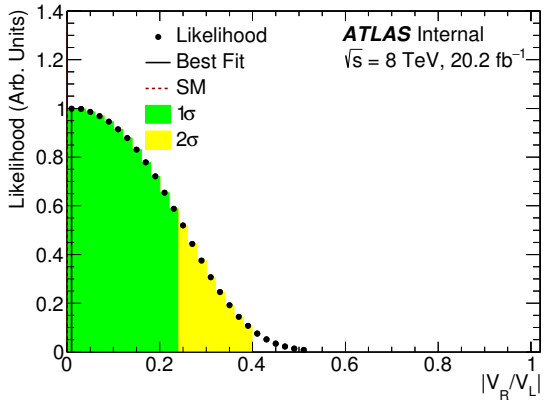

(b) $|V_\mathrm{R}/V_\mathrm{L}|$ (stat. + syst.)

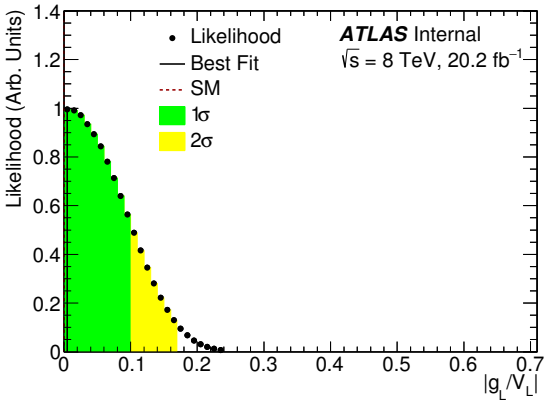

(c) $|g_\mathrm{L}/V_\mathrm{L}|$ (stat. only)

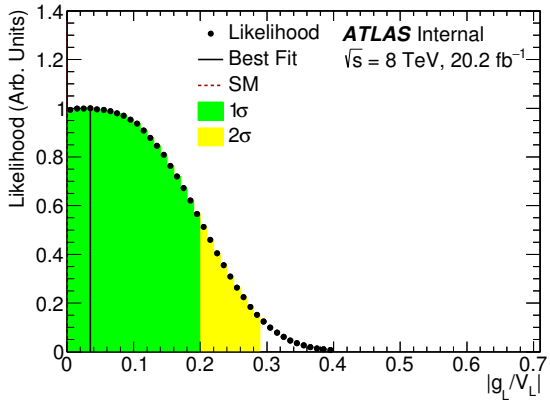

(d) $|g_\mathrm{L}/V_\mathrm{L}|$ (stat. + syst.)

Figure 7.29: Likelihood profiles for $|V_\mathrm{R}/V_\mathrm{L}|$ (top) and $|g_\mathrm{L}/V_\mathrm{L}|$ (bottom) with statistical only (left) and statistical and systematic (right) uncertainties incorporated.

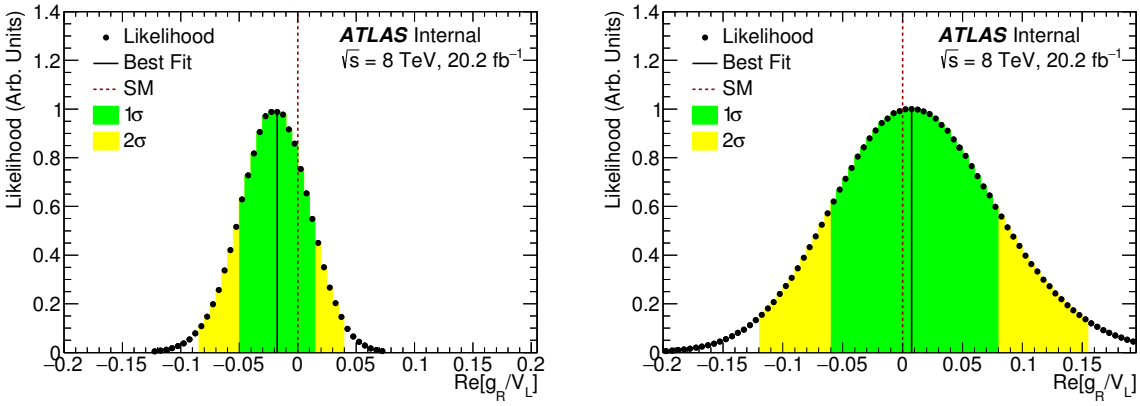

(a) $\mathrm{Re}\,[g_\mathrm{R}/V_\mathrm{L}]$ (stat. only)

(b) $\mathrm{Re}\,[g_\mathrm{R}/V_\mathrm{L}]$ (stat. + syst.)

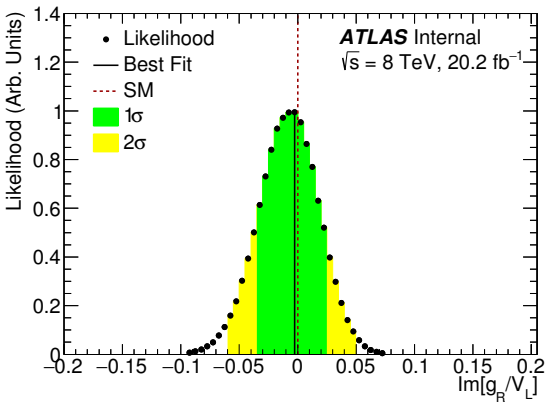

(c) $\mathrm{Im}\,[g_\mathrm{R}/V_\mathrm{L}]$ (stat. only)

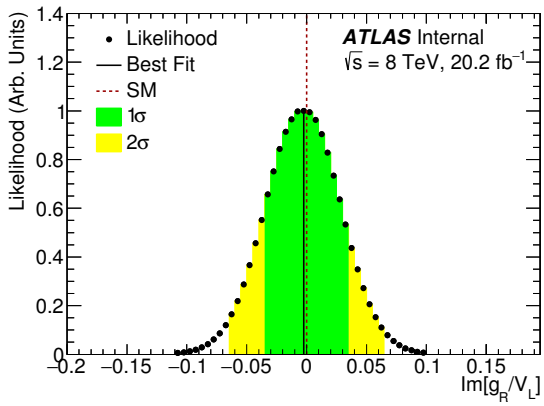

(d) $\mathrm{Im}\,[g_\mathrm{R}/V_\mathrm{L}]$ (stat. + syst.)

Figure 7.30: Likelihood profiles for $\mathrm{Re}\,[g_\mathrm{R}/V_\mathrm{L}]$ (top) and $\mathrm{Im}\,[g_\mathrm{R}/V_\mathrm{L}]$ (bottom) with statistical only (left) and statistical and systematic (right) uncertainties incorporated.

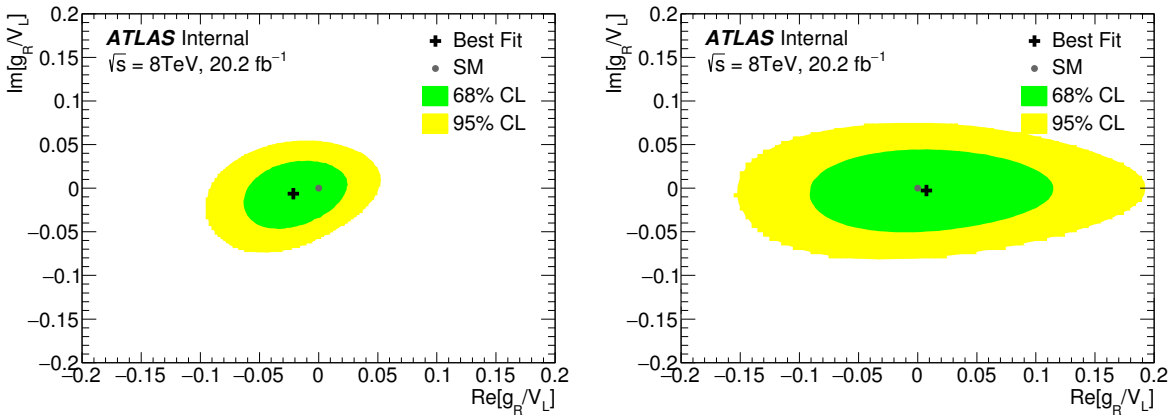

(a) $\mathrm{Im}\,[g_\mathrm{R}/V_\mathrm{L}]$ vs. $\mathrm{Re}\,[g_\mathrm{R}/V_\mathrm{L}]$ (stat. only)

(b) $\mathrm{Im}\,[g_\mathrm{R}/V_\mathrm{L}]$ vs. $\mathrm{Re}\,[g_\mathrm{R}/V_\mathrm{L}]$ (stat. + syst.)

Figure 7.31: Joint likelihood profiles for $\mathrm{Re}\,[g_\mathrm{R}/V_\mathrm{L}]$ as a function of $\mathrm{Im}\,[g_\mathrm{R}/V_\mathrm{L}]$ with statistical only (left) and statistical and systematic (right) uncertainties incorporated.

Table 7.7 shows the contribution of each source of systematic uncertainty to the two most sensitive coupling rations $\mathrm{Re}\,[g_\mathrm{R}/V_\mathrm{L}]$ and $\mathrm{Im}\,[g_\mathrm{R}/V_\mathrm{L}]$, respectively. The leading systematic uncertainties for $\mathrm{Re}\,[g_\mathrm{R}/V_\mathrm{L}]$ and $\mathrm{Im}\,[g_\mathrm{R}/V_\mathrm{L}]$ are the same as for f_1 and δ_- respectively. The measurement of $\mathrm{Im}\,[g_\mathrm{R}/V_\mathrm{L}]$ is dominated by the data statistics uncertainty.

Source	$\sigma(\mathrm{Re}\,[g_\mathrm{R}/V_\mathrm{L}])$	$\sigma(\mathrm{Im}\,[g_\mathrm{R}/V_\mathrm{L}])$
Data statistics	0.030	0.027
Jets	0.039	0.009
Leptons	0.017	<0.001
E_T^{miss}	<0.001	<0.001
Generator	0.030	0.010
Parton shower and hadronisation	<0.001	0.003
PDF variations	<0.001	<0.001
Background normalisation	<0.001	<0.001
Multijet normalization	<0.001	<0.001
W+jets shape	0.007	0.009
Luminosity	<0.001	<0.001
MC statistics	<0.001	0.013
Other	<0.001	<0.001
Total systematics	0.061	0.017
Total statistics + systematics	0.068	0.032

Table 7.7: Sources of systematic uncertainty on the measurement of coupling rations $\mathrm{Re}\,[g_\mathrm{R}/V_\mathrm{L}]$ and $\mathrm{Im}\,[g_\mathrm{R}/V_\mathrm{L}]$. Individual sources are evaluated separately for shifts up and down, and symmetrised uncertainties $\sigma(\mathrm{Re}\,[g_\mathrm{R}/V_\mathrm{L}])$ and $\sigma(\mathrm{Im}\,[g_\mathrm{R}/V_\mathrm{L}])$ are given. The total systematic uncertainty is computed by adding in quadrature all the individual systematic uncertainties and the MC statistics uncertainties. Finally the total statistics and systematic uncertainty is computed by adding in quadrature the total systematics and the expected data statistics.

7.9.4 Comparision between previous two angle analysis and three angle analysis

For a more complete and direct comparison with the previous measurement done from double differential angular decay rates at 7 TeV [12], Figure 7.32 shows both joint likelihood profiles in the space of the parameters $\mathrm{Re}\,[g_\mathrm{R}/V_\mathrm{L}]$ and $\mathrm{Im}\,[g_\mathrm{R}/V_\mathrm{L}]$.

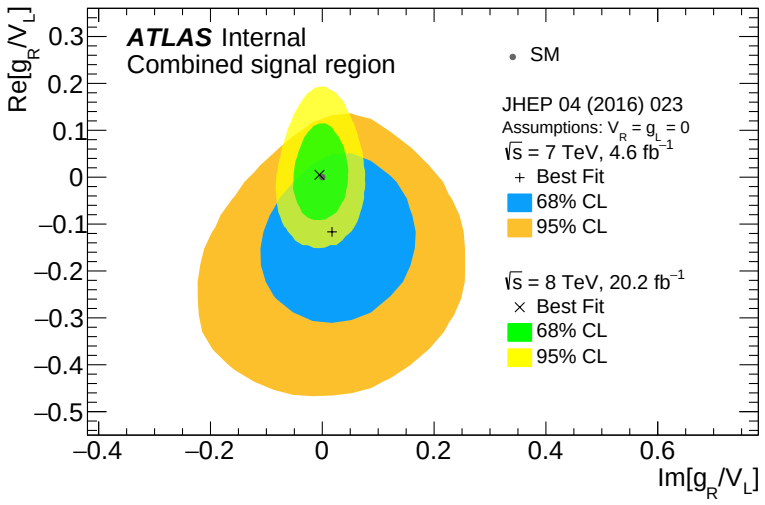

Figure 7.32: Comparison of the joint likelihood profiles of the parameter $\mathrm{Re}\,[g_\mathrm{R}/V_\mathrm{L}]$ as a function of $\mathrm{Im}\,[g_\mathrm{R}/V_\mathrm{L}]$ for Ref. [12] and the results from the analysis presented in this note. In both cases statistical and systematic uncertainties are incorporated. The grey point represents SM expectation. Regions shown in blue/green and orange/yellow represent the 68% and 95% C.L., respectively. A black cross or x mark indicate the observed value of each case. In the previous ATLAS result $V_\mathrm{R} = g_\mathrm{L} = 0$ is assumed while no assumptions are considered in this analysis.

7.9.5 Angular coefficients extracted from data with SM-like model

Finally, in Figure 7.33, a distribution of the deconvolved angular coefficients extracted from data, compared with the SM prediction is shown. The migration matrix used to deconvolve is fixed here to that of the SM prediction.

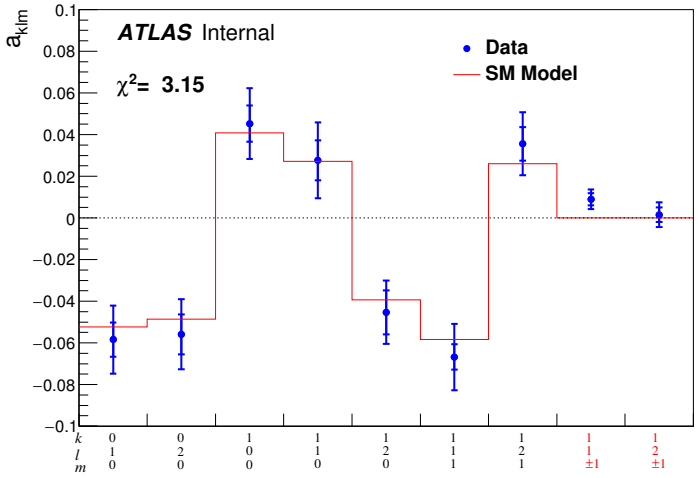

(a) deconvolved coefficients

Figure 7.33: Deconvolved coefficients from data using the migration matrix from the SM. Data are shown as blue points with statistical and systematic uncertainties while SM prediction is shown as a red line. In addition, the χ^2 value is shown. Real parts of the coefficients are indicated with black labelling on the x-axis while imaginary parts are indicated with red labelling.

7.10 CONCLUSION

The analysis presented in this publication uses the triple-differential decay rate in electroweak production and subsequent decay of single top quarks to constrain the complex parameters of the effective Lagrangian that describes the properties of the Wtb vertex. An analysis of angular distributions of the decay products of single top quarks produced in the t-channel

constrains these parameters simultaneously. The analysis is applied to 20.2 pb^{-1} of pp collision data at a centre-of-mass energy of 8 TeV collected with the ATLAS detector at the LHC. The selected events contain one isolated electron or muon, large E_T^{miss} and exactly two jets, with one of them identified as likely to contain a b-hadron. A cut-based analysis is used to discriminate the signal events from background, and then electron and muon channels are merged. The OSDE technique is used to perform an angular analysis of the triple-differential decay rate in order to determine six observables simultaneously, that is, five generalised helicity fractions and phases, as well as the polarisation of the produced top quark. Detector effects are deconvolved from the data by measuring differential rates using Fourier techniques, in particular a variant of the ordinary convolution theorem. The fraction f_1 of decays containing transversely polarised W bosons is measured to be $f_1 = 0.296^{+0.048}_{-0.051}$ (stat. + syst.). The phase δ_- between amplitudes for transversely and longitudinally polarised W bosons recoiling against left-handed b quarks, is measured to be $\delta_- = 0.002\pi^{+0.016\pi}_{-0.017\pi}$ (stat. + syst.), giving no indication of CP violation. The fraction of longitudinal to transverse W bosons accompanied by right-handed b-quarks are also constrained at 95% C.L. to $f_1^+ < 0.118$ and $f_0^+ < 0.085$. Based on these measurements limits are placed at 95% C.L. on the ratio of the complex coupling parameters g_{R} and V_{L} such that $\text{Re}\,[g_{\text{R}}/V_{\text{L}}] \in [-0.122, 0.168]$ and $\text{Im}\,[g_{\text{R}}/V_{\text{L}}] \in [-0.066, 0.059]$. Constraints are also placed on the magnitudes of the ratios $|V_{\text{R}}/V_{\text{L}}|$, and $|g_{\text{L}}/V_{\text{L}}|$. Finally the polarisation of single top quarks in the t-channel is constrained to be $P > 0.718$ (95% C.L.). None of the above measurements make assumptions on the value of any of the other parameters or couplings and all of them are in agreement with the SM expectations.

APPENDIX

A.1 FLAVOR SCHEMES IN SINGLE TOP T-CHANNEL PRODUCTION

The t-channel or W-gluon fusion single top production can be calculated in two different schemes in Fig A1. The top right one is the so called four-flavor scheme(or 2 to 3 process) where proton is considered to be composed of only four light quarks(u, d, c and s); the b and $\bar{b}$ quarks arise from the splitting of a virtual gluon into $b\bar{b}$. If the mass of the b quark taken to be 0, a singularity arises in the case that the final $\bar{b}$ is collinear with the incoming gluon. When computing the total cross section, the collinear terms is proportional to $\ln(\frac{Q^2+m_t^2}{m_b^2})$,where $Q^2 \equiv -q^2$ is the virtuality of the W boson of four-momentum q. Since the total cross section of this calculation contains these logarithmically enhanced terms, the perturbation series do not converge quickly. A PDF of b quark, $b(x, \mu^2)$, is introduced to resolve this difficulty by summing the logarithms to all orders of perturbation theory and describes the splitting of gluons into $b\bar{b}$ pairs inside the colliding hadrons [152]. Once a b quark is used, the way one orders the perturbation theory should be changed. The leading order process is now described by the first process in Fig A1(top), or the five-flavor scheme(a 2 to 2 process). In this formalism, the four-flavor scheme is a higher order correction(NLO) of order of $1/\ln((Q^2 + m_t^2)/m_b^2$ with respect to the five-flavor scheme(LO). However, the four-flavor scheme also includes the collinear logarithmically enhanced term that is already summed into the b quark distribution function. A removal of these overlapped terms is required to consider this effect. Additionally, there are also other corrections of order of α_s, these terms, as well as the five-flavor scheme without the collinear part gives the NLO correction.

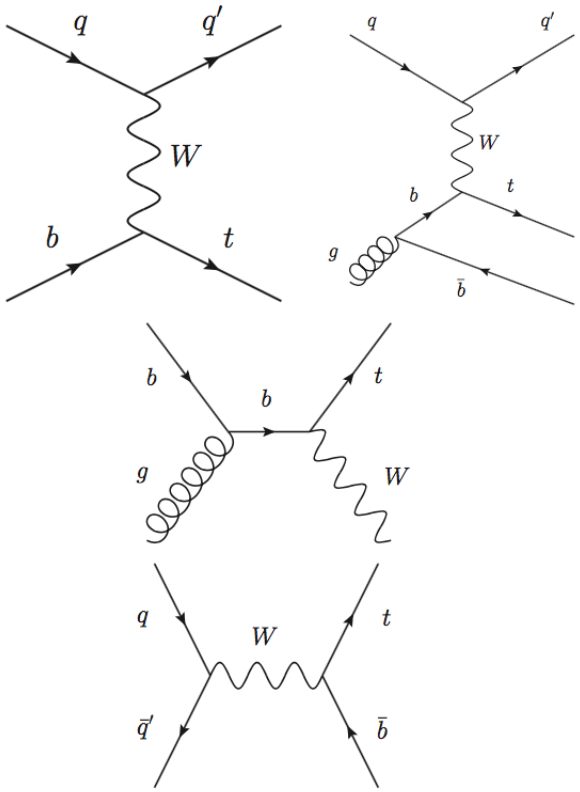

Figure A1: Leading order Feynman diagram of single top production at the LHC: (top) t-channel (middle) Wt associated production (bottom) s-channel.

In reality, different Monte Carlo generators have different ways in their implementations of t-channel single top production. The baseline generator used in this analysis is *Protos*, version 2.2, using the four-flavor scheme, with the CTEQ6L1 PDF(See chapter 5, section Event generation).

A.2 AMPLITUDES AND PHASES IN TERMS OF ANOMALOUS COUPLINGS

A.2.1 Amplitudes

In this section, it is shown how the anomalous couplings $(V_{\rm L}, V_{\rm R}, g_{\rm L}, g_{\rm R})$ are related to the six observable quantities $\vec{\alpha}$, i.e. the generalised helicity fractions and phases. This formula is used to extract constraints on anomalous couplings. Starting with the following relations between amplitudes on one hand and dimensionless form factors (A_0, A_1, B_0 and B_1) on the other, from Ref. [54]:

$$\begin{aligned}
\frac{4\,|\vec{q}|}{m_t}B_1 &= \left|A_{1,\frac{1}{2}}\right|^2 - \left|A_{-1,-\frac{1}{2}}\right|^2, \\
2B_0 &= \left|A_{1,\frac{1}{2}}\right|^2 + \left|A_{-1,-\frac{1}{2}}\right|^2, \\
-\frac{2\,|\vec{q}|}{m_t}A_1 &= \left|A_{0,\frac{1}{2}}\right|^2 - \left|A_{0,-\frac{1}{2}}\right|^2, \\
A_0 &= \left|A_{0,\frac{1}{2}}\right|^2 + \left|A_{0,-\frac{1}{2}}\right|^2,
\end{aligned} \tag{.1}$$

where $|\vec{q}| = \frac{m_t}{2}(1-x_W^2)$, being m_t the top-quark mass and $x_W = m_W/m_t$. Therefore,

$$\begin{aligned}
\left|A_{1,\frac{1}{2}}\right|^2 &= B_0 + \frac{2\,|\vec{q}|}{m_t}B_1, \\
\left|A_{-1,-\frac{1}{2}}\right|^2 &= B_0 - \frac{2\,|\vec{q}|}{m_t}B_1, \\
2\left|A_{0,\frac{1}{2}}\right|^2 &= A_0 - \frac{2\,|\vec{q}|}{m_t}A_1, \\
2\left|A_{0,-\frac{1}{2}}\right|^2 &= A_0 + \frac{2\,|\vec{q}|}{m_t}A_1.
\end{aligned} \tag{.2}$$

If the b-quark mass m_b is ignored, the dimensionless form factors are expressed as:

$$\begin{aligned}
B_0 &= \left(|V_{\rm L}|^2 + |V_{\rm R}|^2\right)(1-x_W^2) + \frac{1}{x_W^2}\left(|g_{\rm L}|^2 + |g_{\rm R}|^2\right)(1-x_W^2) \\
&- \frac{2}{x_W}{\rm Re}\left[V_{\rm L}g_{\rm R}^* + V_{\rm R}g_{\rm L}^*\right](1-x_W^2), \\
B_1 &= -\left(|V_{\rm L}|^2 - |V_{\rm R}|^2\right) + \frac{1}{x_W^2}\left(|g_{\rm L}|^2 - |g_{\rm R}|^2\right) + \frac{2}{x_W}{\rm Re}\left[V_{\rm L}g_{\rm R}^* - V_{\rm R}g_{\rm L}^*\right],
\end{aligned} \tag{.3}$$

So

$$\begin{aligned}
\left|A_{1,\frac{1}{2}}\right|^2 &= B_0 + \left(1-x_W^2\right)B_1, \\
&= 2\left(1-x_W^2\right)|V_{\rm R}|^2 + \frac{1-x_W^2}{x_W^2}\left(2\,|g_{\rm L}|^2\right) - \frac{4(1-x_W^2)}{x_W}{\rm Re}\left[V_{\rm R}g_{\rm L}^*\right], \\
&= \frac{2(1-x_W^2)}{x_W^2}\left(x_W^2\,|V_{\rm R}|^2 + |g_{\rm L}|^2 - 2x_W{\rm Re}\left[V_{\rm R}g_{\rm L}^*\right]\right), \\
&= \frac{2(1-x_W^2)}{x_W^2}\,|x_WV_{\rm R} - g_{\rm L}|^2\,. \qquad (.4)
\end{aligned}$$

Similarly, one can obtain

$$\left|A_{-1,-\frac{1}{2}}\right|^2 = \frac{2(1-x_W^2)}{x_W^2}\,|x_WV_{\rm L} - g_{\rm R}|^2 \qquad (.5)$$

To get $A_{0,\frac{1}{2}}$ and $A_{0,-\frac{1}{2}}$ one can set

$$\begin{aligned}
\alpha\cdot(V_{\rm R} - x_Wg_{\rm L}) &\rightarrow A_{0,\frac{1}{2}}, \\
\beta\cdot(V_{\rm L} - x_Wg_{\rm R}) &\rightarrow A_{0,-\frac{1}{2}}; \qquad (.6)
\end{aligned}$$

and set the sum of their module to A_0,

$$\begin{aligned}
A_0 &= \frac{1}{x_W^2}\left(|V_{\rm L}|^2 + |V_{\rm R}|^2\right)(1-x_W^2) + \left(|g_{\rm L}|^2 + |g_{\rm R}|^2\right)(1-x_W^2) \\
&- \frac{2}{x_W}{\rm Re}\left[V_{\rm L}g_{\rm R}^* + V_{\rm R}g_{\rm L}^*\right](1-x_W^2) \qquad (.7)
\end{aligned}$$

thereby determining the scale α and β to obtain

$$\begin{aligned}
\left|A_{0,\frac{1}{2}}\right|^2 &= \frac{1-x_W^2}{x_W^2}\,|V_{\rm R} - x_Wg_{\rm L}|^2 \\
\left|A_{0,-\frac{1}{2}}\right|^2 &= \frac{1-x_W^2}{x_W^2}\,|V_{\rm L} - x_Wg_{\rm R}|^2 \qquad (.8)
\end{aligned}$$

In summary, one has

$$\begin{aligned}
\left|A_{1,\frac{1}{2}}\right|^2 &= 2\frac{1-x_W^2}{x_W^2}\,|x_WV_{\rm R} - g_{\rm L}|^2\,, \\
\left|A_{0,\frac{1}{2}}\right|^2 &= \frac{1-x_W^2}{x_W^2}\,|V_{\rm R} - x_Wg_{\rm L}|^2\,, \\
\left|A_{-1,-\frac{1}{2}}\right|^2 &= 2\frac{1-x_W^2}{x_W^2}\,|x_WV_{\rm L} - g_{\rm R}|^2\,, \\
\left|A_{0,-\frac{1}{2}}\right|^2 &= \frac{1-x_W^2}{x_W^2}\,|V_{\rm L} - x_Wg_{\rm R}|^2\,. \qquad (.9)
\end{aligned}$$

A.2.2 Phases

Only $V_{\rm R}$ and $g_{\rm L}$ appear in the amplitudes $A_{1,\frac{1}{2}}$ and $A_{0,\frac{1}{2}}$ while only $V_{\rm L}$ and $g_{\rm R}$ appear in the amplitudes $A_{-1,-\frac{1}{2}}$ and $A_{0,-\frac{1}{2}}$. The relative phases between these two sets of amplitudes cannot be observed in the taken approximation ($m_b = 0$) and therefore it can be fixed it by taking $\arg\left(A_{0,\frac{1}{2}} A^*_{0,-\frac{1}{2}}\right) = 0$. Then the phase angles δ_-, δ_+ can be related to the anomalous couplings by setting

$$\begin{aligned}
\sqrt{\frac{2}{2x_W^2+1}}\,(x_W V_{\rm R} - g_{\rm L}) &= A_{1,\frac{1}{2}} e^{i\delta_+}, \\
\sqrt{\frac{1}{2x_W^2+1}}\,(V_{\rm R} - x_W g_{\rm L}) &= A_{0,\frac{1}{2}}, \\
\sqrt{\frac{2}{2x_W^2+1}}\,(x_W V_{\rm L} - g_{\rm R}) &= A_{-1,-\frac{1}{2}} e^{i\delta_-}, \\
\sqrt{\frac{1}{2x_W^2+1}}\,(V_{\rm L} - x_W g_{\rm R}) &= A_{0,-\frac{1}{2}}.
\end{aligned} \tag{.10}$$

Equations .9-.10 determine the amplitudes given the anomalous couplings. To solve for $V_{\rm L}, V_{\rm R}, g_{\rm L}$ and $g_{\rm R}$ given all the amplitudes and two phase angles requires the inversion of a complex matrix. To this procedure, rotations by an arbitrary phase factors to both $(V_{\rm L}, g_{\rm R})$ and $(V_{\rm R}, g_{\rm L})$ are added so that *both* $V_{\rm L}$ and $V_{\rm R}$ are made real.

A.3 COMBINE ELECTRON AND MUON CHANNEL FIT

The OSDE technique can be used to determine the coefficients vector and their corresponding covariance matrices as we see in Section 7.2.2. In this analysis, we apply OSDE calculation on electron and muon channel events separately, thus a *combination* procedure is required. In this section, we discuss about the method we used to get a combined *deconvolved coefficients vector* and its covariance from two independent deconvolved coefficients vectors extracted from electron and muon channel events separately, and their corresponding independent covariance matrices. We start with a standard χ^2 fit derivation in a linear least square model and show that two independent covariances/coefficients can be added following the equation below to get a combined covariance/coefficients:

$$\begin{aligned} \boldsymbol{C}^{-1} &= \boldsymbol{C}_1^{-1} + \boldsymbol{C}_2^{-1} \\ \boldsymbol{a} &= \boldsymbol{C}(\boldsymbol{C}_1^{-1}\boldsymbol{a}_1 + \boldsymbol{C}_2^{-1}\boldsymbol{a}_2) \end{aligned}$$

where $\boldsymbol{a}_1$ and $\boldsymbol{a}_2$ are the two coefficients vectors that calculated by OSDE technique on the electron and muon channel events, $\boldsymbol{C}_1$ and $\boldsymbol{C}_2$ their corresponding covariance matrices calculated also by the OSDE, $\boldsymbol{a}$ and $\boldsymbol{C}$ the combined coefficients/covariance.

A.3.1 Devonvolution Method

The model of Linear Least Square: $\boldsymbol{y} = \boldsymbol{A}\boldsymbol{a}$

- $\boldsymbol{y}$=measured data
- $\boldsymbol{A}$=matrix(fixed)
- $\boldsymbol{a}$=parameter
- $\boldsymbol{V_y}$=covariance matrix of $\boldsymbol{y}$

An identical expression is to assume the error terms ω_i are identical independent distribution, then we have

$$\boldsymbol{y} = \boldsymbol{A}\boldsymbol{a} + \boldsymbol{\omega} \tag{.11}$$

- Least Squares Principle 1: minimize the expression ($\boldsymbol{W} = \boldsymbol{V}_{\boldsymbol{y}}^{-1}$)

$$S(\boldsymbol{a}) = (\boldsymbol{y} - \boldsymbol{A}\boldsymbol{a})^T \boldsymbol{W} (\boldsymbol{y} - \boldsymbol{A}\boldsymbol{a}) \quad \text{or} \quad \chi^2 = \frac{1}{2} S(\boldsymbol{a})$$

Derivative of χ^2 are below:

$$\begin{aligned} \boldsymbol{g} &= \frac{\partial \chi^2}{\partial \boldsymbol{a}} \\ \boldsymbol{H} &= \frac{\partial^2 \chi^2}{\partial a_i a_j} \end{aligned} \tag{.12}$$

Before we give the explicit expression of those two derivatives, let's look at some matrix calculus.

Define:

$$\frac{\partial \boldsymbol{y}}{\partial \boldsymbol{x}} = \begin{bmatrix} \frac{\partial y_1}{\partial x_1} & \frac{\partial y_1}{\partial x_2} & \frac{\partial y_1}{\partial x_3} & \cdots & \frac{\partial y_1}{\partial x_n} \\ \frac{\partial y_2}{\partial x_1} & \frac{\partial y_2}{\partial x_2} & \frac{\partial y_2}{\partial x_3} & \cdots & \frac{\partial y_2}{\partial x_n} \\ \vdots & \vdots & \vdots & \ddots & \vdots \\ \frac{\partial y_d}{\partial x_1} & \frac{\partial y_d}{\partial x_2} & \frac{\partial y_d}{\partial x_3} & \cdots & \frac{\partial y_d}{\partial x_n} \end{bmatrix}$$

i. If

$$\boldsymbol{y} = \boldsymbol{A}\boldsymbol{x}, \tag{.13}$$

then

$$\frac{\partial \boldsymbol{y}}{\partial \boldsymbol{x}} = \boldsymbol{A}$$

ii. And

$$\frac{\partial \boldsymbol{y}}{\partial \boldsymbol{z}} = \boldsymbol{A} \frac{\partial \boldsymbol{x}}{\partial \boldsymbol{z}} \tag{.14}$$

iii.

$$\alpha = \boldsymbol{x}^T \boldsymbol{A} \boldsymbol{x}$$

$$\frac{\partial \alpha}{\partial \boldsymbol{x}} = \boldsymbol{x}^T (\boldsymbol{A} + \boldsymbol{A}^T) \tag{.15}$$

iv. If

$$\alpha = \boldsymbol{y}^T \boldsymbol{x},$$

then

$$\frac{\partial \alpha}{\partial \boldsymbol{z}} = \boldsymbol{x}^T \frac{\partial \boldsymbol{y}}{\partial \boldsymbol{z}} + \boldsymbol{y}^T \frac{\partial \boldsymbol{x}}{\partial \boldsymbol{z}} \tag{.16}$$

v. The most important one is

$$\alpha = \boldsymbol{x}^T \boldsymbol{A} \boldsymbol{x},$$

then

$$\frac{\alpha}{\partial \boldsymbol{z}} = \boldsymbol{x}^T (\boldsymbol{A} + \boldsymbol{A}^T) \frac{\partial \boldsymbol{x}}{\partial \boldsymbol{z}} \tag{.17}$$

$$\begin{aligned} \boldsymbol{g} &= \frac{\partial \chi^2}{\partial \boldsymbol{a}} = -\boldsymbol{A}^T \boldsymbol{W} \boldsymbol{y} + (\boldsymbol{A}^T \boldsymbol{W} \boldsymbol{A}) \boldsymbol{a} \\ \boldsymbol{H} &= \frac{\partial^2 \chi^2}{\partial a_i a_j} = (\boldsymbol{A}^T \boldsymbol{W} \boldsymbol{A}) \end{aligned} \tag{.18}$$

Solution (from $\partial F / \partial \boldsymbol{a} = 0$) is linear transformation of the data vector $\boldsymbol{y}$:

$$\hat{\boldsymbol{a}} = \left[(\boldsymbol{A}^T \boldsymbol{W} \boldsymbol{A})^{-1} \boldsymbol{A}^T \boldsymbol{W} \right] \boldsymbol{y} = \boldsymbol{B} \boldsymbol{y} \tag{.19}$$

Covariance matrix of $\hat{\boldsymbol{a}}$ by "error" propagation:

$$\begin{aligned} V[\hat{\boldsymbol{a}}] &= \boldsymbol{B} V[\boldsymbol{y}] \boldsymbol{B}^T \\ &= \left[(\boldsymbol{A}^T \boldsymbol{W} \boldsymbol{A})^{-1} \boldsymbol{A}^T \boldsymbol{W} \right] \cdot \boldsymbol{W}^{-1} \cdot \left[(\boldsymbol{A}^T \boldsymbol{W} \boldsymbol{A})^{-1} \boldsymbol{A}^T \boldsymbol{W} \right]^T \\ &= (\boldsymbol{A}^T \boldsymbol{W} \boldsymbol{A})^{-1} \boldsymbol{A}^T \boldsymbol{W} \cdot \boldsymbol{W}^{-1} \cdot \boldsymbol{W} \boldsymbol{A} (\boldsymbol{A}^T \boldsymbol{W} \boldsymbol{A})^{-1} \\ &= (\boldsymbol{A}^T \boldsymbol{W} \boldsymbol{A})^{-1} \\ &= \text{inverse of } \boldsymbol{H} \end{aligned} \tag{.20}$$

A.3.2 Combine Electron and Muon Channels

In the analysis of this thesis, angular coefficients and their convariance matrices are determined separately for electrons and muon. They are combined by the following equations:

$$\begin{aligned} \boldsymbol{C}^{-1} &= \boldsymbol{C}_1^{-1} + \boldsymbol{C}_2^{-1} \\ \boldsymbol{a} &= \boldsymbol{C}(\boldsymbol{C}_1^{-1}\boldsymbol{a}_1 + \boldsymbol{C}_2^{-1}\boldsymbol{a}_2), \end{aligned}$$

which maybe described by experessing the total total χ^2 of the two different measurements and assuming they are independent.

$$\begin{aligned} \chi_1^2 &= \frac{1}{2}(\boldsymbol{y}_1 - \boldsymbol{A}_1\boldsymbol{a}_1)^T\boldsymbol{W}_1(\boldsymbol{y}_1 - \boldsymbol{A}_1\boldsymbol{a}_1) \\ \chi_2^2 &= \frac{1}{2}(\boldsymbol{y}_2 - \boldsymbol{A}_2\boldsymbol{a}_2)^T\boldsymbol{W}_2(\boldsymbol{y}_2 - \boldsymbol{A}_2\boldsymbol{a}_2) \\ \chi^2 &= \chi_1^2 + \chi_2^2 \end{aligned}$$

It's not difficult to derive the results from using

$$\begin{aligned} \boldsymbol{g} &= \frac{\partial\chi^2}{\partial\boldsymbol{a}} \\ \boldsymbol{H} &= \frac{\partial^2\chi^2}{\partial a_i a_j}, \end{aligned} \tag{.21}$$

which χ^2 is now the sum of those two $\chi_i^2 (i = 1, 2)$ represents two independent channels.

A.4 DERIVATION OF THE FORWARD-BACKWARD ASYMMETRY IN THE NORMAL DIRECTION

In this section a relationship between the forward-backward asymmetry in the normal direction [139, 140], $A_{\rm FB}^{\rm N}$, is derived as well as the quantities measured in this analysis. $A_{\rm FB}^{\rm N}$ is not a separate independent observable but is completely determined by $\vec{\alpha} \equiv \left\{ f_1, f_1^+, f_0^+, \delta_+, \delta_-, P \right\}$ and therefore it can be calculated and compared with the measurement in Ref. [139, 140]. The derivation is most easily accomplished starting from expressions from the *two-angle analysis*, where the normalized double-differential decay rate $\rho(\theta^*, \phi^*)$ is expressed in spherical harmonics:

$$\rho(\theta^*, \phi^*) = \sum_{lm} a_{lm} Y_l^m(\theta^*, \phi^*). \tag{.22}$$

The asymmetry $A_{\rm FB}^{\rm N}$ is simply defined in the interval $[-1, 1]$ as

$$A_{\rm FB}^{\rm N} = \frac{N_{\rm evt}(\cos\phi^* > 0) - N_{\rm evt}(\cos\phi^* < 0)}{N_{\rm evt}(\cos\phi^* > 0) + N_{\rm evt}(\cos\phi^* < 0)} \tag{.23}$$

being $N_{\rm evt}(\cos\phi^* > 0)$ and $N_{\rm evt}(\cos\phi^* < 0)$ the number of events in each hemisphere in $\cos\phi^*$. These can be derived from Equation .22 by integration over their corresponding hemispheres

$$\begin{aligned} N_{\rm evt}(\cos\phi^* > 0) &= \int_0^{\pi} d\phi^* \int_0^{\pi} d\theta^* a_{lm} Y_l^m(\theta^*, \phi^*) d\cos\theta^*, \\ N_{\rm evt}(\cos\phi^* < 0) &= \int_{\pi}^{2\pi} d\phi^* \int_0^{\pi} d\theta^* a_{lm} Y_l^m(\theta^*, \phi^*) d\cos\theta^*. \end{aligned} \tag{.24}$$

In addition, the normalization of the PDF requires that

$$N_{\rm evt}(\cos\phi^* > 0) + N_{\rm evt}(\cos\phi^* < 0) = 1. \tag{.25}$$

The integration of ϕ^* is simple, and the asymmetry is only generated by $m \neq 0$ terms

$$A_{\rm FB}^{\rm N} = N_{\rm evt}(\cos\phi^* > 0) - N_{\rm evt}(\cos\phi^* < 0) = 2 \sum_{0<l<2}^{-l\le m\le l, m\neq 0} \int_0^\pi a_{lm} \sqrt{\frac{2l+1}{4\pi}} \sqrt{\frac{(l-m)!}{(l+m)!}} P_l^m(\cos\theta^*) \frac{(-1)^m - 1}{im} \cdot d\cos\theta^*.$$

Let

$$R_l^m = \int_0^\pi P_l^m(\cos\theta) d\cos\theta. \tag{.26}$$

Explicit expressions for these integrals (from Ref. [153], and taking into account the different phase convention used there for the associated Legendre function) are:

$$\begin{aligned} R_l^m &= \frac{2m}{l} \cdot \frac{[(l/2)!]^2 (l+m)!}{[(l-m)/2]![(l+m)/2]!(l+1)!}, \quad (l, m\ even), \\ R_l^m &= -\frac{m\pi}{l \cdot 2^{2l+1}} \cdot \frac{(l+m)!(l+1)!}{\{[(l+1)/2]!\}^2 [(l-m)/2]![(l+m)/2]!} \quad (l, m\ odd), \\ R_l^m &= 0 \quad (l+m = odd). \end{aligned} \tag{.27}$$

In Ref. [12] it is shown that the only nonvanishing coefficients in the double-differential decay rate are $a_{0,0}$, $a_{1,0}$, $a_{2,0}$, $a_{1,1}$, $a_{1,-1}$, $a_{2,1}$, $a_{2,-1}$. The first three contribute nothing because $m = 0$, and $A_{\rm FB}^{\rm N}$ reduces to:

$$A_{\rm FB}^{\rm N} = -\frac{\sqrt{6\pi}}{2} \left(\frac{a_{11}}{i} + \frac{a_{1,-1}}{i} \right) = \sqrt{6\pi} {\rm Im}\left[a_{11}\right]$$

Since we know from Ref. [133]

$$a_{1,1} = -a_{1,-1}^* = P \frac{\sqrt{3\pi}}{16} \sqrt{f_1(1-f_1)} \left\{ \sqrt{f_1^+ f_0^+} e^{i\delta_+} + \sqrt{(1-f_1^+)(1-f_0^+)} e^{-i\delta_-} \right\}$$

we have

$$A_{\rm FB}^{\rm N} = \frac{3\sqrt{2}}{16} \pi P \sqrt{f_1(1-f_1)} \left\{ \sqrt{f_1^+ f_0^+} \sin\delta_+ - \sqrt{(1-f_1^+)(1-f_0^+)} \sin\delta_- \right\}. \tag{.28}$$

If the anomalous couplings are small, we have

$$\delta_- = -tan^{-1}\left((x_W^{-1} - x_W) {\rm Im}\left[g_R\right] \right) \tag{.29}$$

where $x_W = m_W/m_t$ and other quantities unaffected to first order, and under those circumstances, inserting SM values into Equation .28, we have

$$A_{\rm FB}^{\rm N} = 0.64 P {\rm Im}\left[g_{\rm R}\right], \tag{.30}$$

in agreement with Ref. [54].

The coefficient a_{11} in a *two-angle analysis* expansion of the PDF can be related to the coefficient a_{111} in the present analysis in the following way:

$$a_{11} = -\frac{\sqrt{3}}{4}\pi a_{111} \tag{.31}$$

so that Equation .28 can also be written as:

$$A_{\rm FB}^{\rm N} = -\frac{3\sqrt{2}}{4}\pi^{\frac{3}{2}}{\rm Im}\left[a_{111}\right]$$

and $A_{\rm FB}^{\rm N}$ can practically be read from the plot of the deconvolved coefficients.

Similarily, we can also derive $A_{\rm FB}^{\rm T}$, $A_{\rm FB}$ and $A_{\rm FB}^{B}$

$$\begin{aligned} A_{\rm FB}^{\rm T} &= -\frac{3\sqrt{2}}{4}\pi^{\frac{3}{2}}{\rm Re}\left[a_{111}\right] \\ A_{\rm FB} &= -\sqrt{6\pi}a_{010} \\ A_{\rm FB}^{W} &= -\sqrt{6\pi}a_{100} \\ A_{\rm FB}^{B} &= \sqrt{6\pi}a_{100} \end{aligned} \tag{.32}$$

A.5 ADDITIONAL JOINT LIKELIHOOD PROJECTIONS

The analysis performed in this note is a combined simultaneous fit to the single top-quark t-channel differential decay rate which yields a multidimensional likelihood function. This function can be calculated from the angular coefficients extracted in the analysis and projected in many ways. The most important projections have been show in Section 7.9, other projections are shown in this appendix to give a more complete picture. Thus, additional joint likelihood projections are shown in Figures A2-A3 for the generalised helicity fractions and phases. Figure A2 shows the joint likelihood profiles for δ_- and P as a function of f_0^+ while Figure A3 shows the joint likelihood profiles for the parameters f_0^+, δ_- and P as a function of f_1^+.

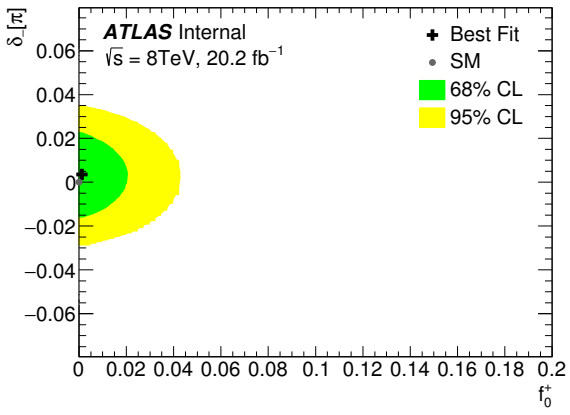

(a) δ_- vs. f_0^+ (stat. only)

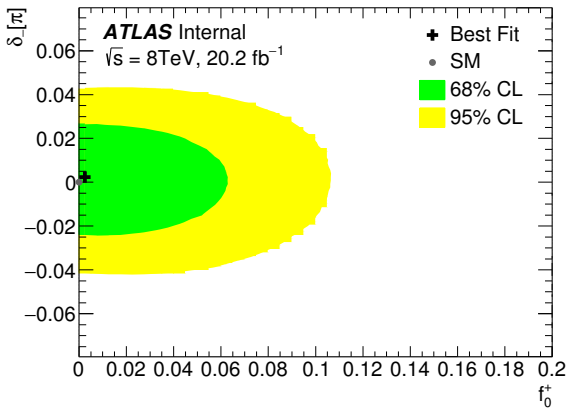

(b) δ_- vs. f_0^+ (stat. + syst.)

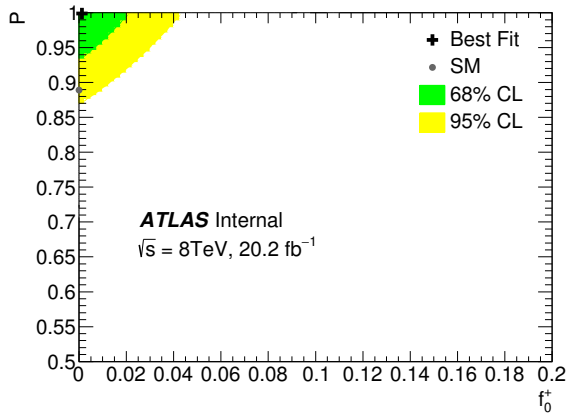

(c) P vs. f_0^+ (stat. only)

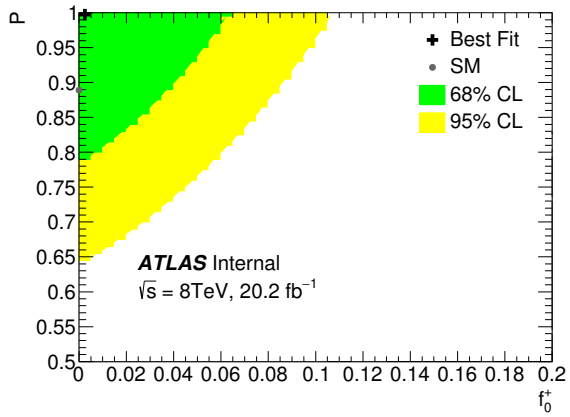

(d) P vs. f_0^+ (stat. + syst.)

Figure A2: Joint likelihood profiles for the parameters δ_- (a–b) and P (c–d) as a function of f_0^+ with statistical only (left) and statistical and systematic (right) uncertainties incorporated. The grey point represents SM expectation. Regions shown in green and yellow represent the 68% and 95% C.L., respectively. A black cross indicates the observed value.

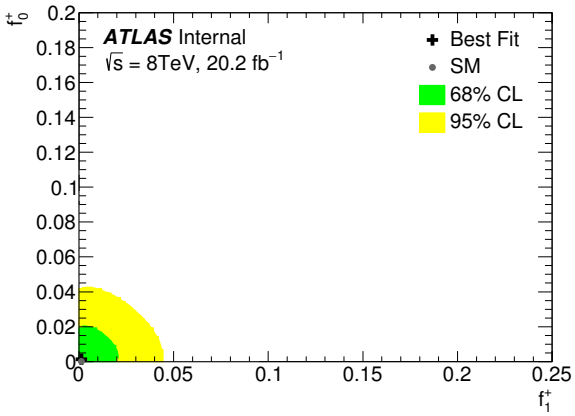

(a) f_0^+ vs. f_1^+ (stat. only)

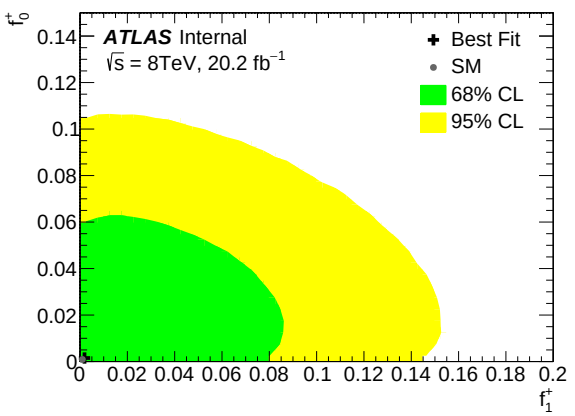

(b) f_0^+ vs. f_1^+ (stat. + syst.)

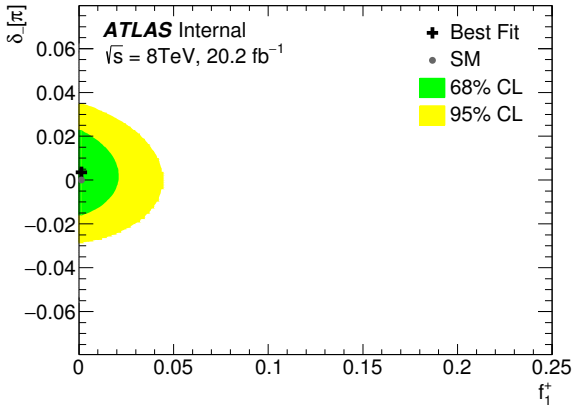

(c) δ_- vs. f_1^+ (stat. only)

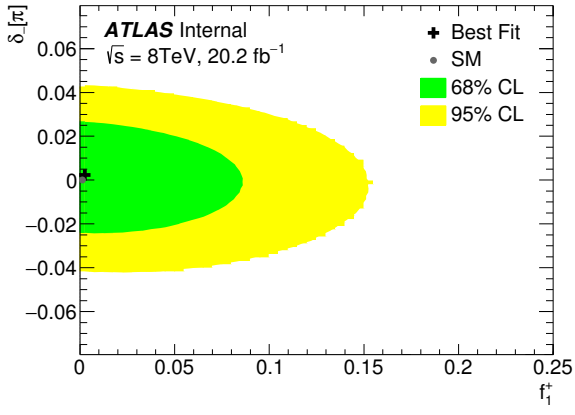

(d) δ_- vs. f_1^+ (stat. + syst.)

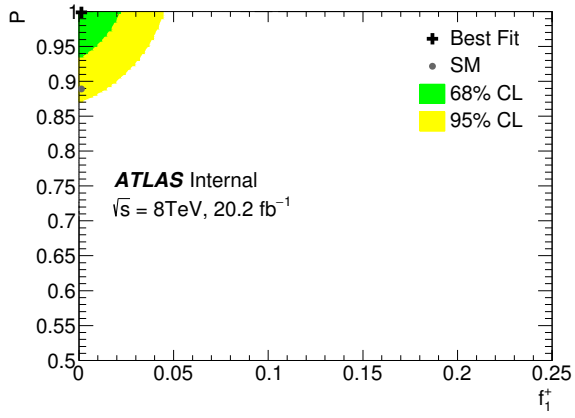

(e) P vs. f_1^+ (stat. only)

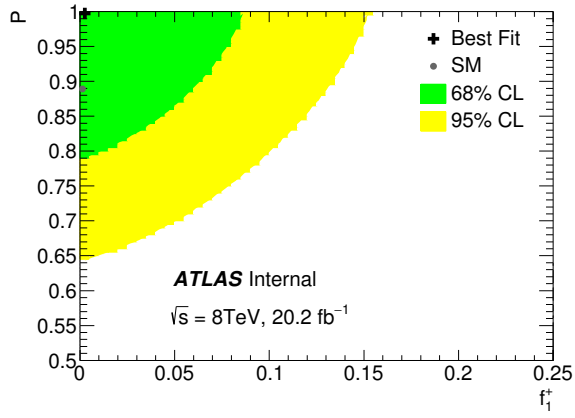

(f) P vs. f_1^+ (stat. + syst.)

Figure A3: Joint likelihood profiles for the parameters f_0^+ (a–b), δ_- (c–d) and P (e–f) as a function of f_1^+ with statistical only (left) and statistical and systematic (right) uncertainties incorporated. The grey point represents SM expectation. Regions shown in green and yellow represent the 68% and 95% C.L., respectively. A black cross indicates the observed value.

Figure A4 shows additional joint likelihood projections for the anomalous coupling constants. In particular, it shows the joint likelihood profiles for $|g_L/V_L|$ as a function of $|V_R/V_L|$.

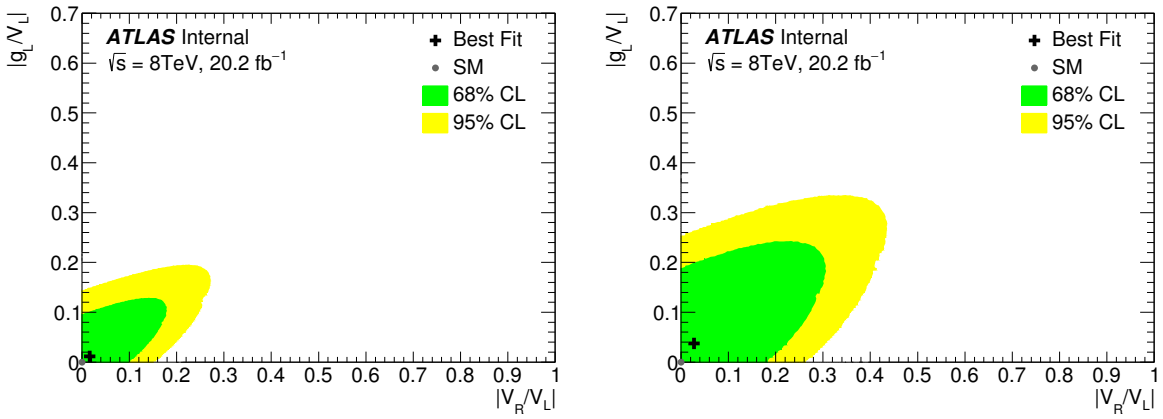

(a) $|g_L/V_L|$ vs. $|V_R/V_L|$ (stat. only)

(b) $|g_L/V_L|$ vs. $|V_R/V_L|$ (stat. + syst.)

Figure A4: Joint likelihood profiles for the parameter $|g_L/V_L|$ as a function of $|V_R/V_L|$ with statistical only (left) and statistical and systematic (right) uncertainties incorporated. The grey point represents SM expectation. Regions shown in green and yellow represent the 68% and 95% C.L., respectively. A black cross indicates the observed value.

BIBLIOGRAPHY

[1] Antonio Pich. The standard model of electroweak interactions. arXiv:0705.4264 .

[2] J.-H. Yu Q.-H. Cao, B. Yan and C. Zhang. A general analysis of wtb anomalous couplings (2015). arXiv: 1504.03785 [hep-ph].

[3] Martin Wiebusch Werner Bernreuther, Patrick Gonzalez. The top quark decay vertex in standard model extensions. arXiv:0812.1643[hep-ex].

[4] Florent Fayette. Strategies for precision measurements of the charge asymmetry of the w boson mass at the lhc within the atlas experiment. arXiv:0906.4260.

[5] ATLAS Collaboration. The ATLAS Experiment at the CERN Large Hadron Collider. *JINST*, 3:S08003, 2008. doi: 10.1088/1748-0221/3/08/S08003. URL http://inspirehep.net/record/796888?ln=en.

[6] ATLAS Collaboration. Atlas overview and main results,, . ATLAS-COM-PHYS-2013-310.

[7] The ATLAS Collaboration ATLAS Collaboration. *ATLAS liquid argon calorimeter:Technical design report, tech.rep.*, . CERN,1996.

[8] J.J. Goodson. *Search for Supersymmetry in States with Large Missing Transverse Momentum and Three Leptons including a Z-Boson*. PhD thesis, Stony Brook University, May 2012. URL http://inspirehep.net/record/1186191?ln=en. Presented 17 Apr 2012.

[9] The atlas luminosity measurement taskforce. http://project-atlas-lucid.web.cern.ch/project-atlas-lucid/taskforce/main.html. Accessed: 2017-01-05.

[10] A Annovi and etc. Development of ftk architecture: a fast hardware track trigger for the atlas detector. arXiv:0910.1126.

[11] ATLAS Collaboration. Performance of Missing Transverse Momentum Reconstruction in ATLAS studied in Proton-Proton Collisions recorded in 2012 at 8 TeV. ATLAS-CONF-2013-082, 2013. URL https://cds.cern.ch/record/1570993.

[12] ATLAS Collaboration. Search for anomalous couplings in the Wtb vertex from the measurement of double differential angular decay rates of single top quarks produced in the t-channel with the ATLAS detector. *JHEP*, 04:023, 2016. doi: 10.1007/JHEP04(2016)023. URL https://arxiv.org/abs/1510.03764.

[13] J. J. Thomson M.A. F.R.S. *XL. Cathode Rays.* Philosophical Magazine. 44 (269): 293316. doi:10.1080/14786449708621070.

[14] Ernest Rutherford (1911). *The scattering of alpha and beta particles by matter and the structure of the atom.* Philosophical Magazine, volume 21 (1911), pages 669-688.

[15] James (1932). Chadwick. *Possible Existence of a Neutron.* Nature. 129 (3252): 312.

[16] Chen Ning Yang. *Elementary particles.* a short history of some discoveries in atomic physics.

[17] P. A. M. Dirac (1928). *The Quantum Theory of the Electron.* Proceedings of the Royal Society A. 117 (778): 610624. .

[18] C. D. (1933). Anderson. *The Positive Electron.* Physical Review. 43 (6): 491494.

[19] Ivar Waller. *The Noble Foundation (1949).* Nobel Prize in Physics 1949 Presentation Speech.

[20] H. Yukawa. *On the Interaction of Elementary Particles.* Proc. Phys. Math. Soc. Jap. 17 (48).

[21] SETH H. NEDDERMEYER and CARL. D. ANDERSON. *Note on the Nature of Cosmic-Ray Particles.* Phys. Rev., Vol. 51, 884.

[22] H.; Occhialini Lattes, C. M. G.; Muirhead and etc. *Processes Involving Charged Mesons.* Nature 159, 694-697 (24 May 1947).

[23] C.C. Butler G.D. Rochester. *Evidence for the Existence of New Unstable Elementary Particles.* Nature 160 (1947) 855-857.

[24] Steven Weinberg. *A Model of Leptons.* Phys. Rev. Lett. 19, 1264 Published 20 November 1967.

[25] S.L. Glashow. *Partial Symmetries of Weak Interactions.* Nucl.Phys. 22 (1961) 579-588.

[26] Slam. *Weak and Electromagnetic Interactions.* Selected papers of Abdus Salam* 244-254.

[27] Peter W. Higgs. *Broken Symmetries and the Masses of Gauge Bosons*, . 1964PhRvL..13..508H.

[28] ATLAS; CMS (26 March 2015). *Combined Measurement of the Higgs Boson Mass in pp Collisions at s=7 and 8 TeV with the ATLAS and CMS Experiments.* arXiv:1503.07589Freely accessible.

[29] Peter W. Higgs. *Broken Symmetries and the Masses of Gauge Bosons*, . 1964PhRvL..13..508H.

[30] G. S. Guralnik et al. *Global Conservation Laws and Massless Particles.* Phys. Rev. Lett. 13, 585 Published 16 November 1964.

[31] Gerald S. Guralnik. *The History of the Guralnik, Hagen and Kibble development of the Theory of Spontaneous Symmetry Breaking and Gauge Particles.* arXiv:0907.3466.

[32] G Zweig. *TAn SU3 model for strong interaction symmetry and its breaking.* CERN-TH-401.

[33] M. Y. Han and Y. Nambu. *Three-Triplet Model with Double SU(3) Symmetry.* Physical Review, vol. 139, Issue 4B, pp. 1006-1010,1965PhRv..139.1006H.

[34] O. W. Greenberg. *Spin and Unitary-Spin Independence in a Paraquark Model of Baryons and Mesons.* Phys. Rev. Lett. 13, 598 Published 16 November 1964.

[35] H. David Politzer. *Reliable Perturbative Results for Strong Interactions?* Phys. Rev. Lett. 30, 1346 Published 25 June 1973.

[36] David J. Gross and Frank Wilczek. *Ultraviolet Behavior of Non-Abelian Gauge Theories.* Phys. Rev. Lett. 30, 1343 Published 25 June 1973.

[37] The ALEPH Collaboration and etc al. *Electroweak Measurements in Electron-Positron Collisions at W-Boson-Pair Energies at LEP.* arXiv:1302.3415.

[38] J. Beringer; et al. (2012). *2012 Review of Particle Physics - Gauge and Higgs Bosons.* 2012PhRvD..86a0001B.

[39] E. J. Konopinski. *Fermi's Theory of Beta-Decay.* Rev. Mod. Phys. 27, 254 Published 1 July 1955.

[40] E. Ambler C. S. Wu and et al. *Experimental Test of Parity Conservation in Beta Decay.* Phys. Rev. 105, 1413 Published 15 February 1957.

[41] Alan Douglas Martin F. Halzen. Quarks and leptons: An introductory course in modern particle physics,wiley press.

[42] M. Gell-Mann. The interpretation of the new particles as displaced charge multiplets. *Il Nuovo Cimento (1955-1965)*, 4(2):848–866, 1956. ISSN 1827-6121. doi: 10.1007/BF02748000. URL http://dx.doi.org/10.1007/BF02748000.

[43] Vernon D.Barger and Roger J.N.Phillips. Collider physics,westview press.

[44] Nicola Cabibbo. Unitary symmetry and leptonic decays. Phys. Rev. Lett. 10, 531 Published 15 June 1963.

[45] J. Iliopoulos S. L. Glashow and etc. Weak interactions with lepton-hadron symmetry. Phys. Rev. D 2, 1285Published 1 October 1970.

[46] ATLAS Collaboration. Measurement of the $t\bar{t}$ production cross-section using $e^{-}\mu$ events withb-tagged jets in pp collisions at $\sqrt{s} = 7$ and 8 tev with the atlas detector,, . arXiv:1406.5375,.

[47] ATLAS Collaboration. *Fiducial, total and differential cross-section measurements of t-channel single top-quark production in pp collisions at 8 TeV using data collected by the ATLAS detector*, . arXiv:1702.02859.

[48] M. Jezabek and J. H. Kuhn. *QCD Corrections to Semileptonic Decays of Heavy Quarks*. Nucl. Phys. B 314, 1 (1989).

[49] Y. L. Dokshitzer I. I. Y. Bigi and et al. *Production and Decay Properties of Ultraheavy Quarks*. Phys. Lett. B 181, 157 (1986).

[50] W. Buchmuller and D. Wyler. Effective lagrangian analysis of new interactions and flavor conservation. Nucl. Phys.B268(1968)621.

[51] J. A. Aguilar-Saavedra. A minimal set of top anomalous couplings, . Nucl.Phys.B812(2009)181,arXiv:hep-ph/0811.3842.

[52] J. A. Aguilar-Saavedra. A minimal set of top-higgs anomalous couplings, . Nucl.Phys.B821(2009)215, arXiv:hep-ph/0904.2387.

[53] Chong Sheng Li Jun Gao and Hua Xing Zhu4. *Top-Quark Decay at Next-to-Next-to-Leading Order in QCD*. PRL 110, 042001 (2013).

[54] J.A. Aguilar-Saavedra and J. Bernabeu. W polarisation beyond helicity fractions in top quark decays. Nucl. Phys. B 840 (2010) 349.

[55] M. Jacob and G. C. Wick. On the general theory of collisions for particles with spin. *Annals Phys.*, 7:404–428, 1959. doi: 10.1016/0003-4916(59)90051-X. URL `http://www.sciencedirect.com/science/article/pii/S0003491600960226`.

[56] B. Grzadkowski and M. Misiak. Anomalous wtb coupling effects in the weak radiative b-meson decay. arXiv:0802.1413.

[57] ATLAS Collaboration. Measurement of the w boson polarization in top quark decays with the atlas detector, . arXiv:1205.2484 [hep-ex].

[58] CMS Collaboration. Measurement of the w-boson helicity in top-quark decays from $t\bar{t}$ production in lepton+jets events in pp collisions at $\sqrt{s} = 7$ tev, . arXiv:1308.3879 [hep-ex].

[59] ATLAS Collaboration. Comprehensive measurements of t-channel single top-quark production cross sections at $\sqrt{s} = 7$ tev with the atlas detector, . arXiv:1406. 7844 [hep-ex].

[60] CMS Collaboration. Measurement of the single-top-quark t-channel cross section in pp collisions at $\sqrt{s} = 7$tev, . arXiv:1209.4533 [hep-ex].

[61] K. Schmitz K. Hsieh and etc. Global analysis of general $su(2)su(2)u(1)$ models with precision data. arXiv:1003.3482.

[62] Robert J. Oakes Junjie Cao and etc. Supersymmetric effects in top quark decay into polarized w-boson. arXiv:hep-ph/0306278.

[63] Gabriel A. Gonzalez-Sprinberg and etc. Top quark tensor couplings. arXiv:1105.5601.

[64] Thomas Kramer Roberto Contino and etc. Warped/composite phenomenology simplified. arXiv:hep-ph/0612180.

[65] Oliver Sim Brning and etc. Lhc design report,. Report number CERN-2004-003-V-1.

[66] About cern. https://home.cern/about, . Accessed: 2017-01-05.

[67] CERN-LEP-84-01. *LEP deisign report*. CERN,Geneva,1984.

[68] The ALICE Collaboration. The alice experiment at the cern lhc, . Journal of Instrumentation 3, S08004 (2008).

[69] The CMS Collaboration. The cms experiment at the cern lhc, . Journal of Instrumentation 3, S08004 (2008).

[70] THE ATLAS COLLABORATION. *Journal of Instrumentation 3*. S08003(2008).

[71] The LHCb Collaboration. The lhcb experiment at the cern lhc, . Journal of Instrumentation 3, S08004 (2008).

[72] The accelerator complex. https://home.cern/about/accelerators, . Accessed: 2017-01-05.

[73] Linear accelerator 2. https://home.cern/about/accelerators/linear-accelerator-2, . Accessed: 2017-01-05.

[74] Mike Lamont. Status of the lhc. Journal of Physics:Conference Series 455 (2013) 012001,doi:10.1088/1742-6596/455/1/012001.

[75] ATLAS Collaboration. Inner detector technical design report, vol. i, . CERN/LHCC/97-16, 1997.

[76] ATLAS Collaboration. Inner detector technical design report, vol. ii, . CERN/LHCC/97-17, 1997.

[77] THE ATLAS COLLABORATION. *ATLAS Pixel Detector Technical Design Report.* CERN LHCC 98-13(May 1988).

[78] Fabian. Hugging. Studies on atlas pixel modules. International Workshop on Semiconductor Pixel Detectors for Particles and X-Ray (Pixel 2002), Carmel, CA. 2002.

[79] G. et al. Aad. Atlas pixel detector electronics and sensors. Journal of Instrumentation, 07/2008, Volume 3, Issue 7.

[80] INP) M. Turala (Cracow. *Silicon tracking detectors: Historical overview.* Nucl. Instrum. Meth. A541 89-95(2005).

[81] et al. Kondo, Taka. Construction and performance of the atlas silicon microstrip barrel modules. Nuclear Instruments and Methods in Physics Research Section A: Accelerators, Spectrometers, Detectors and Associated Equipment 485.1 (2002): 27-42.

[82] The ATLAS TRT Collaboration. The atlas transition radiation tracker (trt) proportional drift tube: design and performance. Journal of Instrumen-tation,2008.

[83] T. kesson et al. Aging studies for the atlas transition radiation tracker (trt). Nucl. Instrum.Meth. A 515 (2003) 166.

[84] T. Akesson et al. Status of design and construction of the trt for the atlas experiment at the lhc,. Nuclear Instruments and Methods in Physics Research A 522 (2004) 131145.

[85] The ATLAS Collaboration ATLAS Collaboration. *ATLAS tile calorimeter:Technical design report, tech.rep.*, . CERN,1996.

[86] Sandro Palestini. The muon spectrometer of the atlas experiment. ATL-COM-MUON-2003-005.

[87] Stefan Ask. Status of the forward physics projects in atlas. arXiv:0706.0644.

[88] ATLAS Collaboration. Atlas central solenoid: Technical design report, tech. rep., . ATLAS-TDR-6 ; CERN-LHCC-97-018, Geneva : CERN, 1997. - 101 p.

[89] ATLAS Collaboration. Performance of the ATLAS Trigger System in 2010. *Eur. Phys. J.*, C72:1849, 2012. doi: 10.1140/epjc/s10052-011-1849-1. URL `https://link.springer.com/article/10.1140/epjc/s10052-011-1849-1`.

[90] ATLAS Collaboration. Expected Performance of the ATLAS Experiment - Detector, Trigger and Physics. 2009. URL `https://cds.cern.ch/record/1125884?ln=en`.

[91] Peter Jenni and etc. Atlas high-level trigger, data-acquisition and controls : Technical design report. ATLAS-TDR-16 ; CERN-LHCC-2003-022.

[92] Rudolph Kalman and Emil. A new approach to linear filtering and prediction problems. Transactions of the ASME Journal of Basic Engineering 82 no. Series D, (1960).

[93] ATLAS Collaboration. Reconstruction of primary vertices at the atlas experiment in run 1 proton-proton collisions at the lhc, . arXiv:1611.10235.

[94] Rudolf Frhwirth Wolfgang Waltenberger and Pascal Vanlaer2. Adaptive vertex fitting. Journal of Physics G: Nuclear and Particle Physics 34 no. 12, (2007) N343.

[95] Matteo Cacciari, Gavin P. Salam, and Gregory Soyez. The Anti-k(t) jet clustering algorithm. *JHEP*, 04:063, 2008. doi: 10.1088/1126-6708/2008/04/063. URL https://arxiv.org/abs/0802.1189.

[96] G. Aad et al. ATLAS Collaboration. *Electron performance measurements with the ATLAS detector using the 2010 LHC proton-proton collision data*, . arXiv:1110.3174.

[97] ATLAS Collaboration. Electron reconstruction and identification efficiency measurements with the ATLAS detector using the 2011 LHC proton-proton collision data. *Eur. Phys. J.*, C74(7):2941, 2014. doi: 10.1140/epjc/s10052-014-2941-0. URL https://arxiv.org/abs/1404.2240.

[98] ATLAS Collaboration. Measurement of the muon reconstruction performance of the ATLAS detector using 2011 and 2012 LHC protonproton collision data. *Eur. Phys. J.*, C74(11):3130, 2014. doi: 10.1140/epjc/s10052-014-3130-x. URL https://arxiv.org/abs/1407.3935.

[99] ATLAS Collaboration. Top Reconstruction Group twiki. 2015. URL https://twiki.cern.ch/twiki/bin/view/AtlasProtected/TopReconstructionGroup.

[100] ATLAS Collaboration. Object selection and calibration, background estimations and MC samples for top quark analyses using the full 2012 data set. (ATL-COM-PHYS-2013-1016), 2013. URL https://cds.cern.ch/record/1563201.

[101] ATLAS Collaboration. Topcommonobjects twiki. 2014. URL http://twiki.cern.ch/twiki/bin/view/AtlasProtected/TopCommonObjects.

[102] ATLAS Collaboration. Electron efficiency measurements with the ATLAS detector using the 2012 LHC proton-proton collision data. (ATLAS-CONF-2014-032), 2014. URL https://cds.cern.ch/record/1706245.

[103] ATLAS Collaboration. Measurement of the b-tag Efficiency in a Sample of Jets Containing Muons with 5 fb-1 of Data from the ATLAS Detector. ATLAS-CONF-2012-043, 2012. URL https://cds.cern.ch/record/1435197.

[104] ATLAS Collaboration. Calibration of the performance of b-tagging for c and light-flavour jets in the 2012 ATLAS data. ATLAS-CONF-2014-046, 2014. URL http://cdsweb.cern.ch/record/1741020.

[105] ATLAS Collaboration. Luminosity determination in pp collisions at $\sqrt{s} = 8$ TeV using the ATLAS detector at the LHC. *Eur. Phys. J.*, C76(12):653, 2016. doi: 10.1140/epjc/s10052-016-4466-1. URL http://inspirehep.net/record/1481187?ln=en.

[106] Matthew D.Schwartz. Quantum field theory and the standard model. Page 422.

[107] Y. L. Dokshitzer. Calculation of the structure functions for deep inelastic scattering and e+e annihilation by perturbation theory in quantum chromodynamics. Sov. Phys. JETP 46 (1977) 641653.

[108] V. N. Gribov and L. N. Lipatov. Deep inelastic ep scattering in perturbation theory. Sov. J. Nucl. Phys. 15 (1972) 438450.

[109] Marilyn Marx Michael H. Seymour. *Monte Carlo Event Generators*. arXiv:1304.6677.

[110] Torbjrn Sjstrand. *Monte Carlo Tools*. arXiv:0911.5286.

[111] ATLAS Collaboration. MC12a twiki. 2014. URL https://twiki.cern.ch/twiki/bin/viewauth/AtlasProtected/AtlasProductionGroupMC12a.

[112] ATLAS Collaboration. MC12b twiki. 2014. URL https://twiki.cern.ch/twiki/bin/viewauth/AtlasProtected/AtlasProductionGroupMC12b.

[113] ATLAS Collaboration. The ATLAS Simulation Infrastructure. *Eur. Phys. J.*, C70: 823–874, 2010. doi: 10.1140/epjc/s10052-010-1429-9. URL https://arxiv.org/abs/1005.4568.

[114] S. Agostinelli et al. GEANT4: A Simulation toolkit. *Nucl. Instrum. Meth.*, A506: 250–303, 2003. doi: 10.1016/S0168-9002(03)01368-8. URL http://inspirehep.net/record/593382?ln=en.

[115] Elzbieta Richter-Was, D. Froidevaux, and Luc Poggioli. ATLFAST 2.0 a fast simulation package for ATLAS. ATL-PHYS-98-131, 1998. URL https://cds.cern.ch/record/683751.

[116] J. Pumplin, D. R. Stump, J. Huston, H. L. Lai, Pavel M. Nadolsky, and W. K. Tung. New generation of parton distributions with uncertainties from global QCD analysis. *JHEP*, 07:012, 2002. doi: 10.1088/1126-6708/2002/07/012. URL https://arxiv.org/abs/hep-ph/0201195.

[117] Borut Paul Kersevan and Elzbieta Richter-Was. The Monte Carlo event generator AcerMC versions 2.0 to 3.8 with interfaces to PYTHIA 6.4, HERWIG 6.5 and ARIADNE 4.1. *Comput. Phys. Commun.*, 184:919–985, 2013. doi: 10.1016/j.cpc.2012.10.032. URL https://arxiv.org/abs/hep-ph/0405247.

[118] Borut Paul Kersevan and Ian Hinchliffe. A Consistent prescription for the production involving massive quarks in hadron collisions. *JHEP*, 09:033, 2006. doi: 10.1088/1126-6708/2006/09/033. URL https://arxiv.org/abs/hep-ph/0603068.

[119] ATLAS Collaboration. *Search for anomalous couplings in the Wtb vertex from the measurement of triple differential angular decay rates of single top quarks produced in the t-channel at $\sqrt{s} = 8$ TeV with the ATLAS detector*, . ATLAS-TOPQ-2015-11-001.

[120] ATLAS Collaboration. Estimation of non-prompt and fake lepton backgrounds in final states with top quarks produced in proton-proton collisions at $\sqrt{s} = 8$ TeV with the ATLAS detector. ATLAS-CONF-2014-058, 2014. URL https://cds.cern.ch/record/1951336.

[121] ATLAS Collaboration. Measurement of the t-channel single top-quark production cross section in pp collisions at $\sqrt{s} = 7$ TeV with the ATLAS detector. *Phys. Lett.*, B717: 330–350, 2012. doi: 10.1016/j.physletb.2012.09.031. URL https://arxiv.org/abs/1205.3130.

[122] Peter Baernreuther, Michal Czakon, and Alexander Mitov. Percent Level Precision Physics at the Tevatron: First Genuine NNLO QCD Corrections to $q\bar{q} \to t\bar{t} + X$. *Phys.Rev.Lett.*, 109:132001, 2012. doi: 10.1103/PhysRevLett.109.132001. URL https://journals.aps.org/prl/abstract/10.1103/PhysRevLett.109.132001.

[123] Michal Czakon and Alexander Mitov. Top++: A Program for the Calculation of the Top-Pair Cross-Section at Hadron Colliders, 2011. URL https://arxiv.org/abs/1112.5675.

[124] Michal Czakon and Alexander Mitov. NNLO corrections to top-pair production at hadron colliders: the all-fermionic scattering channels. *JHEP*, 1212:054, 2012. doi: 10.1007/JHEP12(2012)054. URL https://link.springer.com/article/10.1007/JHEP12(2012)054.

[125] Michal Czakon and Alexander Mitov. NNLO corrections to top pair production at hadron colliders: the quark-gluon reaction. *JHEP*, 1301:080, 2013. doi: 10.1007/JHEP01(2013)080. URL https://arxiv.org/abs/1210.6832.

[126] Michal Czakon, Paul Fiedler, and Alexander Mitov. The total top quark pair production cross-section at hadron colliders through $O(alpha_S^4)$. *Phys. Rev. Lett.*, 110:252004, 2013. doi: 10.1103/PhysRevLett.110.252004. URL https://arxiv.org/abs/1303.6254.

[127] Matteo Cacciari, Michal Czakon, Michelangelo Mangano, Alexander Mitov, and Paolo Nason. Top-pair production at hadron colliders with next-to-next-to-leading logarithmic soft-gluon resummation. *Phys. Lett. B*, 710:612–622, 2012. doi: 10.1016/j.physletb.2012.03.013. URL https://arxiv.org/abs/1111.5869.

[128] Charalampos Anastasiou, Lance J. Dixon, Kirill Melnikov, and Frank Petriello. High precision QCD at hadron colliders: Electroweak gauge boson rapidity distributions at NNLO. *Phys. Rev.*, D69:094008, 2004. doi: 10.1103/PhysRevD.69.094008. URL https://arxiv.org/abs/hep-ph/0312266.

[129] B Acharya, J-F Arguin, M Barisonzi, IM Besana, M Bosman, IC Brock, R Calkins, D Charkaborty, M Cobal, M Cristinziani, J Ferrando, L Fiorini, A Henrichs, B Heinemann, C Helsens, G Khoriauli, T Kuhl, A Juste, T Lari, F Meloni, L Mir, J Nadal, E Nuncio-Quiroz, M Pinamonti, B Radics, U de Sanctis, E Shabalina, L-Y Shan, K Suruliz, DB Ta, C Troncon, and V Vorwerk. Estimation of the W+Jets Background for Top Quark Re-Discovery in the Single Lepton+Jets Channel. ATL-PHYS-INT-2010-136, Dec 2010. URL https://cds.cern.ch/record/1312980.

[130] John M. Campbell, R. Keith Ellis, and Ciaran Williams. Vector boson pair production at the LHC. *JHEP*, 07:018, 2011. doi: 10.1007/JHEP07(2011)018. URL https://arxiv.org/abs/1105.0020.

[131] ATLAS Collaboration. Measurement of the top quark pair production cross-section with ATLAS in the single lepton channel. *Phys. Lett.*, B711:244–263, 2012. doi: 10.1016/j.physletb.2012.03.083. URL https://arxiv.org/abs/1201.1889.

[132] ATLAS Collaboration. Comprehensive measurements of t-channel single top-quark production cross sections at $\sqrt{s} = 7$ TeV with the ATLAS detector. *Phys. Rev.*, D90 (11):112006, 2014. doi: 10.1103/PhysRevD.90.112006. URL https://arxiv.org/abs/1406.7844.

[133] Joseph Boudreau, Carlos Escobar, James Mueller, Kevin Sapp, and Jun Su. Single top quark differential decay rate formulae including detector effects, 2013. URL https://arxiv.org/abs/1304.5639.

[134] Joseph Boudreau, Carlos Escobar, James Mueller, and Jun Su. Deconvolving the detector in Fourier space. *J. Phys. Conf. Ser.*, 762(1):012041, 2016. doi: 10.1088/1742-6596/762/1/012041. URL http://iopscience.iop.org/article/10.1088/1742-6596/762/1/012041/meta.

[135] M. Fischer, S. Groote, J. G. Korner, and M. C. Mauser. Complete angular analysis of polarized top decay at $O(\alpha_s)$. *Phys. Rev.*, D65:054036, 2002. doi: 10.1103/PhysRevD.65.054036. URL https://arxiv.org/abs/hep-ph/0101322.

[136] Stuart C. Schwartz. Estimation of probability density by an orthogonal series. *Ann. Math. Statist.*, 38(4):1261–1265, 08 1967. URL http://dx.doi.org/10.1214/aoms/1177698795.

[137] S. Brooks, A. Gelman, G. Jones, and X.L. Meng. *Handbook of Markov Chain Monte Carlo*. Chapman & Hall/CRC Handbooks of Modern Statistical Methods. CRC Press, 2011. ISBN 9781420079425. URL https://books.google.ch/books?id=qfRsAIKZ4rIC.

[138] J. von Neumann. Various techniques used in connection with random digits. monte carlo method. *Appl. Math. Series*, 12:36–38, 1951. URL https://dornsifecms.usc.edu/assets/sites/520/docs/VonNeumann-ams12p36-38.pdf.

[139] ATLAS Collaboration. Search for $\mathcal{CP}$ violation in single top quark events in pp collisions at $\sqrt{s} = 7$ TeV with the ATLAS detector. (ATLAS-CONF-2013-032), 2013. URL https://cds.cern.ch/record/1527128.

[140] ATLAS Collaboration. Probing the Wtb vertex structure with t-channel single top-quark events in pp collisions at $\sqrt{s} = 8$ TeV with the ATLAS detector. (ATLAS-CONF-2016-097), Sep 2016. URL https://cds.cern.ch/record/2216165.

[141] Gary J. Feldman and Robert D. Cousins. A Unified approach to the classical statistical analysis of small signals. *Phys. Rev.*, D57:3873–3889, 1998. doi: 10.1103/PhysRevD.57.3873. URL https://arxiv.org/abs/physics/9711021.

[142] ATLAS Collaboration. Jet energy measurement and its systematic uncertainty in proton-proton collisions at $\sqrt{s} = 7$ TeV with the ATLAS detector. *Eur. Phys. J.*, C75:17, 2015. doi: 10.1140/epjc/s10052-014-3190-y. URL https://arxiv.org/abs/1406.0076.

[143] ATLAS Collaboration. Jet energy resolution in proton-proton collisions at $\sqrt{s} = 7$ TeV recorded in 2010 with the ATLAS detector. *Eur. Phys. J.*, C73(3):2306, 2013. doi: 10.1140/epjc/s10052-013-2306-0. URL https://arxiv.org/abs/1210.6210.

[144] ATLAS Collaboration. Calibration of b-tagging using dileptonic top pair events in a combinatorial likelihood approach with the ATLAS experiment. (ATLAS-CONF-2014-004), 2014. URL http://cdsweb.cern.ch/record/1664335.

[145] Frits A. Berends, H. Kuijf, B. Tausk, and W. T. Giele. On the production of a W and jets at hadron colliders. *Nucl. Phys.*, B357:32–64, 1991. doi: 10.1016/0550-3213(91)90458-A. URL http://inspirehep.net/record/300269?ln=en.

[146] Michiel Botje et al. The PDF4LHC Working Group Interim Recommendations, 2011.

[147] Richard D. Ball et al. Parton distributions with LHC data. *Nucl. Phys.*, B867:244–289, 2013. doi: 10.1016/j.nuclphysb.2012.10.003. URL https://arxiv.org/abs/1207.1303.

[148] Stephen Parke Gregory Mahlon. Single top quark production at the lhc: Understanding spin. arXiv:hep-ph/9912458.

[149] Reinhard Schwienhorst, C. P. Yuan, Charles Mueller, and Qing-Hong Cao. Single top quark production and decay in the t-channel at next-to-leading order at the LHC. *Phys. Rev.*, D83:034019, 2011. doi: 10.1103/PhysRevD.83.034019. URL https://journals.aps.org/prd/abstract/10.1103/PhysRevD.83.034019.

[150] M. Jezabek and Johann H. Kühn. V-A tests through leptons from polarized top quarks. *Phys. Lett.*, B329:317–324, 1994. doi: 10.1016/0370-2693(94)90779-X. URL https://arxiv.org/abs/hep-ph/9403366.

[151] Bohdan Grzadkowski and Mikolaj Misiak. Anomalous Wtb coupling effects in the weak radiative B-meson decay. *Phys. Rev.*, D78:077501, 2008. doi: 10.1103/PhysRevD.78.077501. [Erratum: Phys. Rev. **D**84, (2011) 059903].

[152] S. Willenbrock T. Stelzer, Z. Sullivan. Single-top-quark production via w-gluon fusion at next-to-leading order. arXiv:hep-ph/9705398[hep-ex].

[153] Donald W. Jepse, Eugene F. Haugh, and Joseph O. Hirschfelder. The integral of the associated legendre function. *Proceedings of the National Academy of Sciences of the United States of America*, 41(9):645–647, 1955. ISSN 00278424. URL http://www.jstor.org/stable/89148.